An ALMA View of Molecular Gas in Brightest Cluster Galaxies

by

Adrian Vantyghem

A thesis
presented to the University of Waterloo
in fulfillment of the
thesis requirement for the degree of
Doctor of Philosophy
in
Physics & Astronomy

Waterloo, Ontario, Canada, 2018

Examining Committee Membership

The following served on the Examining Committee for this thesis. The decision of the Examining Committee is by majority vote.

External Examiner:	Christine Wilson Professor, Dept. of Physics and Astronomy, McMaster University
Supervisor:	Brian McNamara Professor, Dept. of Physics and Astronomy, University of Waterloo
Internal Member:	Avery Broderick Professor, Dept. of Physics and Astronomy, University of Waterloo
Internal Member:	Niayesh Afshordi Professor, Dept. of Physics and Astronomy, University of Waterloo
Internal-External Member:	Pierre-Nicholas Roy Professor, Dept. of Chemistry, University of Waterloo

I hereby declare that I am the sole author of this thesis. This is a true copy of the thesis, including any required final revisions, as accepted by my examiners.

I understand that my thesis may be made electronically available to the public.

Statement of Contributions

Chapters 2, 3, 4, and 5 of this thesis contain original research written by myself, Adrian Vantyghem. Chapters 2, 3, and 4 have been published in the peer-reviewed journal The Astrophysical Journal (ApJ). The paper references are:

Vantyghem, A. N.; McNamara, B. R.; Russell, H. R.; Hogan, M. T.; Edge, A. C.; Nulsen, P. E. J.; Fabian, A. C.; Combes, F.; Salomé, P.; Baum, S. A.; Donahue, M.; Main, R. A.; Murray, N. W.; O'Connell, R. W.; O'Dea, C. P.; Oonk, J. B. R.; Parrish, I. J.; Sanders, J. S.; Tremblay, G.; and Voit, G. M., 2016, The Astrophysical Journal, Volume 832, Issue 2, 22 pp., doi:10.3847/0004-637X/832/2/148.

Vantyghem, A. N.; McNamara, B. R.; Edge, A. C.; Combes, F.; Russell, H. R.; Fabian, A. C.; Hogan, M. T.; McDonald, M.; Nulsen, P. E. J.; Salomé, P., 2017, The Astrophysical Journal, Volume 848, Issue 2, 12 pp., doi:10.3847/1538-4357/aa8fd0

Vantyghem, A. N.; McNamara, B. R.; Russell, H. R.; Edge, A. C.; Nulsen, P. E. J.; Combes, F.; Fabian, A. C.; McDonald, M.; Salomé, P., 2018, The Astrophysical Journal, Volume 864, Issue 2, 15 pp., doi:10.3847/1538-4357/aad2e0

Chapter 5 has been submitted for publication. The paper reference is:

Vantyghem, A. N.; McNamara, B. R.; Russell, H. R.; Edge, A. C.; Nulsen, P. E. J.; Combes, F.; Fabian, A. C.; McDonald, M.; Salomé, P., (2018). Manuscript submitted for publication.

In each of these publications, I, A. N. Vantyghem, am the first author, having analyzed the data and written the manuscript. The second author, Dr. B. R. McNamara, is my supervisor. Drs. B. R. McNamara and H. R. Russell led the proposals to obtain the data. The remaining authors are collaborators that provided comments on how to improve the manuscript before submission for publication.

Abstract

In this thesis I use ALMA observations to map the distribution and kinematics of molecular gas in the brightest cluster galaxies of three galaxy clusters: 2A0335+096, RXJ0821+0752, and RXCJ1504-0248. The goal is to understand how the coldest gas in clusters is formed, identify any long-lived structures that could fuel sustained black hole accretion, and explore star formation in cluster environments. I use the $J = 1 \rightarrow 0$ and $J = 3 \rightarrow 2$ rotational transitions of carbon monoxide (CO) as tracers of the total molecular gas distribution. The two transitions provide different resolutions and fields of view.

The molecular gas in all three central galaxies are complex and disturbed. None show evidence for rotationally-supported nuclear structures, such as a disk or ring, that would be expected from either a merger origin or long-lived cooling flow. Instead, the molecular gas is either clumpy with no clear velocity structure or extends away from the galactic center in filaments that are several kiloparsecs long. The molecular filaments are coincident with nebular and bright X-ray emission, suggesting that they have condensed out of the hot intracluster medium. They are also generally associated with cavities in the X-ray emission inflated by the active galactic nucleus (AGN), suggesting that AGN feedback has stimulated the formation of molecular gas. The narrow velocity gradients along the filaments are only consistent with freefall if the filament is situated close to the plane of the sky. This is a common feature in brightest cluster galaxies. Since ram pressure is ineffective at slowing dense molecular clouds, the filaments must either be pinned to the hot atmosphere by magnetic fields or have condensed in-situ relatively recently.

In RXCJ1504-0248 I combine the ALMA analysis with spatially-resolved ultraviolet emission tracing young stars. The central gas falls on the Kennicutt-Schmidt relation, while the filament has elevated star formation surface densities. The ongoing consumption of a finite fuel supply by star formation, or spatial variations in the CO-to-H_2 conversion factor, may be diminishing the molecular gas surface density to produce this effect. Despite their drastic differences in morphology and environment, the molecular gas in clusters is still converted into stars following the same relation as in spirals and starbursts.

I have also detected the $J = 3 \rightarrow 2$ transition from ^{13}CO, an optically thin isotopologue of ^{12}CO, in RXJ0821.0+0752. This enables a measurement of the conversion between CO intensity and molecular column density for the first time in a galaxy cluster. The CO-to-H_2 conversion factor in RXJ0821+0752 is half of the Galactic value. If this value applies to other clusters, then it would alleviate the high coupling efficiencies required for molecular filaments to be uplifted by X-ray cavities. This analysis also provides reassurance that the molecular gas masses measured in BCGs are unlikely to be overwhelmingly biased by adopting the Galactic conversion factor.

Acknowledgements

I would like to thank everyone who helped make this thesis possible. First and foremost, thank you to Brian McNamara for his support and supervision over these years, even though there have been too many of them. Next, my collaborators for their helpful comments and discussion. In particular Helen Russell, who helped me find my footing when I first started. Thank you to my friends, family, and the other graduate students for helping to keep me (somewhat) sane. Finally, and most importantly, my fiancée Laura Richards, who has been there for me every step of the way.

Table of Contents

List of Tables

List of Figures

Abbreviations

2MASS Two Micron All-Sky Survey

AGN Active Galactic Nucleus

ALMA Atacama Large Millimeter/submillimeter Array

BCG Brightest Cluster Galaxy

HIFLUGCS HIghest X-ray FLUx Galaxy Cluster Sample

HST Hubble Space Telescope

ICM Intracluster Medium

IR Infrared

IRAM Institut de Radioastronomie Millimétrique

JCMT James Clerk Maxwell Telescope

LTE Local Thermodynamic Equilibrium

OVRO Owens Valley Radio Observatory

U/LIRGs (Ultra) Luminous Infrared Galaxies

UV Ultraviolet

Chapter 1

Introduction

In hierarchical structure formation, small scale primordial perturbations have grown and merged under the influence of gravity into the massive structures we observe today. At the present epoch, clusters of galaxies are the most massive bound structures in the Universe. The richest clusters are comprised of thousands of member galaxies, with total masses up to $10^{15}\,M_\odot$. They serve as important tools for cosmology, as their mass composition reflects that of the Universe: 85% of the mass is made of dark matter, and the remainder is comprised of baryons (Planck Collaboration et al., 2016).

BCGs reside at the centers of clusters. They are the largest and most luminous galaxies in the Universe. Their stellar populations, like normal elliptical galaxies, are typically old and quiescent. Nevertheless, they are rich in both molecular gas (Edge, 2001; Edge et al., 2002; Salomé & Combes, 2003) and star formation (McNamara, 2004; O'Dea et al., 2008; McDonald et al., 2011; Donahue et al., 2015; Tremblay et al., 2015), with molecular gas masses up to $10^{11}\,M_\odot$ and star formation rates of several to hundreds of solar masses per year. BCGs also exhibit spectacular emission-line nebulae, indicative of a warm population of ionized gas (Lynds, 1970; Heckman, 1981; Cowie et al., 1983; Hu et al., 1985; O'Dea et al., 1994; Crawford et al., 1999).

The stellar mass in cluster galaxies accounts for only a few percent of the total mass. About 90% of the baryonic mass is contained in a hot, diffuse plasma that permeates the entire cluster, known the intracluster medium (ICM) (Lin et al., 2003). First discovered through its prodigious X-ray emission (luminosities of $10^{43} - 10^{45}$ erg s^{-1} ; Giacconi et al. 1971; Gursky et al. 1971; Forman et al. 1972), the detection of Fe-K emission at $6 - 7$ keV identified the ICM as a thermal plasma (Mitchell et al., 1976; Serlemitsos et al., 1977). The gas temperature is typically $10^7 - 10^8$ K, and the densities range from 10^{-4} cm^{-3} in

the outskirts to 10^{-2} cm^{-3} in the cluster core. The ICM, also referred to as the hot gas or hot atmosphere, is comprised of hydrogen, helium, and heavier metals at about 1/3 of solar abundances. The hot gas is in hydrostatic equilibrium, tracing the underlying gravitational potential of the cluster (Hitomi Collaboration et al., 2016).

1.1 The Cooling Flow Problem

A classical "cooling flow" cluster is characterized by cool ($\sim$ keV), dense ($\sim 10^{-2}$ cm^{-3}) intracluster medium in the cluster core. Since the primary emission mechanism is collisional, the X-ray emissivity is proportional to the square of the gas density (e.g. Sarazin, 1988). As a result, a dense core produces a strong peak in X-ray surface brightness, which can account for more than 10% of the cluster's total X-ray luminosity. If unopposed by heating, the intracluster medium will radiate away its thermal energy in a cooling time,

$$t_{\rm cool} = E_{\rm th}/L_X = \frac{p}{(\gamma-1)n_e n_H \Lambda(T,Z)}, \tag{1.1}$$

where we have used $L_X = \int n_e n_H \Lambda(T,Z) {\rm d}V \approx n_e n_H \Lambda(T,Z) V$. Here p is the gas pressure, n_e and n_H are the electron and proton densities, $\gamma = 5/3$ is the ratio of specific heats for an ideal gas, $\Lambda(T,Z)$ is the cooling function, and T and Z are the gas temperature and metal abundance. At the centers of clusters the cooling time falls below 1 Gyr, indicating that copious amounts of hot gas should be cooling to low temperatures.

The cooling region ($r_{\rm cool}$) is defined where the cooling time of the gas is less than the time since the last major heating event (e.g. major merger). As the gas within $r_{\rm cool}$ radiates, its entropy decrease must correspond to an increase in density. Since the pressure at $r_{\rm cool}$ is dictated by the weight of the overlying gas, an increase in density can only be achieved by an inward gas flow. This is the classical schematic of a cooling flow (Fabian & Nulsen, 1977; Cowie & Binney, 1977; Fabian, 1994). The enhanced gas density further leads to an increase in X-ray emissivity, causing the intracluster medium to rapidly cool to low temperatures ($< 10^4$ K). The observed X-ray luminosities of galaxy clusters imply gas condensation rates of hundreds to thousands of solar masses per year.

Observational signatures of cooling flows should manifest in a multitude of wavebands. The strongest spectroscopic signatures of cooling gas are X-ray emission lines below the Fe L complex at 1 keV. After the gas has condensed, it should power luminous emission-line nebulae that trace atomic and ionized gas at 10^4 K. Subsequent cooling will form massive reservoirs of cold, molecular gas (< 100 K) that are ultimately consumed in star formation.

Although each of these signatures have been detected, they are only present at levels an order of magnitude or more lower than expected in cooling flows.

Early X-ray observations apparently confirmed the presence of cooling gas in several galaxy clusters. Line emission from the Fe L complex was detected at low significance at a level consistent with the predictions of a classical cooling flow from gas at a few million to a few tens of millions of degrees (Canizares et al., 1982, 1988). However, far more sensitive observations with the *XMM-Newton* Reflection Grating Spectrometer failed to corroborate this result (e.g. Peterson et al., 2001; Kaastra et al., 2001; Tamura et al., 2001a,b; Sakelliou et al., 2002). In general, the temperature drop towards the centers of clusters is limited to a factor of about three (Peterson & Fabian, 2006). Robust X-ray spectroscopy measures the cooling rate of the most extreme systems to be $\sim 100\,\mathrm{M_\odot\ yr^{-1}}$, ten times lower than predicted from the classical cooling flow model (e.g. Morris & Fabian, 2003).

Indirect evidence for gas cooling – filaments of nebular emission from warm, ionized gas (Heckman, 1981), star formation (Johnstone et al., 1987; McNamara & O'Connell, 1989), and reservoirs of cold, molecular gas (Edge, 2001; Salomé & Combes, 2003) – are abundant in clusters with short central cooling times. However, as is the case for X-ray line emission, these products of cooling are also present at only $5-10\%$ of the levels expected from classical cooling flows. Star formation in BCGs generally persists at only a few $\mathrm{M_\odot\ yr^{-1}}$, reaching a few hundreds of $\mathrm{M_\odot\ yr^{-1}}$ in some exceptional cases. Cooling flows should result in condensation at hundreds to thousands of $\mathrm{M_\odot\ yr^{-1}}$. The bulk of the cooled gas is expected to reside in molecular form with temperatures $\ll 100$ K. Indeed, up to a few $10^{10}\,\mathrm{M_\odot}$ has been detected in BCGs (Edge, 2001; Salomé & Combes, 2003). However, persistent cooling at $> 100\,\mathrm{M_\odot\ yr^{-1}}$ should produce $> 10^{11}\,\mathrm{M_\odot}$ of molecular gas in the characteristic timescale of 1 Gyr. Detailed comparisons show that the amount of molecular gas accounts for $5-10\%$ of the material deposited by a classical cooling flow.

Taken together, the tracers of cooling gas indicate that cooling flows do not exist in their classical form. Instead the rate of cooling is largely suppressed, with some residual cooling persisting at about 10% of the classical rate. The literature has adopted the more general nomenclature of "cool core clusters" to refer to these systems. They are identified by central cooling times that fall below ~ 3 Gyr (Hudson et al., 2010). The paucity of cooling gas in cool core clusters indicates that a source of heat is responsible for suppressing the rate of cooling, offsetting radiative losses.

1.2 Active Galactic Nucleus Feedback

The solution to the cooling flow problem requires a source of heating that is closely coupled to the global rate of cooling. If the rate of heating is not tied to the rate of cooling, then the ultimate fate of the gas depends on the balance between the two. If cooling dominates, it will tend to run away in the same manner as an uninhibited cooling flow, leading to copious amounts of cold gas and stars in the central galaxy. If heating dominates, cooling is never able to compete and the cooling time is driven well above the age of the system. The central cooling times in cool core clusters do not fall into either of these categories. In the HIFLUGCS sample, which is comprised of the brightest X-ray clusters, 44% have central cooling times shorter than 1 Gyr, and none have central cooling times exceeding the Hubble time (Hudson et al., 2010). Moreover, if the heating rate is not tied to the rate of cooling, then a balance between the two must be entirely coincidental. Therefore, while mechanisms like conduction may help to offset radiative losses, they cannot be solely responsible for preventing cooling flows.

Feedback from active galactic nuclei (AGN) is now widely regarded as the dominant mechanism in suppressing cooling flows (reviewed by McNamara & Nulsen, 2007, 2012; Fabian, 2012). Elliptical depressions in X-ray surface brightness were first identified in *ROSAT* imaging of the Perseus and Cygnus A clusters (Boehringer et al., 1993; Carilli et al., 1994). These are known as X-ray cavities, and are the primary observational signature of active galactic nucleus (AGN) feedback in X-rays. The vast improvement in spatial resolution and sensitivity provided by the *Chandra* X-ray observatory led to detections of cavities in essentially all cool core clusters that it has observed. In samples of the brightest cool core clusters, more than 70% host X-ray cavities (Dunn et al., 2005; Bîrzan et al., 2012). As projection effects and X-ray statistics can make cavities difficult to detect, the fraction of cool core clusters hosting cavities may be closer to unity (Panagoulia et al., 2014). The diameters of X-ray cavities vary tremendously, from less than 1 kpc in M87 (Forman et al., 2005, 2007) to nearly 200 kpc in the MS0735.6+7421 and Hydra A clusters (McNamara et al., 2005, 2011; Nulsen et al., 2005; Wise et al., 2007; Vantyghem et al., 2014). High resolution X-ray imaging has also revealed shock fronts encompassing X-ray cavities and sound waves propagating to larger radii (e.g. Fabian et al., 2006).

The fraction of systems hosting cavities is comparable to the fraction that are radio bright (Burns, 1990). Comparisons between X-ray and radio observations have shown a striking anti-correlation between cavities and synchrotron emission from radio jets. A clear example of this is seen in the MS0735.6+7421 galaxy cluster, shown in Fig. 1.1 (McNamara et al., 2005, 2011; Vantyghem et al., 2014). The 200 kpc diameter cavities are clearly visible as nearly circular depressions in the X-ray emission (blue). The radio

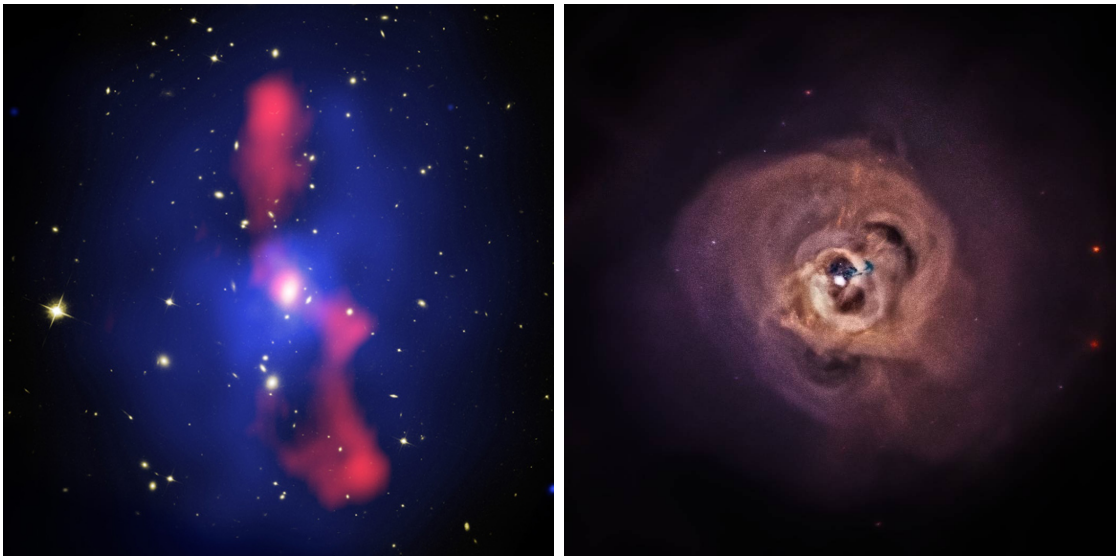

Figure 1.1: *Left:* A composite X-ray (blue), radio (red), and optical (yellow) image of the MS0735.6+7421 galaxy cluster (McNamara et al., 2005, 2011; Vantyghem et al., 2014). The radio jets fill a pair of large X-ray cavities. *Right:* X-ray image of the Perseus cluster showing a wealth of structure, including cavities and shock fronts (Fabian et al., 2006).

emission (red) emanates from the cluster center in a counter-propagating jetted flow, filling the cavities at their maximal extent. The implication is that X-ray cavities are bubbles within the intracluster medium that have been inflated by relativistic particles launched by the central AGN. This process is known as "radio-mode" AGN feedback, and is likely suppressing cooling and star formation in all massive ellipticals at late times (Bower et al., 2006; Croton et al., 2006; Best et al., 2007).

In a feedback process, the amount of heat transfered back into the system depends on the rate of cooling. A cluster that is initially experiencing a cooling phase will proceed along the standard cooling flow path, with the hot atmosphere condensing into atomic and molecular gas. These clouds are channeled toward the cluster center, where a small fraction are subsequently accreted onto the central supermassive black hole. This liberates the stored gravitational potential energy, launching jets of relativistic particles. These jets inflate X-ray cavities and drive shock fronts and sound waves, heating the intracluster medium and offsetting radiative losses. Sufficient heating will quench the cooling flow, preventing gas from condensing until the AGN is starved of its fuel supply. Cooling can then reestablish itself, and the cycle can repeat in a long-lived feedback loop.

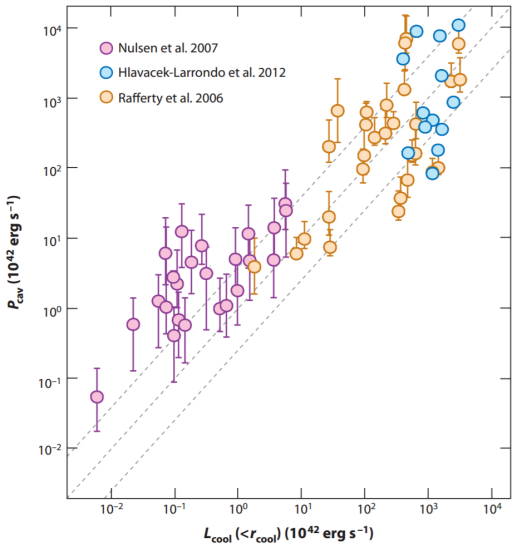

Figure 1.2: The mechanical power output by AGN in low redshift clusters (Rafferty et al., 2006), massive clusters (Hlavacek-Larrondo et al., 2012), and giant ellipticals (Nulsen et al., 2007). The AGN power is well-matched with the luminosity of the gas that is prevented from cooling to low temperatures. Figure adapted from Fabian (2012).

For AGN feedback to be a viable means of suppressing cooling flows, the AGN must efficiently heat the surrounding gas. X-ray observations, through the detection of X-ray cavities, provide the most direct means of measuring the mechanical energy output by the AGN. The cavity volume multiplied by its confining pressure is a measure of the pV work expended to inflate the cavity against its surroundings (Churazov et al., 2000; McNamara et al., 2000). The total mechanical energy output by the AGN is given by the cavity enthalpy, which is the pV work plus the internal energy that supports the cavities against collapse. It is given by

$$H = \frac{\gamma}{\gamma - 1} pV = 4pV \tag{1.2}$$

for a relativistic gas ($\gamma = 4/3$) filling its volume. The mean power output by the AGN is then estimated by dividing the energy output by the cavity age. Assuming that the cavity dynamics are dictated by buoyancy, the terminal speed of a cavity is $v_T = \sqrt{2gV/SC}$. Here g is the local gravitational acceleration, S is the cavity's cross-sectional area, and $C = 0.75$ is the drag coefficient (Churazov et al., 2001; Bîrzan et al., 2004). The buoyancy timescale is then $t_{\rm buoy} = R/v_T = R\sqrt{SC/2gV}$, which is $\sim 10^8$ yr for many cavity systems.

Studies of galaxy groups and clusters have demonstrated that AGN are outputting ample energy to suppress cooling flows. The cavity powers in these systems are enormous, ranging from 10^{41} erg s^{-1} in groups to 10^{46} erg s^{-1} in rich clusters. A direct comparison between AGN power output ($P_{\rm cav}$, also referred to as cavity power) and cooling luminosity is shown in Fig. 1.2 (Fabian, 2012). The cooling luminosity is defined as the difference between the total X-ray luminosity within the cooling radius and the luminosity from gas that could be condensing out of the intracluster medium without violating observations. The dashed lines indicate balance between AGN power output and radiative losses assuming pV, $4pV$, and $16pV$ per cavity. More than half of the systems lie above the $4pV$ line of equality, indicating that AGN are liberating enough energy to offset radiative losses. Simulations have shown that buoyant cavities can heat the surrounding gas as they rise through a cluster atmosphere (e.g. Weinberger et al., 2017).

AGN feedback is fueled by accretion onto the nuclear supermassive black hole. Assuming that the rest mass is converted into mechanical energy with efficiency ϵ, the total amount of mass required to fuel an AGN outburst with enthalpy $E_{\rm cav}$ is

$$M_{\rm acc} = \frac{E_{\rm cav}}{\epsilon c^2}. \tag{1.3}$$

The corresponding accretion rate is

$$\dot{M}_{\rm acc} = \frac{P_{\rm cav}}{\epsilon c^2}. \tag{1.4}$$

The accretion efficiency is generally taken to be about 10% (e.g. Rafferty et al., 2006). Since AGN enthalpies and powers range from $10^{56} - 10^{62}$ erg and $10^{41} - 10^{46}$ erg s^{-1}, respectively, the requisite accretion masses and mass accretion rates are $10^3 - 10^9\,{\rm M}_\odot$ and $10^{-5} - 1\,{\rm M}_\odot$ yr^{-1}. Star formation in these systems consumes gas about 700 times faster than the nuclear black hole (Ferrarese & Merritt, 2000).

How accretion on sub-pc scales is so closely connected to gas cooling on 100 kpc scales is a critical problem in AGN feedback. Accreting the hot gas directly is unfeasible for powerful AGN, as not enough gas falls within the radius of influence of the black hole. Instead, molecular gas is expected to be the crucial component that completes the feedback loop. It is the final product of cooling before gravitational processes cause it to collapse and form stars. Its angular momentum can also be effectively shed through a combination of ram pressure and collisions with other clouds, allowing it to be channeled toward the nuclear black hole (Pizzolato & Soker, 2005, 2010).

1.3 Molecular Gas Observations

Molecular hydrogen, H_2, is the most abundant molecule in the Universe. As the primary ingredient in star formation, it plays a key role in galaxy evolution. Unfortunately, cold H_2 is not directly observable in emission. As a symmetric molecule, it has no permanent dipole moment and no corresponding dipolar rotational transitions. Its lowest energy transitions are quadrupolar, requiring temperatures > 100 K to be excited. The typical temperatures of molecular clouds (~ 20 K) are not high enough to observe these transitions, so cold H_2 is effectively invisible in emission.

Carbon monoxide ($^{12}CO^{16}O$[1]) is the workhorse tracer for the bulk distribution of molecular gas. It is the next most abundant molecule, with a typical abundance of 10^{-4} relative to H_2. CO has a weak permanent dipole moment ($\mu = 0.11\,\mathrm{Debye} = 0.11 \times 10^{-18}\,\mathrm{esu\ cm}$) and low excitation energy ($h\nu/k = 5.53$ K). As a result, its ground rotational transition ($J = 1 \rightarrow 0$; $\nu_{\mathrm{rest}} = 115.2712$ GHz) is easily excited by collisions with H_2. Higher frequency transitions (i.e. those with higher rotational quantum number) are excited by progressively warmer and denser gas. For example, the CO(3-2) transition is significantly excited for gas temperatures above 33 K and densities above $2 \times 10^4\ \mathrm{cm}^{-3}$.

Rotational transitions from CO isotopologues, such as ^{13}CO, offer complementary information to the standard CO observations. Since the $[^{12}CO]/[^{13}CO]$ abundance ratio is ~ 50, varying from 30 to 100 in the Milky Way (Langer & Penzias, 1990), ^{13}CO line emission is expected to be optically thin. As a result, it can be used to constrain the column density of molecular clouds, which is not possible with optically thick CO emission. This requires the gas density and temperature to be known, which is often problematic. This problem is best addressed by observing multiple transitions along the CO Spectral Line Energy Distribution (CO-SLED). This allows the measured line intensities to be inverted into gas temperature, density, and column density. When fewer CO-SLED measurements are available, more assumptions need to be made. One common assumption is that the gas is in local thermodynamic equilibrium (LTE), so the excitation temperature of each transition is equal to the kinetic temperature of the gas.

1.3.1 Molecular Gas Mass

A considerable effort has been made to infer the total molecular gas mass given the observation of a single CO emission line, generally CO(1-0). The observed quantity is the

[1]Throughout this thesis CO is used interchangeably with $^{12}CO^{16}O$. Any differing isotopes are stated explicitly.

integrated intensity, ${}^{12}W_{10}$[2], in units of K km s^{-1}. The CO-to-H_2 conversion factor, $X_{\rm CO}$, also known as the X-factor, is then defined such that

$$N(\mathrm{H_2}) = X_{\rm CO}\, {}^{12}W_{10}, \tag{1.5}$$

where $N(\mathrm{H_2})$ is the total H_2 column density in cm^{-2}. This can equivalently be expressed as a mass-to-light ratio, relating the total molecular gas mass, $M_{\rm mol}$, to the line luminosity, $L_{\rm CO}$ (in K km s^{-1} pc^2):

$$M_{\rm mol} = \alpha_{\rm CO} L_{\rm CO}. \tag{1.6}$$

In the Milky Way $X_{\rm CO}$ is measured to be 2×10^{20} cm^{-2} (K km s^{-1})$^{-1}$, or equivalently $\alpha_{\rm CO} = 4.3\,\mathrm{M_\odot}$(K km s^{-1} pc^2)$^{-1}$ (Bolatto et al., 2013).

Direct calibrations of the X-factor are conducted largely in local molecular clouds. Several techniques have been developed to accomplish this task: the virial method (e.g. Scoville et al., 1987; Solomon et al., 1987; McKee & Ostriker, 2007), excitation of optically thin CO isotopologues (Dickman, 1978; Pineda et al., 2010), γ-ray emission (e.g. Lebrun et al., 1983), and dust emission (e.g. Dame et al., 2001). Combining each of these methods yields the aforementioned $X_{\rm CO}$ with a scatter of about 50% within the disk of the Milky Way.

The Galactic X-factor is also commonly applied to extragalactic sources, where individual molecular clouds are not resolved. Independent calibrations in these systems, where possible, confirm the applicability of the Galactic conversion factor, even when averaged over an entire galaxy (Bolatto et al., 2013). This is because the contribution of each cloud to the luminosity, provided they do not overlap, is approximately proportional to its mass. Both the CO luminosity and molecular gas mass are therefore proportional to the number of clouds within the beam, and the conversion factor is constant. This is known as the mist model. Although each individual cloud is optically thick, the ensemble behaves as though it is optically thin so long as the number density of clouds is low enough to avoid overlap in both position and velocity space.

Deviations from the Galactic X-factor may occur under several circumstances, including low gas metallicities and extreme gas conditions. In low metallicity galaxies, CO becomes a poor tracer of the total H_2 distribution, as the $\tau_{\rm CO} = 1$ surface retreats inward with decreasing metallicity (Bolatto et al., 1999; Wolfire et al., 2010). For two clouds of the same mass and differing metallicities, the smaller CO-emitting region in the metal-poor cloud will result in a lower luminosity, requiring a larger X-factor to yield the same mass.

[2]The superscript refers to the carbon isotope in the CO molecule, and the subscripts refer to the upper and lower values of J in the transition.

The extreme gas conditions in starburst galaxies and (Ultra) Luminous Infrared Galaxies (U/LIRGs) also affect the X-factor. Their molecular gas is warmer and denser, resulting in more highly excited gas and boosting the CO luminosity relative to molecular clouds in the Milky Way. The net effect decreases the X-factor to $\alpha_{\rm CO} \approx 0.8\,{\rm M}_\odot(\ {\rm K\ km\ s^{-1}\ pc^2}\ )^{-1}$, $5-6$ times lower than the Galactic value (Downes & Solomon, 1998; Papadopoulos et al., 2012).

Brightest cluster galaxies lack a direct calibration of the X-factor. With no better alternative, CO observations of BCGs adopt the Galactic conversion factor. In most cases this is expected to be a reasonable assumption. The hot atmospheres in cluster cores have central metallicities that are only slightly sub-solar ($\sim 0.8\,{\rm Z}_\odot$). If the metallicity of molecular clouds in the BCG reflect that of the ICM, then we would expect CO to be a reliable tracer of the H_2 distribution. Additionally, BCGs typically exhibit star formation rates of several to several tens of solar masses per year. The high end is consistent with several U/LIRGs, but the high SFRs in U/LIRGs are also commonly associated with major merger activity. This is rarely the case in BCGs, so the molecular gas is expected to have lower densities and temperatures, and therefore an X-factor closer to Galactic. A notable exception is the Phoenix cluster, where the exceptional star formation rate ($500-800\,{\rm M}_\odot\ {\rm yr}^{-1}$) warrants the adoption of a sub-Galactic X-factor (Russell et al., 2017a). Thus, while the Galactic X-factor may be justified in these systems, it remains a significant source of uncertainty.

1.4 Molecular Gas in Normal Galaxies

Before considering the molecular gas in galaxy clusters, it is instructive to first provide context based on other systems.

Spiral galaxies, such as the Milky Way, are the archetypal gas-rich galaxy. They are characterized by their spiral arms and blue colours, indicating ongoing star formation. A sample spiral galaxy, NGC 1637, is shown in the upper left panel of Fig. 1.3. The molecular gas and star formation in spiral galaxies is confined to a thin disk, as shown in the bottom panel of Fig. 1.3. Consequently, the molecular gas experiences ordered motion as it revolves about the Galactic center. The global supply of molecular gas is also long-lived, taking several Gyr for it to be consumed by star formation. For context, the molecular gas mass and star formation rate of the Milky Way are $1.0\times10^9\,{\rm M}_\odot$ (Heyer & Dame, 2015) and $1\,{\rm M}_\odot\ {\rm yr}^{-1}$ (Robitaille & Whitney, 2010), respectively.

U/LIRGs exhibit more extreme star formation rates, from several tens to hundreds of solar masses per year (Rieke et al., 2009). LIRGs are characterized by infrared luminosities

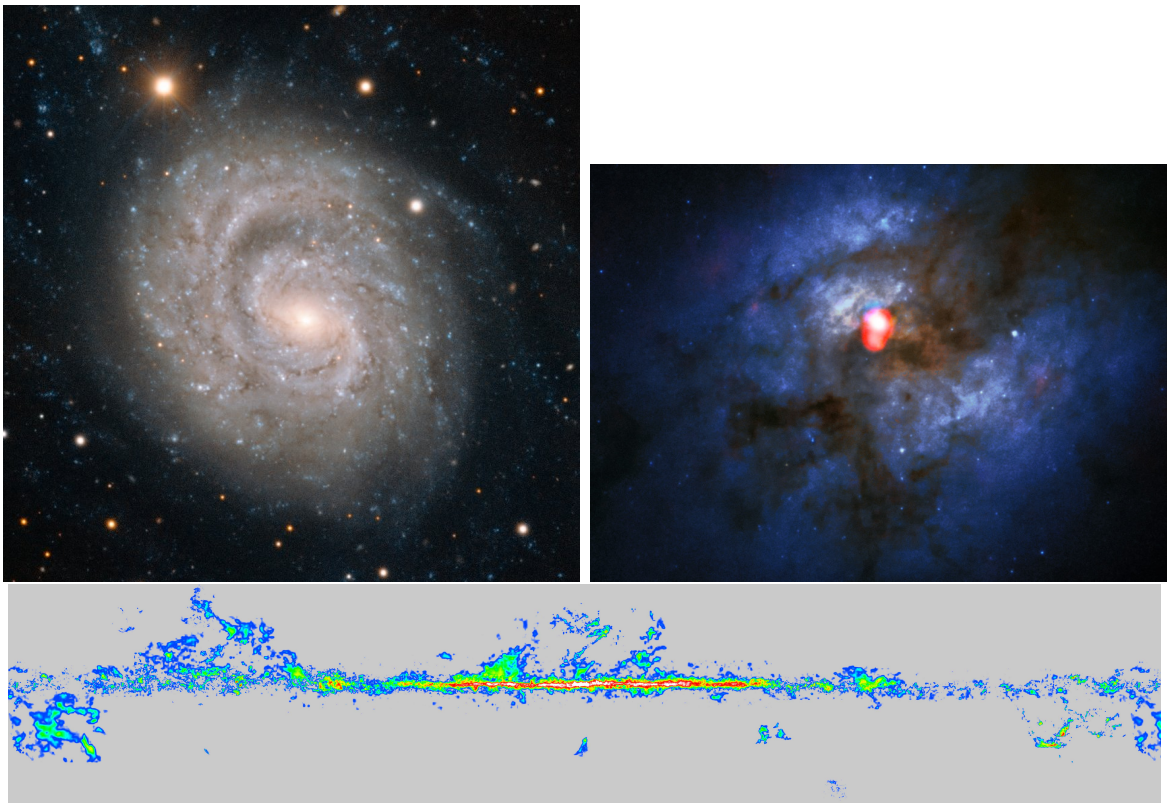

Figure 1.3: In spiral galaxies, such as the Milky Way and NGC 1637 (Credit: ESO), the molecular gas is confined in a thin disk that revolves about the galaxy nucleus. The molecular gas in the disk of the Milky Way is shown in the bottom image (Dame et al., 2001). In ULIRGs the molecular gas is confined to a small, dense region near the galactic center. The ULIRG Arp 220 is shown in the upper right. Its molecular gas is shown in red, as traced by water, CS, and HCN (Credit: ALMA(ESO/NAOJ/NRAO)/NASA/ESA and The Hubble Heritage Team (STScI/AURA)).

of $10^{11} - 10^{12}\,L_\odot$ at $40\,\mu$m, while ULIRGs are even brighter. This emission arises from dust heated by a starburst and/or an AGN. A large fraction of U/LIRGs are found to be major mergers (e.g. Sanders et al., 1986; Armus et al., 1987). They contain upwards of $10^9\,M_\odot$ of molecular gas (Downes & Solomon, 1998). Unlike spiral galaxies, their molecular gas is strongly confined to the central few kpc of the galactic nuclei. The prototypical ULIRG Arp 220 is shown in Fig. 1.3 (right). Its molecular gas (red) is centrally condensed compared to the dust and stellar light.

Elliptical galaxies are "red and dead." They have very little molecular gas and star formation, so their stellar populations are old and passive. In the volume-limited ATLAS-3D sample, only 22% of the 259 ellipticals were detected in CO (Young et al., 2011). Only in a few exceptional cases does the molecular gas mass exceed $10^9\,M_\odot$. The detections all span the range $10^7 - 10^9\,M_\odot$, while the highest upper limits are only $10^8\,M_\odot$.

A noteworthy subset of ellipticals are radio-loud active galaxies, which contain radio jets launched by an AGN. Indeed, BCGs also fall into this category, but their position at the centers of cluster distinguish them from other radio-loud galaxies. Fast outflows of both ionized and molecular gas have been detected in nearby radio galaxies (Morganti et al., 2005; Nesvadba et al., 2006; Alatalo et al., 2011; Dasyra & Combes, 2011; Morganti et al., 2015). This suggests that radio jets can couple to dense gas clouds, driving them outward at velocities up to 1000 km s^{-1} and mass flow rates of several tens of solar masses per year. This represents a viable mechanism for quenching star formation, regulating the growth of galaxies by removing their fuel supply.

1.5 Molecular Gas in Galaxy Clusters

Early searches for HI (Burns et al., 1981; Valentijn & Giovanelli, 1982; Shostak et al., 1983; McNamara et al., 1990; Dwarakanath et al., 1995) and CO (Grabelsky & Ulmer, 1990; McNamara & Jaffe, 1994; Antonucci & Barvainis, 1994; Braine & Dupraz, 1994; O'Dea et al., 1994) in BCGs yielded upper limits of $< 10^{10}\,M_\odot$. Improvements in receiver technology, combined with the strategic targeting of systems bright in nebular emission with rapidly cooling atmospheres, finally resulted in the first detections of the low-J transitions of CO in over a dozen BCGs (Edge, 2001; Edge & Frayer, 2003; Salomé & Combes, 2003). Around the same time, rovibrational emission from warm ($1000 - 2500$ K) H_2 was detected in 23 BCGs (Edge et al., 2002).

The hypothesis that molecular clouds form out of the condensing intracluster medium is well motivated by these cold gas detections and observations at other wavelengths.

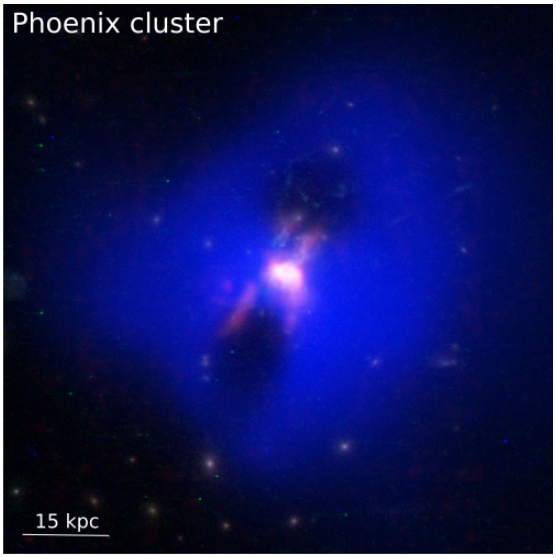

Figure 1.4: In the Phoenix cluster (Russell et al., 2017a), half of the molecular gas (red) trails a pair of cavities in the X-ray emission (blue).

Signatures of gas cooling, including molecular gas and star formation, are observed almost exclusively in clusters where the central cooling time falls below $\sim 5{\times}10^8$ yr, or equivalently where the entropy is less than 30 keV cm^2 (Cavagnolo et al., 2008; Rafferty et al., 2008; Voit et al., 2008; Werner et al., 2014; Pulido et al., 2018). The observed molecular gas masses are also consistent, within a factor of a few, with that expected from the reduced cooling rates inferred from X-ray observations (Edge, 2001). Correlations between star formation rate and the rate of mass deposition from the ICM further support this picture (Egami et al., 2006; O'Dea et al., 2008).

In recent years, the advent of the Atacama Large Millimeter/submillimeter Array (ALMA) has allowed the molecular gas in BCGs to be observed with unprecedented spatial and velocity resolution. The pre-existing single dish observations were limited in resolution by the size of their antennae, with a 30 m dish (e.g. IRAM-30) achieving a resolution of 20 arcseconds at the frequency of the CO(1-0) line. Interferometers correlate the signals between multiple dishes to achieve much better resolution, as determined by the largest separation between dishes instead of the diameter of the dish. The generation of interferometers preceding ALMA were capable of achieving resolutions of a few arcseconds at CO(1-0). In its complete configuration, ALMA consists of 54 12m antennas with up to 16 km baselines, easily enabling sub-arcsecond CO observations with exquisite sensitivity.

Several BCGs have now been observed with ALMA, their molecular gas reservoirs being resolved for the first time (David et al., 2014; McNamara et al., 2014; Russell et al., 2014, 2016, 2017a; Tremblay et al., 2016; Simionescu et al., 2018). While a long-lived cooling flow may be expected to deposit most of the cooled gas in a small region coincident with the galactic center, such as in a rotationally-supported disk, the ALMA observations have shown that this is rarely the case. Instead, molecular filaments extending radially outward have been detected in several systems. These filaments are coincident with nebular emission (see e.g. Conselice et al., 2001; Hatch et al., 2006; Werner et al., 2011; McDonald et al., 2012a; Canning et al., 2013), and trail buoyantly rising X-ray cavities. The Phoenix cluster (Fig. 1.4) is a clear example of this. Half of the molecular gas, traced by its ALMA CO(3-2) emission (red), is situated along the inner edges of a pair of X-ray cavities. The implication is that AGN feedback is either disrupting a nuclear supply of molecular gas or the gas has cooled in situ from low entropy ICM lifted by the cavities (Revaz et al., 2008; McNamara et al., 2016).

Uplift in the wakes of rising cavities has also been identified in the hot atmosphere. In M87, bright filaments of metal-enriched gas extend along the direction of radio jets (Simionescu et al., 2008). Anisotropic distributions of metal-enriched gas have similarly been observed in about 15 other clusters, with higher metallicities detected along the direction of X-ray cavities (Simionescu et al., 2009; Kirkpatrick et al., 2009, 2011; Gitti et al., 2011; Kirkpatrick & McNamara, 2015). These results indicate that AGN play a pivotal role in redistributing gas throughout cluster atmospheres. More powerful AGN are capable of displacing gas to higher altitudes (Kirkpatrick et al., 2011; Kirkpatrick & McNamara, 2015).

Simulations corroborate the observational evidence that AGN feedback is integral to the formation of cold clouds. An atmosphere in global thermal equilibrium remains susceptible to local thermal instabilities (McCourt et al., 2012). Overdensities in the ICM are introduced by the AGN, either by injecting turbulence or by lifting low entropy gas from the cluster core. If a blob in equilibrium is perturbed to a new position, where it is now an overdensity, then it will become thermally unstable only if it cools faster than it returns to its equilibrium position (Voit et al., 2017; Voit, 2018). In simulations, cold clumps develop along the propagation direction of the AGN jets (Gaspari et al., 2012, 2013; Li & Bryan, 2014a). They then decouple from the hot atmosphere and rain back onto the BCG in a process known as "chaotic cold accretion." This occurs when the azimuthally-averaged $t_{\rm cool}/t_{\rm ff}$ falls below ~ 10 (Sharma et al., 2012; Prasad et al., 2015). However, this threshold is not statistically distinct from the $t_{\rm cool}$ threshold at 5×10^8 yr (Hogan et al., 2017b).

Redshifted absorption lines have been detected in NGC5044 and A2597 (David et al., 2014; Tremblay et al., 2016). The narrow linewidths (~ 5 km s^{-1}) imply that the absorb-

ing bodies are individual molecular clouds. The AGN serves as the backlight, with the molecular clouds lying in between the AGN and the observer. The redshifted velocities therefore indicate that these clouds are infalling onto the central supermassive black hole, potentially fueling a future cycle of AGN feedback. This closes the feedback loop; cold gas condenses from the cooling atmosphere, accretes onto the nuclear black hole, and fuels powerful AGN outbursts.

1.6 This Thesis

In this thesis I present ALMA observations of three cool core galaxy clusters: 2A0335+096, RXJ0821.0+0752, and RXCJ1504.1-0248. In each object the CO(1-0) and CO(3-2) were observed, with resolutions of about 0.6 and 0.2 arcseconds, respectively. An additional detection of ^{13}CO(3-2) was obtained in RXJ0821.0+0752. This work was conducted contemporaneously with most other ALMA observations of BCGs, as discussed in the Section 1.5. As a result, this thesis represents a critical piece in our understanding of the molecular gas in cluster environments.

This field is cresting its era of phenomenology. The goal of this work is to map the distribution and kinematics of the molecular gas, which was not possible with single dish observations or the previous generation of interferometers. With these data I identify any gas flows and equilibrium structures present in the system. These features are used to explore the origin and potential fate of the molecular gas. They are compared to perturbations in the hot atmosphere, such as bright filaments and X-ray cavities. When possible, the molecular gas is also compared to ongoing star formation. Any nuclear gas is considered for its potential role in fueling AGN feedback.

The detection of ^{13}CO(3-2) provides a unique advancement in the understanding of the molecular gas in BCGs. In conjunction with CO(1-0) and CO(3-2), this detection enables a simplistic measurement of the CO-to-H_2 conversion factor, which had previously been unavailable. This is the critical quantity used in measuring molecular gas masses, so its measurement reveals any systematic bias in previous results.

This thesis is organized as follows. In Chapter 2 I present the analysis of 2A0335+096. In Chapter 3 I use the detection of ^{13}CO(3-2) in RXJ0821.0+0752 to constrain the CO-to-H_2 conversion factor. Chapter 4 presents my analysis of RXCJ1504.1-0248. In Chapter 5 I return to RXJ0821, this time focusing on the molecular gas distribution in combination with a *Chandra* X-ray analysis. Finally, Chapter 6 summarizes this thesis and its main conclusions.

Chapter 2

Molecular Gas Along a Bright Hα Filament in 2A 0335+096 Revealed by ALMA

Abstract

We present ALMA CO(1-0) and CO(3-2) observations of the brightest cluster galaxy (BCG) in the 2A 0335+096 galaxy cluster ($z = 0.0346$). The total molecular gas mass of $1.13 \pm 0.15 \times 10^9$ $M_\odot$ is divided into two components: a nuclear region and a 7 kpc long dusty filament. The central molecular gas component accounts for $3.2 \pm 0.4 \times 10^8$ $M_\odot$ of the total supply of cold gas. Instead of forming a rotationally-supported ring or disk, it is composed of two distinct, blueshifted clumps south of the nucleus and a series of low-significance redshifted clumps extending toward a nearby companion galaxy. The velocity of the redshifted clouds increases with radius to a value consistent with the companion galaxy, suggesting that an interaction between these galaxies < 20 Myr ago disrupted a preexisting molecular gas reservoir within the BCG. Most of the molecular gas, $7.8 \pm 0.9 \times 10^8$ $M_\odot$, is located in the filament. The CO emission is co-spatial with a 10^4 K emission-line nebula and soft X-rays from 0.5 keV gas, indicating that the molecular gas has cooled out of the intracluster medium over a period of $25 - 100$ Myr. The filament trails an X-ray cavity, suggesting that the gas has cooled from low entropy gas that has been lifted out of the cluster core and become thermally unstable. We are unable to distinguish between inflow and outflow along the filament with the present data. Cloud velocities along the filament are consistent with gravitational free-fall near the plane of the sky, although their increasing blueshifts

with radius are consistent with outflow.

2.1 Introduction

Located at the centers of galaxy clusters, brightest cluster galaxies (BCGs) are the largest and most luminous galaxies in the universe. They are giant elliptical galaxies with extended stellar envelopes and predominantly old, "red and dead" stellar populations. However, BCGs situated in cooling flow clusters (Fabian, 1994), where the cooling time of the hot gas is shorter than the age of the system, harbour upward of $10^9\,M_\odot$ of molecular gas, approaching $10^{11}\,M_\odot$ in the most extreme systems (Edge, 2001; Salomé & Combes, 2003). Star formation proceeding at rates of several to tens of solar masses per year, which exceeds the star formation rates of many spiral galaxies, is also observed in these systems (McNamara, 2004; O'Dea et al., 2008; McDonald et al., 2011; Donahue et al., 2015; Tremblay et al., 2015).

Molecular clouds and stars in BCGs likely form from the cooling of the hot intracluster medium (ICM). Correlations between star formation rate and the rate of mass deposition from the ICM support this picture (Egami et al., 2006; O'Dea et al., 2008). Furthermore, cold gas and star formation are observed almost exclusively in systems where the central cooling time is below a sharp threshold of $\sim 5\times10^8$ yr (Rafferty et al., 2008), or equivalently where the entropy is less than 30 keV cm^2 (Voit et al., 2008; Cavagnolo et al., 2008). This threshold has been attributed to the onset of thermal instabilities in the ICM (Gaspari et al., 2012; Voit & Donahue, 2015). These systems also host diffuse emission-line nebulae, which are likely the ionized skins of molecular clouds (Heckman, 1981; Hu et al., 1985; O'Dea et al., 1994; Jaffe et al., 2005; Oonk et al., 2010). Alternatively, the peculiar emission line ratios in BCGs (e.g. Heckman et al., 1989) may originate from primarily neutral gas that is excited by collisions with energetic particles (Ferland et al., 2009).

Although the reservoirs of molecular gas observed in BCGs are quite massive, they constitute only a few percent of the mass expected from unimpeded cooling (Peterson & Fabian, 2006). Instead, feedback from the active galactic nucleus (AGN) is heating the ICM and regulating the rate of cooling (McNamara & Nulsen, 2007, 2012; Fabian, 2012). High resolution *Chandra* X-ray imaging of cool core clusters shows that AGN launch jets that inflate cavities, drive shock fronts, and generate sound waves, offsetting radiative losses from the ICM (e.g. McNamara et al., 2000; Blanton et al., 2001; Fabian et al., 2006). The rate of heating is closely tied to the rate of cooling in a large sample of groups and clusters (Bîrzan et al., 2004; Dunn & Fabian, 2006; Rafferty et al., 2006), and is sufficient to prevent the bulk of the hot gas from cooling.

Accretion of molecular gas potentially plays a key role in forming a feedback loop, as it connects residual cooling of the ICM with energetic outbursts from the AGN (e.g. Pizzolato & Soker, 2005; Gaspari et al., 2013; Li & Bryan, 2014a). While the effects of AGN feedback on the hot atmosphere are clear, little is known about its connection to the cold gas. Radio-jets are known to couple to emission-line nebulae, driving outflows of ionized (Morganti et al., 2005; Nesvadba et al., 2006; Villar-Martín et al., 2006) and molecular gas (Alatalo et al., 2011; Morganti et al., 2015) in radio galaxies. NGC1275, at the center of the Perseus cluster, hosts a filamentary Hα nebula with two prominent filaments extending toward an X-ray cavity (Fabian et al., 2003), suggesting that the filaments have been drawn out of a central reservoir. These filaments are well correlated with soft X-ray emission as well as molecular hydrogen (Lim et al., 2012) and CO (Salomé et al., 2006, 2011). Infalling molecular gas toward the center of the BCG suggests that the uplifted gas is returning in a molecular "fountain" (Lim et al., 2008). Narrow, redshifted absorption lines have been observed in NGC5044 (David et al., 2014) and A2597 (Tremblay et al., 2016), indicating that molecular clouds are inflowing toward the central black hole. ALMA Early Science observations of A1835 revealed $10^{10}\,M_\odot$ of molecular gas being uplifted by the X-ray cavities in a bipolar outflow (McNamara et al., 2014). PKS0745-191 harbours an even more dramatic outflow – virtually all of its molecular gas has been swept from the BCG in three low-velocity filaments (Russell et al., 2016). These results have led McNamara et al. (2016) to postulate that molecular gas condenses out of low entropy ICM that is lifted from the cluster center by X-ray cavities.

Here we present ALMA Cycle 1 observations of the molecular gas in the BCG of 2A 0335+096 (also known as RXJ0338+09), traced by CO(1-0) and CO(3-2) line emission. 2A 0335+096 is one of the brightest X-ray objects on the sky (Edge et al., 1990; Reiprich & Böhringer, 2002), and has a center with a short radiative cooling time (Schwartz et al., 1980; Singh et al., 1986, 1988; White et al., 1991). Its X-ray atmosphere is complex, containing a series of cool clumps (Mazzotta et al., 2003; Werner et al., 2006), a cold front that was likely induced by sloshing motions (Mazzotta et al., 2003; Sanders et al., 2009), and several cavities corresponding to multiple generations of AGN feedback with a total enthalpy of 5×10^{59} erg (Sanders et al., 2009). Multiphase gas in the ICM traces an extended Hα filament within the BCG with a total luminosity of $L_{\mathrm{H}\alpha} = 8\times10^{41}$ erg s^{-1} (Romanishin & Hintzen, 1988; Donahue et al., 2007; Sanders et al., 2009). Farage et al. (2012) argued that the Hα filament consists of a 2 kpc, counter-rotating disk within the 17 kpc filament. Single dish IRAM-30m observations detected the 2A 0335+096 BCG at CO(1-0), measuring a total molecular gas mass of $2.7\pm0.3\times10^9\,M_\odot$ (Edge & Frayer, 2003, corrected for cosmology). Optical, UV, and IR observations of the BCG show ongoing star formation at a rate of several solar masses per year (Romanishin & Hintzen, 1988; Donahue et al., 2007;

O'Dea et al., 2008). X-ray spectroscopy from *Chandra* and *XMM-Newton* indicate that the 0.5 keV gas within the ICM is cooling out of the hot atmosphere and depositing mass onto the BCG at $< 30\,M_\odot\ yr^{-1}$ (Sanders et al., 2009). The ALMA observations presented here resolve the spatial and velocity structure of the molecular gas within the BCG, revealing a striking correlation between molecular gas and the Hα filament.

Throughout this paper we assume a standard Λ-CDM cosmology with $H_0 = 70$ km s^{-1} Mpc^{-1}, $\Omega_{m,0} = 0.3$, and $\Omega_{\Lambda,0} = 0.7$. At the redshift of 2A 0335+096 ($z = 0.0346$; McNamara et al., 1990), the angular scale is $1'' = 700$ pc and the luminosity distance is 150 Mpc. This paper is organized as follows. Details of the ALMA observations and data reduction are given in Section 2.2. Our results pertaining to the morphological and kinematic distribution of the molecular gas and its relation to other wavelengths are described in Section 2.3. The origin of the molecular gas is discussed in Section 2.4, and the main results are summarized in Section 2.5.

2.2 Observations and Data Reduction

The brightest cluster galaxy (BCG) in the 2A 0335+096 galaxy cluster (RA: 03:38:40.50, Dec: +09:58:12.3) was observed by ALMA Cycle 1 (Program ID 2012.1.00837.S, PI McNamara) centered at 111.394 GHz and 334.169 GHz to cover the CO(1-0) and CO(3-2) lines. The CO(1-0) observation was divided into two blocks, which were observed in band 3 on July 22, 2014 and March 08, 2015. Both observations had an on-source integration time of 35 minutes. For the July 2014 (March 2015) observation the array was configured with 33 (30) antennas with baselines of $17 - 716$ m ($12 - 280$ m), each with a primary beam diameter of $56''$. Our observations employed the frequency division correlator mode, so had a frequency resolution of 488.281 kHz (1.31 km s^{-1}) over a 1.875 GHz bandwidth. The CO(3-2) line was observed in band 7 with one 30 minute on-source integration on August 12, 2014. The observation used 34 antennas with baselines of $19 - 915$ m and a primary beam of $18.5''$. At CO(3-2) the velocity resolution in frequency division correlator mode is 0.44 km s^{-1}. Velocity channels are binned together during imaging to improve sensitivity. An additional baseband with 2 GHz bandwidth was included in order to image the continuum.

The observations were primarily calibrated in CASA version 4.4.0 (McMullin et al., 2007) using the automatic pipeline scripts. Additional phase self-calibration on the nuclear continuum improved the signal-to-noise of the CO(1-0) observation by a factor of 1.2. The nuclear continuum flux at CO(3-2) was too faint to perform successful self-calibration.

The phase calibrator chosen automatically at the time of the March 2015 CO(1-0) observation was located 10° away from 2A 0335+096 and has a flux 10 times fainter than the calibrator used in the July 2014 CO(1-0) observation. The resulting phase solutions determined by the pipeline were poor, and a manual recalibration of the data did not improve these solutions to an acceptable level. The phase self-calibration also did not rectify the problem. We therefore do not include this observation in our analysis.

Images of the continuum were created for each band by imaging the line-free channels. An unresolved point source was detected in each image. At 109.84 GHz the nuclear continuum flux is 6.854 ± 0.044 mJy in the July 2014 observation and 6.36 ± 0.15 mJy in the March 2015 observation. This implies a variability of $7.2 \pm 2.3\%$ over an 8 month period, which is consistent with the variability seen in other BCGs with active cores (Hogan et al., 2015b). At 335.12 GHz (August 2014) the nuclear continuum flux is 1.14 ± 0.15 mJy. The corresponding spectral index, following the convention $S_\nu \propto \nu^{-\alpha}$ and considering only the 2014 observations, is $\alpha = 1.61 \pm 0.27$. The location of the continuum source is consistent with 5 GHz VLBI (Sanders et al., 2009). No continuum emission is associated with the nearby companion galaxy. Imaging the continuum in narrow velocity channels (3 km s^{-1}) shows no evidence of line absorption against the continuum emission.

Images of line emission were reconstructed using CLEAN with a Briggs weighting of 2. No continuum subtraction was applied to the CO(3-2) observation, as the continuum flux is small compared to the line emission. The resulting images had a synthesized beam of $1.3'' \times 0.92''$ (PA $-34.5°$) at CO(1-0) and $0.39'' \times 0.23''$ (PA $-50.0°$) at CO(3-2). The RMS noise in 20 km s^{-1} line-free channels was 0.56 mJy beam^{-1} and 0.61 mJy beam^{-1} at CO(1-0) and CO(3-2), respectively. In regions of low signal-to-noise we further bin the spectra to either 40 km s^{-1} or 60 km s^{-1} channels, as needed. Missing short spacings will filter out emission on spatial scales larger than $\sim 11''$ at CO(1-0) and $\sim 3''$ at CO(3-2).

A reference velocity of 10368 km s^{-1} ($z = 0.0346$) was adopted for this analysis. This is a stellar absorption measurement of the BCG that was measured by Huchra. The result was first published in McNamara et al. (1990, quoting private communication with Huchra) and subsequently in the 2MASS catalog (Lavaux & Hudson, 2011; Huchra et al., 2012), who quote an uncertainty of 10 km s^{-1}. The center of the CO(1-0) and CO(3-2) emission is better estimated by the adopted systemic velocity than by the redshifts adopted by previous studies. For reference, a redshift of $z = 0.0349$, which is used by Donahue et al. (2007) and Farage et al. (2012), corresponds to a velocity of +92 km s^{-1} in our adopted frame.

2.3 Results

2.3.1 Distribution of Molecular Gas

The *HST* WFPC2 F606W image presented in the middle frame of Fig. 2.1 shows the central 28×28 kpc of the galaxy cluster, encompassing the BCG and a nearby companion galaxy that is situated 5 kpc in projection from the BCG and well within its light profile. Stellar absorption lines from the two galaxies indicate that the companion is offset from the BCG by 212 ± 58 km s^{-1} in velocity space (Gelderman, 1996). This low velocity suggests that the radial distance between the galaxies is small, so the companion is not just a chance projection. However, this information is not sufficient to determine the true 3D distance or relative velocity between the BCG and companion. Outside of the shown field of view, the closest galaxies are 25 kpc and 28 kpc from the BCG, respectively. These both lie well beyond the molecular gas, so are unlikely to be relevant in our analysis.

Maps of the integrated CO(1-0) and CO(3-2) flux are presented alongside the *HST* image in Fig. 2.1. These maps were created by summing the flux in each pixel over the velocity range -500 to 500 km s^{-1}, which encompasses all of the observed flux (see Fig. 2.2). The maps have been corrected for the response of the primary beam, with contour levels determined from the line-free regions of an uncorrected map. Significant CO emission is observed in two primary locations: near the nucleus of the BCG and in a filament situated beyond a nearby companion galaxy. The filament falls outside of the CO(3-2) field of view.

Fig. 2.2 shows the CO(1-0) spectrum extracted from a $17.5'' \times 22''$ (12.3×15.4 kpc) box encompassing all of the observed flux. This region is similar in size to the $21.5''$ IRAM 30m beam. The spectrum was well-fit by a single Gaussian component centered at -92 ± 14 km s^{-1} with a linewidth of 213 ± 33 km s^{-1} (full width at half maximum; FWHM). Spectral fitting throughout this work used the LMFIT [1] package with one to three Gaussian components, as necessary. Each spectrum has been corrected for the response of the primary beam as well as instrumental broadening introduced by the velocity binning. Table 2.1 lists the best-fitting parameters for all spectra.

The total CO(1-0) flux recovered by these observations is 4.8 ± 0.6 Jy km s^{-1}, which is consistent with the OVRO measurement of 7.1 ± 2.4 Jy km s^{-1} within 2σ (Edge & Frayer, 2003). This flux constitutes 43 ± 7 % of the IRAM 30m flux (11.4 ± 1.1 Jy km s^{-1}; Edge 2001), implying that over half of the molecular gas is undetected in our observations. Similar recovered fractions were noted in ALMA observations of NGC5044 (David et al.,

[1] https://lmfit.github.io/lmfit-py/

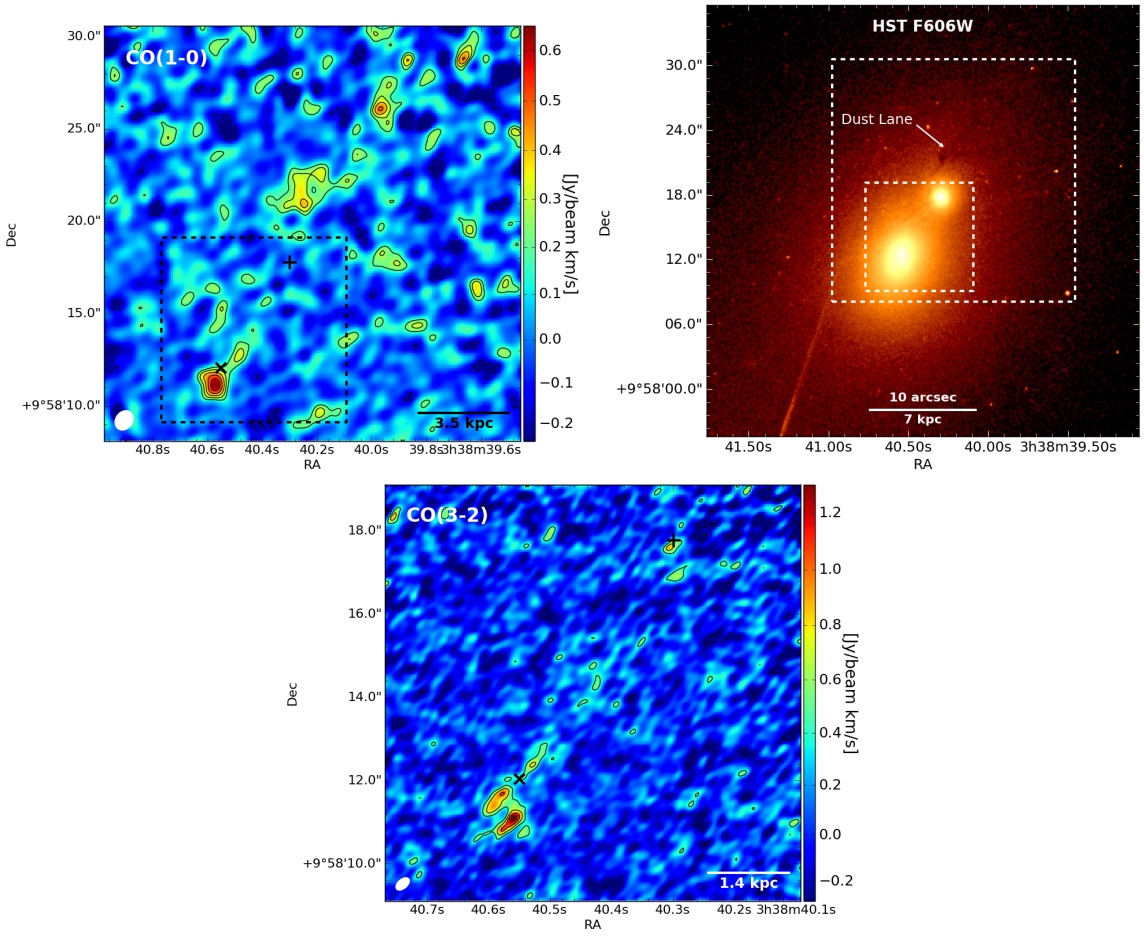

Figure 2.1: *Top-left:* Integrated flux of the CO(1-0) ALMA image. The contours are -2, 2, 3, 4, 5σ, ... , where $\sigma = 0.095$ Jy beam^{-1} km s^{-1}. The $\times$ indicates the position of radio AGN determined from VLBI (Sanders et al., 2009), and the + indicates the flux centroid of the companion galaxy determined from the HST F606W image. The 1.13×0.92 arcsec (PA $-35°$) synthesized beam is shown in white in the lower left corner. The box indicates the CO(3-2) frame shown in the bottom panel. *Top-right: HST* WFPC2 F606W optical image of the 2A 0335+096 BCG and the nearby companion galaxy. The large and small boxes correspond to the CO(1-0) and CO(3-2) fields of view, respectively. *Bottom:* Integrated flux of the CO(3-2) ALMA image, with contours set at -3, 3, 5, 7, and 9σ, where $\sigma = 0.145$ Jy beam^{-1} km s^{-1}. The 0.32×0.20 arcsec beam is shown in white in the lower left corner.

Table 2.1: Parameters of Molecular Features

CO line	Region	χ^2/dof	Velocity center (km s^{-1})	FWHM (km s^{-1})	Integrated intensity (Jy km s^{-1})	Gas Mass (10^8 M$_\odot$)
J=1-0	Total	101/107	-92 ± 14	213 ± 33	4.8 ± 0.6	11.3 ± 1.5
	BCG	154/67	-219 ± 21	266 ± 57	0.73 ± 0.13	1.7 ± 0.3
			109 ± 12	164 ± 32	0.63 ± 0.11	1.5 ± 0.3
	Filament	132/107	-96 ± 11	196 ± 25	3.3 ± 0.4	7.8 ± 0.9
	South BCG	136/107	-172 ± 16	297 ± 38	0.99 ± 0.11	2.33 ± 0.26
	North BCG	131/107	134 ± 18	238 ± 43	0.560 ± 0.088	1.31 ± 0.21
	Inner filament	291/214	-28.1 ± 3.6	100.9 ± 8.8	1.22 ± 0.09	2.86 ± 0.21
			-164.7 ± 3.0	34.5 ± 8.1	0.32 ± 0.06	0.74 ± 0.14
	Outer filament	240/211	-132.0 ± 3.4	55.6 ± 8.6	0.75 ± 0.10	1.77 ± 0.23
			-258.3 ± 8.1	51 ± 21	0.27 ± 0.10	0.64 ± 0.22
			-31.6 ± 6.9	38 ± 19	0.22 ± 0.09	0.51 ± 0.21
J=3-2	BCG	54/34	-223 ± 15	188 ± 36	4.8 ± 0.8	1.60 ± 0.28
			121 ± 27	282 ± 71	4.7 ± 1.0	1.58 ± 0.33
	South BCG	108/74	-160 ± 10	279 ± 17	6.37 ± 0.45	2.14 ± 0.15
			-281.1 ± 3.5	73 ± 11	1.5 ± 0.3	0.50 ± 0.10
	South BCG: NE Clump	80/77	-201.4 ± 7.6	275 ± 18	2.46 ± 0.14	0.83 ± 0.05
	South BCG: SW Clump	65/74	-147 ± 19	300 ± 32	1.92 ± 0.23	0.64 ± 0.08
			-278.6 ± 3.2	77 ± 10	0.89 ± 0.16	0.30 ± 0.05
	BCG Spur	83/74	127 ± 24	368 ± 67	3.1 ± 0.5	1.03 ± 0.16
			93.5 ± 7.4	79 ± 23	0.95 ± 0.36	0.32 ± 0.12
	Diffuse Gas	32/34	188.3 ± 4.9	117 ± 13	2.56 ± 0.23	0.86 ± 0.08
			22.2 ± 8.2	46 ± 30	0.45 ± 0.22	0.15 ± 0.08
	Companion Galaxy	36/37	224 ± 19	256 ± 46	1.65 ± 0.25	0.56 ± 0.09

Notes: All spectra have been corrected for the response of the primary beam and instrumental broadening. Masses determined from the CO(3-2) line have been calculated assuming $\mathrm{CO}(3-2)/\mathrm{CO}(1-0) = 7$.

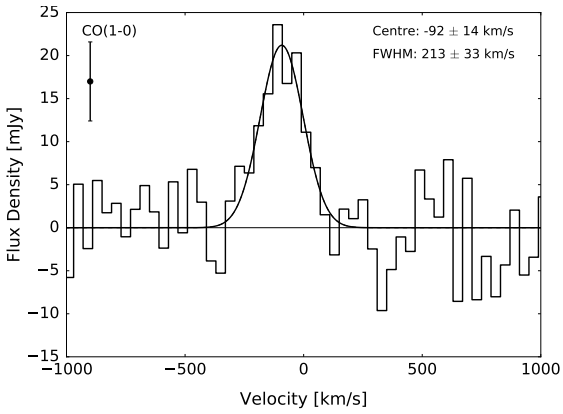

Figure 2.2: CO(1-0) spectrum extracted from a $17.5'' \times 22''$ box that encompasses both the BCG and the extended filament. The best-fit parameters are given in Table 2.1. The error bar indicates the RMS variation in the line-free channels.

2014) and A1664 (Russell et al., 2016). Missing short spacings filter out emission on scales larger than 11 arcsec at CO(1-0) or 3 arcsec at CO(3-2).

Gas in the BCG

Near the nucleus of the BCG the molecular gas is distributed amongst a series of clumps of varying size. At CO(1-0) the emission is mostly concentrated in an unresolved clump located south of the nucleus. At CO(3-2) this feature is further resolved into two clumps of comparable size. The brighter of these clumps is coincident with significant dust extinction in the optical imaging, which is discussed further in Section 2.3.5. No molecular gas is concentrated at the location of the AGN. Toward the northwest the CO emission extends in a small spur that breaks into a series of small, faint clouds. These clouds are distributed in the direction of a nearby companion galaxy that itself hosts a small association of molecular gas.

A spectrum was extracted from a $4.5'' \times 4.5''$ box centered on the nucleus at both CO(1-0) (Fig. 2.3 *top*) and CO(3-2) (Fig. 2.4). This regions includes all of the southern emission and most of the clouds to the northwest. Both spectra are best fit by two Gaussian components, with one blueshifted to ~ -200 km s^{-1} and one redshifted to ~ 100 km s^{-1} with respect to the systemic stellar velocity of the BCG. The total integrated flux in this region is 1.36 ± 0.17 Jy km s^{-1} at CO(1-0).

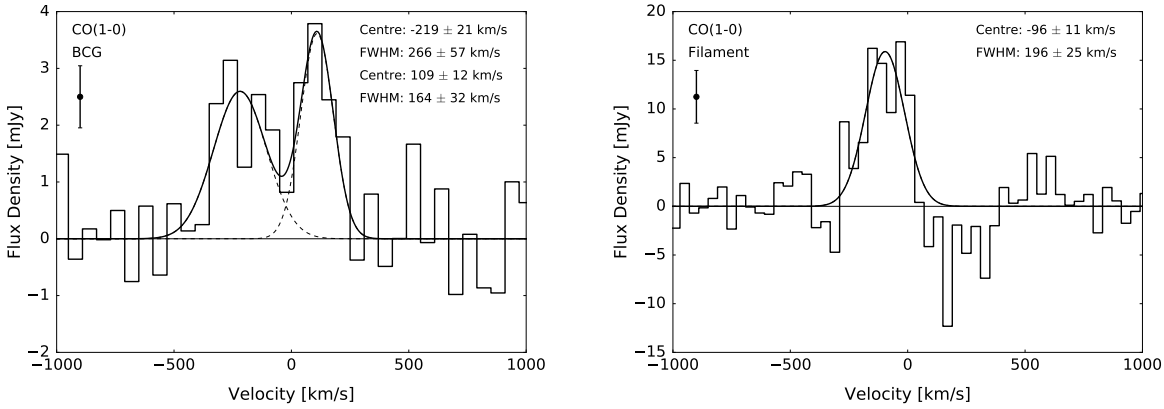

Figure 2.3: CO(1-0) spectra from a $4.5'' \times 4.5''$ box centered on the BCG (top) and an $8'' \times 8.5''$ box enclosing the filament (bottom). The spectra are each fit by a single Gaussian component, and the best-fit parameters are given in Table 2.1. The error bars indicate the RMS variation in the line-free channels.

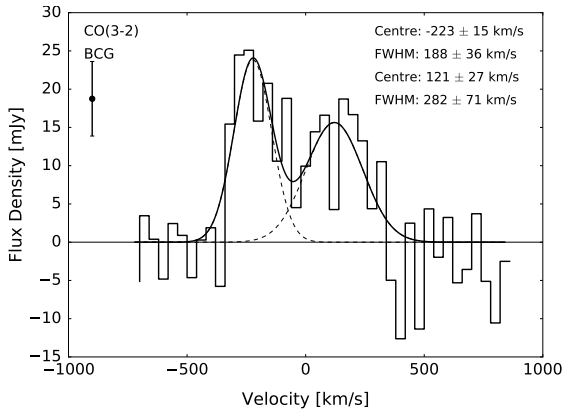

Figure 2.4: CO(3-2) spectrum of the BCG extracted from the same region as Fig. 2.3 (top panel). The best-fit parameters are given in Table 2.1. The error bar indicates the RMS variation in the line-free channels.

Additional spectra were extracted for the distinct structures within the BCG. At CO(1-0) these include the southern unresolved clump as well as the spur extending to the northwest, which are identified in Fig. 2.5. The resulting spectra are shown in the bottom panels of Fig. 2.6. Both are well-fit by a single velocity component that, when combined, accounts for the two peaks observed in the total BCG spectrum in Fig. 2.3. The blueshifted emission is observed exclusively in the southern clump, while the spur to the northwest is entirely redshifted. Both are relatively broad, with FWHM of 297 ± 38 km s^{-1} and 238 ± 43 km s^{-1}, respectively.

These regions can be subdivided further at CO(3-2), as shown in Fig. 2.7. The "South BCG" region is the same as in CO(1-0) (Fig. 2.5) to allow for a direct comparison, but has also been split into two regions that are not shown in the figure, one for each clump. Toward the northwest the emission has also been divided into two regions based on distance from the nucleus. Neither of these regions correspond 1:1 with the "North BCG" region in Fig. 2.5, which extends midway into the "Diffuse Gas" region. All CO(3-2) spectra are shown in Fig. 2.8, with all fit parameters listed in Table 2.1. Multiple velocity components are required for several of the spectra. In the northwestern regions most of the linewidths are narrow (< 100 km s^{-1}), so the multiple peaks likely arise from giant molecular clouds or associations of different velocities. South of the BCG, multiple velocity components are only required to fit the larger of the two clumps, lying to the southwest. This clump is coincident with dust extinction, although the northeastern clump may still be coincident with dust if it is located on the far side of the BCG.

Filament

Beyond the companion galaxy the molecular gas is located in a 7 kpc long filament that is coincident with an extended region of significant dust extinction. Most of the emission is localized in the inner portion of the filament, with a second, smaller region at the filament tail reaching 5σ significance. These two regions are connected by a faint channel that is not evident in Fig. 2.1, but is significantly detected in the maps presented in Section 2.3.3. This is because the channel has a narrow linewidth, so is drowned out by the noise when integrated between -500 and 500 km s^{-1}. Fig. 2.3 (*bottom*) shows the CO(1-0) spectrum of the filament extracted from an $8'' \times 8.5''$ box. We are unable to obtain a CO(3-2) spectrum of the filament because it lies outside of the field of view. The CO(1-0) spectrum is well-fit by a single Gaussian component with an integrated flux of 3.3 ± 0.4 Jy km s^{-1}, which is more than double the integrated flux within the BCG.

Spectra of the inner and outer clumps in the filament are shown in Fig. 2.6, with the regions identified in Fig. 2.5. Two velocity components are significantly detected in the

inner filament. They are slightly blueshifted with respect to the BCG, with the primary component moving at -28.1 ± 3.6 km s^{-1} and the secondary at -164.7 ± 3.0 km s^{-1}. The outer filament consists of three velocity components, moving at -31.6 ± 6.9 km s^{-1}, -132.0 ± 3.4 km s^{-1}, and -258.3 ± 8.1 km s^{-1}. The primary component is the central line, which is blueshifted by 100 km s^{-1} relative to the main peak in the inner filament. Along the entire filament the broadest component is the primary peak in the inner filament, which still has a linewidth of only 101 ± 9 km s^{-1} FWHM. All of the other peaks have widths in the range of $30 - 60$ km s^{-1}. These linewidths are much narrower than for the gas in the BCG, reflecting the depth of the underlying gravitational potential.

Companion Galaxy

A small clump of gas detected in CO(3-2) is coincident with the nucleus of the companion galaxy. This emission lies within the noise of the CO(1-0) data. The clump is also unresolved at CO(3-2), so spreading the total flux over the larger CO(1-0) beam will decrease the observed brightness. A single-Gaussian fit to its CO(3-2) spectrum, shown in Fig. 2.8, shows that the gas is redshifted to 224 ± 19 km s^{-1} with respect to the systemic stellar component of the BCG. This is consistent with its stellar velocity of 212 ± 58 km s^{-1}, implying that the molecular gas is bound to the companion galaxy. This molecular gas linewidth of 256 ± 46 km s^{-1} FWHM is fairly typical of small elliptical galaxies, so the molecular gas may be virialized within the galaxy. Following the mass conversion discussed in Section 2.3.2 and assuming a line flux ratio of $\mathrm{CO}(3-2)/\mathrm{CO}(1-0) \approx 7$, the total molecular gas mass within the companion galaxy is $5.6 \pm 0.9 \times 10^7$ M$_\odot$.

2.3.2 Molecular Gas Mass

The integrated flux of the CO(1-0) line ($S_{\mathrm{CO}}\Delta v$) can be converted to a molecular gas mass, assuming a constant CO-to-H_2 conversion factor (X_{CO}), according to the equation (Solomon et al., 1987; Solomon & Vanden Bout, 2005; Bolatto et al., 2013)

$$M_{\mathrm{mol}} = 1.05 \times 10^4 X_{\mathrm{CO,Gal}} \left(\frac{S_{\mathrm{CO}}\Delta v \, D_L^2}{1+z} \right) \mathrm{M}_\odot. \tag{2.1}$$

Here $S_{\mathrm{CO}}\Delta v$ is expressed in Jy km s^{-1}, D_L is the luminosity distance in Mpc, and z is the redshift of the BCG. We assume a Galactic CO-to-H_2 conversion factor, $X_{\mathrm{CO,gal}} = 2 \times 10^{20}$ cm^{-2} (K km s^{-1})$^{-1}$, which is typical of molecular clouds in the disk of the Milky Way. However, the conversion factor is not universal. In particular, low metallicity regions

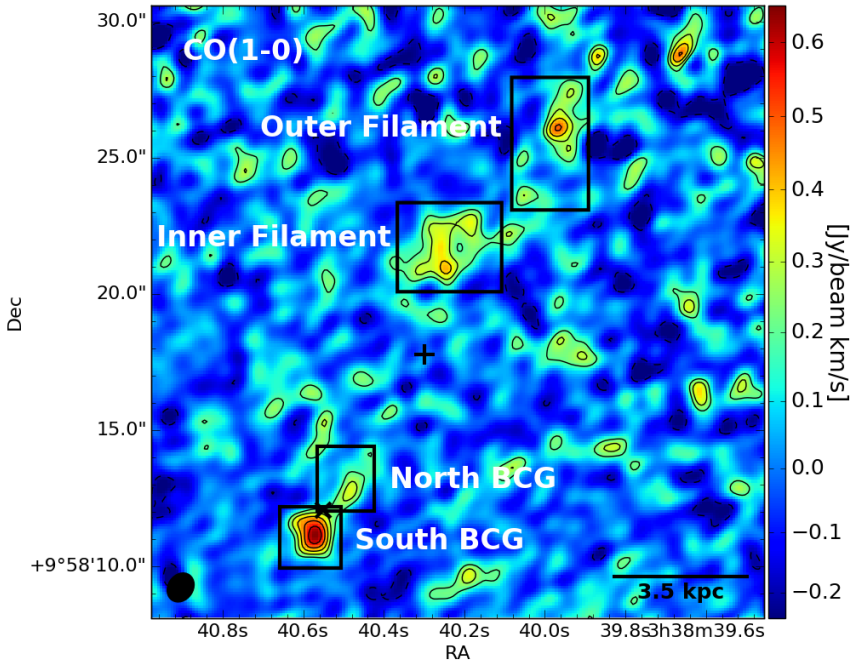

Figure 2.5: CO(1-0) integrated intensity map identifying regions with distinct molecular gas features. The spectra associated with these regions are shown in Fig. 2.6. The field of view is 22" (15.4 kpc) on a side, showing the same area as in Fig. 2.1. The × and + indicate the centroids of the BCG and companion galaxy, respectively.

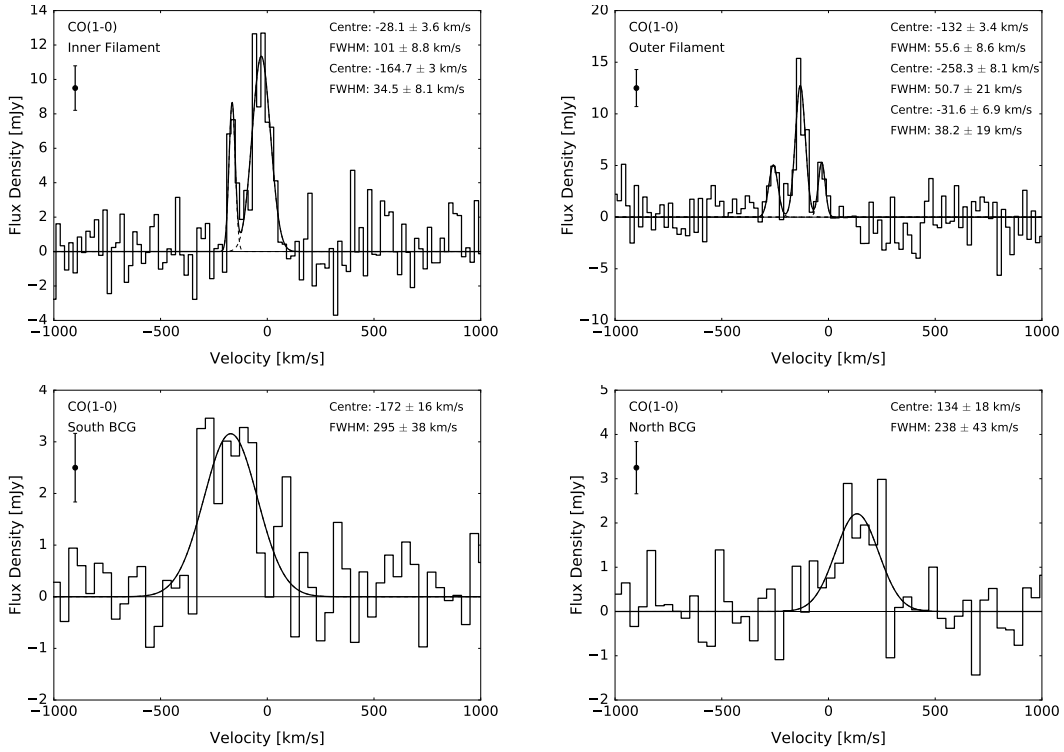

Figure 2.6: CO(1-0) spectra extracted from the regions shown in Fig. 2.5. The best-fit parameters are given in Table 2.1. The error bar indicates the RMS variation in the line-free channels. The "Inner Filament" and "Outer Filament" spectra are presented with 20 km s^{-1} velocity channels, while the "South BCG" and "North BCG" have been binned up to 40 km s^{-1} to improve the signal-to-noise ratio.

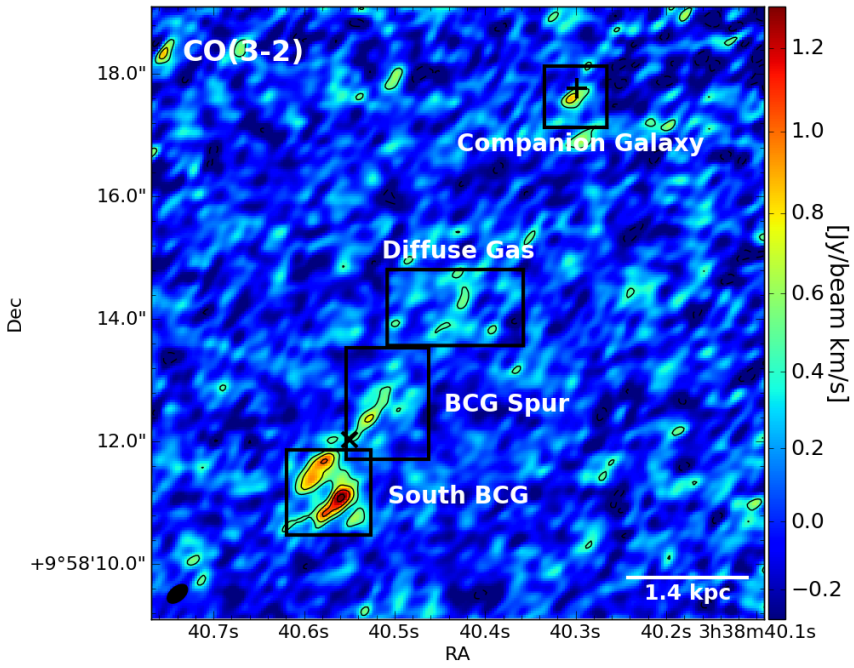

Figure 2.7: CO(3-2) integrated intensity map with regions highlighting the different structures seen in the BCG and the companion galaxy. The associated spectra are shown in Fig. 2.8. The field of view is 10″ (7 kpc) on a side, showing the same area as in Fig. 2.1.

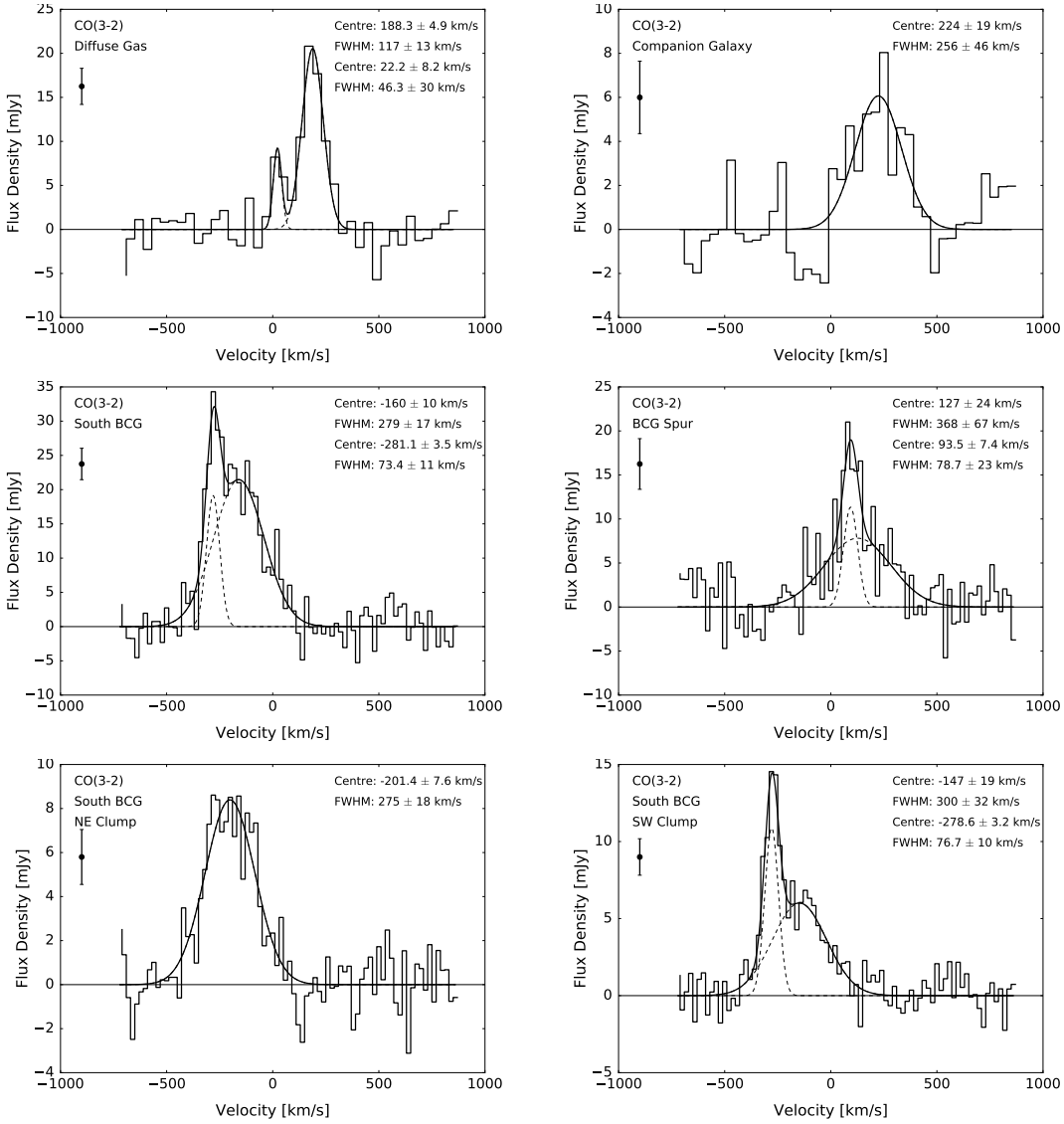

Figure 2.8: CO(3-2) spectra extracted from the regions shown in Fig. 2.7. Additional spectra are shown for each of the two clumps within the South BCG region, which were extracted from $0.6'' \times 0.6''$ boxes. The best-fit parameters are given in Table 2.1. Each spectrum was initially extracted with 20 km s^{-1} velocity bins. The "Diffuse Gas" spectrum was binned up to 40 km s^{-1} channels to improve the signal-to-noise ratio, and "Companion Galaxy" was binned to 60 km s^{-1}. The error bar indicates the RMS variation in the line-free channels.

tend to have high values of $X_{\rm CO}$. The Galactic conversion factor can be approximately applied down to metallicities of $\sim 0.5\,{\rm Z}_\odot$ (Bolatto et al., 2013). In 2A 0335+096, the metallicity inferred from the intracluster medium peaks at $0.95 \pm 0.06\,{\rm Z}_\odot$ at the cluster center (Sanders et al., 2009), so the Galactic $X_{\rm CO}$ should be appropriate. On the other hand, LIRG and starburst galaxies are known to have very low values of $X_{\rm CO}$. However, the Spitzer-derived total IR luminosity of the BCG, $6.7 \times 10^9\,{\rm L}_\odot$ (Donahue et al., 2011), is well below the $10^{11}\,{\rm L}_\odot$ threshold for a LIRG. Narrow absorption features observed in NGC5044 (David et al., 2014) and A2597 (Tremblay et al., 2016) suggest that molecular clouds in BCGs have similar linewidths to those of the Milky Way. We therefore expect that the Galactic value is appropriate here. Our broad conclusions are not affected by a factor of few difference in the adopted conversion factor.

The total CO(1-0) flux detected in our observations, 4.8 ± 0.6 Jy km s^{-1}, corresponds to a molecular gas mass of $1.13 \pm 0.15 \times 10^9\,{\rm M}_\odot$. Of this, $3.2 \pm 0.4 \times 10^8\,{\rm M}_\odot$ is localized to the BCG and $7.8 \pm 0.9 \times 10^8\,{\rm M}_\odot$ is contained in the elongated filament north of the companion galaxy. Table 2.1 lists the molecular gas mass associated with each CO(1-0) spectrum.

Masses are derived from CO(3-2) assuming a constant CO(3-2)/CO(1-0) flux ratio. This ratio was determined by smoothing the CO(3-2) data cube to the CO(1-0) resolution and extracting the spectrum from a 5×5 arcsec box centered on the BCG for each line. The spectra were each fitted with two Gaussian components. Summing the fluxes of each component, the resulting flux ratio is ${\rm CO}(3-2)/{\rm CO}(1-0) = 7.2 \pm 1.4$. We therefore adopt a factor of 7 difference between the two integrated fluxes, with the caveat that the conversion is only accurate to $\sim 20\%$. The ratio of integrated brightness temperature (in units of K km s^{-1}) is 0.80 ± 0.16. For optically thick CO emission this ratio indicates that the gas is approximately thermalized, implying gas densities above 10^4 cm^{-3}.

2.3.3 Velocity Distribution

In order to study the velocity structure of the molecular gas, we extracted spectra from each pixel of the datacube averaged over a box the size of the synthesized beam. Each spectrum was fit with a single Gaussian component. The significance of the line was tested using a Monte Carlo analysis following the prescription of Protassov et al. (2002, see Section 5.2), with detections requiring a 2σ significance. Spectra containing a line detection were then tested with a second component following the same prescription. The resulting velocity (centroid and FWHM) maps are presented alongside the integrated flux for the corresponding component in Fig. 2.9 and 2.10 for CO(1-0) and CO(3-2), respectively. The

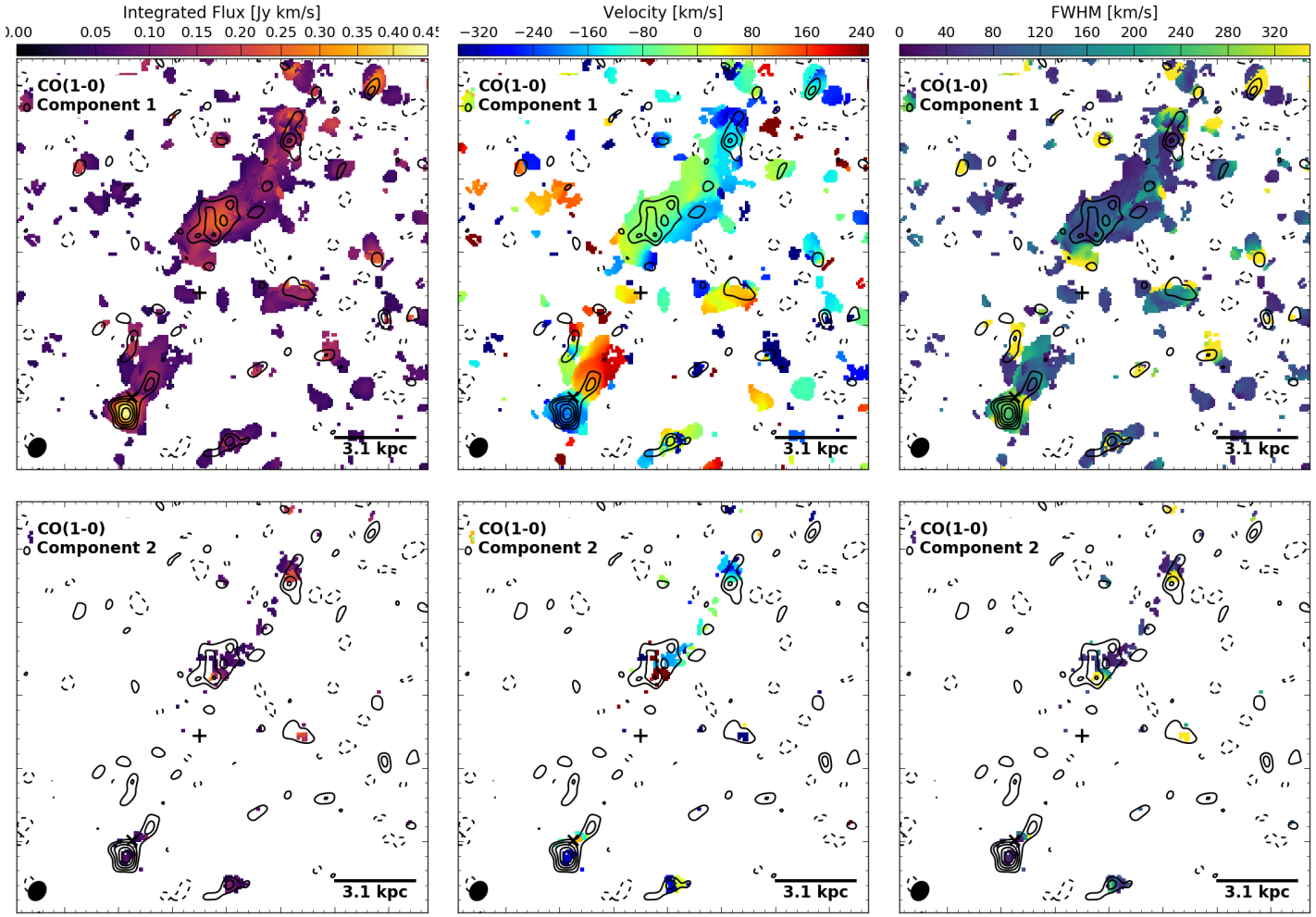

Figure 2.9: Maps of integrated flux (*left*), velocity centroid (*middle*), and FWHM (*right*) obtained from pixel-by-pixel fitting of the CO(1-0) datacube, as described in the text. Only pixels containing flux detected at $> 2\sigma$ are shown. The contours are the same as in Fig. 2.1 (top). The $\times$ and $+$ indicate the centroids of the BCG and companion galaxy, respectively.

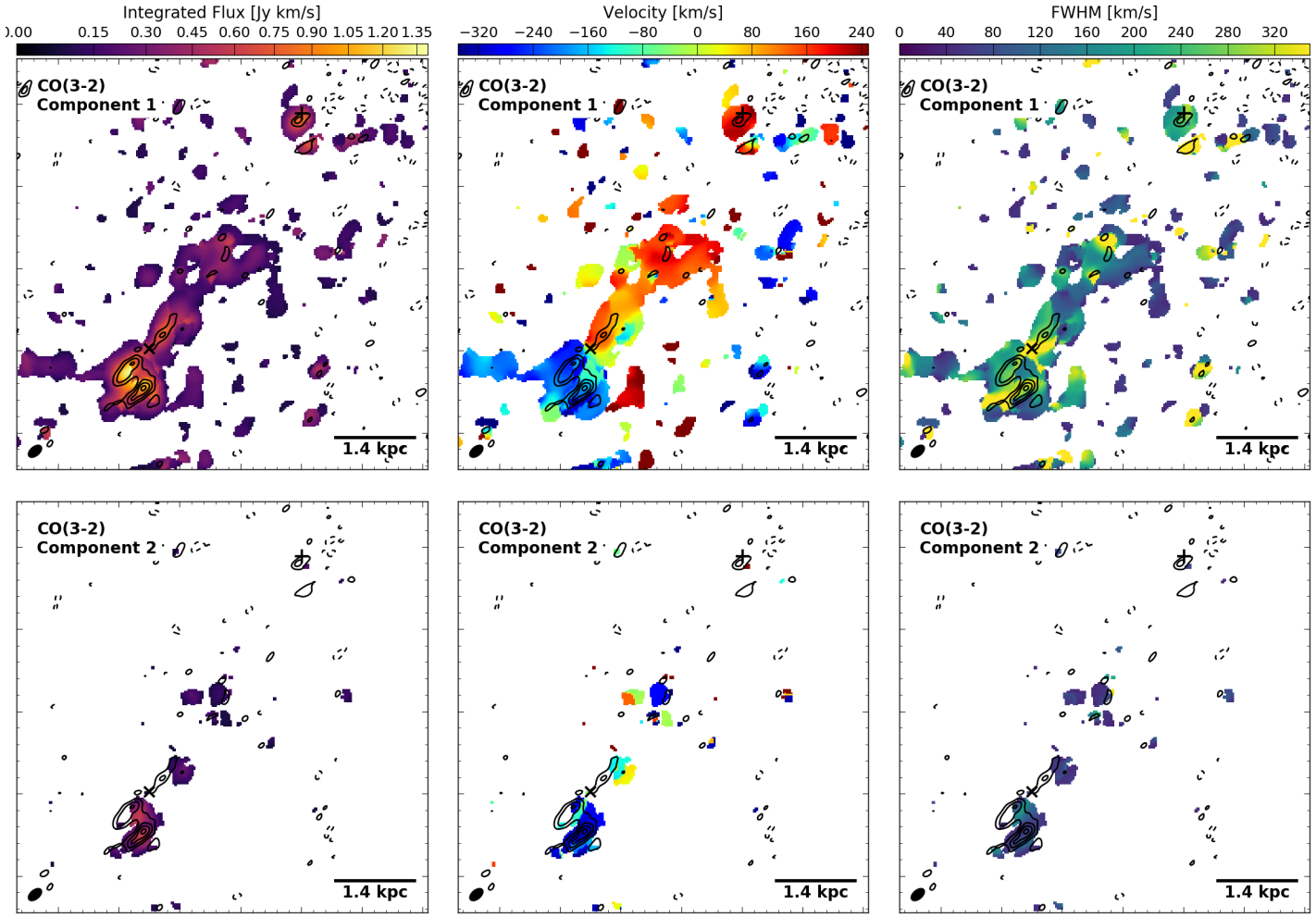

Figure 2.10: Maps of integrated flux (*left*), velocity centroid (*middle*), and FWHM (*right*) of a two-component fit to the CO(3-2) emission line. Only pixels containing flux detected at $> 2\sigma$ are shown. The contours are the same as in Fig. 2.1 (bottom). The $\times$ and $+$ indicate the centroids of the BCG and companion galaxy, respectively.

CO(1-0) maps were created with 40 km s^{-1} bins, with each pixel additionally tested with 20 km s^{-1} bins to ensure that the narrow features toward the tail of the filament could be recovered. 20 km s^{-1} velocity bins were used for the CO(3-2) map. The maps have been overlaid with the corresponding contours from Fig. 2.1.

The spatial distribution of molecular gas recovered by these maps is consistent with the integrated maps in Fig. 2.1, with the molecular gas divided between the BCG and a long filament north of the companion galaxy. Significant emission is detected along the entire length of the filament, confirming that the two clumps seen in Fig. 2.1 are connected by a faint channel. The apparent disconnect between the inner and outer filament seen in Fig. 2.1 arises because the maps were integrated over a velocity range much broader than the linewidth of this channel, drowning out the signal.

A large velocity gradient is present within the core of the BCG. South of the nucleus the gas is blueshifted to -210 ± 10 km s^{-1}, while the velocity of the spur extending to the north increases from 80 ± 10 km s^{-1} near the nucleus up to about 200 km s^{-1}. The blueshifted emission is relatively broad, with a FWHM of 260 ± 20 km s^{-1}, while the redshifted emission is considerably narrower, with a FWHM of $90 - 130$ km s^{-1}. The smooth gradient observed between these regions results from the beam smearing together regions of disparate velocities. This velocity gradient is more pronounced at CO(3-2), where the velocity changes abruptly across the nucleus.

South of the BCG nucleus the two clumps identified at CO(3-2) share a broad velocity component (FWHM $200 - 300$ km s^{-1}) with a shallow velocity gradient ranging from of -120 km s^{-1} in the southwest to -200 km s^{-1} in the northeast. A second velocity component is present in the southwestern clump, with a velocity of -270 km s^{-1} and FWHM of 80 km s^{-1}.

North of the BCG nucleus the CO(3-2) emission becomes more diffuse farther from the galactic center, with significant detections obtained further from the nucleus than at CO(1-0). This emission follows the same gradient as the CO(1-0) emission, increasing from 80 km s^{-1} near the nucleus to $180 - 250$ km s^{-1} in the diffuse clouds. A small region with higher velocity (170 km s^{-1}), broad (230 km s^{-1}) emission is observed immediately north of the nucleus, beside the 80 km s^{-1} emission. This map also reveals a significant detection coincident with the companion galaxy, which has a velocity of 240 km s^{-1} and a FWHM of $200 - 300$ km s^{-1}.

Several distinct velocity structures are observed along the filament. Most of the emission originates from the "Inner Filament" (Fig. 2.5), which occupies a very narrow range in velocity (-20 to -40 km s^{-1}) with a FWHM of only $70 - 100$ km s^{-1}. Toward the tail of the filament the velocity becomes increasingly blueshifted to -145 km s^{-1}, where it then

bends northward and the velocity further increases in magnitude to -230 km s^{-1}. Finally, a narrow tendril protrudes westward from the southern edge of the inner filament, with a velocity of -120 km s^{-1} to -170 km s^{-1} and a linewidth comparable to the inner filament. Multiple velocity components are detected at the interface between this tendril and the inner filament, extending all the way along the filament.

2.3.4 Velocity Profiles

Position-velocity (PV) diagrams of the molecular gas in both the BCG and the elongated filament are presented in Fig. 2.11. For each PV diagram the flux was averaged over the width of the slit as a function of both slit position and velocity channel. One slit was placed along the extended axis of the molecular gas within the BCG, encompassing both the clump to the SE and spur to the NW. This slit was 1.3″ wide at CO(1-0) and 0.84″ wide at CO(3-2), both with a position angle (PA) of 147°. A second, 0.52″ wide slit was placed roughly orthogonal to this (PA 47°) in order to separate the two clumps identified at CO(3-2) but unresolved at CO(1-0). Finally, a 1.5″ wide slit (PA 130°) was placed lengthwise along the filament at CO(1-0). The position indicated in the PV diagrams runs from the bottom edge of the slits shown on the integrated flux maps to the top edge, with zero offset corresponding to the midpoint of the slit.

The position-velocity diagrams along the long axis of the BCG (Fig. 2.11 top) are qualitatively consistent between CO(1-0) and CO(3-2). The gas south of the nucleus is blueshifted and very broad. Extending toward the other side of the nucleus the velocity increases roughly linearly until the edge of the diffuse emission noted in CO(3-2) (see Fig. 2.7). Gas coincident with the companion galaxy is also detected at CO(3-2), where the velocity is comparable to that of the diffuse emission.

The perpendicular cut across the nucleus in CO(3-2) shows the phase space information for the two clumps south of the BCG nucleus. The velocities of both clumps are ~ -275 km s^{-1}. The brighter clump is best fit by two velocity components in the velocity maps shown in Fig. 6. The narrow component is also visible in the PV diagram, and appears to extend between the two clumps. The similar velocities in these structures indicates that the clumps are likely related dynamically.

All of the emission along the extended filament is confined to the range of -200 to 0 km s^{-1}. However, the gas appears to be separated into two clumps. Higher blueshifted velocities are observed toward the tail of the filament, with velocities closer to systemic appearing at its base. The velocity of the inner portion of the filament is relatively constant

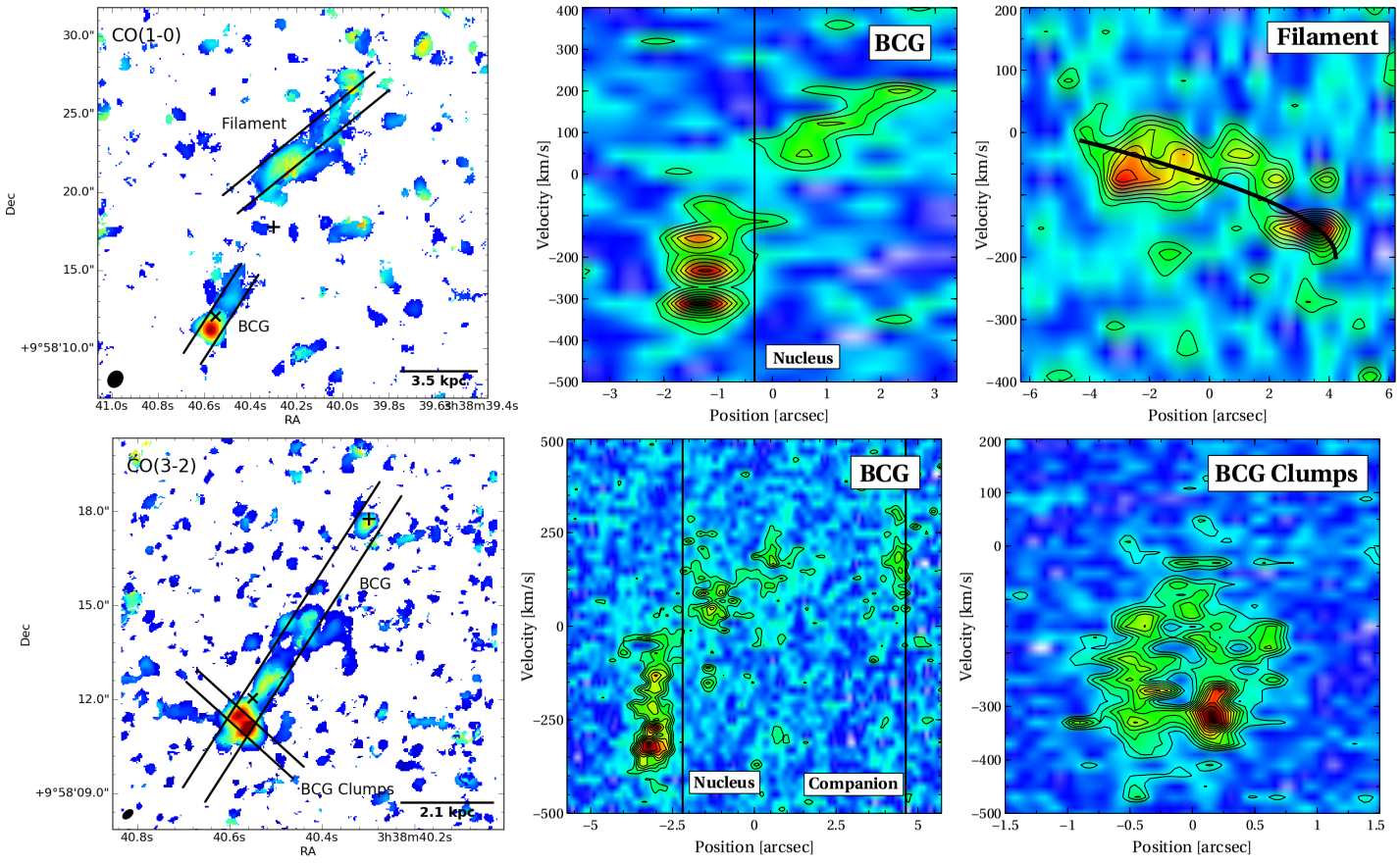

Figure 2.11: CO(1-0) (*top*) and CO(3-2) (*bottom*) position-velocity (PV) diagrams along the BCG (*center*), elongated filament (*top-right*), and a perpendicular cut across the BCG (*bottom-right*). In all cases the eastern (left) end of the slit corresponds to a negative position. The left column shows the location of the slits overlaid on the integrated fluxes determined from the velocity maps of Figs. 2.9 and 2.10. The vertical lines in the PV diagrams indicate the locations of the BCG nucleus and companion galaxy. The PV diagram of the extended filament in CO(1-0) (top-right) is overlaid with a gravitational free-fall model, as discussed in Section 2.4.3.

along its entire 4″ (3 kpc) length. An infall model has been overlaid on this PV diagram (see Section 2.4.3).

2.3.5 Spatial Correlation with Dust Extinction

Two regions of significant extinction were noted by Donahue et al. (2007) in the archival *HST* WFPC2 F606W image of 2A 0335+096. A wedge-shaped region is located southwest of the BCG nucleus, and an elongated filament extends north of the companion galaxy as seen in Fig. 2.1. Both of these regions are coincident with significant amounts of molecular gas.

The calibrated HST WFPC2 F606W image was obtained from the Hubble Legacy Archive. All magnitudes quoted here have been transformed to the Johnson V-band using $m_V(\mathrm{Vega}) - m_{\mathrm{F606W}}(\mathrm{ST}) = 0.04$ derived for the Kinney et al. (1996) elliptical galaxy template in the IRAF tool Synphot. The $V-I$ colour of the template galaxy, 1.3, is similar to that of a BCG, 1.2, so this conversion should be appropriate (Whiley et al., 2008). The quoted magnitudes have also been corrected for foreground Galactic extinction ($\mathrm{A_{F606W}}$), K-correction, evolution of the stellar population, and surface brightness dimming. The applied corrections are shown in Table 2.2.

In order to quantify the dust extinction we model the 2D distribution of stellar light using the galaxy-fitting code Galfit-M (Häußler et al., 2013), an extended version of Galfit (Peng et al., 2002, 2010). A Sérsic profile significantly overestimates the flux in the core of the BCG, an effect that is common in BCGs (Lauer et al., 2007; McNamara et al., 2009) and is thought to be caused by black hole scouring (Kormendy et al., 2009). The BCG is better modelled by the core-Sérsic profile (Graham et al., 2003), which is a Sérsic profile that transitions to a power law below the break radius r_b and is given by

$$I = I' \left[1 + \left(\frac{r_b}{r}\right)^{\alpha}\right]^{\gamma/\alpha} \exp\left[-\kappa \left(\frac{r^{\alpha} + r_b^{\alpha}}{r_e^{\alpha}}\right)^{1/(\alpha n)}\right]. \tag{2.2}$$

Here r_e and n are the effective radius and Sérsic index defined in the typical Sérsic profile, and the coefficient κ is a function of n. The transition and inner power law are described by the indices α and γ, respectively.s The companion galaxy is modelled using a normal Sérsic profile and fit simultaneously with the BCG.

Structures unrelated to the BCG and companion galaxies' stellar light were masked out prior to fitting. These included background galaxies, a bright foreground star in the SE, and the obvious dust features in the filament and the BCG nucleus. A wide detector artefact

Table 2.2: Photometric Corrections

Galactic extinction[a] (mag)	K[b] (mag)	Evolution[b] (mag)	$(1+z)^4$ (mag)
0.989	0.073	−0.047	0.148

Notes: [a] Schlafly & Finkbeiner (2011) [b] Poggianti (1997)

at the edge of the CCD was also masked out, and limits the fittable area considerably. The resulting fit parameters are shown in Table 2.3. The companion galaxy is well-modelled by a Sérsic profile with index 1.8 and total V-band magnitude 16.8. Using the same photometric corrections as the BCG, its absolute magnitude of −19.1 is slightly brighter than a dwarf galaxy.

Several biases are present in this fitting procedure. First, the fittable area is small due to the foreground star and a large detector artefact near the edge of the CCD. Since 2A 0335+096 is a nearby cluster, these fits do not extend far into the envelope of the galaxy. The full shape of the BCG's light profile cannot be traced, so its effective radius is unconstrained. This also results in a large Sérsic index, since a power law provides a sufficient fit beyond the core. Second, the light profiles of galaxies are best fit when their position angle and ellipticity are allowed to vary as a function of radius. Isophotal variations are not currently supported by Galfit-M. Using the ELLIPSE task in IRAF to extract elliptical isophotes of the stellar light favours a position angle of $-5°$ to $-10°$ in the center, twisting to $-30°$ beyond 10 arcsec. Similarly, the axis ratio b/a is consistent at large radii with the 0.7 measured here, but decreases to 0.65 in the core.

In Fig. 2.12 we present a map of the dust extinction, showing the ratio of image surface brightness to the model brightness (I/I_0). Regions with significant extinction are highlighted by the labelled ellipses, with the corresponding extinction (both the peak extinction in a pixel and mean within the ellipse) tabulated in Table 2.4. These regions were confirmed by eye in the original image. Systematic errors are clearly visible in the residuals of the extinction map, primarily perpendicular to the BCG–companion axis. Positive and negative residuals near the BCG centroid (red ×) correspond to a double-peaked nucleus, so the extinction northwest of region A does not correspond to dust. The extinction surrounding the labelled dust features is generally $\lesssim 5\%$, though increases to $\sim 10\%$ around the filament. Model residuals surrounding the identified regions also typically have $I/I_0 \geq 1$, so the tabulated optical depths and dust masses may be underestimated.

The mean optical depth τ is computed from the mean extinction via $I/I_0 = \mathrm{e}^{-\tau}$.

Table 2.3: 2D Optical Fitting Results

	Units	BCG	Companion
$I(r_b)$[1]	mag arcsec^{-2}	19.310 ± 0.005	–
r_b	arcsec	0.924 ± 0.007	–
α		2.56 ± 0.05	–
γ		0.081 ± 0.004	–
$m_{\rm tot}$	mag	–	16.736 ± 0.003
r_e	arcsec	Unconstrained[2]	0.997 ± 0.002
$\frac{{\rm d}\ln I}{{\rm d}\ln r}$		-1.35[3]	–
n		19.6 ± 2.8	1.838 ± 0.005
b/a		0.7010 ± 0.0004	0.884 ± 0.001
PA	degrees	-21.85 ± 0.06	7.8 ± 0.5

Notes: [1]$I(r_b)$ is related to I' in Eqn 2.2 via $I' = I(r_b)\ 2^{-\gamma/\alpha}\ \exp\left[\kappa\ (2^{1/\alpha}\ r_b/r_e)^{1/n}\right]$. [2]The BCG radii probed by the HST imaging only show a bend at the break radius. The Sérsic component is close to a power law, with the corresponding effective radius lying outside of the HST field of view. [3]Since the effective radius is unconstrained, we quote the logarithmic derivative at a radius of $20''$ instead.

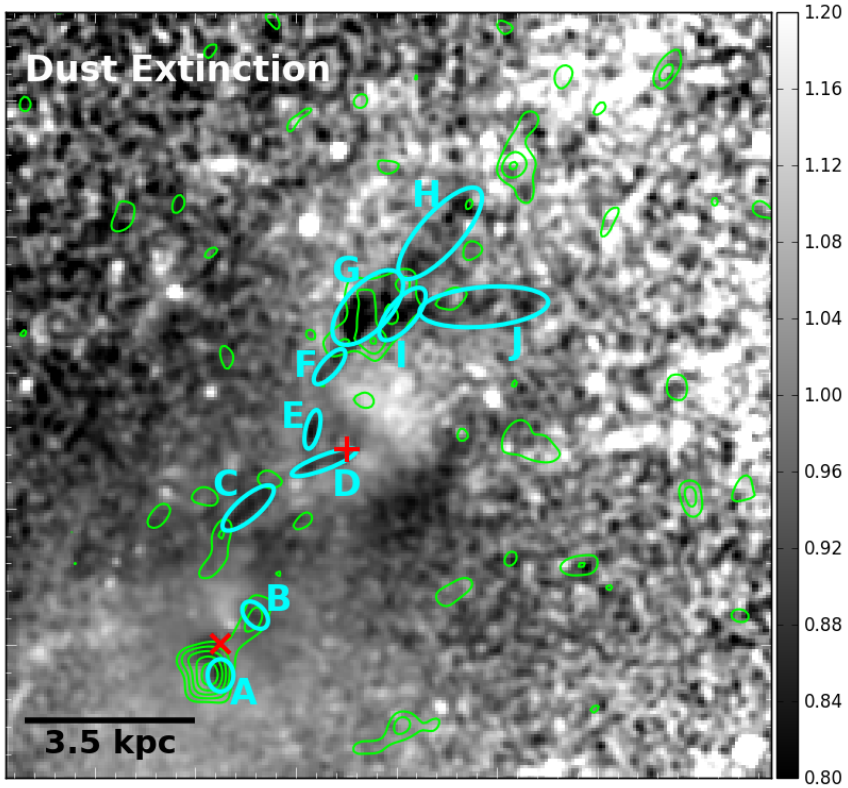

Figure 2.12: Dust extinction map of the HST F606W image. Regions with significant dust extinction are identified by the cyan ellipses, with statistics shown in Table 2.4. The BCG and companion galaxy centroids are identified by the red × and +, respectively. The image is shown in the same field of view as the ALMA CO(1-0) image (Figs. 2.1 and 2.9). The CO(1-0) contours from Fig. 2.1 have been overlaid for reference.

Table 2.4: Dust Extinction

Region	Area (10^{42} cm^2)	$(I/I_0)_{\rm min}$	I/I_0	$<\tau>$	N_H (10^{20} cm^{-2})	$M_{\rm dust}$ (10^5 M$_\odot$)
A	2.58	0.82 ± 0.03	0.923 ± 0.005	0.080 ± 0.005	3.42 ± 0.23	7.4 ± 0.5
B	2.0	0.88 ± 0.04	0.938 ± 0.006	0.064 ± 0.006	2.75 ± 0.27	4.6 ± 0.5
C	4.52	0.80 ± 0.06	0.896 ± 0.007	0.110 ± 0.007	4.69 ± 0.32	17.7 ± 1.2
D	3.12	0.81 ± 0.02	0.944 ± 0.005	0.057 ± 0.005	2.45 ± 0.23	6.4 ± 0.6
E	1.58	0.72 ± 0.05	0.884 ± 0.010	0.123 ± 0.012	5.25 ± 0.50	6.9 ± 0.7
F	2.3	0.76 ± 0.09	0.922 ± 0.014	0.081 ± 0.015	3.46 ± 0.63	6.7 ± 1.2
G	13	0.48 ± 0.08	0.884 ± 0.007	0.123 ± 0.008	5.26 ± 0.35	57.0 ± 3.8
H	14.9	0.56 ± 0.10	0.962 ± 0.009	0.039 ± 0.009	1.66 ± 0.39	20.7 ± 4.8
I	5.24	0.56 ± 0.09	0.886 ± 0.012	0.121 ± 0.013	5.16 ± 0.23	22.6 ± 2.5
J	15.6	0.51 ± 0.10	0.959 ± 0.008	0.042 ± 0.009	1.79 ± 0.36	23.3 ± 4.7
Total						173 ± 8

This is converted into column density (N_H), assuming a standard V-band Galactic extinction curve (Cardelli et al., 1989), through $N_H = 2.05 \times 10^{21} \tau_V$ cm^2 and finally to dust mass. Region A is coincident with a clump of molecular gas identified at CO(3-2). Taking $\mathrm{CO}(3-2)/\mathrm{CO}(1-0) = 7$, the corresponding molecular gas mass is 9.5×10^7 M$_\odot$ and gas-to-dust ratio is 130, which is similar to the Milky Way value. Regions F through I are coincident with the extended filament. The total dust mass in these regions is $1.07 \pm 0.07 \times 10^7$ M$_\odot$. With a molecular gas mass of $7.8 \pm 0.9 \times 10^8$ M$_\odot$, the local gas-to-dust ratio is 66. This is a factor of two lower than the gas-to-dust ratio in the BCG. Regions B and D are coincident with molecular gas in the northern spur and companion galaxy, respectively, although neither traces the gas distribution well. Attributing all of the molecular gas in the spur to region B results in a gas-to-dust ratio of 290, although the differing spatial distributions add considerable uncertainty to this value.

Treating the dust as a thin screen, for regions G–J, where the minima of I/I_0 are about 0.5, the dust must lie on or in front of the midplane of the BCG. The velocity of the molecular gas in these regions is within a few tens of km s^{-1} from the systemic value, and the FWHM is 100 km s^{-1} at its broadest. Taken together, these suggest that the filament is oriented roughly perpendicular to the line of sight, possibly flowing on a nearly radial trajectory toward the BCG. The lesser peak extinction within the BCG, where the minimum of $I/I_0 \simeq 0.82$, means that the location of the dust along our line of sight is poorly constrained.

Overall the most significant associations of molecular gas are coincident with significant dust extinction. Dust shielding in these regions may be promoting the formation of molecular gas. It is also possible that the more extended associations (such as along the spur) do not have detected dust extinction because the dust has been spread out over a larger area, resulting in too low a column density for visible dust extinction.

2.3.6 Spatial Correlation with X-ray and Hα Filaments

2A 0335+096 hosts a bright Hα nebula with total luminosity $L_{\rm H\alpha} = 0.8 \times 10^{42}$ erg s^{-1} (Donahue et al., 2007). While the Hα nebula is not associated with any structures in the $0.5 - 7$ keV *Chandra* X-ray image, multi-temperature fits reveal a 0.5 keV component in the ICM that is spatially coincident with the Hα emission (Sanders et al., 2009). Similar spatial correlations have been observed in several other cool core clusters, including Perseus (Fabian et al., 2003, 2008), M87 (Sparks et al., 2004; Werner et al., 2013), and several nearby giant ellipticals (Werner et al., 2014). Filaments of molecular gas have been detected along the Hα filaments in Perseus (Salomé et al., 2006; Lim et al., 2008; Salomé et al., 2008; Lim et al., 2012), implying that the co-spatial gas in the filaments occupies 5–6 decades in temperature.

Multiphase gas spanning many decades in temperature is also observed here. Fig. 2.13 shows the Hα nebula from Donahue et al. (2007) overlaid with contours of the CO(1-0) emission. The two distributions are qualitatively very similar. Bright Hα emission near the BCG extends in a spur toward the companion galaxy. The emission extends beyond the companion galaxy into a filament coincident with the extended filament of molecular gas seen in CO(1-0) emission. However, the most luminous nebular emission is in the BCG, while the molecular gas is observed preferentially in the filaments. This may be due to line emission that has been resolved out by the interferometer. Only 40% of the single dish flux has been recovered here, so a diffuse component of cold gas may be present in the BCG.

Integral field spectroscopy of the Hα nebula reveals that the [N II] λ6583 line and the molecular gas are co-located in both position and velocity space (Farage et al., 2012). Broad, blueshifted emission is slightly offset to the south of the BCG with a velocity of about -120 km s^{-1} (-240 km s^{-1} in our adopted frame). Near the companion galaxy the Hα nebula becomes redshifted with respect to the systemic velocity, with blueshifted emission extending along the direction of the filament. Farage et al. (2012) also detected nebular emission $5 - 10$ kpc southeast of the BCG nucleus. Its redshifted velocity led them to conclude that the nebula is in rotation about the center of the BCG with a velocity amplitude of 130 km s^{-1}. Molecular gas either does not extend along the southeastern arm

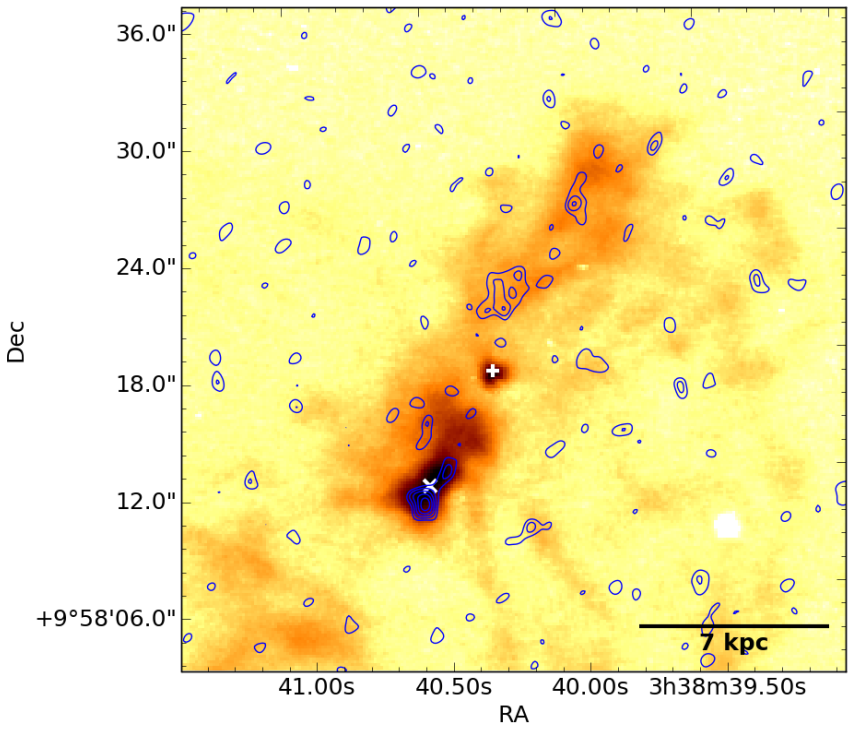

Figure 2.13: Hα emission from Donahue (2007) overlaid with the CO(1-0) contours from Fig. 2.1. The $\times$ and + indicate the nuclei of the BCG and companion galaxy, respectively. The coordinate reconstruction of the Hα image is accurate to ~ 1 arcsec.

of the filament or is too faint to detect, so we are unable to corroborate this finding. The lack of molecular gas to the southeast may arise if the surrounding atmosphere lacks the dense regions required to form H_2, or if H_2 production is enhanced by the presence of dust grains to the northwest. Since our observations trace only the high density molecular gas (see Section 2.3.2), molecular gas may lie to the southeast but falls below our detection limit.

2.4 Discussion

2.4.1 Origin of the Molecular Gas

With a total molecular gas mass exceeding $10^9\,M_\odot$, 2A 0335+096 harbours significantly more molecular gas than is typically observed in early-type galaxies. Identifying the origin of this gas is critical in understanding the evolution of the BCG. Two primary mechanisms could be contributing this gas: stripping of merging galaxies or cooling from the hot atmosphere.

Large supplies of molecular gas are observed preferentially in BCGs at the centers of galaxy clusters with cooling times falling below a Gyr. These systems are associated with bright emission-line nebulae and enhanced star formation. Thus the presence of molecular gas should in general be linked to residual cooling of the hot atmosphere.

The presence of a companion galaxy located 5 kpc from the BCG in projection raises the possibility of a merger origin for the molecular gas in this system. Its low stellar velocity (~ 200 km s^{-1} ; Gelderman, 1996) relative to the BCG suggests that the galaxies also have a small radial separation. The trail of molecular gas oriented toward the companion galaxy may then be indicative of an interaction between the two galaxies.

Before delving further into the origin of the molecular gas, we emphasize the difference in dynamics between the two components. The inner edge of the filament is slightly blueshifted with respect to the stellar component of the BCG, while all nuclear gas north of the BCG is redshifted. Since the components are not smoothly connected in phase space, we treat them separately in our discussion.

Mergers with donor galaxies can supply gas to the BCG through several distinct avenues. Repeated mergers between the BCG and gas-rich donor galaxies are unlikely given the low number of member galaxies in this low richness cluster (Schwartz et al., 1980), and because the high velocity dispersion of a cluster decreases the merger rate. We instead focus only on a merger with the nearby companion galaxy. A tidal interaction between the galaxies may result in either the stripping of cold gas from the companion or the disruption of a pre-existing gas supply within the BCG. Alternatively, ram pressure stripping would form a tail that may correspond to the filament.

Tidal Interaction

In the nucleus of the BCG, the opposed redshifted and blueshifted velocities are suggestive of rotation. This velocity pattern is consistent with the H_2 kinematics derived from K-band

integral field spectroscopy (Wilman et al., 2011) as well as lower resolution Hα integral field spectroscopy of the nuclear barred structure (Hatch et al., 2007; Farage et al., 2012). The peak-to-peak velocity difference observed in CO(1-0) is ~ 400 km s^{-1} over a spatial scale of about 2 kpc. This is expected of molecular gas in merger remnants, which generally exhibits large-scale rotation with high velocities (Ueda et al., 2014).

Although ordered motion seems plausible at CO(1-0), the higher resolution CO(3-2) maps show a highly asymmetric distribution of cold gas that is inconsistent with being a rotationally-supported disk. Two times more molecular gas is located south of the nucleus versus the north side, and the gas velocity jumps abruptly across the nucleus. This asymmetry indicates that any ordered structure must be in the process of forming, as the gas is not in an equilibrium structure. If the gas is orbiting the BCG, then it will form one complete spiral when the gas on the innermost orbit has circled the galaxy one more time than the gas on the outermost orbit. With resolved scales of $1-2$ kpc and velocities of ~ 200 km s^{-1}, the corresponding disk formation timescale is $\sim 3 \times 10^7$ yr. Since no disk-like structure is observed, the gas is either moving mainly in the plane of the sky or we are observing the system very recently after the stripping began.

Gas clumps oriented toward the companion galaxy have velocities that increase roughly linearly with projected radius to values matching the stellar velocity of the companion galaxy. An interaction between the companion galaxy and the BCG can account for the molecular gas via two scenarios: either the gas is tidally stripped from the companion, or the passage of the companion through a pre-existing gas supply has dredged up the gas. Differentiating between the original source of the molecular gas is difficult with the current data. Given the greater recession velocity of the companion, if it has already interacted with the BCG, it is now receding from the BCG, moving outward in projected radius and away behind the midplane of the BCG.

In the first scenario, direct stripping from the companion would initially maintain the sign of the velocity, with the magnitude decreasing as the gas is slowed by the gravity of the BCG. At later times the gas will reverse direction and fall back onto the BCG. The persistent redshifted velocities observed here then imply that the interaction was recent, as the clouds have not yet reversed in direction. If even half of the gas distributed between the galaxies originated in the companion, then its molecular gas mass would have initially been $\sim 1.2 \times 10^8$ M$_\odot$, double its current mass. This is relatively gas-rich compared to the ellipticals in Virgo (e.g. Young et al., 2011). A merger with a gas-rich donor galaxy is certainly possible, but is unlikely to expect a priori.

Following the second scenario, gas originating in the BCG that is pulled outward by the companion would have a velocity that increases with radius as it is accelerated away

from the BCG, as observed. When the companion is far enough away, the BCG will again dominate the potential and any gas that is not bound to the companion will rain back onto the BCG. The 1.5 kpc gap between the companion and the farthest extent in the spur suggests that this has occurred recently and the clumps between galaxies may now be dominated once again by the BCG. Although no stellar dispersion is available for the companion, the linewidth of its molecular gas (260 km s^{-1}) is typical of a normal galaxy, suggesting that the molecular gas has had time to settle into its gravitational potential well. From the "BCG" spectrum presented in Fig. 2.3, the masses of the redshifted and blueshifted peaks are consistent, containing $1.5 \pm 0.3 \times 10^8\,M_\odot$ and $1.7 \pm 0.3 \times 10^8\,M_\odot$, respectively. If these originated from the same reservoir, then the tidal disruption would have removed $\sim 50\%$ of the pre-existing gas supply.

With a projected separation of 4.5 kpc, an interaction between these galaxies would have occurred roughly 20 Myr ago, assuming the line of sight speed of the companion is representative of its 3D velocity. However, if the velocity is this low near the cluster core, then the companion cannot be on its first passage through the cluster, as several orbits would be required to decelerate the galaxy. If the companion is on its first passage then it must be travelling near the plane of the sky. Its transverse velocity would be several times greater than its line of sight velocity, decreasing the interaction time by a factor of a few.

Importantly, tidal interactions affect all matter within the galaxy, without regard to its phase. Stars should therefore be affected just as strongly as the molecular gas. This is not observed in the *HST* imaging, as the stellar light does not show strong deviations from a smooth profile. Removing half of a pre-existing gas reservoir via tidal forces is therefore unlikely. It is possible that an interaction between these galaxies has not yet begun, potentially from a radial offset between them, but the similarity in velocity between the companion and the series of clumps appears too striking to be a coincidence.

We again emphasize that the tidal stripping discussed here only attempts to account for the molecular gas within the BCG; the filament must be formed separately. The molecular filament cannot have originated from an older merger, as the merger rate is low and the gas would have already fallen onto the BCG. Instead we must invoke a separate mechanism entirely, such as cooling from the hot atmosphere. It is far more likely that the molecular gas is produced via one primary mechanism, and that the companion galaxy has merely disrupted a pre-existing gas supply.

Ram Pressure Stripping

In the dense cores of galaxy clusters, the ram pressure exerted on atomic gas in an infalling galaxy is enough to overcome its gravitational binding energy, allowing the gas to be efficiently stripped from its host galaxy (Haynes et al., 1984; di Serego Alighieri et al., 2007; Grossi et al., 2009). Molecular gas is more difficult to strip than atomic gas because molecular clouds have a much smaller surface area than atomic nebulae and they reside deeper within the galaxy's gravitational potential. Galaxies in the Virgo cluster with strong HI deficiencies have minimal molecular gas deficiencies (Kenney & Young, 1989), and the CO detection rate in the cluster is the same as in the field (Young et al., 2011). However, ram pressure stripping of molecular gas has still been observed in the Virgo (e.g. Vollmer et al., 2008), Norma (Jáchym et al., 2014), and Coma clusters (Jáchym et al., 2017). If the companion galaxy is indeed falling into the cluster, then ram pressure stripping might be a viable source of the $7.8 \times 10^8\,M_\odot$ of molecular gas in the filament. This, however, is not a viable mechanism for supplying the large reservoirs of molecular gas in BCGs in general, since molecular gas is observed preferentially in BCGs residing at the centers of clusters with short central cooling times.

The Norma cluster galaxy ESO 137-001 is the first system found to contain a large amount of molecular gas in a ram pressure stripped tail, with a total molecular gas mass exceeding $10^9\,M_\odot$ (Jáchym et al., 2014). This molecular gas is associated with a 40 kpc long tail of Hα emission and an 80 kpc long X-ray tail, with a total HI upper limit of $\sim 2 \times 10^9\,M_\odot$. The presence of soft X-ray emission in the tail is expected to arise from the mixing of the cold, stripped interstellar medium with the hot intracluster gas (Sun et al., 2006; Tonnesen et al., 2011). Jáchym et al. (2014) suggest that the molecular gas in the outer extent of the tail has formed in situ out of stripped atomic gas, while the inner reaches of the tail may also be comprised of molecular clouds that were stripped directly from the infalling galaxy.

The spatial correlation of molecular gas with Hα and X-ray emission in ESO 137-001 resembles the filament trailing the companion galaxy in 2A 0335+096. Evidently, ram pressure stripping of gas from a high velocity infalling galaxy is able to form a filament similar to that observed in 2A 0335+096. This offers a natural explanation for the significant dust extinction observed along the filament, which would be stripped from the companion galaxy along with the atomic and molecular gas, and would offer a seeding site for in situ molecular gas formation. Since the line of sight speed of the molecular gas along the filament is $\lesssim 200$ km s^{-1}, the high infall velocity required to form the filament via ram pressure stripping would require that most of the motion is along the plane of the sky.

Ram pressure stripping requires a very high relative velocity in order to form the ob-

served filament. Orbit modelling in ESO 137-001 favours infall velocities of $\gtrsim 3000$ km s^{-1}. The necessary relative velocity in 2A 0335+096 is not this severe, since the companion galaxy is situated closer to its cluster center so is in a higher density environment, lessening the demands on velocity. Extrapolating the Sanders et al. (2009) gas density profile assuming a power law of $n_e \propto r^{-1}$, the ICM density at the base of the filament (~ 13 kpc) is ≈ 0.07 cm^{-3}. This is 35 times greater than the ICM density at the location of ESO 137-001, using the β-model parameters in Table 7 of Jáchym et al. (2014). Assuming that the force exerted by ram pressure, ρv^2, is the same here as it is in ESO 137-001, the infall velocity required to produce the tail is ~ 500 km s^{-1}. Since the line of sight velocity of the companion galaxy is 230 km s^{-1}, the inclination of the filament would need to be about 30°.

As discussed in Section 2.4.1, the series of redshifted clumps located between the BCG and the companion suggests that the two galaxies have already interacted. If this is the case, then the companion galaxy must have passed through the BCG on a northwestward trajectory. This scenario is mutually exclusive with the ram pressure stripping origin of the filament, which requires that the companion is on its first passage through the cluster and is travelling to the southeast.

Additionally, the morphology of the filamentary emission differs from what is expected from ram pressure stripping. First, the orientation of the filament does not coincide with the companion galaxy. Extending the inner edge of the filament to the southeast, the shortest distance between the filament and the companion is 2 kpc. Ram pressure stripping should form a tail in a direction directly opposing the direction of motion, which is not the case here. Second, Hα emission and soft X-rays are not confined to the region trailing the companion. Significant Hα emission is observed on both sides of the BCG, with the brightest emission surrounding the molecular gas within the BCG. This emission is visible in the lower left corner of Fig. 2.13 as well as the contours of Fig. 2.14, but its full extent is obscured due to the presence of a bright foreground star. If the filament is formed by ram pressure stripping then the Hα emission should be localized to the tail of the companion galaxy, in addition to whatever emission is associated with the molecular gas in the BCG.

Cooling of the Hot Atmosphere

Cooling from the hot atmosphere naturally explains the spatial correlation of gas over 5–6 decades in temperature. The upper limit on the mass deposition rate of the 0.5 keV X-ray emitting gas is $30\,M_\odot$ yr^{-1} (Sanders et al., 2009), which can form the $7.8 \times 10^8\,M_\odot$ of molecular gas in the filament in 24 Myr or the entire gas reservoir in 40 Myr. Depletion of the molecular gas via star formation proceeding at a rate of $2\,M_\odot$ yr^{-1} (O'Dea et al., 2008)

increases the accumulation time by $< 10\%$. We also note that the cooling gas is distributed on larger scales than the molecular gas. Roughly half of the 0.5 keV gas is located on the side of the BCG opposite the molecular gas. This increases the accumulation time by roughly a factor of two, resulting in a total time of $50 - 90$ Myr. This is approaching the mean outburst interval between generations of AGN outbursts of 10^8 yr (e.g. Vantyghem et al., 2014).

Most of the baryonic content in clusters is contained in the hot atmosphere, offering a vast reservoir which can supply the molecular gas. Approximating the central hot gas density profile in Sanders et al. (2009) with $\rho \propto r^{-1}$, the extrapolated gas mass within 13 kpc, which encloses all of the molecular gas, is $7.9 \times 10^9\,\mathrm{M}_\odot$. This is about 7 times more than is needed to form the entire $1.13 \times 10^9\,\mathrm{M}_\odot$ of molecular gas. However, cooling does not occur over the full azimuth, and the local supply of hot gas is much more restrictive. On the other hand, gas cooling out of the hot atmosphere can be replenished by gas from higher altitudes, providing more than the $7.9 \times 10^9\,\mathrm{M}_\odot$ of gas within the central 13 kpc.

The presence of multiple cavities in the hot atmosphere (Mazzotta et al., 2003; Sanders et al., 2009) indicates that 2A 0335+096 has undergone several cycles of AGN feedback, which would include multiple cycles of cooling. However, if cooling has persisted over multiple cycles then we should expect to see several filaments, similar to those in Perseus (Hatch et al., 2006; Salomé et al., 2011), while only one is observed. Filaments from previous cooling cycles may have fallen back onto the BCG, forming the observed reservoir within the BCG. Conversely, the presence of a single filament is reminiscent of the cooling wake observed in A1795 (Fabian et al., 2001; Crawford et al., 2005), where cooling is stimulated by the motion of the cD galaxy through the hot atmosphere. Sloshing motions in 2A 0335+096 indicate that the BCG is in motion with respect to the cluster, which may establish the preferred direction of cooling.

Gas cooling from the hot atmosphere is expected to be relatively dust-free (Donahue & Voit, 1993). This is because dust grains are rapidly sputtered in the ICM, and can only form when the gas is shielded by UV and X-ray irradiation (Draine & Salpeter, 1979). As noted in Section 2.3.5, significant dust extinction is present over much of the length of the filament. Since dust production from cooling gas is difficult, the dust likely originated from the within the BCG. Hatch et al. (2007) suggested that the dusty nebulae observed in several BCGs have been drawn out of the central molecular gas reservoir, where the high densities can provide shielding long enough for the gas to become polluted with dust.

Recent simulations have suggested that thermal instabilities in the hot atmosphere are induced along the direction of the radio jet (Gaspari et al., 2013; Li & Bryan, 2014a), which is not the case in 2A 0335+096. A bipolar radio jet observed at 1.5 GHz extends 12 arcsec

to the northeast and southwest of the BCG (Sarazin et al., 1995; Donahue et al., 2007), which is orthogonal to the filament. Instead, we argue in Section 2.4.2 that the preferred direction of gas cooling has been imposed by uplift from an X-ray cavity. This enables dust to be lifted out of the BCG, providing seeding sites for the production of molecular gas.

Summary: Gas Origin

While galaxy mergers are unable to account for the high molecular gas masses in cool core galaxy clusters in general, the presence of a close companion in this system has the potential to supply the cold gas. Tidal stripping from the companion galaxy can supply the BCG with cold gas, but does not account for the filament. Instead, the merger may have disrupted a pre-existing gas supply within the BCG, dredging up cold gas as it passed through. However, we do not see evidence for a tidal disruption in the stellar light of either galaxy. Alternatively, the filament observed in 2A 0335+096 resembles the ram pressure stripped tails in other systems (e.g. ESO 137-001). Ram pressure stripping is feasible if the companion is infalling from the northwest with a high relative velocity, and can account for the spatial coincidence of molecular gas, dust extinction, Hα emission, and soft X-rays. However, it does not explain the inclined orientation of the filament or the Hα emission and soft X-ray located southeast of the BCG nucleus. Furthermore, if gas has in fact been dredged up by the companion galaxy, then its implied orbit rules out the possibility of a ram pressure stripping origin of the filament. Cooling of the hot atmosphere provides a feasible mechanism for supplying the molecular gas that is tenable in a much broader sample of cool core clusters. The hot atmosphere harbours more than enough gas to produce the filament, and the 0.5 keV phase is cooling rapidly enough to form the entire molecular gas supply in $\sim 10^8$ yr. The cold gas within the BCG may then correspond to an older cycle of cooling from the hot atmosphere that has fallen onto the BCG.

2.4.2 Origin of the Cooling

Cooling Stimulated by the AGN

Following recent ALMA observations of PKS0745-191 (Russell et al., 2016) and A1835 (McNamara et al., 2014), McNamara et al. (2016) proposed the "stimulated feedback" model. In this model, molecular gas condenses from lower entropy gas that is lifted outward from the cluster core by X-ray bubbles, away from the location where the heating rate matches its cooling rate. Unless the overdensity falls back to its original position within its

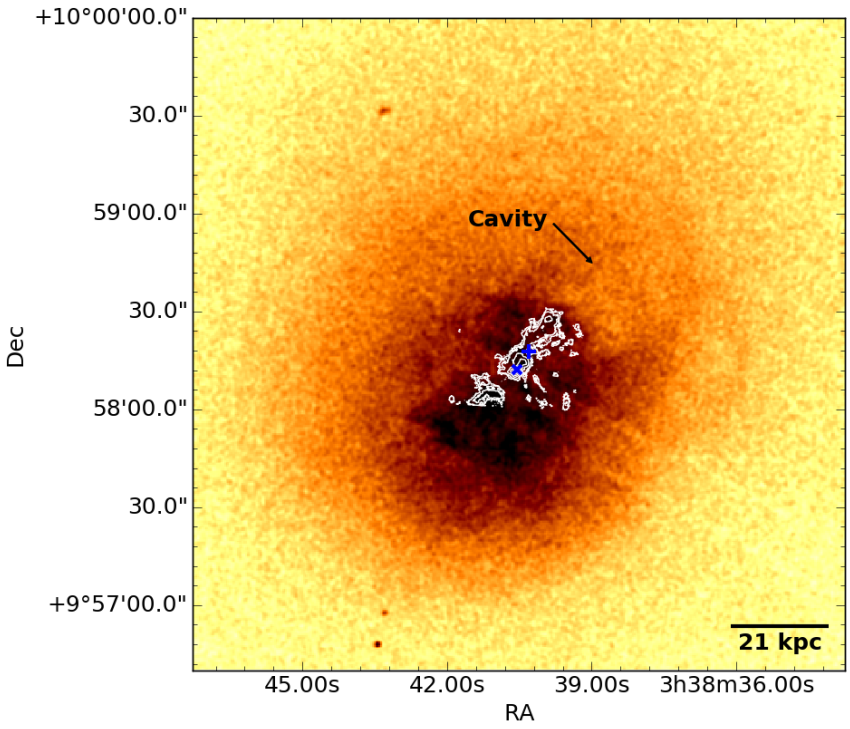

Figure 2.14: Chandra X-ray image of the hot atmosphere of 2A 0335+096. Several X-ray cavities and clumps of cool gas are visible in the image. The Hα nebula, shown in white contours, extends toward the most energetic cavity. Any emission to the south of the contours has been masked out due to contamination by a foreground star.

cooling time, it will condense out of the intracluster medium (Nulsen, 1986; Revaz et al., 2008; Gaspari et al., 2013; Li & Bryan, 2014b), forming molecular gas and emission-line nebulae.

The molecular gas in the PKS0745-191 BCG is distributed along three narrow filaments that are $3-5$ kpc in length (Russell et al., 2016). Two of the filaments are oriented behind X-ray cavities, while the third is coincident with UV emission from young stars. The velocities of the cold gas, which lie within ± 100 km s^{-1} of the systemic velocity, are too low to arise from steady inflow of clouds condensing out of the hot atmosphere. Instead, the velocity distribution of the two filaments oriented toward X-ray cavities are consistent with the majority of the gas flowing outward from the galaxy center.

A similar outflow was observed in the A1835 BCG, where 10^{10} M$_\odot$ of cold gas is located in a bipolar flow behind two X-ray cavities (McNamara et al., 2014). This system hosts comparably low velocities, which were initially interpreted as a face-on disk. However, low velocities have been observed in a growing sample of BCGs observed with ALMA (David et al., 2014; Russell et al., 2014, 2016; Tremblay et al., 2016), indicating that velocities well below the stellar velocity dispersion are common amongst BCGs. Similarly low velocities were also noted in the filamentary optical-line nebulae of BCGs (e.g. Heckman et al., 1989; Jaffe et al., 2005; Hatch et al., 2006; Oonk et al., 2010). Evidently, the gas must either be dynamically young, having not had time to settle into its gravitational potential, or the clouds are supported by pressure from either magnetic fields or the hot gas.

Redshifted CO absorption lines have been observed in NGC5044 (David et al., 2014) and A2597 (Tremblay et al., 2016). The widths of these lines are small (~ 5 km s^{-1}), and are comparable to individual giant molecular clouds within the Milky Way. Since the lines are seen in absorption, the clouds must lie in front of the AGN, blocking its continuum emission. The redshifted velocities indicate that the clouds are falling toward the black hole, and are possibly in the process of being accreted. The presence of both inflow and outflow in BCGs suggests that gas lifted by from the cluster core eventually returns in a circulation flow, or molecular "fountain".

The results presented here are consistent with this stimulated feedback model. *Chandra* imaging of 2A 0335+096, shown in Fig. 2.14, reveals a series of X-ray cavities corresponding to multiple generations of AGN feedback (Mazzotta et al., 2003; Sanders et al., 2009). The Hα nebula, overlaid in white contours in Fig. 2.14, shows a striking connection to the northwestern cavity. The emission extends from the center of the BCG directly toward the X-ray cavity identified in Fig. 2.14, with fainter emission along the cavity's inner edge. As noted in Section 2.3.6, the Hα filament is coincident with soft X-ray emission from 0.5 keV gas as well as $20-30$ K molecular gas. This indicates that the gas is cooling over 5

decades in temperature in the wake of a rising X-ray cavity. Dust grains situated along the filament have presumably been uplifted from the BCG along with the low entropy ICM. This resembles the scene in PKS0745-191, where the two filaments trailing X-ray cavities are correlated with dust extinction. The uplifted dust potentially enhances the formation of molecular gas by offering seeding sites.

A bipolar radio jet observed at 1.5 GHz extends 12 arcsec to the northeast and southwest of the BCG (Sarazin et al., 1995; Donahue et al., 2007). This radio jet traces the most recent generation of AGN feedback, which is orthogonal to the emission-line filament. No molecular gas is observed along this direction, indicating that the radio jet itself has not disrupted the central supply of molecular gas or created thermally-unstable overdensities in the hot atmosphere. Similarly, any cavities formed along this jet have yet to induce a significant amount of thermally unstable cooling.

Cooling Wake from Galaxy Motion

Cooling of the ICM can also be induced by the gravitational wake of a galaxy in motion with respect to the cluster. For example, A1795 hosts a BCG with a velocity of $+150$ km s^{-1} with respect to the mean of all galaxies in the cluster, or $+374$ km s^{-1} compared to the galaxies within 270 kpc (Oegerle & Hill, 1994). The cluster also harbours a luminous emission-line nebula extending in a 50 kpc long filament to the southeast of the BCG (Cowie et al., 1983; Crawford et al., 2005; McDonald & Veilleux, 2009). This filament has also been identified in X-ray imaging (Fabian et al., 2001; Crawford et al., 2005; Ehlert et al., 2015), molecular gas (McDonald et al., 2012a), U-band polarimetry (McNamara et al., 1996), and far-UV imaging (McDonald & Veilleux, 2009). Fabian et al. (2001) argued that this filament was formed from a cooling wake, where the gravitational attraction from the BCG moving through a region with a short cooling time focuses cooling onto its wake. Since the gas cools from the ICM, its velocity reflects that of the cluster instead of the BCG.

In principle either the BCG or the companion galaxy could induce this cooling wake. However, it is more likely that the BCG causes the cooling wake due to its larger gravitational attraction, provided it is in motion with respect to the ICM. Furthermore, the presence of Hα filaments in cool core clusters is not correlated with the presence of galaxies near the BCG (McDonald et al., 2010). If the companion galaxy in 2A 0335+096 is able to induce a cooling wake, then we should expect similar filaments in all cool core clusters hosting galaxies near their core, which is evidently not the case.

Without a direct measurement of ICM velocity it is difficult to determine if the BCG is

in motion with respect to the cluster. However, the X-ray atmosphere of 2A 0335+096 hosts a series of cool clumps and a cold front, which are indicative of an unrelaxed dynamical state (Mazzotta et al., 2003; Sanders et al., 2009). In particular, the X-ray centroid of the cluster is difficult to pinpoint because of the series of cool clumps. The brightest clump of X-ray emission in the $0.5 - 7$ keV band is co-spatial with the Hα emission $6 - 10$ kpc southeast of the BCG nucleus. The offset between the X-ray peak and the BCG, as well as the presence of sloshing motions in the ICM, suggest that the BCG is in motion relative to the cluster. We are unable to constrain the BCG velocity in this system, although sloshing motions in Virgo have velocities of $\sim 50 - 100$ km s^{-1} (Roediger et al., 2011). The low velocity of the main component of the inner filament, -28 ± 4 km s^{-1}, may imply a small line of sight velocity offset between the BCG and cluster, though multiple distinct velocities throughout the filament point to a more complicated picture. Similarly, we cannot confirm that the motion is along the direction of the filament.

As noted in Section 2.4.1, gas cooling from the ICM is expected to be dust-free. This appears to be the case in A1795, where dust extinction is only observed within the central galaxy (Pinkney et al., 1996), and is likely not affecting star formation along the filament (Crawford et al., 2005). The presence of dust along the filament in 2A 0335+096 argues against the cooling wake scenario unless the filament has been enriched with dust from the BCG or companion, perhaps through ram pressure stripping. This possibility has been suggested by Sparks et al. (2004) for the filaments in M87. However, ram pressure stripping requires velocities of several hundred km s^{-1}, even in the dense cluster core.

Cooling Along a Dark Matter Filament

We also note an interesting similarity in the position angles of the BCG and filament and the apparent trajectory of the companion galaxy. BCGs are known to have a common orientation with their host clusters, which are themselves aligned with the cosmological filaments of dark matter they accreted from (Binggeli, 1982; Niederste-Ostholt et al., 2010). The companion galaxy may have accreted along this axis, falling from the southeast and passing through the gas supply in the BCG. Understanding how the filamentary emission is linked to the dark matter distribution is more difficult. Any overdensity caused by the filament should only be significant in the outer extent of the cluster, not in the inner tens of kpc where the emission-line nebula is observed. Direct accretion from the cosmological filament is similarly unlikely, since any accreted gas should be moving at speeds approaching the cluster velocity dispersion. The alignment noted here does not appear to persist in other cool core clusters. Perseus and Virgo, for example, harbour filamentary emission with no preferred orientation (e.g. Young et al., 2002; Salomé et al., 2006). A more likely

possibility is that an infalling galaxy caused an overdensity in the ICM that led to a thermal instability. However, the only galaxy located along the filament is the companion, and it cannot produce both the disrupted central gas and the filament. Thus, the alignment between the major axis of the BCG and filament of molecular gas is most likely coincidental.

Summary: Cooling Origin

While stimulated cooling and the cooling wake are both feasible origins for gas condensation, we favour stimulated cooling throughout the remainder of our discussion. This is mainly because of the connection between the cooling gas and X-ray cavity, which resembles a growing sample of objects that have been observed with ALMA. As a result, stimulated cooling offers a more generally applicable explanation for the presence of molecular gas in cool core clusters.

2.4.3 Molecular Filament: Inflow or Outflow?

We now consider the velocity profile of the molecular filament and investigate whether it is consistent with inflow or outflow. Along the filament the gas velocity becomes increasingly blueshifted farther from the cluster center. At its base the gas is blueshifted to -30 km s^{-1}, while the velocity at the tail is nearly -200 km s^{-1}. This can be consistent with either inflow or outflow, depending on where the gas forms and where it is located along the line of sight. With the present data we are unable to conclusively distinguish between the two.

Molecular gas condensing out of the hot atmosphere should trace the velocity of the gas that it cooled from. In a cooling wake the molecular gas condenses from a hydrostatic atmosphere, resulting in a mean velocity of zero with respect to the cluster. Our adopted frame is measured with respect to the BCG, so an offset is expected if the BCG is indeed oscillating within the cluster. Molecular gas condensing from low entropy gas lifted by an X-ray cavity should initially be flowing away from the cluster center. The observed velocity gradient then depends strongly on both the inclination of the filament as well as its shape. For example, a filament with a constant velocity may have an observed gradient if it becomes progressively more inclined toward the line of sight. We cannot differentiate between these morphologies, so preliminarily assume that the filament is straight.

Eventually the dense molecular clouds are expected to decouple from the hot atmosphere, decelerating and falling back onto the central galaxy in a circulation flow. Recent results from *Hitomi* found that the velocity of the ICM in Perseus is very similar to the cold gas, suggesting that the two phases are held together by magnetic fields for some time

(Hitomi Collaboration et al., 2016). Lim et al. (2008) argued in favour of infall for the filaments nearest the cluster core based on their velocity gradient, while inflowing molecular gas was observed directly in NGC5044 (David et al., 2014) and A2597 (Tremblay et al., 2016) based on the presence of redshifted CO absorption lines. Distinguishing between inflow and outflow does not affect the consistency with the stimulated cooling model, as both are expected to occur at some point in the feedback cycle.

Outflow in the Wake of the Rising Cavity

If the clouds along the filament formed recently and are located in front of the midplane of the BCG, then their increasing velocity with radius implies that the gas is being accelerated away from the BCG nucleus. Localized condensation at the base of the filament followed by direct uplift of the molecular gas is unlikely, since coupling the diffuse X-ray cavity to dense molecular clouds is difficult. This is exacerbated by the high mass of the filament, so the coupling of diffuse to dense gas would need to be remarkably efficient. Instead, the molecular clouds probably condensed in situ from the uplifted, low entropy gas.

The terminal velocity of X-ray cavities is generally $50-60\%$ of the speed of sound, $c_s = \sqrt{\gamma kT/\mu m_{\rm H}}$, where kT is the temperature of the hot gas and we have taken $\gamma = 5/3$ for an ideal gas and $\mu = 0.62$ (e.g. Bîrzan et al., 2004). In a 3.5 keV cluster $c_s \approx 900$ km s^{-1}, so a typical bubble velocity is ~ 500 km s^{-1}. The molecular gas in the filament reaches a line of sight velocity (magnitude) of 200 km s^{-1}, several times lower than the bubble velocity. In order for the two velocities to match, the filament must be inclined at $< 25^\circ$ from the plane of the sky.

Accelerating the molecular gas to a speed comparable to the bubble terminal velocity of ~ 500 km s^{-1} requires that the AGN contribute 2×10^{57} erg to the kinetic energy of the cold gas. Assuming a gravitational acceleration of $g = 2\sigma^2/r$ with $\sigma = 255$ km s^{-1} (McNamara et al., 1990), the potential energy required to lift the gas from 1 kpc to $R \approx 13$ kpc is $\sim 5\times10^{57}$ erg. The total energy requirement is therefore $\sim 7\times10^{57}$ erg, which is only 4% of the enthalpy of the northwestern cavity, 1.6×10^{59} erg (Sanders et al., 2009). Lifting the molecular gas in the wake of the X-ray cavity is therefore energetically feasible.

Clouds in Gravitational Free-fall

When molecular clouds decouple from the hot atmosphere, they should fall ballistically under the influence of gravity. The clouds will initially have the same velocity as the hot gas they cooled from. This is zero in a hydrostatic atmosphere, but can be nonzero if the

clouds have cooled from uplifted gas. Following Lim et al. (2008), we assume that the gravitational potential can be modelled by a Hernquist profile (Hernquist, 1990). A gas cloud undergoing free fall should accelerate to a velocity of

$$v(r)^2 = v(r_0)^2 + 2GM\left(\frac{1}{r+a} - \frac{1}{r_0+a}\right) \tag{2.3}$$

with respect to the hot atmosphere. In the rest frame of the BCG, which has been adopted for these observations, the velocities in the above equation are modified to be $v(r) - v_{\rm ICM}$, where $v_{\rm ICM}$ is the velocity offset between the BCG and the cooling gas. We assume that the initial velocity of the cloud is the same as the ICM, so $v(r_0) = v_{\rm ICM}$. In Eqn 2.3 M is the total gravitating mass of the BCG, a is the scale length, and r_0 is the radius where the cloud originally formed. The inclination angle of the cloud's trajectory and $v_{\rm ICM}$ are both free parameters in this model.

The scale length a is related to the half-light radius R_e according to

$$R_e \approx 1.8153a. \tag{2.4}$$

Taking an effective radius of 19.24 arcsec (13.47 kpc) from the 2MASS K-band catalog, the corresponding scale length is 7.4 kpc. We note that 2MASS photometry is likely missing a significant amount of the total stellar light (Lauer et al., 2007), so this scale length is underestimated. Adopting a larger scale length would result in flatter velocity profiles.

We estimate the total BCG mass using the cluster mass profiles of Main et al. (2015), who modelled the X-ray emission of the ICM with an NFW profile under the assumption of hydrostatic equilibrium. For 2A 0335+096 the total mass interior to 30 kpc is 2.1×10^{12} $M_\odot$. Alternately, 2MASS report a total K-band magnitude of 9.808±0.052 that was extrapolated out to 45 kpc. Assuming a K-band stellar mass-to-light ratio of 0.8 (Bell et al., 2003; Humphrey et al., 2006), the total stellar mass in the BCG of 2A 0335+096 is 4.7×10^{11} $M_\odot$. Combining these values gives a dark matter mass fraction within the BCG of 80%, which is similar to that of Hydra A at a similar radius (Okabe et al., 2016). The total gravitating mass controls the amplitude of the velocity profile, and is degenerate with the inclination angle. Our results are therefore not sensitive to the adopted value of total mass, as the inclination angle, which is not known, can be adjusted to compensate.

From the PV diagrams presented in Fig. 2.11, infall along the extended filament begins at a radius of 11.5 kpc and proceeds over a length of 6 kpc that is oriented 20° from purely radial. The solid black line in Fig. 2.11 shows the velocities resulting from infall along this filament assuming an inclination angle of 25° and a velocity offset of -200 km s^{-1}. The position shown along the x-axis has been transformed into the appropriate radial distance

from the BCG nucleus. The velocity shift corresponds to a bulk offset between the ICM and the stellar component of the BCG. The presence of a cold front seen in the X-ray emission (Mazzotta et al., 2003; Werner et al., 2006; Sanders et al., 2009) indicates non-zero motion between the two components.

Over the 7 kpc length of the filament the gas is primarily located in two clumps. Gravitational free-fall reproduces the observed increase in velocity between these clumps. However, the clumps are not smoothly connected in velocity, and the free-fall model fails to account for this feature. Furthermore, the observed average velocity of the inner portion of the filament does not depend on the radius, while the velocity of the free-fall model increases linearly through this region. Although the free-fall model reproduces the bulk of the observed velocities, differences between the data and the model prevent any definitive conclusions about the gas undergoing free-fall from being drawn. Nevertheless, the velocity gradient is broadly consistent with free-fall. Since this velocity gradient is generic for free-fall in elliptical galaxies, the discovery of additional filaments exhibiting this gradient suggests that some of them, at the very least, are in approximate free-fall.

A number of additional problems with the model adopted here must also be addressed. First, the filament is not oriented radially with respect to the BCG nucleus. This may be caused by a transverse velocity offset between the ICM and the BCG, which would be expected given the presence of a cold front. This model also neglects the gravity of the companion galaxy. Assuming the companion lies in the plane of the sky and has a mass-to-light ratio comparable to the BCG, the inner portion of the filament should experience $3\times$ more gravitational acceleration from the companion galaxy than from the BCG. This could also affect the orientation of the infalling gas. Without a reliable measurement of the line-of-sight separation between the BCG, companion galaxy, and filament, we cannot create a more robust gravitational free-fall model. Finally, the model we have adopted here has a large number of unconstrained parameters, notably the inclination angle and bulk velocity of the ICM. As a result, virtually any linear velocity structure can be reproduced with an appropriate choice of these parameters.

2.4.4 Star Formation

Attributing all of the Hα emission to star formation, the luminosity of 8×10^{41} erg s^{-1} (Donahue et al., 2007) corresponds to a star formation rate of $15 - 20\,\mathrm{M}_\odot\,\mathrm{yr}^{-1}$, using the $L_{\mathrm{H}\alpha} - \mathrm{SFR}$ scaling relations of Kennicutt (1998). This overestimates the true star formation rate, as starlight alone fails to account for the observed spectra of emission-line nebulae (Johnstone et al., 2007). Additional heating sources are required to supplement

the ionization of the nebula. Collisional heating by ionizing particles, such as cosmic rays that penetrate the filament, is favoured in the models of Ferland et al. (2009). Mixing of the gas in the filaments with the hot X-ray emitting plasma was argued to provide the dominant source of heat in Virgo (Werner et al., 2013) and other ellipticals (Werner et al., 2014). The ionization source in 2A 0335+096 is not currently known, although the spatial coincidence between the filaments and 0.5 keV gas suggests that star formation alone does not power the nebula.

An analysis of the $B-I$ colour gradient of the central galaxy shows an excess in blue emission from $4-30$ kpc compared to the central galaxies in clusters without short cooling times (Romanishin & Hintzen, 1988). This extends well beyond the companion galaxy, indicating that active star formation is occurring along the filament. Within 4 kpc the colour gradient reddens to a level consistent with the control sample. Wilman et al. (2011) argued that this reddening cannot be caused by dust extinction, since any attenuation by dust would be negligible in their K-band observation. In the BCG alone, several different measurements place the star formation rate at a few $\mathrm{M_\odot\ yr^{-1}}$. Infrared photometry within a $6''$ aperture, which excludes both the companion galaxy and the filament, derives a SFR of $2.1\,\mathrm{M_\odot\ yr^{-1}}$ (O'Dea et al., 2008). Infrared spectroscopy (Donahue et al., 2011) and UV imaging (Donahue et al., 2007) over regions that include both galaxies but not the filament measure SFRs of 0.7 and $3-7\,\mathrm{M_\odot\ yr^{-1}}$, respectively.

The total molecular gas mass in the BCG is $3.2\times10^8\,\mathrm{M_\odot}$. Using the CO(3-2) line to trace the emitting area yields a molecular gas surface density of $68\,\mathrm{M_\odot\ pc^{-2}}$. Assuming that star formation is distributed over the same area, the maximum SFR to place the 2A 0335+096 BCG within the scatter of the Kennicutt-Schmidt relation (Kennicutt, 1998; Kennicutt & Evans, 2012) is $\sim 0.9\,\mathrm{M_\odot\ yr^{-1}}$. The SFR derived from IR spectroscopy is consistent with this limit. For the $7.8\times10^8\,\mathrm{M_\odot}$ of molecular gas in the filament, the corresponding surface density of molecular gas is $46\,\mathrm{M_\odot\ pc^{-2}}$. Placing this on the Kennicutt-Schmidt relation requires a SFR of roughly $0.09\,\mathrm{M_\odot\ yr^{-1}}$. However, the low confining pressure of the ICM outside of the cluster core reduces the star formation efficiency in systems with similar filaments (e.g. Verdugo et al., 2015; Salomé et al., 2016b,a). We should therefore expect a lower SFR, although the excess blue emission still supports ongoing star formation within the filament.

2.5 Conclusions

In this work we have presented ALMA observations of the CO(1-0) and CO(3-2) lines of the 2A 0335+096 BCG. We detect $1.13\times10^9\,\mathrm{M_\odot}$ of molecular gas that is distributed between

two distinct structures: a component near the center of the BCG and a 7 kpc long filament beginning 6 kpc from the BCG nucleus and extending nearly radially outward. Most of the molecular gas, $7.8 \times 10^8\,M_\odot$, is located in the filament, while $3.2 \times 10^8\,M_\odot$ is located in the nucleus. The nuclear gas is highly asymmetric, with two clumps of comparable mass south of the radio source and several smaller clouds extending toward a nearby companion galaxy. The filament has a shallow velocity gradient that is slightly blueshifted at all points, nearing the systemic velocity of the BCG at its innermost radius. No molecular gas is detected connecting the filament to the BCG nucleus.

Although a companion galaxy is located 5 kpc from the BCG in projection and has a small relative velocity ($\sim 200\,\mathrm{km\,s^{-1}}$), it is unlikely that the molecular gas has been supplied by a merger. Tidal stripping alone could deposit molecular gas onto the BCG, but the filament must then form via completely independent means. A plume of increasingly redshifted clouds extending toward the companion galaxy suggests that the galaxies have already interacted, with the companion galaxy disrupting a pre-existing reservoir of molecular gas within the BCG as it passed through the nucleus at < 20 Myr ago. However, no evidence of stellar disruption is observed in optical imaging, indicating that any tidal interaction must be weak.

Ram pressure stripping is a feasible way to produce the filament, as similar structures have been observed in other systems (e.g. ESO 137-01). However, filamentary emission has also been observed in a number of cool core clusters that do not have nearby companion galaxies. While we cannot definitively rule out ram pressure stripping, it is not representative of cool core clusters in general. Moreover, if the galaxies have already interacted, then ram pressure stripping cannot be a viable mechanism for producing the filament.

The filament of molecular gas is coincident with significant dust extinction, luminous Hα emission, and 0.5 keV X-ray emitting gas. This spatial correlation of gas spanning 5–6 decades in temperature implies that the molecular gas has condensed out of gas cooling from the hot atmosphere. The hot atmosphere offers an abundant source of gas with which to form the molecular gas. Condensation out of the hot atmosphere can form the total molecular gas supply rapidly enough to sustain cycles of AGN feedback every $\sim 10^8$ yr. Condensation can be triggered either in the wake of the BCG or in the uplift behind an X-ray cavity. We favour the uplift interpretation because of its similarity to a growing sample of objects observed with ALMA, which may be representative of cool core clusters in general.

The Hα emission from this cooling filament extends toward an X-ray cavity, with faint emission spreading around its inner edge. This resembles the distribution of molecular gas in a growing number of objects observed with ALMA (e.g. PKS0745-191 and A1835), where

significant amounts of molecular gas reside in massive outflows linked to the buoyantly rising X-ray cavities. Our observations are consistent with the "stimulated feedback" model, where molecular gas condenses out of low entropy gas that is lifted out of thermal equilibrium by X-ray cavities. With an enthalpy of 1.6×10^{59} erg, the X-ray cavity possesses ample energy to lift enough low entropy gas to form the observed molecular gas supply.

As clouds of molecular gas condense out of the uplifted low entropy gas in the hot atmosphere, they should decouple from the hot atmosphere and fall back onto the BCG under the influence of gravity. Initially outflowing gas will eventually decelerate and return to the BCG in an inflow. We are unable to distinguish between inflow and outflow with our observations. The velocity of the molecular gas in the filament increases in magnitude from $-30\,\mathrm{km\,s^{-1}}$ near its base to $-200\,\mathrm{km\,s^{-1}}$ at its tail. This velocity gradient may correspond to gas accelerated by the cavity, but is also consistent with simple models of gravitational infall. This ambiguity, however, does not affect our interpretation that the molecular gas has condensed out of low entropy gas uplifted by an X-ray cavity.

Chapter 3

A ^{13}CO Detection in a Brightest Cluster Galaxy

Abstract

We present ALMA Cycle 4 observations of CO(1-0), CO(3-2), and ^{13}CO(3-2) line emission in the brightest cluster galaxy of RXJ0821+0752. This is one of the first detections of ^{13}CO line emission in a galaxy cluster. Half of the CO(3-2) line emission originates from two clumps of molecular gas that are spatially offset from the galactic center. These clumps are surrounded by diffuse emission that extends 8 kpc in length. The detected ^{13}CO emission is confined entirely to the two bright clumps, with any emission outside of this region lying below our detection threshold. Two distinct velocity components with similar integrated fluxes are detected in the ^{12}CO spectra. The narrower component (60 km s^{-1} FWHM) is consistent in both velocity centroid and linewidth with ^{13}CO(3-2) emission, while the broader ($130 - 160$ km s^{-1}), slightly blueshifted wing has no associated ^{13}CO(3-2) emission. A simple local thermodynamic model indicates that the ^{13}CO emission traces 2.1×10^9 M$_\odot$ of molecular gas. Isolating the ^{12}CO velocity component that accompanies the ^{13}CO emission yields a CO-to-H$_2$ conversion factor of $\alpha_{\rm CO} = 2.3$ M$_\odot$ (K km s^{-1})$^{-1}$, which is a factor of two lower than the Galactic value. Adopting the Galactic CO-to-H$_2$ conversion factor in brightest cluster galaxies may therefore overestimate their molecular gas masses by a factor of two. This is within the object-to-object scatter from extragalactic sources, so calibrations in a larger sample of clusters are necessary in order to confirm a sub-Galactic conversion factor.

3.1 Introduction

The brightest cluster galaxies (BCGs) at the centers of some galaxy clusters are rich in molecular gas (Edge, 2001; Salomé & Combes, 2003). Gas-rich BCGs also host luminous emission-line nebulae (Heckman et al., 1989; Crawford et al., 1999) and star formation rates rivaling those of starburst galaxies (McNamara & Jaffe, 1994; O'Dea et al., 2008; Tremblay et al., 2015). These cooling signatures are observed preferentially when the central cooling time of the hot intracluster gas falls below 1 Gyr (Rafferty et al., 2008), or when the central entropy lies below 30 keV cm^2 (Cavagnolo et al., 2008). The implication is that the molecular gas in BCGs is formed from the cooling of the hot atmosphere.

Uninhibited cooling of the hot atmosphere would produce far more cold gas and star formation than is observed. Instead, the rate of cooling is regulated by active galactic nucleus (AGN) feedback (see McNamara & Nulsen 2007, 2012; Fabian 2012 for reviews). Radio jets launched by the AGN inflate buoyant radio bubbles (X-ray cavities), drive shocks, and generate sound waves, heating the gas throughout the cluster core (e.g. McNamara et al., 2000; Blanton et al., 2001; Fabian et al., 2006). The power output by the AGN is correlated with the cooling rate of the cluster gas in a large sample of groups and clusters (Bîrzan et al., 2004; Dunn & Fabian, 2006; Rafferty et al., 2006), indicating that AGN are capable of preventing the bulk of the hot gas from cooling. Residual cooling from the hot atmosphere can then form the observed molecular gas reservoirs. Accretion of this gas onto the AGN likely fuels AGN feedback, establishing a feedback loop by connecting gas cooling to heating (Pizzolato & Soker, 2005; Gaspari et al., 2013; Li & Bryan, 2014a).

A growing body of evidence indicates that AGN feedback plays a direct role in shaping the distribution of molecular gas. In the Perseus cluster, filamentary Hα emission extends radially from the BCG (Conselice et al., 2001; Hatch et al., 2006), with two prominent filaments oriented towards an X-ray cavity (Fabian et al., 2003). The nebular emission is coincident with soft X-rays, molecular hydrogen (Lim et al., 2012), and CO emission (Salomé et al., 2006, 2011). Recent ALMA observations of BCGs have also revealed molecular filaments that trail X-ray cavities (McNamara et al., 2014; Russell et al., 2016, 2017a; Vantyghem et al., 2016). This gas has either been lifted directly from the cluster core by buoyantly rising radio bubbles, or it has cooled in situ from hot gas that has been uplifted to an altitude where it becomes thermally unstable (Revaz et al., 2008; McNamara et al., 2016). These gas flows comprise a significant fraction of the total molecular gas mass. Redshifted absorption line measurements in other systems imply that molecular clouds are falling toward the central black hole, perhaps indicating that the clouds return to the central galaxy in a circulation flow (David et al., 2014; Tremblay et al., 2016).

The molecular gas in BCGs is observed predominantly using CO[1] as a tracer molecule. Converting the measured intensity of the CO rotational line into a molecular gas mass requires the assumption of a CO-to-H_2 conversion factor. This conversion factor, also referred to as the X-factor, is defined as the ratio between H_2 column density, $N(H_2)$ in cm^{-2}, and integrated intensity of the CO(1-0) line, $W(\mathrm{CO})$ in $\mathrm{K\ km\ s}^{-1}$:

$$N(H_2) = X_{\mathrm{CO}} W(\mathrm{CO}). \tag{3.1}$$

In the Milky Way and nearby spiral galaxies X_{CO} is calibrated to be $2{\times}10^{20}\ \mathrm{cm}^{-2}\ (\ \mathrm{K\ km\ s}^{-1}\ )^{-1}$ (for a review, see Bolatto et al., 2013). However, the Galactic X_{CO} is not universal, and independent calibrations within BCGs are not available. The standard practice has been to adopt the Galactic value with a factor of two uncertainty. This approach is generally justified by the near-solar metallicities at the centers of galaxy clusters. The molecular clouds are also expected to be cold ($\ll 100$ K; Ferland et al., 1994), resembling those in the Galaxy. The linewidths of the individual clouds seen in absorption ($\sim 5\ \mathrm{km\ s}^{-1}$) are similar to giant molecular clouds, further indicating that the cold gas in BCGs resembles Galactic clouds.

Significant deviations from the Galactic X_{CO} are observed in ultra-luminous infrared galaxies (ULIRGs) and jet-driven outflows. The physical conditions of the molecular gas in ULIRGs, which exhibit extreme star formation, differ greatly from those in the disks of normal galaxies. The gas is located in an extended warm phase with volume and column densities that are much higher than in normal disks (e.g. Jackson et al., 1995; Ward et al., 2003). This leads to overluminous CO emission, reducing the standard CO-to-H_2 conversion factor to $X_{\mathrm{CO}} = 0.4 \times 10^{20}\ \mathrm{cm}^{-2}\ (\ \mathrm{K\ km\ s}^{-1}\ )^{-1}$ (Downes & Solomon, 1998).

Massive outflows of molecular gas can be driven by intense radiation or radio jets (Morganti et al., 2005; Nesvadba et al., 2006; Feruglio et al., 2010; Rupke & Veilleux, 2011; Sturm et al., 2011; Alatalo et al., 2011; Dasyra & Combes, 2011; Cicone et al., 2014; Tadhunter et al., 2014; Morganti et al., 2015). The high CO (4-3)/(2-1) ratio in IC 5063 implies that the molecular gas along the jet-driven outflow is optically thin (Dasyra et al., 2016). As a result, the CO-to-H_2 conversion factor may be reduced in these systems by an order of magnitude. Simulations of molecules forming along fast outflows powered by quasar-driven winds indicate that the conversion factor should be 25 times lower than Galactic (Richings & Faucher-Giguere, 2017).

In this work we present an ALMA cycle 4 observation of the CO(1-0), CO(3-2), and ^{13}CO(3-2) emission lines in the BCG of the RXJ0821+0752 galaxy cluster. This represents

[1]When referring to individual transitions, we refer to the most common $^{12}C^{16}O$ isotopologue as simply CO.

one of the first detections of ^{13}CO within a BCG. Previous observations of NGC 1275 in the Perseus cluster detected both the ^{13}CO(2-1) and ^{13}CO(3-2) lines (Bridges & Irwin, 1998), while observations of A1835 and A1068 provided only upper limits (Edge, 2001). Due to the lower abundance of ^{13}CO relative to ^{12}CO, the ^{13}CO emission is generally optically thin. As a result, the ^{13}CO emission traces the full volume of its emitting region, allowing a direct measure of its column density. We use this to estimate the total H_2 column density, and by extension the molecular gas mass. This provides an estimate of the CO-to-H_2 conversion factor that can be compared to the Galactic value in order to evaluate previous mass estimates of BCGs.

RXJ0821+0752 is a cool core galaxy cluster with a brightest cluster galaxy that contains one of the largest cold gas reservoirs known (Edge, 2001). Its luminous CO emission corresponds to a molecular gas mass of $10^{10}\,M_\odot$, assuming the standard Galactic CO-to-H_2 conversion factor. Despite the large CO luminosity, no significant 1-0 S series of H_2 has been detected. Observations of the CO(1-0) and CO(2-1) lines showed that the molecular gas traces the Hα emission, but is not centered on the galaxy (Salomé & Combes, 2004). The IR luminosity of 8.47×10^{44} erg s^{-1} corresponds to a star formation rate of $37\,M_\odot$ yr^{-1} (Quillen et al., 2008; O'Dea et al., 2008). The BCG also hosts significant quantities of dust, with a dust mass of $2.2 \times 10^7\,M_\odot$ assuming a dust temperature of 40 K (Edge, 2001). Unlike other BCGs, the optical emission-line ratios resemble those of HII regions instead of AGN-dominated regions (Crawford et al., 1999).

Throughout this paper we assume a standard Λ-CDM cosmology with $H_0 = 70$ km s^{-1} Mpc^{-1}, $\Omega_{m,0} = 0.3$, and $\Omega_{\Lambda,0} = 0.7$. At the redshift of RXJ0821+0752 ($z = 0.109$; Crawford et al., 1995), the angular scale is $1'' = 2.0$ kpc and the luminosity distance is 510 Mpc.

3.2 Observations and Data Reduction

The brightest cluster galaxy of the RXJ0821+0752 galaxy cluster (RA: 08:21:02.258, Dec: +07:51:47.28) was observed by ALMA Band 3 on 2016 Oct 30 and Nov 4 and Band 7 on 2016 Oct 1 (Cycle 4, ID 2016.1.01269.S, PI McNamara). These observations covered the redshifted CO(1-0) and CO(3-2) lines at 103.848 GHz and 311.528 GHz, respectively. An additional baseband in the Band 7 observation also covered the ^{13}CO(3-2) line at 297.827 GHz. The remaining three Band 3 basebands (91.857, 93.732, and 105.733 GHz) and two Band 7 basebands (299.554 and 309.680 GHz) were used to measure the sub-mm continuum emission. The observations used a single pointing centered on the BCG nucleus with a primary beam of 60 arcsec at CO(1-0) and 20 arcsec at CO(3-2). The total on-source integration time was 86.7 minutes at CO(1-0) and 22.7 minutes at CO(3-2), each split into

$\sim$ 6 minute long observations and interspersed with observations of the phase calibrator. The observations used 40 antennas with baselines ranging from $18-1124$ m for Band 3 and $15-3247$ m for Band 7. The frequency division correlator mode was used for the CO(1-0) and CO(3-2) spectral line observations, providing a 1.875 GHz bandwidth with 488 kHz frequency resolution. This corresponds to a velocity resolution of 1.4 km s^{-1} at CO(1-0) and 0.47 km s^{-1} at CO(3-2), although the data were binned to a coarser velocity channels for subsequent analysis. The remaining basebands were configured with the time division correlator mode with a bandwidth of 2 GHz and frequency resolution of 15.625 MHz. For the ^{13}CO(3-2) line, this corresponds to a velocity resolution of 15.7 km s^{-1} .

The observations were calibrated in CASA version 4.7.0 (McMullin et al., 2007) using the pipeline reduction scripts. Continuum-subtracted data cubes were created using UVCONTSUB and CLEAN. Additional phase self-calibration could not be performed because of the very faint nuclear continuum source. The calibration of the water vapour radiometers failed for the CO(3-2) observation, so some streaks associated with the phase calibration remain in the image. Images of the line emission were reconstructed using Briggs weighting with a robust parameter of 2. An additional *uv* tapering was used to smooth the CO(3-2) and ^{13}CO(3-2) images on scales below 0.1 arcsec. The final CO(1-0) data cube had a synthesized beam of $0.61'' \times 0.59''$ (P.A. $-70.4°$), and the CO(3-2) data cube was smoothed to match the ^{13}CO(3-2) synthesized beam of $0.21'' \times 0.165''$ (P.A. 37.2°). The CO(1-0), CO(3-2), and ^{13}CO(3-2) images were binned to 3, 5, and 16 km s^{-1} velocity channels, respectively. All images were centered around the line emission, which corresponds to a redshift of $z = 0.109$. The RMS noise in the line-free channels were 0.5, 1.1, and 0.3 mJy beam^{-1}, respectively. Images of the continuum were created by combining line-free spectral channels from each baseband. No continuum emission was detected from the nucleus of the BCG. Instead, the continuum emission is coincident with the molecular gas, which is consistent with the structure at 1.4 and 5 GHz (Bayer-Kim et al., 2002).

3.3 Results

3.3.1 Spectra

The full extent of the molecular gas is well-resolved for all observed spectral lines. A spatially integrated spectrum was extracted for each spectral line from a $6.8'' \times 5''$ (13.6×10 kpc) box encompassing all of the significant line emission. The CO(3-2) and ^{13}CO(3-2) images were smoothed to match the resolution of the CO(1-0) image prior to the spectral extraction. Since the extraction region is much larger than either beam size, the smoothing

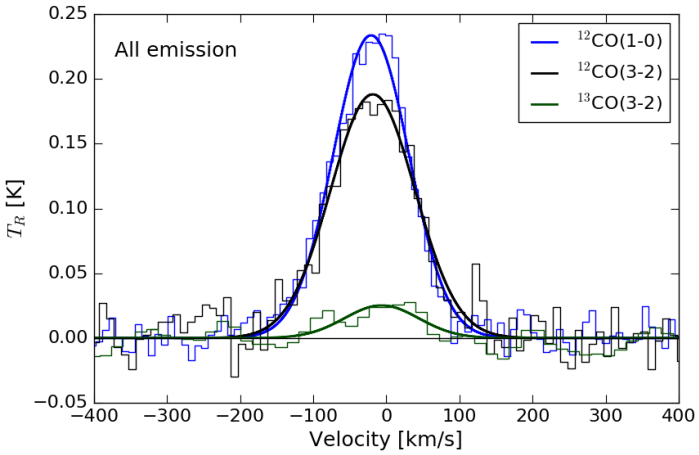

Figure 3.1: CO(1-0), CO(3-2), and ^{13}CO(3-2) spectra extracted from a $6.8'' \times 5''$ (13.6×10 kpc) box encompassing all of the line emission. The CO(1-0) and CO(3-2) spectra have been smoothed to 9 km s^{-1} and 10 km s^{-1}, respectively. The spatial resolution of the CO(3-2) and ^{13}CO(3-2) images were degraded to match the CO(1-0) resolution prior to the spectral extraction.

has little impact on the spectrum. The spectra, shown in Fig. 3.1, are expressed as a brightness temperature:

$$T_R = \frac{\lambda^2}{2k\Omega} S. \tag{3.2}$$

Here λ is the wavelength of the spectral line, k is the Boltzmann constant, and S is the measured flux density. For spatially resolved spectra, Ω is the solid angle of the spectral extraction region, provided it is much larger than the beam.

The spectra are all best fit by a single Gaussian velocity component. The ^{13}CO(3-2) spectrum contains a second peak at -80 km s^{-1}, but the significance of the second component is below 3σ, so has not been included in these fits. The results of the spectral fitting, including the integrated fluxes ($S_{\rm CO}\Delta v$), integrated intensities ($W \equiv \int T_R {\rm d}v$), and peak temperatures ($T_{\rm peak}$), are listed in Table 3.1. The peak temperature is related to the integrated intensity and the line full-width at half-maximum (FWHM) through $T_p = 0.94 W_{\rm CO}/{\rm FWHM}$. The line luminosity, $L'_{\rm CO}$, is also included in Table 3.1. It is defined as (Solomon & Vanden Bout, 2005)

$$L'_{\rm CO} = 3.25 \times 10^7 S_{\rm CO}\Delta v D_L^2 (1+z)^{-3} \nu_{\rm obs}^{-2} \text{ K km s}^{-1} \text{ pc}^2 , \tag{3.3}$$

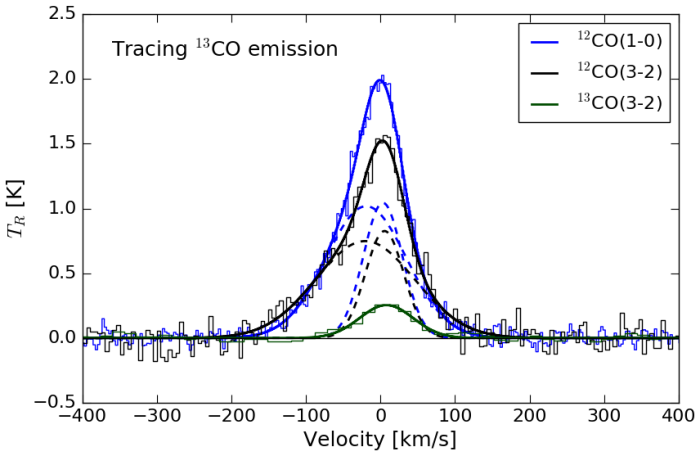

Figure 3.2: CO(1-0), CO(3-2) and ^{13}CO(3-2) spectra extracted from a region encompassing the two ^{13}CO peaks seen in Fig. 3.3. The ^{12}CO spectra were modelled with two Gaussian velocity components, while the ^{13}CO spectrum was modelled with a single velocity component. The individual components for the ^{12}CO spectra are indicated by dashed lines.

where $S_{\rm CO}\Delta v$ is the flux density in Jy km s^{-1}, D_L is the luminosity distance in Mpc, and $\nu_{\rm obs}$ is the observed frequency in GHz.

The total integrated CO(1-0) flux, 8.06 ± 0.08 Jy km s^{-1}, is consistent within 2σ of the IRAM-30m single dish measurement of 9.9 ± 1.0 Jy km s^{-1} (Edge, 2001; Edge & Frayer, 2003). Adopting the Galactic CO-to-H_2 conversion factor yields a molecular gas mass of 2×10^{10} M$_\odot$.

In Table 3.1 we also include the fitted parameters for spectra extracted from a region tracing the ^{13}CO(3-2) emission, which is distributed over smaller spatial scales than the ^{12}CO emission (see Fig. 3.3). This ensures that molecular clouds detected only in ^{12}CO are not biasing the comparisons between ^{12}CO and ^{13}CO. The spectra are shown in Fig. 3.2. Note that the lower resolution of the CO(1-0) image results in some emission lying outside of the extraction region. The resolution of the CO(3-2) images have not been degraded to match the CO(1-0) resolution for these spectra.

The velocity structure of the CO(1-0) and CO(3-2) lines are very similar. Both spectra have a narrow (60 km s^{-1} FWHM) component at approximately 0 km s^{-1} in the adopted frame, as well as a broader (130 − 160 km s^{-1}) component that is blueshifted by about 20 km s^{-1}. The linewidths of the narrow components are consistent, while the

Table 3.1: Spectral Fitting

Line	Velocity Center km s^{-1}	FWHM km s^{-1}	$S_{\rm CO}\Delta v$ Jy km s^{-1}	W(CO) K km s^{-1}	$T_{\rm peak}$ K	$L'_{\rm CO}/10^9$ K km s^{-1} pc^2
All emission						
CO(1-0)	-20.7 ± 0.6	122.1 ± 1.4	8.06 ± 0.08	30.5 ± 0.3	0.235 ± 0.004	4.61 ± 0.05
CO(3-2)	-18.3 ± 1.5	136.1 ± 3.6	65.6 ± 1.5	27.3 ± 0.6	0.189 ± 0.006	4.17 ± 0.10
^{13}CO(3-2)	-6.4 ± 8.2	119 ± 19	7.0 ± 1.0	3.2 ± 0.4	0.025 ± 0.005	0.49 ± 0.07
Region tracing ^{13}CO emission						
CO(1-0)	3.2 ± 0.6	61.7 ± 2.0	1.5 ± 0.1	68.5 ± 5.4	1.04 ± 0.09	0.86 ± 0.06
	-19.2 ± 1.3	127.2 ± 2.2	3.0 ± 0.1	137.7 ± 5.4	1.02 ± 0.04	1.72 ± 0.06
CO(3-2)	5.5 ± 1.6	60.4 ± 5.3	10.4 ± 1.7	53.1 ± 8.8	0.83 ± 0.15	0.66 ± 0.11
	-20.5 ± 3.8	155.8 ± 7.7	24.3 ± 1.8	124.1 ± 9.1	0.75 ± 0.07	1.5 ± 0.1
^{13}CO(3-2)	7.9 ± 1.8	84.5 ± 4.3	4.09 ± 0.18	22.8 ± 1.0	0.25 ± 0.02	0.285 ± 0.013
Primary clump						
CO(3-2)	24.8 ± 1.6	59.0 ± 5.0	4.9 ± 0.7	65.0 ± 9.6	1.04 ± 0.18	0.31 ± 0.04
	-13.6 ± 4.1	152.0 ± 5.7	12.5 ± 0.8	165 ± 11	1.02 ± 0.08	0.80 ± 0.05
^{13}CO(3-2)	24.3 ± 2.1	86.9 ± 5.0	1.96 ± 0.10	28.4 ± 1.4	0.31 ± 0.02	0.136 ± 0.007
Secondary clump						
CO(3-2)	-4.7 ± 1.1	52.8 ± 3.5	6.4 ± 0.7	73.1 ± 8.2	1.3 ± 0.2	0.41 ± 0.04
	-42.3 ± 6.7	142.5 ± 9.3	7.7 ± 0.8	87.9 ± 9.3	0.58 ± 0.07	0.49 ± 0.05
^{13}CO(3-2)	-1.8 ± 1.4	62.6 ± 3.3	1.78 ± 0.08	22.1 ± 1.0	0.33 ± 0.02	0.124 ± 0.006

Notes: All linewidths have been corrected for instrumental broadening.

linewidth of the broader component is larger at CO(3-2) (155.8 ± 7.7 km s^{-1}) than CO(1-0) (127.2 ± 2.2 km s^{-1}). The single peak seen in the ^{13}CO spectrum, which is centered at 8 ± 2 km s^{-1} with a linewidth of 84.5 ± 4.3 km s^{-1}, matches well with the narrow ^{12}CO velocity component. No ^{13}CO(3-2) emission corresponding to the broader ^{12}CO line emission has been detected. We refer to these two velocity components seen in the ^{12}CO spectra – one with associated ^{13}CO emission and one without – as ^{13}CO-bright and ^{13}CO-faint.

3.3.2 Gas Distribution

Maps of integrated flux were created by fitting a one or two Gaussian components to the spectrum of each pixel after averaging over the size of the beam. The significance of the line was tested using a Monte Carlo simulation with 1000 iterations, with a detection requiring a significance of 3σ. The integrated flux maps for the CO(1-0), CO(3-2), and ^{13}CO(3-2) transitions are shown in Fig. 3.3. Contours of the CO(3-2) emission are overlaid on an *HST* WFPC2 F606W image in Fig. 3.4.

The molecular gas is distributed along an ~ 8 kpc long filament, with additional diffuse emission detected in the CO(1-0) map extending toward the northwest. Two clumps of molecular gas are seen in each map, and account for most of the emission. The primary clump, which accounts for 60% of the total CO(1-0) flux, is located at the eastern end of the filament and is 3 kpc north of the BCG nucleus. The secondary clump is 3 kpc west of the primary clump. ^{13}CO emission is only significantly detected near the brightest regions of the primary and secondary clumps. The molecular gas is closely associated with Hα emission (Bayer-Kim et al., 2002; Hamer et al., 2016).

We detect no significant emission centered on the nucleus of the BCG. This spatial offset will be discussed in a forthcoming paper alongside a recent *Chandra* observation. The 3σ upper limits on integrated flux were computed following McNamara & Jaffe (1994), but using flux instead of intensity:

$$S_{\rm CO}\Delta v = \frac{3\sigma_{\rm ch}\Delta V}{\sqrt{\Delta V/\Delta V_{\rm ch}}}\ {\rm Jy\ km\ s^{-1}}\,. \tag{3.4}$$

Here $\sigma_{\rm ch}$ is the RMS deviation in unsmoothed velocity channels in units of Jy, ΔV is the expected full-width at half-maximum of the line, which we assume to be 300 km s^{-1}, and $\Delta V_{\rm ch}$ is the velocity width of each channel. Extracting the CO(1-0) spectrum from a 2 kpc $\times$ 2 kpc box centered on the optical centroid, we obtain a 3σ upper limit of 0.05 Jy km s^{-1}. This translates to a nuclear molecular gas mass $< 1.2 \times 10^8$ M$_\odot$ assuming the Galactic CO-to-H$_2$ conversion factor.

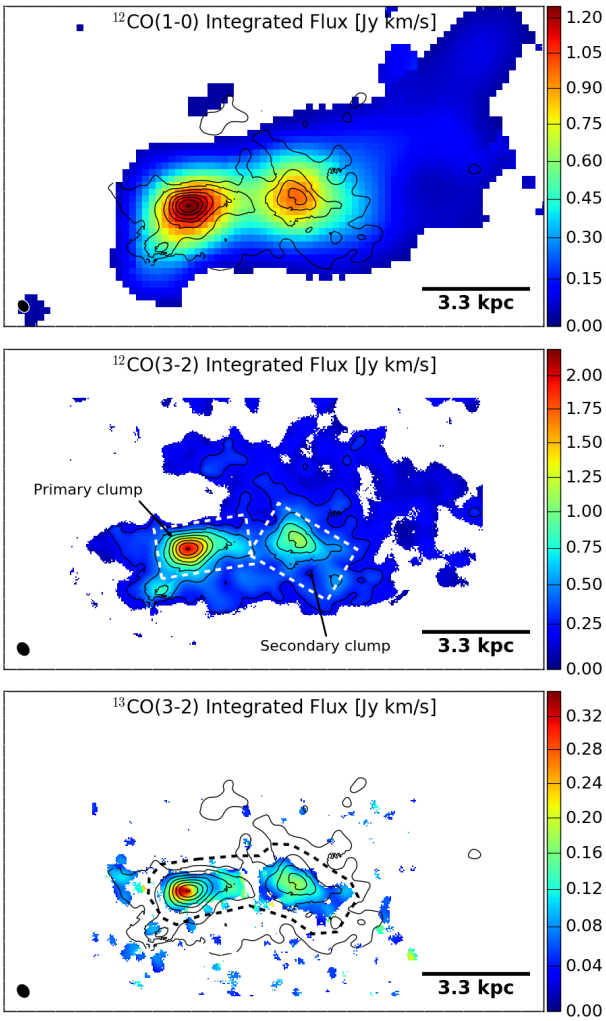

Figure 3.3: Integrated fluxes of the CO(1-0), CO(3-2), and ^{13}CO(3-2) transitions, in units of Jy km s^{-1}. Contours of CO(3-2) emission, ranging from 0.2 to 1.96 Jy km s^{-1} in steps of 0.25 Jy km s^{-1}, have been overlaid on each map. The dashed lines in the center panel indicate the primary (left) and secondary (right) clumps. The dashed line in the bottom panel indicates the region tracing the ^{13}CO emission used to extract the spectra for Table 3.1. The synthesized beam for each image is shown as the black ellipse in the lower left. Each image shares the same 16.5 × 9.8 kpc field-of-view.

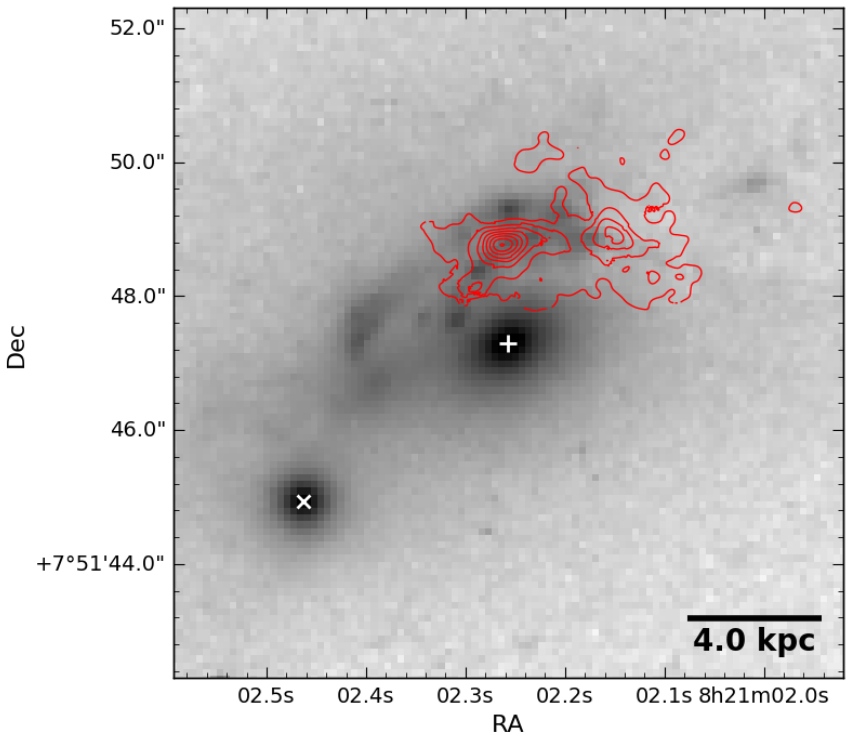

Figure 3.4: HST WFPC2 F606W imaging of the RXJ0821+0752 BCG overlaid with contours of the CO(3-2) emission obtained from ALMA. The + indicates the BCG nucleus, and the × indicates the centroid of a nearby galaxy that may be interacting with the BCG.

The optical imaging shows an arc of excess emission surrounding the northeastern portion of the BCG. The F606W filter covers the wavelength range $4309 - 6457$Åin the rest frame of the BCG, so does not include Hα or [NII] emission. The excess emission may originate from bluer emission lines, such as Hβ, or from stellar continuum tracing localized star formation or a tidal event involving a pre-existing stellar population. The arc is oriented toward a galaxy 7.7 kpc to the southeast of the BCG (SDSS J082102.46+075144.9), suggesting a possible interaction.

Bayer-Kim et al. (2002) obtained optical spectra of the BCG along two slits using the Intermediate dispersion Spectroscopic and Imaging System (ISIS) on the William Herschel Telescope (WHT). These slits encompassed two bright blobs along the arc located 1.6 and 4.3 kpc east-northeast of the BCG nucleus. The blobs show elevated blue continuua compared to the surrounding stellar light. The innermost blob, which lies along the inner arc, is best-fitted by an older starburst with mainly A and F stars, while the blob along the outer arc shows a marginal O star component with significant amounts of all other stellar types. These spectra therefore show that the arc of excess emission is associated with recent star formation.

The primary clump of molecular gas and its diffuse extension to the southeast are coincident with small blobs located along the innermost arc. However, the outer arc, which contains the brightest of the optical blobs and extends toward the nearby galaxy, has little to no associated molecular gas. Additionally, the secondary clump extends toward a region with no enhanced optical emission.

3.3.3 Line Ratios

Important information about the physical state of the molecular gas is encoded in the ratio of brightness temperatures for each of the spectral lines. The CO (3-2)/(1-0) brightness ratio is a function of the gas excitation temperature, $T_{\rm ex}$, and optical depth (see Eqn 3.6). The ^{12}CO/^{13}CO (3-2) brightness ratio additionally depends on the relative isotopologue abundances. Throughout this work we adopt the following notation to refer to these line ratios:

$$\begin{aligned} r_{31} &\equiv T_{32}(^{12}\mathrm{CO})/T_{10}(^{12}\mathrm{CO}) \\ R_{10} &\equiv T_{10}(^{12}\mathrm{CO})/T_{10}(^{13}\mathrm{CO}) \\ R_{32} &\equiv T_{32}(^{12}\mathrm{CO})/T_{32}(^{13}\mathrm{CO}). \end{aligned} \tag{3.5}$$

In Table 3.2 we list a number of published measurements of these ratios for comparison. Note that in some cases the published line ratios may be determined from integrated

intensities (in units of K km s^{-1}) instead of brightness temperature. For two lines with the same linewidth, these are equivalent. We have opted to use brightness temperature over integrated intensity because brightness temperature is the quantity related directly to $T_{\rm ex}$ and optical depth, and the linewidth of the ^{13}CO-faint component differs between CO(1-0) and CO(3-2).

CO (3-2)/(1-0)

From the peak temperatures listed in Table 3.1, the ratio of CO (3-2)/(1-0) brightness temperatures from the spatially integrated spectra is 0.80 ± 0.03. Using the total integrated intensity instead gives a line ratio of 0.895 ± 0.022. The CO (3-2)/(1-0) intensity ratios in other BCGs that have been observed by ALMA are $0.8 - 0.9$ (McNamara et al., 2014; Russell et al., 2014, 2016; Vantyghem et al., 2016). These are consistent with the ratio observed in RXJ0821, indicating that the excitation of the molecular gas is similar.

For the remaining discussion we restrict the line ratio measurements to the region tracing the ^{13}CO emission. This is to more accurately reflect the excitation conditions of the ^{13}CO-emitting gas, which is used to measure the molecular gas mass in Section 3.4. The CO(1-0) and CO(3-2) spectral fits for this region, shown in Table 3.1, were measured at different resolutions. In order to compare these emission lines the CO(3-2) image was first smoothed to the resolution of the CO(1-0) image and the spectrum was re-extracted. The resulting r_{31} line ratio is 0.71 ± 0.15 for the ^{13}CO-bright velocity component and 0.65 ± 0.06 for the ^{13}CO-faint component. The consistency between these two line ratios implies that the two components share similar gas excitation conditions.

Individual molecular clouds in the Milky Way have mean densities of 300 cm^{-3} and temperatures of 10 K, corresponding to a line ratio of $r_{31} = 0.1 - 0.3$ (Scoville & Sanders, 1987). The higher line ratio in RXJ0821 is indicative of enhanced molecular excitation, originating from molecular clouds with higher densities and/or temperatures. In external galaxies the intensity ratio is also higher than in individual molecular clouds. Mao et al. (2010) measured r_{31} in a sample of 125 nearby galaxies, subdividing the sample based on galaxy type. Their mean intensity ratios range from 0.61 ± 0.16 in normal galaxies to 0.96 ± 0.14 in (U)LIRGs. The r_{31} in RXJ0821, which is derived from peak temperatures instead of integrated intensities, is consistent with the Seyfert and AGN-host galaxy populations. It is also consistent with the r_{31} measured in HII regions (e.g. Wilson et al., 1999). The object-to-object scatter in r_{31} is large, so it cannot be used to unambiguously infer excitation conditions based on galaxies with similar line ratios.

Assuming that the gas is thermalized and the emission is optically thick, the CO (3-

2)/(1-0) line ratio can be used to estimate the gas temperature. The Rayleigh-Jeans brightness temperature, T_R, for the $J \rightarrow J-1$ transition is given by:

$$T_R = T_J \Phi_A [f(T_{\rm ex}) - f(T_{\rm bg})](1 - {\rm e}^{-\tau_J}), \tag{3.6}$$

where $T_{\rm ex}$ is the excitation temperature of the transition, Φ_A is the area filling factor, $T_{\rm bg} = 2.73(1+z)$ K is the background temperature, $T_J = h\nu_J/k = T_1 J$ with $T_1 = 5.3$ K for ^{13}CO and 5.5 K for ^{12}CO, and $f(T) \equiv (\exp(T_J/T) - 1)^{-1}$. If the gas is in local thermodynamic equilibrium (LTE), then each transition will share a common excitation temperature that is equal to the gas kinetic temperature. Provided that the ^{12}CO emission is optically thick, $1-\exp(-\tau_{\rm J}) \approx 1$ and the brightness temperature is independent of optical depth. We also assume that the CO(1-0) and CO(3-2) emission originate from the same regions in the molecular clouds, so the area filling factors are the same.

The ratio of CO (3-2)/(1-0) brightness temperatures for the ^{13}CO-bright component, 0.71 ± 0.14, implies an excitation temperature of $T_{\rm ex} \approx 15$ K. Substituting this $T_{\rm ex}$ into Eqn. 3.6 for the CO(3-2) line with its original resolution gives an area filling factor of $\Phi_A \approx 0.1$. The excitation temperature is a steep function of the line ratio, particularly when r_{31} approaches unity. The $\pm 1\sigma$ limits on r_{31}, 0.85 and 0.57, give excitation temperatures of 29 K and 9.3 K, respectively.

An excitation temperature of 15 K is comparable to the low values observed in Galactic clouds. However, it is important to note that $T_{\rm ex}$ determined under the assumption of LTE is a lower limit to the actual kinetic temperature of the gas. The two temperatures are equal only when the gas densities exceed the critical density for each transition, which are $\sim 10^3$ cm^{-3} for CO(1-0) and 3×10^4 cm^{-3} for CO(3-2). At lower densities the collision rate is too low to thermalize the gas. Reproducing the same line ratio with subthermal gas requires higher temperatures.

^{12}CO/^{13}CO (3-2)

Studies of the ^{12}CO/^{13}CO intensity ratio are primarily conducted using the $J = 1 - 0$ transition (e.g. Solomon et al., 1979; Aalto et al., 1995). Individual giant molecular clouds have intensity ratios of $R_{10} = 3 - 5$ (Solomon et al., 1979). In external galaxies, the disks of spiral galaxies exhibit the lowest intensity ratios, with $R_{10} \approx 6 - 8$. Intermediate ratios ($R_{10} \approx 10 - 15$) are observed in starburst galaxies, while extreme ratios ($R_{10} > 20$) are seen in merging systems (Aalto et al., 1995).

If the ^{12}CO and ^{13}CO emission lines are both thermalized and originate from the same physical region in the molecular gas, then R_{32} should be comparable to R_{10}. Israel (2009)

Table 3.2: Line Ratios in Other Galaxies

Object	R_{10}	R_{32}	r_{31}	References
RXJ0821.0+0752				This work
All emission	–	7.6 ± 1.5	0.80 ± 0.03	
All emission†	–	8.5 ± 1.1	0.895 ± 0.022	
Tracing ^{13}CO^{a}	–	3.32 ± 0.66	$^{*}0.71 \pm 0.15$	
Tracing ^{13}CO^{b}	–	> 14	$^{*}0.65 \pm 0.06$	
HII regions				
M17	–	3.7 ± 0.9	0.76 ± 0.19	1
Starburst galaxies				
M82	–	12.6 ± 1.5	0.8 ± 0.2	2, 3
NGC 253	11.5 ± 1.9	11.1 ± 2.2	1.08 ± 0.18	4
NGC 278	8.4 ± 1.3	11.4 ± 1.7	0.88	5
NGC 660	15.7 ± 2.0	12.8 ± 1.9	0.58	5
NGC 3628	12.2 ± 1.8	7.9 ± 1.8	0.44	5
NGC 4666	8.5 ± 1.3	11.3 ± 1.7	0.49	5
NGC 6946	–	~ 7	1.3	6
(U)LIRGs and SMGs				
Arp 220	43 ± 10	8 ± 2	1.0 ± 0.1	7
NGC 6240	45 ± 15	> 32	≈ 1	7
SMM J2135	> 31	20 ± 2	0.68 ± 0.03	8

Notes: †Determined using integrated intensity instead of peak temperature. *Measured from the CO(3-2) image that has been smoothed to match the resolution of the CO(1-0) image. ^{a}The ^{13}CO-bright velocity component. ^{b}The ^{13}CO-faint velocity component. References: 1: Wilson et al. (1999), 2: Petitpas & Wilson (2000), 3: Weiß et al. (2005), 4: Harrison et al. (1999), 5: Israel (2009), 6: Wall et al. (1993), 7: Greve et al. (2009), 8: Danielson et al. (2013).

measured R_{10}, R_{21}, and R_{32} in a sample of five starburst galaxies, and found that R_{32} and R_{10} are consistent to within 50% (see Table 3.2). The measured R_{32} in starbursts range from roughly $8-13$. Several merging systems also exhibit R_{32} ratios that are comparable to R_{10} (e.g. Greve et al., 2009; Danielson et al., 2013). A notable exception is Arp 220, where $R_{10} = 43 \pm 10$ but $R_{32} = 8 \pm 2$ (Greve et al., 2009). This difference is attributed to a multi-component molecular gas distribution. The ^{13}CO is primarily located in dense clumps while the bulk of the ^{12}CO emission originates from an envelope of lower density gas with moderate optical depth ($\tau \approx 1$) (Aalto et al., 1995).

Considering only the total integrated intensities derived from the spatially-integrated spectra, the ^{12}CO/^{13}CO (3-2) line ratio is 8.5 ± 1.1. This global ratio is comparable to the lowest values observed in starburst galaxies. It is also consistent with the R_{32} seen in Arp 220. However, the molecular gas in gas-rich mergers, such as Arp 220, is generally channeled into warm, dense regions at the center of the galaxy, which is not the case in RXJ0821. Thus the global ^{12}CO/^{13}CO (3-2) intensity ratio in RXJ0821 is most closely matched to the conditions of starburst galaxies.

As noted in Section 3.3.1, the ^{13}CO emission is only associated with one of the two observed velocity components. Furthermore, the ^{13}CO emission is confined to a much smaller spatial region than the ^{12}CO emission. In the ^{13}CO-bright velocity component extracted from the region tracing the ^{13}CO emission, the ^{12}CO/^{13}CO (3-2) brightness temperature ratio is 3.32 ± 0.66. This R_{32} is similar to those seen in HII regions (e.g. Wilson et al., 1999), as well as the R_{10} in individual GMCs.

The other velocity component detected in ^{12}CO shows no significant ^{13}CO emission. With an RMS noise of 0.018 K in the ^{13}CO(3-2) spectrum from Fig. 3.2, the 3σ upper limit on peak ^{13}CO(3-2) brightness temperature corresponds to a ^{12}CO/^{13}CO (3-2) line ratio of > 14. The high R_{32} in the ^{13}CO-faint component implies either a higher ^{12}CO/^{13}CO abundance ratio, a reduced optical depth, or extreme conditions from a gas-rich merger.

The isotopologue ratio is controlled by several proceses: (i) ^{12}C is produced primarily in massive stars, while ^{13}C is a secondary product from a later stage of stellar processing. Young stellar ages would therefore enrich the interstellar medium with more ^{12}C than ^{13}C, leading to an increased [^{12}CO]/[^{13}CO] ratio. A top-heavy initial mass function would similarly favour ^{12}C production over ^{13}C. (ii) The lower optical depth of ^{13}CO is less effective at self-shielding from incident UV radiation. This can lead to selective photodissociation, where ^{13}CO is photodissociated throughout a larger fraction of the cloud's volume than ^{12}CO (Bally & Langer, 1982). (iii) In cold environments, ionized carbon atoms are exchanged with the CO isotopologues through chemical fractionation (Watson et al., 1976):

$$^{13}C^{+} + ^{12}CO \leftrightharpoons ^{13}CO + ^{12}C^{+} + \Delta E, \tag{3.7}$$

where $\Delta E = 35$ K. For clouds below about 30 K the forward reaction is favoured and ^{12}CO is converted into ^{13}CO. In hotter environments the reaction reaches an equilibrium. In starburst galaxies the elevated line ratios are attributed to the age of the stellar population. C^{18}O, which is produced alongside ^{12}CO in young stars, is present at normal levels, and only the ^{13}CO is depleted (e.g. Casoli et al., 1992). Early-type galaxies, on the other hand, show boosted ^{13}CO/^{12}CO ratios due to their older stellar populations, which have had time to produce ^{13}C in low-mass stars (Alatalo et al., 2015).

A reduction in optical depth, assuming a constant isotopologue abundance ratio, leads to an increase in R_{32}. Since $\tau \propto N_{\rm CO}/\Delta v$, the ^{12}CO optical depth is related to the ^{13}CO optical depth simply through the ^{12}CO/^{13}CO abundance ratio. Evaluating the optical depth from the ratio of ^{12}CO to ^{13}CO brightness temperatures (Eqn. 3.6), an $R_{32} > 14$ implies an ^{12}CO optical depth < 3.5, assuming $T_{\rm ex} = 15$ K. Optically thin ^{12}CO emission ($\tau < 1$) would require $R_{32} > 31$.

In gas-rich mergers the ^{12}CO/^{13}CO intensity ratio is elevated by turbulent motions introduced by the merger (e.g. Aalto et al., 1995). The turbulent motions increase the linewidth, decreasing optical depth and leading to an increase in the line ratio. Dissipation of this turbulence also heats the molecular gas. The combination of increased linewidth, higher temperatures, and selective photodissociation caused by the decreased ^{13}CO optical depth leads to elevated R_{32} in merging systems. In RXJ0821 this is unlikely to be the case, as the narrow linewidths (< 150 km s^{-1}) are not indicative of turbulence introduced by a merger.

Spatial Variation in Line Ratios

To investigate the spatial variation of the molecular line ratios, we first extract spectra from the two main gas features: the primary and secondary clumps. Both CO(3-2) spectra exhibit the same velocity structure as the composite region tracing the ^{13}CO emission – a narrow peak is located at the systemic velocity and a broader component is blueshifted by about 30 km s^{-1} from the narrower peak. The CO(1-0) spectra were not extracted from these regions because the lower resolution moves a significant fraction of the flux outside of the region.

The R_{32} ratio for the ^{13}CO-bright components of the primary and secondary clumps are 3.4 ± 0.6 and 3.9 ± 0.7, respectively. The main difference between these clumps is the significance of the broad, blueshifted wing. In the primary clump the wing accounts for 70% of the total integrated flux, while in the secondary clump it accounts for only 55%. Computing R_{32} in these clumps from the total intensity ratio, without isolating the ^{13}CO-

bright component, would lead to an artificially high value in the primary clump because of its large linewidth. Instead, the peak temperature ratio of the ^{13}CO-bright component is relatively constant between these two clumps.

A map of the ^{12}CO/^{13}CO (3-2) peak temperature ratio was created using the maps discussed in Section 3.3.2. The temperature ratio was computed from the CO(3-2) velocity component that was closest in velocity to the ^{13}CO(3-2) emission. When two velocity components are detected, this is generally the more redshifted peak. The map is shown in the top panel of Fig. 3.5. On the finer spatial scales used in the R_{32} map, the line ratio in the primary clump is slightly elevated relative to the secondary clump. In the primary clump R_{32} varies from roughly $4-7$, with an upward deviation to 12 near the edge of the ^{13}CO(3-2) detection. The secondary clump hosts an R_{32} that ranges from $3.5-5$.

As the significantly detected ^{13}CO(3-2) emission is confined to the regions that are brightest in CO(3-2), it is important to determine if ^{13}CO throughout the rest of the gas is undetected because of an anomalously high R_{32}, or if an R_{32} similar to the rest of the gas would also lie below our detection threshold. To this effect we have created a map of the maximum R_{32} that would be detectable given the observed ^{12}CO brightness temperature and ^{13}CO noise, $R_{32,\mathrm{max}} = {}^{12}T_{32}/3{}^{13}T_{\mathrm{rms}}$. This map is shown in Fig. 3.5. Since ^{12}CO emission in the fainter regions cannot be uniquely attributed to the ^{13}CO-bright component, we have computed $R_{32,\mathrm{max}}$ for both velocity components and taken the larger value. Gas with an R_{32} below this threshold would have a peak ^{13}CO temperature large enough to be detected by our imaging.

Overlaid on both images in Fig. 3.5 are contours corresponding to an $R_{32,\mathrm{max}}$ of 3, 4, and 5. These are roughly in line with what has been detected throughout the rest of the gas. The primary and secondary clumps fill the majority of a contour of $R_{32,\mathrm{max}} = 5$. Gaps within this contour may indicate slightly elevated line ratios. Outside of the two main clumps, very few regions reach an $R_{32,\mathrm{max}}$ of 5. In these outer regions our observations are only sensitive to ^{13}CO(3-2) intensities large enough to yield $R_{32} \lesssim 3$. As this is smaller than the line ratios observed in the rest of the gas, any ^{13}CO located outside of the two main clumps lies below our detection threshold.

3.4 CO-to-H_2 Conversion Factor

The CO-to-H_2 conversion factor, X_{CO}, relates the integrated intensity of a CO line to the H_2 column density (see Eqn. 3.1). It can equivalently be expressed in terms of integrated properties:

$$M_{\mathrm{mol}} = \alpha_{\mathrm{CO}} L'_{\mathrm{CO}}, \tag{3.8}$$

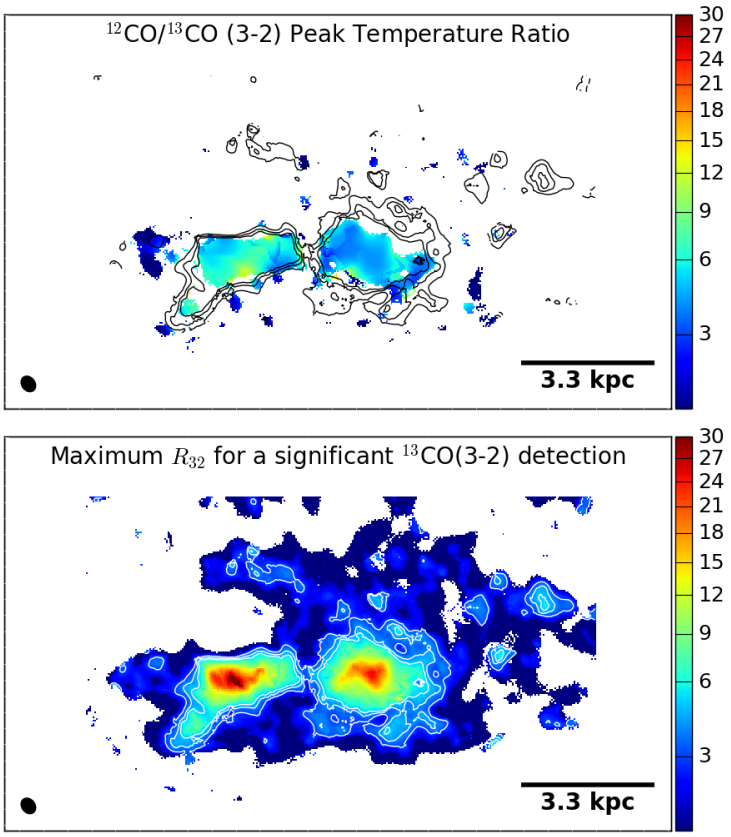

Figure 3.5: *Top:* Map of the ^{12}CO/^{13}CO (3-2) brightness temperature ratio. The ^{12}CO emission has been modelled by two velocity components. The component used in this map is the one with a velocity closest to the ^{13}CO emission. *Bottom:* The largest R_{32} that would be detected in these observations, determined from the ratio of ^{12}CO brightness temperature to the 3× the RMS variation in the $^{13}T_{32}$ spectrum. Gas with an R_{32} below this threshold can be detected at 3σ. The contours in both images correspond to $R_{32,\mathrm{max}}$ of 3, 4, and 5.

where the conversion factor $\alpha_{\rm CO}$ is now a mass-to-light ratio relating the total molecular gas mass (which includes a factor of 1.36 to account for heavier elements) to the CO line luminosity in units of K km s^{-1} pc^2 . In the Milky Way and normal galaxies this conversion factor is $X_{\rm CO} = 2\times10^{20}$ cm^{-2} (K km s^{-1})$^{-1}$, or equivalently $\alpha_{\rm CO} = 4.3\,{\rm M}_\odot$(K km s^{-1} pc^2)$^{-1}$ (Bolatto et al., 2013).

Here we use the ^{13}CO(3-2) emission line to estimate $\alpha_{\rm CO}$ under the assumption of local thermodynamic equilibrium (LTE). We restrict this analysis to the spatial region encompassing the two bright clumps, which is shown in the bottom panel of Fig. 3.3. Additionally, only the ^{13}CO-bright velocity component of the ^{12}CO spectra from this region (Fig. 3.2) are considered. These restrictions ensure that the ^{12}CO and ^{13}CO considered originate from the same molecular gas. As a result, this LTE analysis is only sensitive to a fraction of the total molecular gas mass.

The total ^{13}CO column density can be estimated from the intensity of a single transition ^{13}CO($J \rightarrow J-1$) according to (Mangum & Shirley, 2015):

$$N(^{13}{\rm CO}) = \frac{3h}{8\pi^3\mu^2 J}\frac{Q(T_{\rm ex})}{}\frac{\exp(\frac{J+1}{2}h\nu_J/kT_{\rm ex})}{\exp(h\nu_J/kT_{\rm ex})-1}\tau_J\Delta v. \tag{3.9}$$

Here $\mu = 0.11$ Debye $= 0.11\times10^{-18}$ esu is the ^{13}CO dipole moment, $\frac{1}{2}(J+1)h\nu_J$ is the energy of rotational level J, ν_J is the frequency of the $J \rightarrow J-1$ transition, τ_J is the optical depth of the transition, and Δv is the full linewidth. Assuming that the population in each rotational level is described by a Boltzmann distribution at a common temperature $T_{\rm ex}$, the partition function is $Q(T_{\rm ex}) \approx 2T_{\rm ex}/T_1 + 1/3$, where $T_1 \equiv h\nu_1/k = 5.3$ K. For the ^{13}CO(3-2) transition, this expression becomes

$$N(^{13}{\rm CO}) = 0.83\times10^{14}\ {\rm cm}^{-2}\,(T_{\rm ex}+0.88)\frac{{\rm e}^{15.9\ {\rm K}/{\rm T_{ex}}}}{1-{\rm e}^{-15.9\ {\rm K}/{\rm T_{ex}}}}\tau_J\Delta v. \tag{3.10}$$

In the limit of optically thin ^{13}CO emission ($1-{\rm e}^{-\tau}\approx\tau$), the optical depth τ_J can be determined from Eqn. 3.6:

$$\tau_J \approx \frac{T_R}{T_J\Phi_A[f(T_{\rm ex})-f(T_{\rm bg})]}. \tag{3.11}$$

This approximation begins to break down at $\tau \gtrsim 0.1$. In this regime the optical depth derived from Eqn. 3.11 must be multiplied by a factor of $\tau_J/(1-{\rm e}^{-\tau_J})$. From Section 3.3.3, the excitation temperature and area filling factor are $T_{\rm ex} = 15$ K and $\Phi_A = 0.1$. The corresponding ^{13}CO(3-2) optical depth obtained from Eqn. 3.11 is $\tau_3 = 0.30$, and the finite optical depth correction evaluates to ≈ 1.16.

The optical depth can also be determined from the ratio of ^{12}CO and ^{13}CO brightness temperatures:

$$\tau_J(^{13}\mathrm{CO}) \approx -\ln\left(1 - \frac{T_R(^{13}\mathrm{CO})}{T_R(^{12}\mathrm{CO})}\right). \tag{3.12}$$

Note that the dependence on Φ_A has reduced out of this expression, as it is assumed that both ^{12}CO and ^{13}CO originate from the same area. This method yields an optical depth of 0.36, which is consistent with Eqn 3.11 after the $\tau_J/(1-\mathrm{e}^{-\tau_J})$ correction.

The resulting column density in the optically thin limit, expressed now in terms of integrated intensity ($W_J = T_R/0.94\ \Delta v$), is

$$N_{\mathrm{thin}}(^{13}\mathrm{CO}) = 0.78\times10^{14}\ \mathrm{cm}^{-2}\,(T_{\mathrm{ex}}+0.88)\frac{\mathrm{e}^{15.9\ \mathrm{K}/\mathrm{T_{ex}}}}{1-\mathrm{e}^{-15.9\ \mathrm{K}/\mathrm{T_{ex}}}} \times \frac{^{13}W_{32}}{T_J\Phi_A[f(T_{\mathrm{ex}})-f(T_{\mathrm{bg}})]}, \tag{3.13}$$

and the corrected optical depth is $N = N_{\mathrm{thin}}\times\tau_J/(1-\mathrm{e}^{-\tau_J})$. For $T_{\mathrm{ex}} = 15$ K, $\Phi_A = 0.1$, and $^{13}W_{32} = 22.8$ K km s^{-1}, the total ^{13}CO column density is 1.74×10^{17} cm^{-2}. Assuming the abundance ratios $[^{12}\mathrm{CO}]/[^{13}\mathrm{CO}] = 50$ and $[^{12}\mathrm{CO}]/[\mathrm{H_2}] = 10^{-4}$ (Dickman, 1978; Frerking et al., 1982) yields an $\mathrm{H_2}$ column density of $N_{\mathrm{H_2}} = 8.7\times10^{22}$ cm^{-2}. The total molecular gas mass is then computed from $M_{\mathrm{mol}} = 1.36 m_{\mathrm{H_2}} N_{\mathrm{H_2}} A_{\mathrm{source}}$, where $A_{\mathrm{source}} = \Phi_A A_{\mathrm{reg}}$ is the surface area of the molecular gas and $A_{\mathrm{reg}} = 11.2$ kpc^2 is the area of the region used to extract the spectra. This gives a total molecular gas mass of $2.1\times10^9\,\mathrm{M_\odot}$.

The CO-to-$\mathrm{H_2}$ conversion factor is calibrated using CO(1-0) luminosity. Since some CO(1-0) emission is spread outside of this region from its lower resolution, it is estimated from the CO(3-2) luminosity (0.66×10^9 K km s^{-1} pc^2; see Tab. 3.1) assuming a constant r_{31} of 0.71. The inferred CO(1-0) luminosity for the ^{13}CO-bright velocity component is $L'_{10} = L'_{32}/r_{31} = 9.3\times10^8$ K km s^{-1} pc^2, giving a CO-to-$\mathrm{H_2}$ conversion factor of $\alpha_{\mathrm{CO}} = 2.26\,\mathrm{M_\odot}(\mathrm{K\ km\ s^{-1}\ pc^2})^{-1}$. This is half of the Galactic value.

The total luminosity of both CO(1-0) components from within the region tracing the ^{13}CO emission, assuming an r_{31} of 0.7, is 3×10^9 K km s^{-1} pc^2. Adopting this total luminosity in place of that from the ^{13}CO-bright component only yields a CO-to-$\mathrm{H_2}$ conversion factor of $\alpha_{\mathrm{CO}} = 0.7\,\mathrm{M_\odot}(\mathrm{K\ km\ s^{-1}\ pc^2})^{-1}$, which is 6 times lower than the Galactic value. This is comparable to the standard value of $\alpha_{\mathrm{CO}} = 0.8\,\mathrm{M_\odot}(\mathrm{K\ km\ s^{-1}\ pc^2})^{-1}$ in ULIRGs and starburst galaxies (Downes & Solomon, 1998; Bolatto et al., 2013). However, this conversion factor uses the molecular gas mass that was measured from the single ^{13}CO velocity component, whereas two distinct components were detected at ^{12}CO. Any mass in the ^{13}CO-faint velocity component has therefore been neglected in this measurement.

In order to investigate the dependence of the molecular gas mass measurement on the spatial region used to extract the spectra, we repeat this analysis for the region containing all of the line emission. The line ratio throughout the entire gas distribution is $r_{31} = 0.80 \pm 0.03$, corresponding to $T_{\rm ex} = 22$ K and $\Phi_A = 0.0126$. The ^{13}CO(3-2) optical depth computed from Eqn. 3.12 is 0.14. The total ^{13}CO column density is 1.3×10^{17} cm^{-2}, which is slightly lower than the column density obtained from the smaller region. This implies a molecular gas mass of 2.47×10^9 M$_\odot$ over the 13.6×10 kpc box used to obtain the spectra. The corresponding CO-to-H$_2$ conversion factor, using the full CO(1-0) luminosity, is $0.53\,{\rm M}_\odot(\ {\rm K\ km\ s^{-1}\ pc^2}\ )^{-1}$, in close agreement with the smaller region when both velocity components are included in the line luminosity. From these measurements, about 85% of the molecular gas mass traced by ^{13}CO is contained within the primary and secondary clumps.

The absence of ^{13}CO emission from the broad, blueshifted wing implies that the measured molecular gas mass does not trace the entire supply of molecular gas. The molecular gas mass that is traced by the ^{13}CO-bright velocity component is 2.1×10^9 M$_\odot$. Assuming that the CO-to-H$_2$ conversion factor in this parcel of gas is the same as the remainder of the gas, the total CO(1-0) luminosity gives a total molecular gas mass of 1.1×10^{10} M$_\odot$.

3.4.1 Underlying Assumptions

LTE models are highly simplistic in nature. Several assumptions, both direct and indirect, have been required to enable this analysis. Here we discuss the major assumptions, and comment on how they may affect our results.

^{13}CO Abundance

Without a direct probe of the H$_2$ content of the molecular gas, converting the measured ^{13}CO column density into an H$_2$ column density requires the assumption of a ^{13}CO abundance. We assumed a CO abundance of $[^{12}{\rm CO}]/[{\rm H_2}] = 10^{-4}$ and an isotopologue abundance ratio of $[^{12}{\rm CO}]/[^{13}{\rm CO}] = 50$. The estimated CO-to-H$_2$ conversion factor depends linearly on the assumed $[^{13}{\rm CO}]/[{\rm H_2}]$. In many extragalactic observations these quantities are not measured directly, so these assumptions are common.

For cloud metallicities above $\sim 0.1\,{\rm Z}_\odot$ the CO/H$_2$ abundance ratio varies linearly with metallicity (Bialy & Sternberg, 2015). In cool core clusters the molecular gas is likely formed from the cooling of the hot atmosphere, so the cloud abundance should be related to the metallicity of the hot atmosphere. In RXJ0821 the metallicity is $\sim 0.4\,{\rm Z}_\odot$ within

the central 10 kpc of the cluster core, and peaks at $\sim 0.8\,Z_\odot$ at about 30 kpc (Bayer-Kim et al. 2002; Vantyghem et al. in prep). If the abundance in the molecular clouds reflects the central metallicity, then the CO/H_2 abundance ratio would be overestimated and, and the CO-to-H_2 conversion factor underestimated, by a factor of 2.5. A declining metallicity profile is also observed in Perseus, where Panagoulia et al. (2013) suggested that the missing metals near the core are locked up in cold dust. The molecular clouds may therefore be more metal-rich than the central atmosphere, implying an abundance ratio closer to solar.

The isotopologue ratio of 50 was chosen to represent the midpoint of this observed range in the Milky Way, which increases radially from 24 in the Galactic Center to > 100 at large radii (Langer & Penzias, 1990; Milam et al., 2005). Variations in the isotopologue ratio are controlled by stellar processing, selective photodissociation, and chemical fractionation (see Section 3.3.3). The data available for extragalactic sources seems to indicate that the isotopologue ratio increase with redshift, with values of ~ 40 in local starbursts and 100 or higher in ULIRGs (Henkel et al., 2014). An elevated isotopologue ratio in RXJ0821 would bring the measured conversion factor closer to the Galactic value. Reconciling the two would require $^{12}CO/^{13}CO \approx 100$.

^{13}CO Emitting Area

Throughout this analysis we have assumed that the ^{12}CO and ^{13}CO emission originate from the same emitting area, thus sharing a common area filling factor. This assumption can break down in two ways. First, differences between the ^{12}CO and ^{13}CO optical depths can lead to selective photodissociation of ^{13}CO in the lower density outskirts of individual molecular clouds. As a result, ^{13}CO will be confined to the central regions of the clouds, while ^{12}CO extends throughout the cloud and is well-mixed with H_2. This would decrease the ^{13}CO filling factor, and the measured optical depth must be modified by the ratio of the areas. The true ^{13}CO optical depth would then be underestimated in our analysis, leading to an underestimate in the conversion factor. For significant selective photodissociation, the ^{13}CO emission will originate from a portion of the cloud with different physical conditions than the ^{12}CO emission. The temperature, density, and column density for the gas containing ^{12}CO and ^{13}CO would need to be measured independently.

Second, the ^{12}CO and ^{13}CO may be distributed over different spatial regions in the entire cloud ensemble. In these observations ^{13}CO is detected only in the two bright clumps, while diffuse ^{12}CO encompasses a larger envelope. This may indicate that the diffuse emission contains little ^{13}CO, from little stellar processing, significant selective photodissociation, or other processes that enhance the $^{12}CO/^{13}CO$ abundance ratio. However, as shown

in Section 3.3.3, we can only detect ^{13}CO outside of the two main clumps if the ^{13}CO abundance is abnormally large. By restricing the LTE analysis to the region tracing the ^{13}CO emission (see Fig. 3.3, bottom), we ensure that the ^{12}CO and ^{13}CO emission trace the same cloud ensemble.

Thermal Equilibrium

The fundamental assumption of the LTE model is that each rotational transition can be described by a common excitation temperature that is equal to the kinetic temperature of the molecular gas. This approximation is only satisfied if the density of the molecular gas exceeds the critical density for the transition, which is $\sim 10^3$ cm^{-3} for CO(1-0) and 3×10^4 cm^{-3} for CO(3-2). In this regime, collisions with H_2 occur rapidly enough to thermalize the CO molecules.

The CO (3-2)/(1-0) peak temperature ratio of 0.71 for the ^{13}CO-bright component implies thermalized emission only if the gas temperature is 15 K. Alternatively, the gas may be hotter and subthermally excited. Subthermal excitation of the CO(3-2) line modeled under LTE conditions can lead to an underestimate in column density. For example, Nishimura et al. (2015) performed an LTE analysis using both ^{13}CO(1-0) and ^{13}CO(2-1) in the Orion giant molecular cloud. The column density derived using ^{13}CO(2-1) was a factor of three lower than that derived using ^{13}CO(1-0), which they attribute to subthermal excitation.

Within the central 10 kpc of the RXJ0821 galaxy cluster, the pressure of the hot atmosphere is 2×10^{-10} erg cm^{-3} (Hogan et al. priv comm). This confining pressure sets the minimum pressure of the molecular clouds. If the gas is in pressure balance, then a kinetic temperature of 15 K corresponds to a density of 9×10^4 cm^{-3}, which exceeds the CO(3-2) critical density by a factor of three. The molecular gas should then be thermalized for any temperature up to $\sim$ 50 K. Additionally, the pressure in self-gravitating clouds exceeds the confining pressure, indicating that the molecular gas in this system is likely thermalized.

3.5 Discussion

In the subset of the molecular gas traced by ^{13}CO emission, the CO-to-H_2 conversion factor is $\alpha_{CO} = 2.26\,M_\odot(\text{ K km s}^{-1}\text{ pc}^2\text{ })^{-1}$, or equivalently $X_{CO} = 1.04{\times}10^{20}$ cm^{-2} (K km s^{-1})$^{-1}$. This is the first measurement of X_{CO} in a BCG. Previous works have simply adopted the

Galactic value, justifying the decision based on the high metal abundances at the centers of galaxy clusters and the low expected temperature of gas condensing from the hot atmosphere. Our results indicate that $X_{\rm CO}$ in RXJ0821 is half of the Galactic value. Given the high scatter in extragalactic determinations of $X_{\rm CO}$, this measurement is broadly consistent with the Galactic value. Continuing to adopt the Galactic value in other BCGs may lead to an overestimate of $M_{\rm mol}$, but is likely accurate to within a factor of two.

Accurate measurements of the molecular gas mass in BCGs are crucial in understanding the gas origin and its role in AGN feedback. In particular, molecular flows trailing X-ray cavities have been detected in several BCGs (Salomé et al., 2011; McNamara et al., 2014; Russell et al., 2016, 2017a; Vantyghem et al., 2016), with the cold gas either lifted directly by the cavities or has cooled in situ from uplifted, hot gas. By Archimedes' principle, the maximum mass of uplifted gas is limited by the mass displaced by the X-ray cavities. Each of the observed outflows requires a high coupling efficiency between the cavities and uplifted gas, with the displaced mass exceeding the uplifted molecular gas mass by factors of a few. For example, $10^{10}\,{\rm M}_\odot$ of cold gas in A1835 trails the X-ray cavities, which have displaced $3\times10^{10}\,{\rm M}_\odot$ of hot gas (McNamara et al., 2014). Reducing the CO-to-H_2 conversion factor alleviates the requirement of a high coupling efficiency.

In jet-driven molecular outflows, the outflowing gas may become optically thin while the gas in the disk remains optically thick (Dasyra et al., 2016). In RXJ0821 the ^{12}CO/^{13}CO line ratios in the ^{13}CO-bright component imply ^{12}CO optical depths $\gg 1$, indicating that its molecular gas, which is spatially offset from the galactic nucleus, does not resemble the gas in jet-driven outflows. The ^{13}CO-faint component is also consistent with moderate ^{12}CO optical depths. Extending these results to the gas flows observed in other BCGs implies a gentler lifting process than in fast, jet-driven outflows.

3.6 Conclusions

We have presented new ALMA cycle 4 observations of the CO(1-0), CO(3-2), and ^{13}CO(3-2) emission lines in the BCG of the cool core cluster RXJ0821+0752. The is the first detailed study of a ^{13}CO emission line in a BCG. We have used the optically thin ^{13}CO emission to estimate the molecular gas mass without relying on the Galactic CO-to-H_2 conversion factor. Our results are summarized as follows:

- The molecular gas is primarily situated in two clumps located 3 kpc north to northwest of the galactic nucleus, with $< 1.2\times10^8\,{\rm M}_\odot$ coincident with the BCG nucleus.

These clumps and their surrounding diffuse emission are part of an 8 kpc long filament. ^{13}CO(3-2) emission is only detected within the two bright clumps. Any ^{13}CO emission located outside of these clumps lies below our detection threshold.

- Both of the ^{12}CO spectra extracted from a region tracing the ^{13}CO emission contain two velocity components. The narrower component (~ 60 km s^{-1} FWHM) is consistent in both velocity centroid and linewidth with the ^{13}CO(3-2) emission. The broader ($130 - 160$ km s^{-1}), slightly blueshifted (~ 30 km s^{-1}) wing has no associated ^{13}CO(3-2) emission.

- Assuming that the molecular gas is in local thermodynamic equilibrium at a temperature of 15 K, the molecular gas mass traced by the ^{13}CO emission is 2.1×10^9 M$_\odot$. Isolating the ^{12}CO velocity component that accompanies the ^{13}CO emission yields a CO-to-H$_2$ conversion factor of $\alpha_{\rm CO} = 2.26\,{\rm M}_\odot(\ {\rm K\ km\ s^{-1}\ pc^2}\ )^{-1}$, which is a factor of two lower than the Galactic value.

Adopting the Galactic conversion factor in BCGs, as is currently the common practice, may lead to slight overestimates of $M_{\rm mol}$. However, the factor of two difference between the the measured and Galactic CO-to-H$_2$ conversion factors is comparable to object-to-object variations (Bolatto et al., 2013). Continuing to adopt the Galactic conversion factor in BCGs should be reasonable until this analysis, or a complete excitation analysis, can be conducted in other systems.

Chapter 4

Molecular Gas Filaments and Star-Forming Knots Beneath an X-ray Cavity in RXC J1504-0248

Abstract

We present recent ALMA observations of the CO(1-0) and CO(3-2) emission lines in the brightest cluster galaxy of RXCJ1504.1−0248, which is one of the most extreme cool core clusters known. The central galaxy contains 1.9×10^{10} $M_{\odot}$ of molecular gas. The molecular gas morphology is complex and disturbed, showing no evidence for a rotationally-supported structure in equilibrium. 80% of the gas is situated within the central 5 kpc of the galactic center, while the remaining gas is located in a 20 kpc long filament. The cold gas has likely condensed out of the hot atmosphere. The filament is oriented along the edge of a putative X-ray cavity, suggesting that AGN activity has stimulated condensation. This is energetically feasible, although the morphology is not as conclusive as systems whose molecular filaments trail directly behind buoyant radio bubbles. The velocity gradient along the filament is smooth and shallow. It is only consistent with free-fall if it lies within 20° of the plane of the sky. The abundance of clusters with comparably low velocities suggests that the filament is not free-falling. Both the central and filamentary gas are coincident with bright UV emission from ongoing star formation. Star formation near the cluster core is consistent with the Kennicutt-Schmidt law. The filament exhibits increased star formation surface densities, possibly resulting from either the consumption of a finite molecular gas supply or spatial variations in the CO-to-H_2 conversion factor.

4.1 Introduction

Brightest cluster galaxies (BCG) are the most massive galaxies in the Universe. Those located at the centers of cool core clusters exhibit filamentary nebulae that span five orders of magnitude in temperature (Werner et al., 2013). The filaments contain massive molecular gas ($\sim$ 100 K) reservoirs (Edge, 2001; Edge et al., 2002; Edge & Frayer, 2003; Salomé & Combes, 2003), warm (10^4 K), ionized gas (e.g. Lynds, 1970; Heckman, 1981; Cowie et al., 1983; Hu et al., 1985; Crawford et al., 1999), and hot (10^7 K) gas emitting soft X-rays (e.g. Fabian et al., 2001, 2003; Werner et al., 2013; Walker et al., 2015). Star formation in these systems proceeds at rates of up to $10^3\,M_\odot\,yr^{-1}$ (e.g. McNamara, 2004; O'Dea et al., 2008; McDonald et al., 2011; Donahue et al., 2015; Tremblay et al., 2015), and is correlated with the intracluster medium (ICM) mass deposition rate (O'Dea et al., 2008). These signatures of cold gas are observed preferentially in systems in which the central cooling time of the ICM falls below 1 Gyr, or equivalently when the central entropy falls below 30 keV cm^2 (Cavagnolo et al., 2008; Rafferty et al., 2008; Werner et al., 2014; Pulido et al., 2018). The presence of this cooling time threshold indicates that cold gas is formed by condensation from the hot cluster atmosphere.

Despite the strong evidence for cold gas condensing out of the ICM, the observed molecular gas masses and star formation rates in BCGs are an order of magnitude lower than those expected from uninhibited cooling. It is now widely accepted that energetic feedback from active galactic nuclei (AGN) offsets radiative losses, regulating the rate of ICM cooling (see McNamara & Nulsen, 2007, 2012, for a review). High resolution X-ray imaging has revealed bubbles (cavities) in the hot cluster atmosphere that were inflated by radio jets launched by the AGN. The sizes and confining pressure of these cavities provide a direct estimate of the average power output by the AGN. The jet power is closely coupled to the cooling rate of the cluster atmosphere in a large sample of galaxy groups and clusters (Bîrzan et al., 2004; Dunn & Fabian, 2006; Rafferty et al., 2006), indicating that AGN are capable of preventing the majority of the hot gas from condensing.

Molecular gas is expected to play a crucial role in the AGN feedback cycle, as it connects gas condensation on large scales to accretion onto the nuclear supermassive black hole. Ram pressure from molecular clouds travelling through the ICM, as well as collisions between clouds, both provide natural mechanisms for cold clouds to shed their angular momentum and accumulate at the centers of BCGs (Pizzolato & Soker, 2005, 2010). Simulations suggest that cold clouds condense from non-linear overdensities in the ICM that are generated by cycles of AGN feedback, and proceed to rain onto the central galaxy (Gaspari et al., 2012, 2013; McCourt et al., 2012; Sharma et al., 2012; Li & Bryan, 2014b).

Observations have also demonstrated a link between molecular gas and AGN. Nebular

emission in BCGs is typically confined to filaments that extend radially from the cluster core (e.g. Conselice et al., 2001; Hatch et al., 2006; McDonald et al., 2012a). In the Perseus cluster, two prominent nebular filaments are coincident with soft X-rays (Fabian et al., 2003), molecular hydrogen (Hatch et al., 2005; Lim et al., 2012), and CO emission (Salomé et al., 2006, 2011), and extend toward an X-ray cavity. Similar morphologies are observed in the nebular emission in several BCGs (e.g. Werner et al., 2011; Canning et al., 2013). ALMA observations have revealed molecular filaments trailing X-ray cavities in other BCGs (McNamara et al., 2014; Russell et al., 2016, 2017a; Vantyghem et al., 2016). This gas has either been lifted directly from the cluster core by buoyantly rising radio bubbles, or it has cooled in situ from hot gas that has been uplifted to an altitude where it becomes thermally unstable (Revaz et al., 2008; McNamara et al., 2016).

In this work we examine the molecular gas in the RXCJ1504.1-0248 BCG (hereafter RXCJ1504) using new ALMA observations of the CO(1-0) and CO(3-2) emission lines. CO is the most common molecule used to observe molecular gas. The main constituent of molecular gas, H_2, is a symmetric molecule, so does not possess the dipolar transitions used to observe cold (~ 20 K) gas (e.g. Bolatto et al., 2013). The two observed CO transitions provide differing resolutions and field-of-views, with CO(1-0) tracing larger scale gas and CO(3-2) showing finer structure.

RXCJ1504, at redshift $z = 0.2169$, is one of the most massive cool core clusters known. It is also compact, leading to an extremely bright X-ray core. A classical cooling flow model yields a mass deposition rate of $1500 - 1900\,M_\odot\ yr^{-1}$ (Böhringer et al., 2005). The molecular gas mass, $3 \times 10^{10}\,M_\odot$, obtained from IRAM-30m CO(1-0) observations (Edge private communication), and star formation rate, $140\,M_\odot\ yr^{-1}$ (Ogrean et al., 2010), are also among the highest known. These factors indicate that RXCJ1504 is experiencing a cycle of extreme cooling, and is therefore a prime target for studying the connection between molecular gas and AGN feedback.

Throughout this paper we assume a standard ΛCDM cosmology with $H_0 = 70$ km s^{-1} Mpc^{-1}, $\Omega_{m,0} = 0.3$, and $\Omega_{\Lambda,0} = 0.7$. At the redshift of RXCJ1504 ($z = 0.216902$; SDSS Collaboration et al., 2016), the angular scale is $1'' = 3.5$ kpc and the luminosity distance is 1073 Mpc.

4.2 Observations and Data Reduction

The BCG of the RXC J1504.1-0248 galaxy cluster (R.A.: 15:04:07.503, decl.: -2:48:17.04) was observed by ALMA Bands 3 and 7 (Cycle 4, ID 2016.1.01269.S, PI McNamara),

centered on the CO(1-0) and CO(3-2) lines at 94.725 and 284.161 GHz, respectively. The CO(1-0) observations were divided into four blocks, two of which were taken on 27 October 2016 and the others on 2 November 2016 and 10 May 2017. The total on-source integration time was 151 minutes. The CO(3-2) observation was conducted in a single block on 4 July 2017, with a total on-source integration time of 34 minutes. Each observation was split into ~ 6 minute on-source integrations interspersed with observations of the phase calibrator. The observations used a single pointing centered on the BCG nucleus with a primary beam of 65 arcsec at CO(1-0) and 22 arcsec at CO(3-2). The CO(1-0) observations used between 38 and 47 antennas with baselines ranging from $16-1124$ m, and the CO(3-2) observation used 45 antennas with baselines from $21-2650$ m. The frequency division correlator mode was used for the CO spectral line observations, providing a 1.875 GHz bandwidth with 488 kHz frequency resolution. This corresponds to a velocity resolution of 1.5 km s^{-1} at CO(1-0) and 0.5 km s^{-1} at CO(3-2), although the data were smoothed to coarser velocity channels for subsequent analysis. An additional three basebands with the time division correlator mode, each with a 2 GHz bandwidth and frequency resolution of 15.625 MHz, were employed for each spectral line in order to measure the sub-mm continuum.

The observations were calibrated in CASA version 4.7.0 (McMullin et al., 2007) using the pipeline reduction scripts. Continuum-subtracted data cubes were created using UVCONTSUB and CLEAN. Additional phase self-calibration provided a 50% increase in the signal-to-noise of the continuum at CO(1-0) and a 30% increase at CO(3-2). Images of the line emission were reconstructed using Briggs weighting with a robust parameter of 0.5. An additional *uv* tapering was used to smooth the CO(3-2) image on scales below 0.1 arcsec. The synthesized beams of the final CO(1-0) and CO(3-2) data cubes were 0.71×0.61 arcsec (P.A. $-77°$) and 0.25×0.19 arcsec (P.A. $-57°$), respectively. The data cubes were binned to velocity resolutions of 20 km s^{-1} and 10 km s^{-1}, respectively, and the RMS noise in line-free channels were 0.2 and 0.65 mJy beam^{-1}. Images of the continuum were created by combining line-free spectral channels from each baseband. We detected a continuum source located near the BCG nucleus with a flux density of 8.734 ± 0.015 mJy at 101.7945 GHz and 5.462 ± 0.045 mJy at 291.4581 GHz. Imaging the continuum in narrow velocity channels (2 km s^{-1}) shows no evidence of line absorption against the continuum emission.

The gas velocities reported here are measured in the rest frame of the BCG, with $z = 0.216902 \pm 0.000016$ (SDSS Collaboration et al., 2016). This redshift was measured using optical emission lines, so it traces the nebular gas within the BCG. Stellar absorption line measurements would provide a more robust tracer of the BCG systemic velocity. Gas motions may be affected by non-gravitational processes, such as turbulence, whereas stellar motion is a direct tracer of the gravity of the BCG. An earlier SDSS data release provided

an absorption line-only measurement of the BCG velocity (Abazajian et al., 2004). This differs from the aforementioned value by only 30 km s^{-1} , which is well below the accuracy of the absorption measurement (150 km s^{-1}).

Throughout this work we compare the ALMA images with archival UVIS F689m and ACS F165LP images from the *Hubble Space Telescope*. Each of these images are mutually offset, so have been shifted to align with the ALMA CO(3-2) image. The ALMA CO(1-0) and CO(3-2) images used the same phase calibrator, so the locations of the continuum source in the BCG nucleus are consistent. Identifying the centroids of the F689m and F165LP images is difficult as they both contain filamentary continuum emission near the galactic nucleus. Fortunately, an additional point source (R.A.: 15:04:07.2782, decl.: -2:48:10.0075) was detected in the ALMA imaging, with a flux density of $79 \pm 11\mu$Jy at 101.7945 GHz. This emission originates from a galaxy located 7.4 arcsec NW of the BCG. The HST F689m image was shifted by 0.48 arcsec (N 30° E) in order to line up this galaxy with the sub-mm continuum.

The F165LP image contains no compact sources to compare to the F689m or ALMA images. However, the same filamentary structure appears in each image. The F165LP image was shifted manually by 1.37 arcsec (W 5° S) in order to line up similar features in the two HST images. This shift is probably accurate to a few tenths of an arcsecond, although this is difficult to quantify. An 8° counter-clockwise rotation was also applied to the F165LP image in order to better align the UV emission with the molecular filament seen in the CO(3-2) image. The choice of aligning each image with the ALMA images was arbitrary. Only relative distances are used in this work, so any systematic errors in absolute positions do not affect our results.

4.3 Results

4.3.1 AGN Continuum

Our ALMA observations of the continuum point source in RXCJ1504 extend previous radio measurements to mm-wavelengths. The spectral energy distribution (SED) is shown in Fig. 4.1, and has been fit with a power law of the form $S \propto \nu^{-\alpha}$. The GMRT 327 MHz and VLA 1.4 GHz observations, shown in blue, both include emission from a radio mini-halo. Giacintucci et al. (2011) isolated the contribution from the AGN by modelling the spatial distribution with a two dimensional Gaussian. Error bars are included for both the blue (GMRT and VLA) and red (ALMA) points, but are unavailable for the other

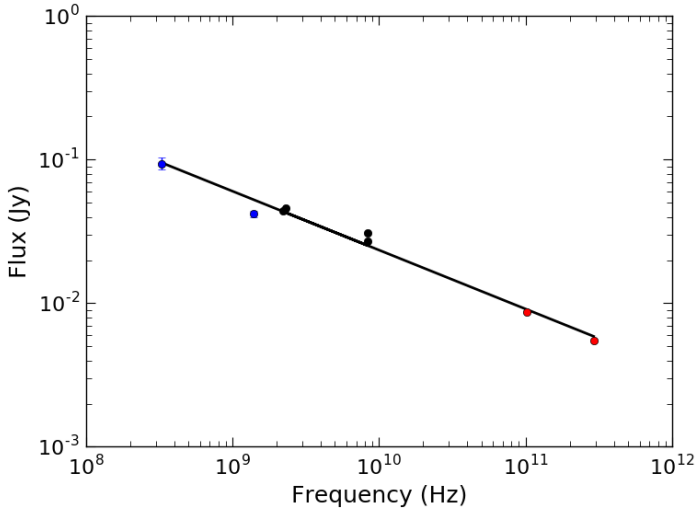

Figure 4.1: The radio to millimeter spectral energy distribution for the RXCJ1504 BCG. The ALMA measurements are shown in red. A contribution from the radio minihalo has been removed to obtain the blue points (Giacintucci et al., 2011). The error bars for the blue and red points are shown, but are smaller than the marker. No uncertainties are available for the black points.

VLBI measurements (black points: Bourda et al., 2010; Petrov, 2013). The spectral index of the power law is $\alpha = 0.41 \pm 0.03$. This is a flat-spectrum source that is consistent with synchrotron emission from the AGN.

4.3.2 Integrated Spectra

The spatially-integrated CO(1-0) and CO(3-2) spectra were extracted from a polygonal region tracing the significant CO(1-0) emission, which was determined from the maps presented in Section 4.3.4. The region measured ~ 28 kpc along its long axis and 11.4 kpc in the orthogonal direction. The integrated CO(1-0) and CO(3-2) spectra are shown in Figs. 4.2. The spectra have been corrected for the response of the primary beam.

All spectra throughout this work were fit by either one or two Gaussian components. The LMFIT package[1] was used to perform the spectral fitting. Each spectral component was tested using a Monte Carlo analysis with at least 1000 iterations, with a detection

[1]https://lmfit.github.io/lmfit-py/

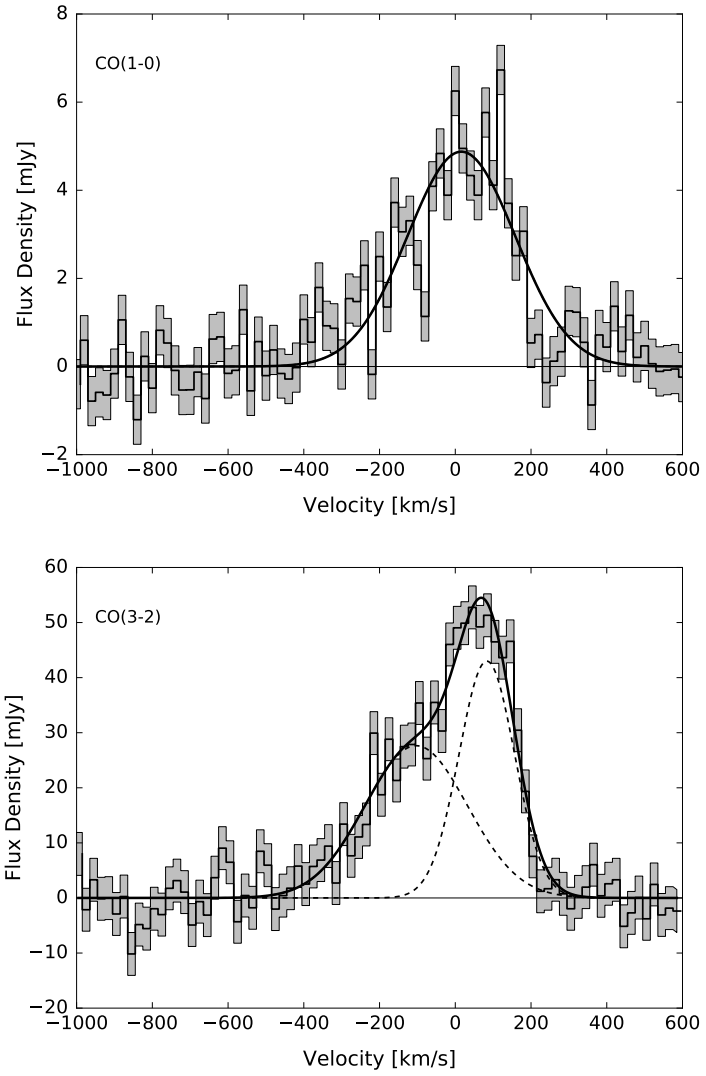

Figure 4.2: Spatially-integrated CO(1-0) (top) and CO(3-2) (bottom) spectra. The shaded areas indicate the rms noise in line-free channels.

requiring a 3σ significance (see Section 5.2 of Protassov et al., 2002). The presence of one component was required before attempting to fit a second. Instrumental broadening has been incorporated into the model.

The spatially-integrated CO(1-0) spectrum was best fit by a single component centered at 16.0 ± 6.5 km s^{-1} with a FWHM of 335 ± 15 km s^{-1} and integrated flux of 1.74 ± 0.07 Jy km s^{-1}. The higher signal-to-noise in the CO(3-2) spectrum show that the spatially-integrated spectrum is better fit by two velocity components. The first component, with an integrated flux of 9.4 ± 3.1 Jy km s^{-1}, is centered at -103 ± 51 km s^{-1} with a FWHM of 319 ± 72 km s^{-1}. The other component is redshifted to 83.2 ± 7.9 km s^{-1} and has a FWHM of 173 ± 23 km s^{-1}. A list of the best-fitting parameters can be found in Table 4.1.

Previous single dish measurements of RXCJ1504-0248 with the IRAM-30m telescope recovered an integrated CO(1-0) flux of 3.84 ± 0.62 Jy km s^{-1} (Edge, unpublished). The integrated flux measured by ALMA is $45 \pm 8\%$ of this single dish measurement. Similar recovered fractions were measured in RXJ0821 (Vantyghem et al., 2016), NGC5044 (David et al., 2014), and A1664 (Russell et al., 2014). Missing short spacings filter out emission on scales larger than 9.2 arcsec at CO(1-0) and 6 arcsec at CO(3-2).

The ratio of integrated flux densities determined from the spatially-integrated spectra is CO $(3-2)/(1-0) = 9.0 \pm 0.4$ in flux units, or CO $(3-2)/(1-0) = 1.00 \pm 0.04$ in intensity units. This is higher than the CO $(3-2)/(1-0) \approx 7$ measured in other BCGs (e.g. Russell et al., 2016; Vantyghem et al., 2014, 2016). The equal CO(1-0) and CO(3-2) intensities indicate that the molecular clouds are thermalized. This is the case when the H_2 density exceeds the critical density for the transition, which is ~ 700 cm^{-3} for CO(1-0) and $\sim 2 \times 10^4$ cm^{-3} for CO(3-2). The molecular gas in RXCJ1504 therefore resides primarily in dense clouds, as opposed to a more diffuse, volume-filling phase.

In addition to model fitting with one or two Gaussians, we have also numerically integrated the spectra following the approach of Young et al. (2011). Briefly, integrated fluxes were computed by summing each spectrum over velocity. The uncertainty in the integrated flux, σ_F, is determined from

$$\sigma_F^2 = (\Delta v)^2 \sigma^2 N_l (1 + N_l/N_b). \tag{4.1}$$

Here Δv is the velocity bin size, σ is the rms in line-free channels, N_l is the number of velocity bins, and N_b is the number of bins used to measure the baseline. Numerical integration is well-suited to measuring the total integrated flux, particularly when multiple Gaussians are required to fit the spectrum. The fluxes in multi-component spectra have large uncertainties due to degeneracies in fitting overlapping Gaussians. Adding these uncertainties

in quadrature to determine the total flux is inappropriate, as the individual components are not independent. The total fluxes and masses quoted for multi-component spectra throughout this work therefore adopt the values measured via numerical integration.

4.3.3 Molecular Gas Mass

The integrated flux ($S_{\rm CO}\Delta v$) of the CO(1-0) line can be converted to molecular gas mass through (Solomon et al., 1987; Solomon & Vanden Bout, 2005; Bolatto et al., 2013)

$$M_{\rm mol} = 1.05 \times 10^4 \frac{X_{\rm CO}}{X_{\rm CO,gal}} \left(\frac{S_{\rm CO}\Delta v \ D_L^2}{1+z} \right) \ {\rm M}_\odot. \tag{4.2}$$

Here z is the redshift of the source, D_L is the luminosity distance in Mpc, and $S_{\rm CO}\Delta v$ is in Jy km s^{-1}. The CO-to-H_2 conversion factor, $X_{\rm CO}$, is an empirically-derived quantity that is poorly constrained in BCGs. Standard practice, which we have applied here, has been to adopt the Galactic value of $X_{\rm CO,gal} = 2 \times 10^{20}$ cm^{-2} (K km s^{-1})$^{-1}$ (Bolatto et al., 2013).

Whether the Galactic $X_{\rm CO}$ is appropriate for BCGs is unknown. In the disks of normal, solar metallicity galaxies, Bolatto et al. (2013) recommend adopting the Galactic conversion factor with a factor of two uncertainty. The metal abundances in the hot cluster atmospheres surrounding BCGs are typically $\sim 0.6 - 0.8\,{\rm Z}_\odot$, which is high enough for the Galactic $X_{\rm CO}$ to be applicable. However, $X_{\rm CO}$ also depends on excitation conditions. The warm, dense gas in starbursts and (Ultra-) Luminous Infrared Galaxies (U/LIRGs) result in a conversion factor roughly five times lower than Galactic. The star formation rate in RXCJ1504-0248 ($136\,{\rm M}_\odot$ yr^{-1}; Ogrean et al., 2010) may be high enough to justify a LIRG-like $X_{\rm CO}$.

Recently, the detection of a ^{13}CO line in the galaxy cluster RXJ0821.0+0752 allowed $X_{\rm CO}$ to be estimated for the first time in a BCG (Vantyghem et al., 2017). This study obtained an $X_{\rm CO}$ that is a half of the Galactic value, albeit with large systematic uncertainties. We continue to follow the standard practice of adopting the Galactic $X_{\rm CO}$ until more direct calibrations in BCGs are available.

In order to compute molecular gas mass from a CO(3-2) flux, we first convert it to a CO(1-0) flux by adopting the CO (3-2)/(1-0) line ratio of 9 measured from the spatially-integrated spectra. From the integrated spectra presented in Section 4.3.2, the total molecular gas mass measured with the higher-fidelity CO(3-2) spectrum is $1.9 \pm 0.1 \times 10^{10}\,{\rm M}_\odot$.

Table 4.1: Parameters of Molecular Features

Region	J_{up}	χ^2/dof	Velocity Center (km s^{-1})	FWHM (km s^{-1})	Integrated Flux† (Jy km s^{-1})	Gas Mass† (10^8 M$_\odot$)	Integrated Flux* (Jy km s^{-1})	Gas Mass* (10^8 M$_\odot$)
Integrated	1	223/97	16.0 ± 6.5	335 ± 15	1.74 ± 0.07	173 ± 7	1.90 ± 0.02	189 ± 2.5
	3	94/74	-103 ± 51	319 ± 72	9.4 ± 3.1	104 ± 34	17.2 ± 0.8	190 ± 9
			83.2 ± 7.9	173 ± 23	7.9 ± 3.0	87 ± 33		
Central 5 kpc	3	225/154	-85 ± 13	362 ± 25	10.8 ± 0.8	119 ± 9	13.78 ± 0.67	152 ± 7
			127 ± 4	121 ± 13	3.35 ± 0.59	37.0 ± 6.5		
Central Clump	3	268/157	-48 ± 5	413 ± 12	11.68 ± 0.29	129 ± 3.2	11.38 ± 0.53	126 ± 6
NE Clump	3	180/157	129.7 ± 2.6	116 ± 6	2.2 ± 0.1	24.3 ± 1.1	2.38 ± 0.35	26.3 ± 3.9
Nuclear Clump	3	63/74	-164 ± 15	414 ± 21	6.02 ± 0.44	66.5 ± 4.9	7.10 ± 0.40	78.4 ± 4.4
			-30 ± 8	130 ± 26	1.17 ± 0.34	12.9 ± 3.8		
Filament	3	250/74	-134 ± 11	123 ± 25	1.18 ± 0.24	13.0 ± 2.7	4.33 ± 0.65	48 ± 8
			37 ± 5	144 ± 12	3.33 ± 0.25	36.8 ± 2.8		
Inner Filament	3	202/157	-124.7 ± 3.4	101 ± 8	1.10 ± 0.08	12.1 ± 0.9	0.79 ± 0.28	8.7 ± 3.1
Middle Filament	3	287/157	1.2 ± 2.7	82.2 ± 6.5	1.65 ± 0.11	18.2 ± 1.2	1.63 ± 0.46	18.0 ± 5.0
Outer Filament	3	103/77	80.3 ± 4.2	94 ± 10	1.57 ± 0.14	17.3 ± 1.5	0.92 ± 0.48	10.2 ± 5.3

Notes: All spectra have been corrected for the response of the primary beam and instrumental broadening. Masses determined from the CO(3-2) line have been calculated assuming CO $(3-2)/(1-0) = 9$ (in flux units), determined from the spatially-integrated spectra.

†Determined by the model fitting of one or two Gaussians.

*Determined by numerically integrating the spectrum.

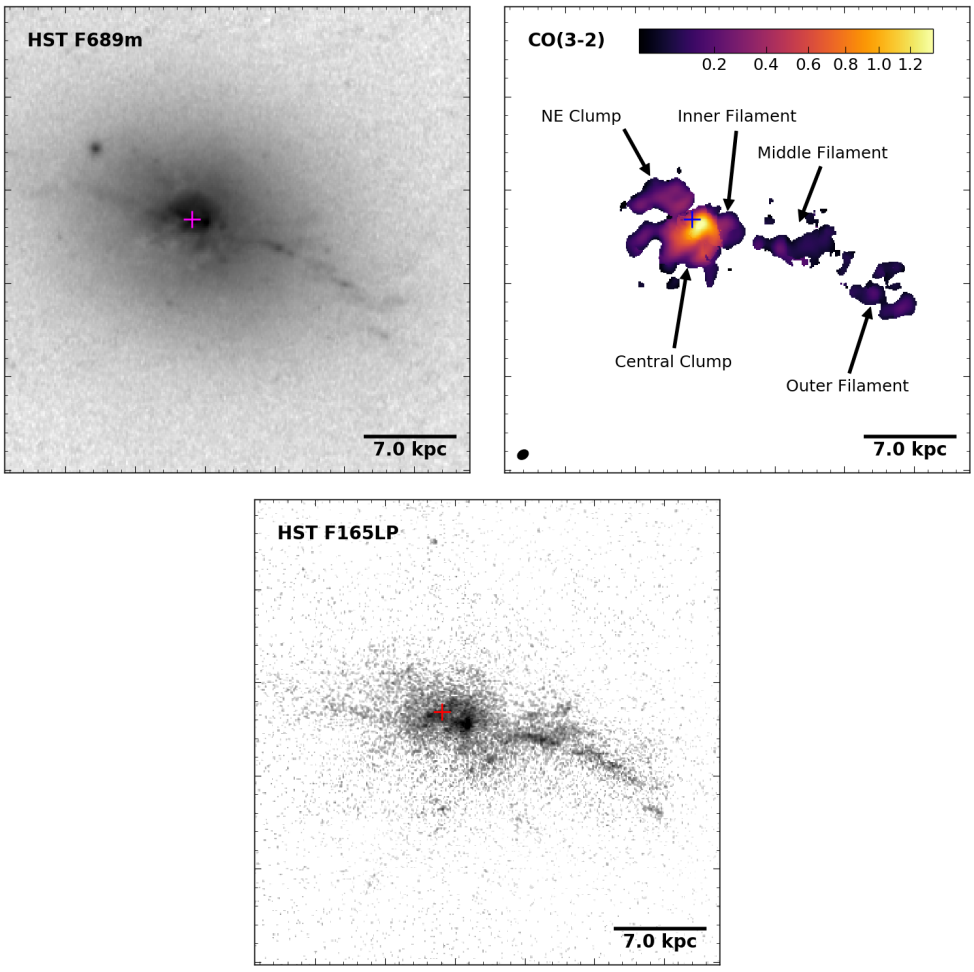

Figure 4.3: HST UVIS F689m (top-left), ALMA CO(3-2) (top-right), and HST ACS F165LP (bottom) images showing the same 35 kpc × 35 kpc field-of-view. The colorbar in the center panel shows the CO(3-2) integrated flux in Jy km s^{-1}. The cross indicates the position of the nuclear sub-mm continuum source. The black ellipse in the lower left corner shows the size of the synthesized beam.

4.3.4 Molecular Gas Distribution and Kinematics

Maps of integrated flux, velocity, and FWHM were created by applying the spectral fitting routine discussed in Section 4.3.2 to the spectra extracted from individual pixels, which were averaged over a box the size of the synthesized beam. 2500 iterations were used for the Monte Carlo analysis, with a detection requiring 3σ significance. The CO(3-2) integrated flux map is shown alongside the *HST* UVIS F689m and ACS F165LP images in Fig. 4.3. The location of the sub-mm continuum is indicated by the cross. The maps of velocity and FWHM are shown in Fig. 4.4. The CO(1-0) maps are not shown because they are consistent with the CO(3-2) maps, but have a lower resolution and sensitivity.

At the redshift of RXJ1504, the F689m filter covers the wavelength range $5340-5960$Å. This range excludes both the [OIII]/Hβ and [NII]/Hα emission line complexes. As a result, only the continuum emission from old and young stars is present in Fig. 4.3 (left). Similarly, the F165LP filter is sensitive to FUV photons, tracing the young stellar population. The filamentary emission observed in the optical (Fig. 4.3, left) is also seen in the ultraviolet, indicating that this emission stems from young stars.

The molecular gas distribution is complex and disturbed. The CO line emission peaks 0.8 kpc away from the sub-mm continuum source. Nearly 80% of the molecular gas is located within 5 kpc of the galactic center. This region comprises a large, central clump and a smaller clump to the NE. Beyond this region, a clumpy, 20 kpc long filament extends radially from the galactic center. It is coincident with continuum emission from the young stellar population observed in both *HST* images. Spectral fits for these regions, as well as others discussed below, are provided in Table 4.1.

These morphological features are comprised of at least three distinct velocity components. The first is redshifted emission from the NE clump and a portion of the large, central clump. Next, the filament extends from a galactocentric distance of 20 kpc all the way into the central clump, with a smooth velocity gradient throughout. Finally, a broad, blueshifted clump is coincident with the sub-mm continuum source. The filament and blueshifted clump have been grouped together in the right panels of Fig. 4.4, while the remaining emission is shown on the left. Two velocity components were required to fit the spectra of gas in the immediate vicinity of the sub-mm continuum source.

The NE clump and much of the central clump are part of the same kinematic structure. These regions share a common line-of-sight velocity, reaching a maximum of 150 km s^{-1}. Toward the galactic center the velocity transitions sharply from 60 km s^{-1} to -40 km s^{-1} over a distance of 1 kpc, which is about four resolution elements. Closest to the AGN, where multi-component emission is detected, the redshifted component is moving close to

the systemic velocity. The linewidths throughout the emission east of the BCG nucleus vary between 70 and 150 km s^{-1}. The narrowest regions tend to be farthest from the nucleus, although no clear gradients in the linewidth are present.

The filament exhibits a smooth velocity gradient, ranging from -110 km s^{-1} near the cluster core to 150 km s^{-1} at a radius of 20 kpc. The linewidths along the filament are narrow, ranging from 30 to 100 km s^{-1} without a clear radial dependence. These linewidths are comparable to those in the filaments observed in other systems (e.g. Russell et al., 2016; Vantyghem et al., 2016). The filament is clumpy. In addition to the two clumps visible in the integrated flux map shown in Fig. 4.3, a third clump forms part of the large central clump. It is distinguished as part of the filament by its velocity and linewidth. The blueshifted velocity connects smoothly to the middle portion of the filament, while the linewidth is consistent with that at larger radii. A region outlining the full extent of the filament is shown in the lower right panel of Fig. 4.4. Individual spectral fits for this region and each of the three smaller clumps within it are provided in Table 4.1. The total molecular gas mass in the filament is $4.8 \times 10^9\,M_\odot$, with the three clumps each having comparable masses.

The nuclear gas in the right panels of Fig. 4.4 is marked by a sharp jump in both velocity centroid and linewidth. The innermost velocity in the filament is -110 km s^{-1}, while the gas coincident with the sub-mm continuum has a velocity of -180 km s^{-1}. A more drastic change is seen in the linewidth, which changes abruptly from 110 km s^{-1} in the filament to 300 km s^{-1} at the nucleus. As a result, we consider the nuclear gas to be dynamically distinct from the filament.

Alternatively, the sharp change in velocity can be attributed to the presence of a second velocity component coincident with the nucleus. If the filament hosted two velocity components, one of which not being detected significantly, then the best-fitting model would have a moderate central velocity. When the faint component becomes significant, the best-fitting model will have two peaks: one more blueshifted and one more redshifted than the single-component model. This will result in an apparent jump in velocity at the interface between one- and two-component regions. This interface would also exhibit a decrease in linewidth, as the two components are each narrower than a single-component fit to the spectrum. However, the velocity jump seen toward the cluster core shows a significant *increase* in linewidth. The second velocity component also smoothly connects to the redshifted emission on the other side of the galaxy, so is likely unrelated to the filament. Thus the central clump does not connect smoothly in phase space to the adjacent filament.

As discussed in Section 4.3.2, the total molecular gas mass determined from the CO(3-2) spectrum is $1.9 \pm 0.1 \times 10^{10}\,M_\odot$. The gas within the central 5 kpc, which includes

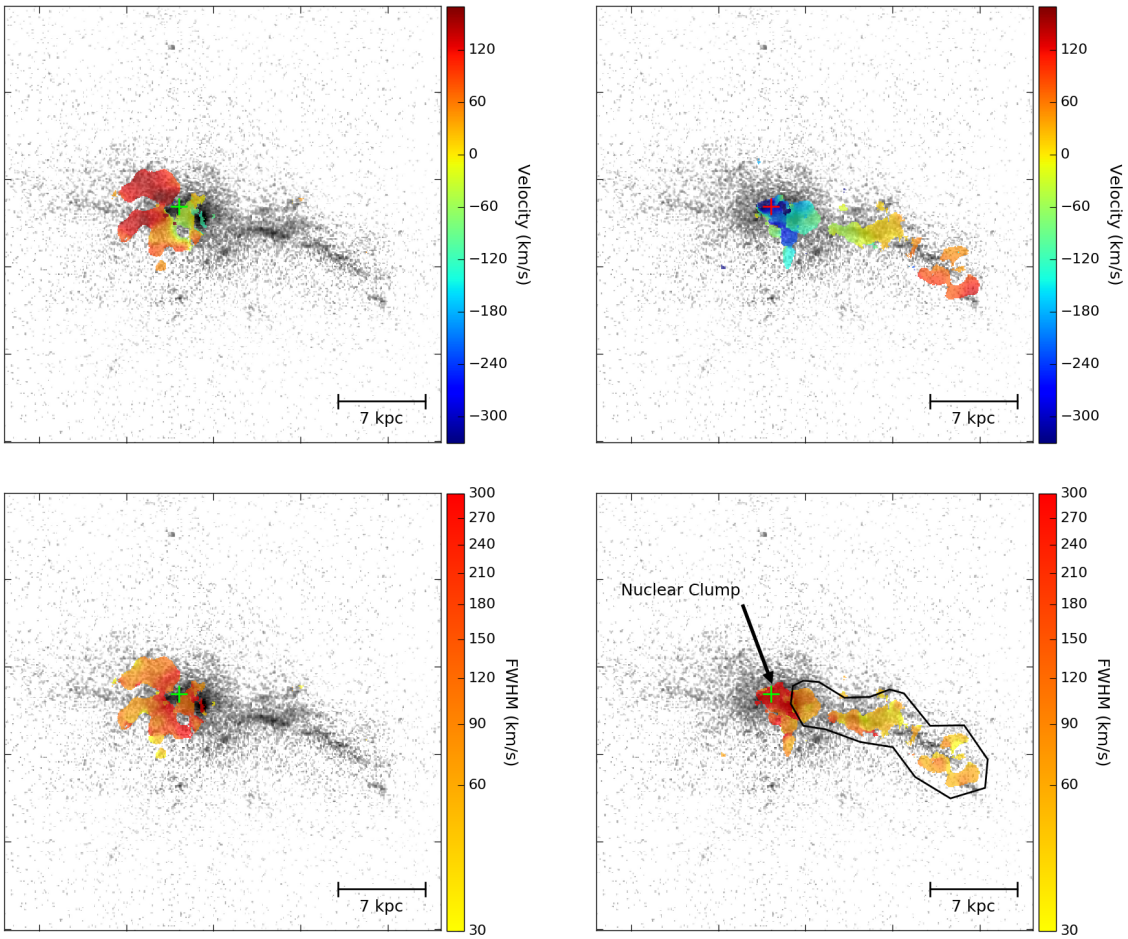

Figure 4.4: Maps of velocity centroid (top) and FWHM (bottom) overlaid on the HST ACS F165LP image. The emission from the filament and the broad, nuclear component were isolated in the right panels. The remaining emission, consisting of the redshifted clump to the NE and some central gas near the systemic velocity, is shown on the left. Two velocity components are present near the continuum source, which is indicated by the cross. The full extent of the filament, which extends into the central clump, is outlined in the lower right panel.

both the central and NE clumps, accounts for 80% ($1.5 \times 10^{10}\,M_\odot$) of the total mass. Most of this gas is concentrated within the central clump, with only 16% ($2.6 \times 10^9\,M_\odot$) located in the NE clump. The remaining 20% of molecular gas is contained within the middle and outer clumps of the filament. After including the contribution coming from the component within the central clump, the total filament mass is $4.8 \times 10^9\,M_\odot$, or about 25% of the total gas mass. The mass of the nuclear, blueshifted clump is best estimated from a fairly restrictive (3.5×2.6 kpc) region encompassing only the nuclear emission. A multi-component fit yields a total mass for the broad component of $6.5 \times 10^9\,M_\odot$. This is 40% of the central clump, and 35% of the total gas mass. The mass of the redshifted kinematic component is complicated by overlapping contributions from the broad component and inner filaments that make up the central clump. Removing these contributions yields a total mass of $7.2 \times 10^9\,M_\odot$ for the redshifted structure.

Hosting both blueshifted and redshifted emission, the nuclear velocity structure could be interpreted as rotation. The filament, whose velocity gradient has the opposite sign, is dynamically distinct from the nuclear gas. However, the morphology of the nuclear gas does not resemble a rotationally-supported equilibrium structure, such as a disk. An equilibrium structure should straddle the gravitational center. Instead, the blueshifted emission is exclusively coincident with the nucleus, while the redshifted emission extends to both the NE and SE. Any resolved equilibrium structure would need to be in the early stages of formation. The linewidth of the blueshifted emission also differs significantly from the redshifted gas, indicating that it is not part of a common structure.

The broad linewidth of the gas coincident with the continuum point source may indicate that it has settled within the underlying potential. If it is an unresolved disk then it must be < 1.2 kpc in diameter, much smaller than the 7 kpc disk observed in Hydra A (Hamer et al., 2014). However, the velocity of this component is ~ -250 km s^{-1}, making it the most blueshifted gas in the system. Since this would also be located at the kinematic center of the BCG, all of the remaining gas would be redshifted in comparison. This is unlikely to be the case. If the gas has only recently formed, then the entirely redshifted emission implies a highly asymmetric origin of the cold gas. Alternatively, if some of the gas has survived for longer than a dynamical time, the gas velocities should have begun to center on the systemic velocity of the BCG, and by extension the nuclear disk.

4.3.5 Spatial Correlation with UV Emission

In Fig. 4.5 we present a direct comparison between the CO(3-2) emission and UV continuum. The distribution of molecular gas and young stars are qualitatively similar on large

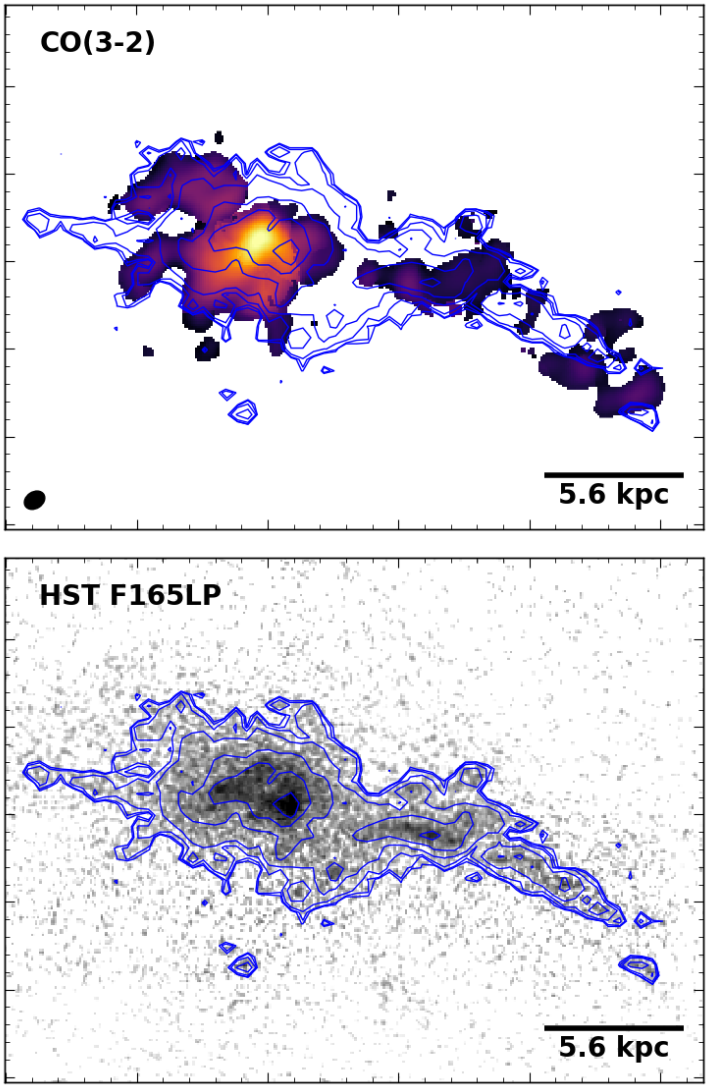

Figure 4.5: The ALMA CO(3-2) (top) and HST F165LP (UV; bottom) images that were shown in Fig. 4.3, but overlaid with contours of the UV emission.

scales. Both are brightest near the galactic center and contain a filament extending to the SW.

It is important to note that the HST F165LP image was shifted manually in order to align the UV and CO emission both in the center and along the filament. Spatial offsets between the molecular gas and young stars could be present, but would be missed due to this manual alignment. However, the UV and CO morphologies agree relatively well. Additional shifting of the UV emission to better line up certain features would generally degrade the correlation between other structures.

For this reason comparisons on smaller scales should be taken with caution. Nevertheless, we note that the molecular gas and star formation in the outer portions of the filament are possibly anti-correlated. The three clumps within the outer filament are not coincident with enhanced UV emission. Instead, a clump of UV emission lies just beyond the outermost molecular clump. Similarly, UV emission connects the middle and outer molecular clumps, passing in between two of the molecular clumps in the outer filament. This anti-correlation may indicate that active star formation along the filament has already churned through the local gas supply.

4.4 Discussion

4.4.1 Gas Origin

The massive molecular gas reservoirs in BCGs are strongly linked to condensation from the hot atmosphere. Most directly, molecular gas and star formation are only present in clusters where the central cooling times fall below ~ 1 Gyr (Rafferty et al., 2008; Pulido et al., 2018). Rates of mass condensation in the hot atmosphere are also correlated with the star formation rate of the BCG (O'Dea et al., 2008). Both of these correlations indicate that the presence of molecular gas in a central cluster galaxy depends on the atmospheric properties of its host cluster.

Alternative supplies of molecular gas include minor mergers and stripping. The frequency of minor mergers and the efficiency of tidal stripping are not affected by the presence of a cool core. Moreover, roughly 85% of elliptical galaxies have $< 10^8$ $M_\odot$ of molecular gas (Young et al., 2011). Accumulating 10^{10} $M_\odot$ of cold gas, as observed in several systems, would take hundreds to thousands of mergers. Ram pressure stripping, on the other hand, is potentially linked to the presence of cool cores because it is more efficient in their dense cores. However, small spirals will be stripped well outside of the central galaxy and high

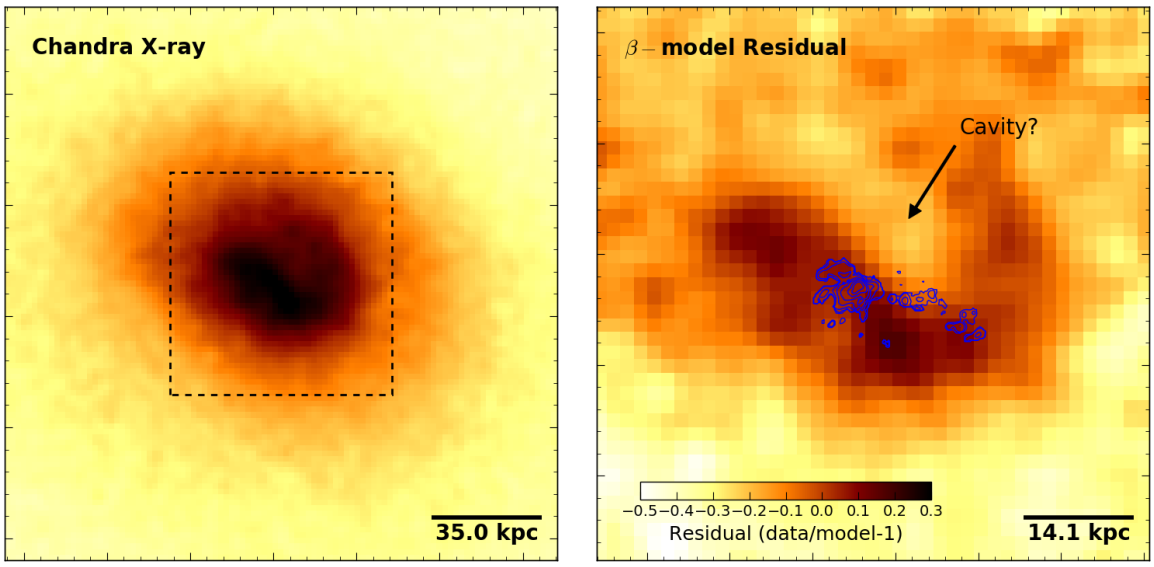

Figure 4.6: Left: Chandra X-ray image in the $0.5 - 7$ keV band. The dashed box indicates the field-of-view for the right panel. Right: Residual X-ray surface brightness after subtracting a double β-model. Contours of the CO(3-2) emission are overlaid.

mass systems (LIRGs, ULIRGs) will remain bound (Kirkpatrick et al., 2009). Large spiral galaxies on nearly radial trajectories will deposit their gas within the central 10 kpc, but these are rare and each galaxy should only contribute a few $\times 10^8\,M_\odot$ of molecular gas. As a result, minor mergers, tidal stripping, and ram pressure stripping are all unlikely to be viable mechanisms for supplying the rich reservoir of cold gas in BCGs.

RXCJ1504 has one of the most extreme cooling cores ever discovered. Its hot atmosphere is condensing at a rate of $\sim 80\,M_\odot\ \mathrm{yr}^{-1}$ (Ogrean et al., 2010), which can supply its $1.9 \times 10^{10}\,M_\odot$ of molecular gas in 2.4×10^8 yr. This is well-matched to both the central cooling time, 2.3×10^8 yr, and the timescale to be consumed by star formation, 1.4×10^8 yr (see Section 4.4.3). The total amount of hot gas within the central 15 kpc, $4 \times 10^{10}\,M_\odot$, also exceeds the total molecular gas mass. Condensation of the hot atmosphere can therefore fuel the production of molecular gas.

Here we explore the potential triggers that could result in the formation of the molecular filament. These processes must produce nonlinear density perturbations in the cluster atmosphere, which then become thermally unstable and condense into the observed molecular gas (Pizzolato & Soker, 2005, 2010).

A *Chandra* X-ray image of the cluster from a combined 160 ks exposure (observation IDs

4935, 5793, 17197, 17669, and 17670) is shown in Fig. 4.6. The X-ray surface brightness profile was extracted from elliptical annuli centered on the optical centroid of the BCG with 2.5″ (8.8 kpc) widths along their major axis. The axis ratio (1.2) and position angle (53° east of north) were determined qualitatively. The profile was well-fit by a double-β model (Cavaliere & Fusco-Femiano, 1976), which was then subtracted from the original image to produce the residual map in the right panel of Fig. 4.6. Contours of the CO(3-2) emission are overlaid on this image.

A positive residual straddles the central clump of molecular gas. It is oriented from NE to SW and contains two bright peaks located about 10 kpc from the BCG nucleus. The positive residual curves northward at the SW tail of this filament, forming an arc that is associated with what could be an X-ray cavity, as indicated in Fig. 4.6 (right). The residual image reproduces the sloshing fronts identified in a single 40 ks *Chandra* exposure (Giacintucci et al., 2011). The southern front is demarcated by the sharp drop in X-ray surface brightness in the lower-left area of Fig. 4.6 (right). The northwestern edge is located just outside of the field of view of the residual image. The cavity was not detected in the previous *Chandra* analysis, likely due to the lower signal-to-noise that was available.

The feature identified as a potential cavity is poorly defined, so it is not clear if it is a real cavity. Archival observations of the radio continuum are low resolution, so cannot be used to identify any synchrotron emission originating within the surface brightness depression. However, X-ray cavities are nearly ubiquitous in cool core clusters. At least 70% of the clusters in the Brightest 55 sample host radio bubbles (Dunn et al., 2005). Accounting for the presence of cavities that are undetected due to projection effects can boost this fraction to $\sim 100\%$ (Bîrzan et al., 2012). Since RXCJ1504 is one of the most extreme cooling cores known, it is likely that it hosts AGN activity. In addition, an analysis of a volume-limited sample showed that all sources with at least 30000 X-ray counts within the central 20 kpc have clearly detected cavities (Panagoulia et al., 2014). The central 20 kpc of RXCJ1504 contains 40000 X-ray counts, suggesting that the identified surface brightness depression is a real cavity.

If the identified feature does correspond to a real cavity, then its projected size is approximately 10×7 kpc. At a projected distance of 10 kpc from the BCG nucleus, the gas temperature, density, and pressure are 4.57 keV, 0.15 cm^{-3}, and 2×10^{-9} erg cm^{-3}, respectively. The corresponding cavity enthalpy, buoyancy time, and jet power are 5.6×10^{59} erg, 20 Myr, and 9.1×10^{44} erg s^{-1}, respectively. These properties were calculated following the standard analysis (see e.g. Bîrzan et al., 2004; Rafferty et al., 2006; Vantyghem et al., 2014). Note that the gravitational acceleration used to compute the buoyancy time was determined from the Hernquist profile in Section 4.4.2, as the cavity is sufficiently close to the BCG nucleus.

For comparison, the cavity power can also be estimated from the scaling relation (Cavagnolo et al., 2010)

$$\log P_{\rm cav} = 0.75(\pm 0.14) \log P_{1.4} + 1.91(\pm 0.18). \tag{4.3}$$

Here $P_{\rm cav}$ is in units of 10^{42} erg s^{-1} and $P_{1.4}$, the radio power at 1.4 GHz, is in 10^{40} erg s^{-1}. The RXCJ1504 BCG contains a 42 mJy point source at 1.4 GHz (Bauer et al., 2000; Giacintucci et al., 2011). The corresponding 1.4 GHz luminosity is 5.8×10^{24} W Hz^{-1} and the power is 8×10^{40} erg s^{-1}. The scaling relation then yields a cavity power of $(3.9 \pm 2.0) \times 10^{44}$ erg s^{-1}. This is 2.5σ smaller than the cavity power derived from the X-ray observation.

Merger

While repeated minor mergers with donor galaxies are unable to supply the molecular gas themselves, the passage of a galaxy through the cluster core may perturb the hot atmosphere enough to instigate condensation. Several small galaxies are situated along the axis of the filament, the closest of which is 25 kpc east of the BCG. This galaxy is moving at approximately 65 km s^{-1} with respect to the BCG, so it is a cluster member and could have interacted with the BCG in the past. However, the molecular gas extends only 5 kpc east of the BCG nucleus. Either the cluster atmosphere immediately trailing the galaxy has not had time to condense, or this galaxy is unrelated to the molecular gas. The latter is more likely. Galaxies pass through cluster cores only rarely, so the high fraction of gas-rich BCGs in cool core clusters is likely unrelated to the motion of the member galaxies. Additionally, the molecular gas distributions in other cool core clusters observed by ALMA were not explained by perturbations caused by member galaxies. A merger-induced formation process for the molecular gas is unlikely.

Stimulated Cooling

Previous ALMA observations of BCGs have revealed molecular filaments that are exclusively oriented toward X-ray cavities (e.g. McNamara et al., 2014; Russell et al., 2016, 2017a; Vantyghem et al., 2016). The velocities along these filaments lie below the terminal velocity of a rising bubble, indicating that the filaments may be caught in the updraft of the buoyantly rising bubble. The cold gas is either lifted directly from a reservoir at the center of the BCG, or it has condensed in situ from the intracluster medium that has been uplifted. In the "stimulated cooling" conjecture, low entropy gas from the cluster core is

lifted by a radio bubble to a radius where its cooling time is shorter than the time required to fall to its equilibrium position (McNamara et al., 2016). The low velocities observed in molecular filaments indicate that this infall time, t_I, is longer than the free-fall time. A thermal instability would then ensue when $t_{\rm cool}/t_I \lesssim 1$.

The molecular gas in RXCJ1504 is mostly confined to the central 5 kpc, with a filament extending 20 kpc to the WSW. The velocity gradient along the filament resembles those oriented behind X-ray cavities in other systems. As seen in the right panel of Fig. 4.6, the molecular filament is associated with both the putative X-ray cavity as well as a region of enhanced X-ray emission. Other BCGs also exhibit a spatial correlation between molecular and X-ray filaments (e.g. Vantyghem et al., 2016). However, those filaments generally trail directly behind X-ray cavities, which is not the case in RXCJ1504. Instead, the cavity is located very close to the cluster core and the filament extends along its inner edge.

The poor spatial correlation between the filament and the cavity may be indicative of complex hot phase dynamics within the cluster core. Giacintucci et al. (2011) identified two cold fronts that were likely created by the sloshing of the cool core. This suggests that the BCG is in motion with respect to the cluster potential. The combination of sloshing and continued AGN activity could stir the hot atmosphere in the cluster core. Nonlinear overdensities developed in this medium would not necessarily trail directly behind the cavity.

The maximum amount of gas that can be lifted by a cavity is limited by the amount of gas that it has displaced. The mass of hot gas that has been displaced by the putative cavity is $M_{\rm disp} = 2\mu m_p n_e V \approx 10^{10}\,{\rm M}_\odot$, where n_e is the gas density, V is the cavity volume, m_p is the proton mass, and $\mu = 0.62$. The factor of two accounts for protons and electrons (i.e. $n = n_e + n_p$). Since the total molecular gas mass within the filament is $4.8 \times 10^9\,{\rm M}_\odot$, the cavity could have lifted enough low entropy gas to form the filament. This requires an efficient coupling between the cavity and filament, but a similar efficiency is measured in other BCGs (e.g. McNamara et al., 2014; Russell et al., 2017a). Its proximity to the cluster core also suggests that the cavity may still be influencing the dynamics of the filament. The filament is not purely radial. The middle portion is situated along the inner edge of the cavity, bending toward the SW at higher altitudes. The non-radial directionality of the filament may therefore arise because the inner portion of the filament is caught in an updraft behind the cavity.

As discussed in Section 4.4.1, gas condensation out of the hot atmosphere would take 2.4×10^8 yr to form the total molecular gas supply. The putative cavity is likely only involved in stimulating the production of the filament, with the central gas originating from an older cycle of cooling. Forming the filament alone, which accounts for about 25%

of the molecular gas mass, would take 60 Myr. This is several times longer than the age of the putative cavity, estimated by its buoyant rise time to be 20 Myr. The AGN outburst therefore does not have enough time to stimulate the formation of the filament through purely radiative cooling. Interpenetration of hot particles into molecular clouds can lead to non-radiative cooling, alleviating this tension (Fabian et al., 2011). This process powers the nebular emission (Ferland et al., 2009), heating the cold gas and cooling the hot gas.

Overall, the case for stimulated cooling is weaker in RXCJ1504 than in several other BCGs. Nevertheless, the cluster core exhibits the AGN activity that is expected to uplift low entropy gas. Sloshing motions can also promote thermally unstable cooling. Much like uplift, they displace the central, low entropy gas to larger altitudes.

4.4.2 Motion Along the Filament

Gravitational infall and outflows generated by AGN activity are both plausible explanations for the smooth velocity gradient along the filament. Infall is perhaps the most natural explanation, as molecular clouds condensing from the surrounding hot atmosphere should then rain back onto the central galaxy. On the other hand, it is the gas that has been uplifted by X-ray cavities that is expected to become thermally unstable. Recently formed clouds should trace the velocity of the uplifted gas, so should initially be outflowing.

A clump reaches its terminal velocity, v_T, when the ram pressure of the medium it moves through balances its weight:

$$\rho_0 v_T^2 A = \Delta\rho V g. \tag{4.4}$$

Here ρ_0 is the density of the surrounding medium, $\Delta\rho = \rho - \rho_0$ is the excess density in the clump, A and V are the effective area and volume of the clump, respectively, and $g = v_K^2/R$ is the gravitational acceleration. Writing $V/A \approx r$ as the approximate size of the clump and rearranging yields

$$\frac{v_T}{v_K} = \sqrt{\left(\frac{\rho}{\rho_0} - 1\right)\frac{r}{R}}. \tag{4.5}$$

If $v_T \geq v_K$ then the clump will be in free-fall, as it never reaches its terminal speed.

The outer filament is comprised of three distinct clumps. Each clump contains approximately 1/3 of the total molecular gas mass in the outer filament, so we take $M_{\rm mol} = 5.7\times10^8\,{\rm M}_\odot$ for a single one of these clumps. The outermost clump is located $R = 16.8$ kpc from the BCG nucleus and is ≈ 1.4 kpc in radius. Conservatively assuming that the molecular gas mass fills its entire volume, the mean clump density is $4 \times 10^{-24}\,{\rm g\,cm^{-3}}$. At a

radius of 16.8 kpc the mean ambient density is $0.14\,\mathrm{cm}^{-3}$, corresponding to a mass density of $\rho_0 = 2\mu m_p n_e = 3 \times 10^{-25}\,\mathrm{g\,cm}^{-3}$. This yields a terminal velocity $v_T \approx v_K$. The outermost clump should therefore be experiencing free-fall.

Repeating this calculation for the middle filament similarly suggests that the molecular clouds should be in free-fall. The total molecular gas mass within the middle filament is $1.8 \times 10^9\,\mathrm{M}_\odot$. The dimensions of this region measure 4.9 kpc $\times$ 2.5 kpc. We assume that the projected length is the same as the width of the filament, 2.5 kpc. At a radius of $R = 10$ kpc the ambient density is $0.156\,\mathrm{cm}^{-3}$. The resulting terminal speed is $v_T \approx 1.25 v_K$. Real molecular clouds are likely smaller and much denser than we have assumed here. The terminal velocities of these clouds would be even larger than we have calculated. The molecular gas in RXCJ1504 should therefore be decoupled from the hot atmosphere, with only gravity dictating its acceleration.

A position-velocity diagram was extracted from the CO(3-2) image using the Python package PVExtractor. The path used to extract the spectra traced the entire length of the filament, passing through the center and extending to the NE clump. Spectra were extracted in 0.6″ (2.1 kpc) intervals along this path, each with a width of 0.75″ (2.6 kpc). The regions are shown in Fig. 4.7. The spectra were modelled in the same way as described in Section 4.3.2. Position-velocity and position-FWHM curves are shown in Fig. 4.8. Positive distances are in the direction of the filament. The central region was best-fit by two velocity components. To distinguish the second component between the two panels, it has been plotted as an open circle.

The position-velocity curve clearly shows the smooth velocity gradient along the filament ($d \gtrsim 2$ kpc). Over the length of the filament the FWHM varies from 45 to 110 km s^{-1}, with regions closer to the nucleus exhibiting broader linewidths. In the central region, which was fit with two velocity components, the velocity of one component appears to connect smoothly to the velocity profile of the filament. However, the FWHM of this component is much broader than the gas in the filament. For this reason we exclude the central region when referring to the filament. NE of the center (negative distances), the velocity is constant at ~ 160 km s^{-1} while the FWHM is larger closer to the nucleus.

The velocity along the filament varies smoothly from -105 km s^{-1} near the nucleus to 120 km s^{-1} at its farthest extent. With a total projected length of 14 kpc, the velocity gradient is 16 km s^{-1} kpc^{-1}. The mass flow rate can be approximated by assuming that the filament was initially a point mass that has stretched as the gas flows toward the galactic center. The inner and outer portions of the filament are moving apart at a speed Δv, which is the peak-to-peak velocity change along the filament. The mass flow rate is

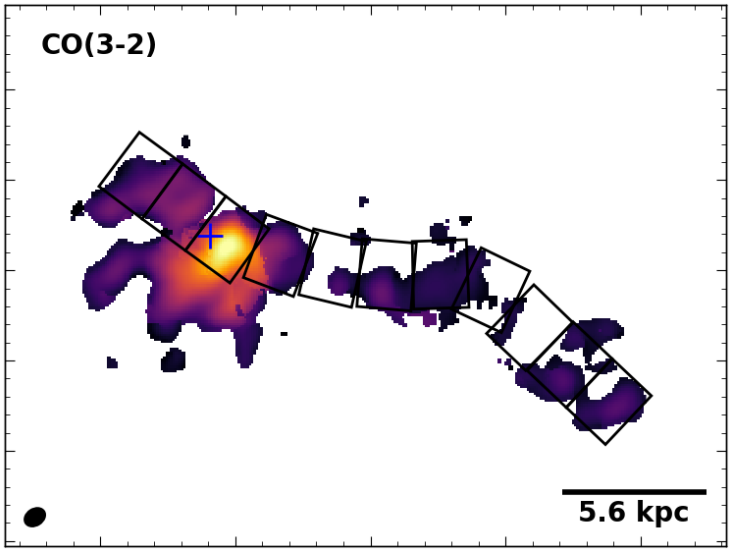

Figure 4.7: Regions used to extract the position-velocity diagram overlaid on the integrated CO(3-2) map.

then

$$\frac{\dot{M}_{\rm flow}}{\rm M_\odot\ yr^{-1}} = \left(\frac{M_{\rm fil}}{10^9\,\rm M_\odot}\right)\left(\frac{\Delta v}{\rm km\ s^{-1}}\right)\left(\frac{L_{\rm fil}}{\rm kpc}\right)^{-1}, \tag{4.6}$$

where $M_{\rm fil}$ and $L_{\rm fil}$ are the mass and length of the filament, respectively. From the masses tabulated in Table 4.1, the total filament mass is $4.8\times10^9\,\rm M_\odot$. From Eqn. 4.6 we estimate a mass flow rate of $75\,\rm M_\odot\ yr^{-1}$.

To test models of gravitational infall, the stellar mass of the BCG was first measured following the prescription of Hogan et al. (2017a). We adopted the 2MASS $K-$band magnitude K_{20}, which is defined at a radius ($r_{K,20}$) within which the mean brightness is 20 mag arcsec^{-2}. This magnitude was corrected for galactic extinction (Schlafly & Finkbeiner, 2011) as well as evolution and the K-correction (Poggianti, 1997). The stellar mass within $r_{K,20}$ (24.6 kpc) was then determined from (Bell et al., 2003)

$$\log\frac{M}{L_K} = -0.206 + 0.135\ (B-V). \tag{4.7}$$

With a $B-V$ colour of 0.45 (Véron-Cetty & Véron, 2010) and $K_{20,\rm corr} = 13.786$, the total stellar mass is $5\times10^{11}\,\rm M_\odot$.

For our models of gravitational infall, we assume that the molecular clouds in the filament are in free-fall within the gravitational potential of the BCG. Describing the BCG

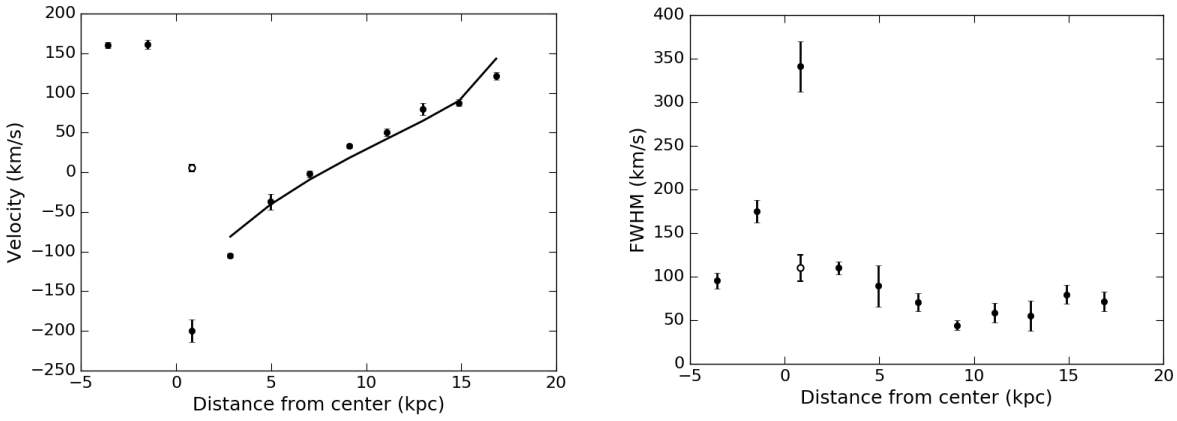

Figure 4.8: Position-velocity and position-FWHM curves extracted from a 0.75″ wide line segment tracing the filament and extending to the redshifted clump NE of center. The positions run from NE to SW, with positive distances corresponding to SW of center. The open circle indicates a second velocity component within a region. Various models of infall were fit to the points corresponding to the filament, as described in the text.

with a Hernquist profile (Hernquist, 1990), the velocity of a cloud dropped from radius r_0 is given by

$$v(r)^2 = v(r_0)^2 + 2GM\left(\frac{1}{r+a} - \frac{1}{r_0+a}\right). \tag{4.8}$$

Here M is the total stellar mass of the BCG and $a = 5.2$ kpc is a scale factor determined from the galaxy's half-light radius ($R_e \approx 1.8153a$). For a hydrostatic atmosphere a condensing cloud should initially be at rest with respect to the ICM, so we take $v(r_0) = 0$. Similarly, initially outflowing gas will eventually slow and come to rest before falling back onto the BCG. Accounting for the inclination of the filament (i) with respect to the plane of the sky and a bulk offset between the BCG and ICM ($v_{\rm ICM}$), the expected line-of-sight velocity is

$$v_{\rm obs}(r) = v(r)\sin i + v_{\rm ICM}. \tag{4.9}$$

The velocity profile of the filament is fitted with this expression. $v_{\rm ICM}$ and i are allowed to vary, while r_0 is fixed to the maximum radial extent of the filament (17.5 kpc).

The best-fitting velocity profile is overlaid on the position-velocity diagram in Fig. 4.8. Dropping a molecular cloud from $r_0 = 17.5$ kpc requires an inclination angle of $-22°$ with a bulk offset of $v_{\rm ICM} = 140$ km s^{-1}. This model underestimates the slope of the velocity profile, and would likely provide a very poor prediction at any extrapolated

distances. Allowing r_0 to vary provides a better fit to the velocity profile, but requires an $r_0 \approx 50$ kpc, which is roughly double the maximum extent of the nebular line emission (Ogrean et al., 2010). Thus, this simplistic infall model implies that, if the gas along the filament is in free-fall, it must lie within $\sim 20^\circ$ of the plane of the sky.

The BCG luminosity used in this analysis has been truncated at $r_{K,20}$, so the corresponding mass likely underestimates the total stellar mass. An increase in M is degenerate with a decrease in the magnitude of the inclination angle. The filament would then be located even closer to the plane of the sky. Using a singular isothermal sphere instead of a Hernquist profile eliminates the dependency on $r_{K,20}$, as the ratio M/r that defines the potential is a constant. The best-fitting velocity profile for this potential is indistinguishable from the Hernquist profile, also requiring the same inclination angle (for fixed r_0).

The requirement that molecular filaments in free-fall must lie close to the plane of the sky is unsettlingly common in BCGs. In virtually all BCGs observed with ALMA, the linewidth of the ensemble molecular gas distribution lies well below the stellar velocity dispersion. Where molecular filaments have been detected, the inclination angles are comparable to those measured here (e.g. Lim et al., 2008; Russell et al., 2016, 2017a; Vantyghem et al., 2016). Moreover, the filaments in several systems do not exhibit velocity gradients, indicating that they are dynamically young and are not currently raining back onto the central galaxy (e.g. Gendron-Marsolais et al. 2018; Tremblay et al. in prep). The paucity of high velocity gas suggests that, despite their high densities, the molecular clouds in BCGs are not in free-fall.

High resolution X-ray spectroscopy of the Perseus cluster obtained by *Hitomi* also suggests that molecular clouds are not free-falling. The velocities of the molecular gas are consistent with the bulk shear measured in the hot atmosphere, suggesting that the molecular gas moves together with the hot atmosphere (Hitomi Collaboration et al., 2016). Ram pressure therefore still plays a role in dictating the motion of molecular clouds. This result is also found in simulations, which measure linewidths that are consistent with observations (e.g. Prasad et al., 2015; Li et al., 2017; Gaspari et al., 2018).

Several factors can alleviate the tension between our simple terminal velocity model and the apparent lack of free-falling clouds in both observations and simulations. First, the average cloud densities may be lower than is implied by the molecular gas alone. The correlation between molecular gas and soft X-ray emission (e.g. Fabian et al., 2006) suggests that molecular gas may be encased by a warm-hot envelope of lower density gas, potentially tethered together by magnetic fields (Fabian et al., 2008; Russell et al., 2016). This would reduce the mean cloud densities and increase their cross-section, making them more susceptible to ram pressure. Our model also assumes that the ICM is at

rest with respect to the BCG. An AGN-driven wind would counteract the motion of the molecular clouds, increasing the ram pressure exerted on the clouds by increasing their relative velocity.

Both of these effects were explored analytically by Li et al. (2018), using the filaments in Perseus (Fabian et al., 2008) as a test case. Without any modifications, the filament density of $n = 2$ cm^{-3} would result in a terminal velocity of ~ 1000 km s^{-1}, well above the observed velocities. Reducing the cloud density by a factor of 3 and introducing an AGN-driven brings the predicted velocities into agreement with observations. Thus, although the cloud densities in RXCJ1504 imply that they should be moving ballistically, the presence of both a warm-hot envelope and an AGN-driven wind can reduce the terminal velocity significantly.

4.4.3 Star Formation Along the Filament

The total extinction-corrected star formation rate (SFR) within the central galaxy was measured using NUV GALEX observations (rest-frame FUV) to be $136\,M_\odot$ yr^{-1} (Ogrean et al., 2010). Applying the correction for the UV-upturn used in the CLASH BCG sample (e.g. Donahue et al., 2015; Fogarty et al., 2015) had a negligible effect on this SFR. Assuming that the current SFR persists, the $1.9 \times 10^{10}\,M_\odot$ of cold gas in the BCG will be consumed in 1.4×10^8 yr. This consumption time ($M_{\rm mol}$/SFR) is comparable to those of starbursts and other BCGs (e.g. Donahue et al., 2015).

We used this global SFR to calibrate local measurements along the filament. The FUV count rates in the HST F165LP image were extracted from the regions shown in Fig. 4.9 (upper left), which were background-subtracted using a large, source-free region within the field of view. The FUV count rate was also extracted from a large box containing all of the observed emission. Local SFRs were then computed by assuming that the UV count rates translate linearly to SFR (e.g. Kennicutt, 1998; Salim et al., 2007), with the total UV count rate fixed to the global SFR. Thus the SFR within each region is the ratio of its UV count rate to the total UV count rate multiplied by the global SFR. Note that the total UV luminosity was converted to a global SFR using the Salim et al. (2007) relation, which assumes a Chabrier IMF and is 30% lower than the Kennicutt (1998) conversion.

The quoted SFR has been corrected for both Galactic extinction and dust extinction intrinsic to the BCG. No attempt has been made to correct for local variations in dust extinction. Based on the maps presented in Ogrean et al. (2010), the SFR in the nucleus may be underestimated by $\sim 40\%$ while the SFR at large radii may be overestimated by $\sim 20\%$. Throughout this work we take the SFR uncertainty to be a factor of two,

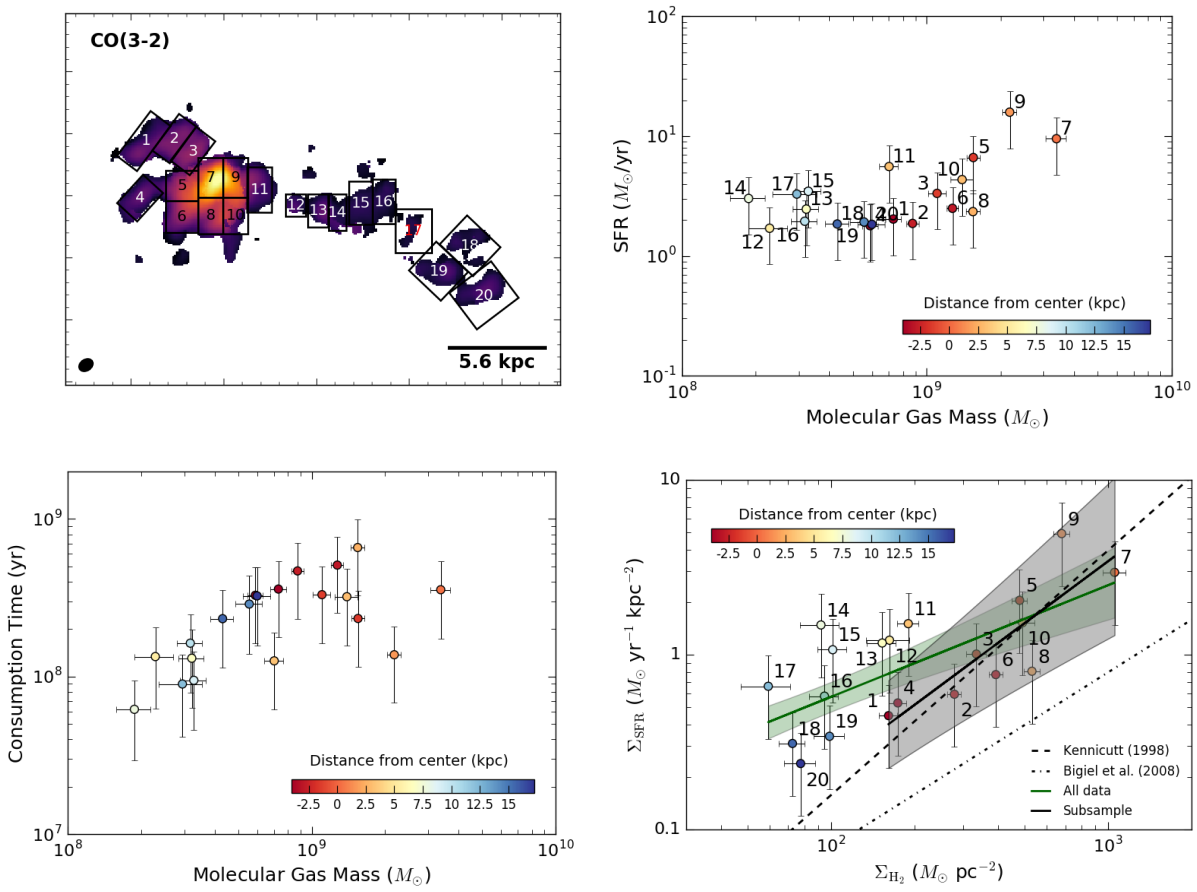

Figure 4.9: The relationship between molecular gas mass and star formation rate throughout the entire gas distribution. The top-left panel shows the regions used to measure the molecular gas masses and star formation rates, overlaid on the integrated CO(3-2) map. The top-right panel shows the $M_{\rm mol} - {\rm SFR}$ relation. The bottom-left panel shows the local consumption timescale ($M_{\rm mol}$/SFR) as a function of molecular gas mass. The bottom-right panel expresses the SFR–$M_{\rm mol}$ relation in terms of surface densities. Each point is labelled with its identifier from the top-left panel, and is also coloured by its distance from the BCG nucleus. Negative distances correspond to points east of the nucleus. The bottom panel shows two fits to the $\Sigma_{\rm SFR} - \Sigma_{\rm H_2}$ relation. The first (green) includes all of the data. The second (gray) excludes regions 11–17, which correspond to the inner and middle portions of the filament. The shaded regions correspond to the 1σ error bounds for the best fits. The relations from Kennicutt (1998) and Bigiel et al. (2008) are also plotted.

which is the approximate accuracy of the SFR calibration. The statistical uncertainties in the local SFRs are small compared to the systematic uncertainty in the global SFR calibration. Spatial variations in dust extinction therefore shift the data points by less than their uncertainty.

Fig. 4.9 also presents the SFR and consumption timescale as a function of molecular gas mass, as well as the relation between star formation and molecular gas surface densities. Surface densities were determined by dividing the appropriate quantity by the area of the extraction region. Each point has been labelled according to the numbers shown in the upper-left panel of Fig. 4.9, and colour-coded by its distance from the BCG nucleus, with negative distances corresponding to eastward points.

The relationship between SFR and molecular gas mass is flat for $M_{\rm mol} < 10^9\,{\rm M}_\odot$, and increases approximately linearly for higher masses. These two regimes are well-separated by their location within the cluster. Regions with high $M_{\rm mol}$ are located at the center of the BCG, while the lower mass regions are situated along the filament. In the outer filament, which joins the flat and approximately linear regimes in the $M_{\rm mol}-{\rm SFR}$ relation, the molecular gas and UV emission are slightly offset (see Fig. 4.5). We have used regions large enough to include both the molecular gas and UV emission. Choosing instead regions that are confined to the molecular gas reduces the SFR so that it is consistent with the linear relation present at higher masses. The consumption timescale (middle panel) for the central gas is roughly constant, with a mean of $3.7 \pm 1.4 \times 10^8$ yr. Since the filamentary gas has a constant SFR, its consumption time increases with $M_{\rm mol}$, with a mean of $1.6 \pm 0.8 \times 10^8$ yr.

The star formation law in spiral and starburst galaxies is well-characterized by the Kennicutt-Schmidt (KS) relation (Kennicutt, 1998; Kennicutt & Evans, 2012), which takes the form

$$\left(\frac{\Sigma_{\rm SFR}}{{\rm M}_\odot\ {\rm yr}^{-1}\ {\rm kpc}^{-2}}\right) = 2.5 \times 10^{-4} \left(\frac{\Sigma_{\rm gas}}{{\rm M}_\odot\ {\rm pc}^{-2}}\right)^{1.4}. \tag{4.10}$$

This expression relates the gas (HI+H_2) surface density, $\Sigma_{\rm gas}$, to the SF surface density, $\Sigma_{\rm SFR}$, over 5 and 7 decades, respectively. When a dense gas tracer is used in lieu of the total gas surface density, the SF law scales linearly (Wu et al., 2005). This is because dense gas tracers probe the gas directly involved in star formation. Spatially resolved observations of spiral galaxies which use $\Sigma_{\rm H_2}$ alone have also recovered a linear scaling (Bigiel et al., 2008).

We have modelled the spatially resolved SF law in RXCJ1504 using the functional form

$$\left(\frac{\Sigma_{\rm SFR}}{{\rm M}_\odot\ {\rm yr}^{-1}\ {\rm kpc}^{-2}}\right) = A \left(\frac{\Sigma_{\rm H_2}}{100\,{\rm M}_\odot\ {\rm pc}^{-2}}\right)^N, \tag{4.11}$$

which uses the molecular gas surface density, Σ_{H_2}, instead of the total gas surface density. At the centers of clusters the confining pressure is high enough to convert $\gtrsim 95\%$ of the gas into molecular form (Blitz & Rosolowsky, 2006). The fits were conducted in log space using the LINMIX package in Python, which employs the Bayesian approach to linear regression described in Kelly (2007). By centering Σ_{H_2} at $100\,M_\odot$ pc^{-2} we obtain more appropriate uncertainties.

Fitting this SF law to the entire gas distribution yields $A = 0.58 \pm 0.11$ and $N = 0.64 \pm 0.18$. The best fit and its 1σ error bounds are shown in green in Fig. 4.9. This scaling is significantly flatter than the nominal $N = 1.4 \pm 0.2$ measured in spirals and starbursts. Restricting the fits to the central gas (regions 1–10) gives $A = 0.23 \pm 0.13$ and $N = 1.18 \pm 0.37$, shown as a black line with gray shaded area in Fig. 4.9. The large uncertainties result from the small dynamic range in Σ_{H_2}. This is consistent with both a KS and linear scaling. Overplotting the KS relation on Fig. 4.9 (dashed black line) passes directly through this subset of the data. Along the filament Σ_{SFR} is systematically higher. The clumps in the outer filament are marginally consistent with lying on the KS relation. Incorporating these regions (18–20) into the fit to the SF law yields $N = 0.98 \pm 0.18$. Σ_{SFR} along the middle filament is even higher, lying well above the mean KS relation with significant scatter.

The linear scaling measured between Σ_{SFR} and Σ_{H_2} in spiral galaxies (Bigiel et al., 2008) has also been plotted in Fig. 4.9. Although the scaling is consistent with that of the central gas, and is even better matched to the data when the outer filament is included in the fit, the normalization lies below that in RXCJ1504. Assuming that these systems share the same intrinsic SF law when expressed in terms of dense gas mass (i.e. $\Sigma_{SFR} \propto \Sigma_{dense}$), the difference between them can be attributed to the fraction of molecular gas concentrated within the dense cores. Reconciling the two normalizations requires that the fraction of gas in the dense cores is $3-4$ times higher in RXCJ1504 than in spirals. The additional confining pressure of the hot atmosphere could be responsible for compressing the molecular clouds. Indeed, the confining pressure dictates the conversion between atomic and molecular gas (e.g. Blitz & Rosolowsky, 2006), and should also influence the prevalence of dense clumps.

The enhanced SFR throughout the majority of the filament indicates that either it is not located on the KS relation or it is affected by systematic uncertainties. We cannot rule out either possibility with the existing data. In Section 4.3.5 we noted that the star formation and molecular gas do not coincide well in the middle and outer portions of the filament. Ongoing star formation could have consumed a portion of the local supply of molecular gas, leading to decreased molecular gas surface densities for the observed SFR. The primary systematic uncertainty is in the calibration of the molecular gas mass using

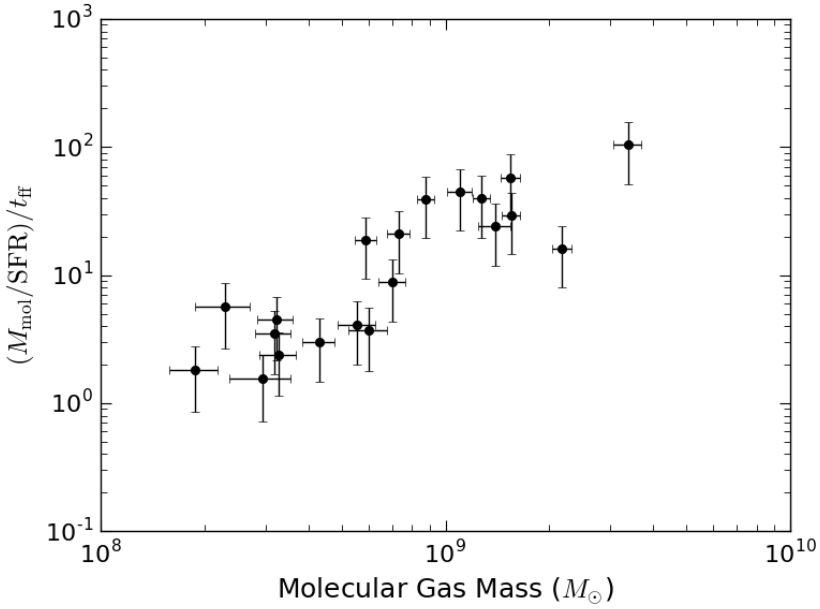

Figure 4.10: The ratio of the consumption timescale ($M_{\rm mol}$/SFR) to the free-fall time for each of the regions shown in Fig. 4.9.

the CO-to-H_2 conversion factor. Reconciling this population with the KS relation requires a four-fold increase in $M_{\rm mol}$. Elevated values of $X_{\rm CO}$ are often found in metal-poor molecular clouds. However, the middle and outer filaments should have similar metallicities as they presumably both formed from the hot atmosphere, but their star formation efficiencies differ.

In Fig. 4.10 we plot the ratio of consumption time to free-fall time for each of the regions shown in Fig. 4.9. The free-fall time was computed from the mass profile presented in Section 4.4.2. This neglects the contribution from the cluster halo, but is accurate within the central ~ 20 kpc, where the molecular gas is located. In all regions the consumption time is longer than the free-fall time. The ratio ranges from a factor of about 3 in the middle filament to ~ 40 within the core. This indicates that the molecular gas should be relatively long-lived. Star formation will not churn through the molecular gas before it falls back onto the BCG.

Other mechanisms, such as photodissociation or evaporation by collisions with hot electrons, could still deplete the molecular gas. Similarly, reduced infall velocities resulting from ram pressure drag, as discussed in Section 4.4.2, will lengthen the time taken for a

molecular cloud to fall onto the BCG. In the middle filament, where the consumption time is shortest, this can result in an infall time longer than the consumption time, so that the gas is consumed before it reaches the galactic center.

If the molecular gas survives long enough to return to the galactic center then it should settle into a rotationally-supported structure, such as a ring or disk, in a few dynamical times. The lack of such a structure suggests that the molecular gas is either dynamically young, having not yet had time to form a disk, or it is continually destroyed and reformed within the central galaxy, with the warmer phase experiencing enough non-gravitational motion to prevent it from forming a disk.

4.5 Conclusions

In this work we have presented ALMA observations of the CO(1-0) and CO(3-2) emission lines in the BCG of the RXC J1504-0248 galaxy cluster. This is one of the most extreme cool core clusters known. The BCG contains $1.9 \pm 0.1 \times 10^{10}\,\mathrm{M}_{\odot}$ of molecular gas that has a complex and disturbed morphology. It is distributed between three distinct structures. The first is a pair of redshifted clumps located within the central 5 kpc of the radio source at the galactic nucleus. Next, a 20 kpc long filament, containing $4.8 \times 10^{9}\,\mathrm{M}_{\odot}$ of cold gas, extends radially to the southwest of the nucleus. Finally, coincident with the AGN is an unresolved structure that is both broader (400 km s^{-1} FWHM) and more blueshifted ($v \approx -250$ km s^{-1}) than the rest of the gas in the BCG. We find no evidence of a long-lived, rotationally-supported structure. Instead, the gas is apparently dynamically young.

The molecular gas has almost certainly formed from the condensation of the intracluster medium. Alternative mechanisms, such as repeated minor mergers or tidal stripping, are implausible. Moreover, the presence of molecular gas and star formation in BCGs is linked to short central cooling times in their hot atmospheres. The molecular filament in RXCJ1504 is oriented along the edge of both a ridge of bright X-ray emission and a putative X-ray cavity. The cavity is energetic enough to stimulate the production of molecular gas by lifting low entropy gas from the cluster center to a radius where it becomes thermally unstable. As the filament does not trail directly behind the cavity, this interpretation is not as clear cut as in other BCGs with molecular filaments.

The velocity gradient along the filament is smooth and shallow. The velocity shear implies a flow rate of $75\,\mathrm{M}_{\odot}\,\mathrm{yr}^{-1}$. Models of gravitational free-fall can reproduce the velocity gradient as long as the filament lies within 20° of the plane of the sky. Assuming that the molecular gas in the outermost clumps fills their volume, then their mean densities

are too high to be slowed by ram pressure. However, low velocities and comparably shallow velocity gradients are common in BCGs. This suggests that molecular clouds are likely moving at sub-freefall velocities, instead of the filaments in many systems lying close to the plane of the sky. Lower terminal velocities can be attained if the mean density of the molecular clouds are reduced. This would be the case if the molecular clouds are tied to a warm, diffuse, volume-filling phase that is susceptible to ram pressure drag.

Filamentary blue and ultraviolet emission in the BCG traces a young stellar population formed at a rate of $136\,M_\odot\ yr^{-1}$. This emission is coincident with both the nuclear gas and the molecular filament. Persisting at its current rate, star formation will consume the molecular gas in 1.4×10^8 yr. This timescale is comparable to both the central cooling time (2.3×10^8 yr) and the time required for mass deposition from the intracluster medium to build up the observed reservoir of cold gas (2.4×10^8 yr). Star formation near the cluster core is consistent with the Kennicutt-Schmidt law. The filament exhibits increased star formation surface densities, possibly resulting from the consumption of a finite molecular gas supply. Alternatively, spatial variations in the CO-to-H_2 conversion factor could introduce systematic variations in the molecular gas surface density.

Chapter 5

An Enormous Molecular Gas Flow in the RXJ0821+0752 Galaxy Cluster

Abstract

We present recent *Chandra* X-ray observations of the RXJ0821.0+0752 galaxy cluster in addition to ALMA observations of the CO(1-0) and CO(3-2) line emission tracing the molecular gas in its central galaxy. All of the CO line emission, originating from a $10^{10}\,M_{\odot}$ molecular gas reservoir, is located several kpc away from the nucleus of the central galaxy. The cold gas is concentrated into two main clumps surrounded by a diffuse envelope. They form a wide filament coincident with a plume of bright X-ray emission emanating from the cluster core. This plume encompasses a putative X-ray cavity that is only large enough to have uplifted a few percent of the molecular gas. Unlike other brightest cluster galaxies, stimulated cooling, where X-ray cavities lift low entropy cluster gas until it becomes thermally unstable, cannot have produced the observed gas reservoir. Instead, the molecular gas has likely formed as a result of sloshing motions in the intracluster medium induced by a nearby galaxy. Sloshing can emulate uplift by dislodging gas from the galactic center. This gas has the shortest cooling time, so will condense if disrupted for long enough.

5.1 Introduction

Located at the centers of galaxy clusters, brightest cluster galaxies (BCGs) are the most massive and luminous galaxies known. They are giant ellipticals with extended, diffuse

stellar envelopes and stellar populations that are primarily old and dormant. However, those located in cool core clusters, where the central atmospheric cooling time falls below ~ 1 Gyr, are replete with cold gas and star formation. Their molecular gas masses, which can exceed $10^{10}\,M_\odot$, surpass those of gas-rich spirals (Edge, 2001; Edge et al., 2002; Edge & Frayer, 2003; Salomé & Combes, 2003). Star formation proceeding at rates of several to several hundred solar masses per year (e.g. McNamara, 2004; O'Dea et al., 2008; McDonald et al., 2011; Donahue et al., 2015; Tremblay et al., 2015; McDonald et al., 2018) place BCGs among starbursts on the Kennicutt-Schmidt relation (Kennicutt, 1998; Kennicutt & Evans, 2012).

An abundance of observational evidence indicates that this cold gas and star formation originates from the condensation of the hot intracluster medium (ICM). Molecular gas is regularly associated with filamentary emission observed in Hα (e.g. Lynds, 1970; Heckman, 1981; Cowie et al., 1983; Hu et al., 1985; Crawford et al., 1999) and soft X-rays (e.g. Fabian et al., 2001, 2003; Werner et al., 2013; Walker et al., 2015), implying that BCGs contain multiphase gas spanning five decades in temperature. Moreover, molecular gas, nebular, emission, and star formation are observed preferentially when the central atmospheric cooling time falls below $\sim 5 \times 10^8$ yr, or equivalently when the entropy falls below 30 keV cm^2 (Cavagnolo et al., 2008; Rafferty et al., 2008; Hogan et al., 2017b; Pulido et al., 2018). Correlations between the rates of star formation and mass deposition from the ICM further support this picture (Egami et al., 2006; O'Dea et al., 2008).

Uninhibited cooling would result in hundreds to thousands of solar masses per year of gas condensing out of the ICM. Despite the wealth of evidence that the ICM is condensing, cooling ensues at only a few percent of the expected rate (Peterson & Fabian, 2006). Instead, active galactic nucleus (AGN) feedback injects heat into the surrounding atmosphere, regulating the rate of cooling (for reviews, see McNamara & Nulsen, 2007, 2012; Fabian, 2012). In the "radio-mode" mechanical feedback that operates in giant ellipticals and galaxy clusters, radio jets launched by the central AGN inflate bubbles (X-ray cavities), drive shock fronts, and generate sound waves in the hot atmosphere (e.g. McNamara et al., 2000; Blanton et al., 2001; Fabian et al., 2006). The power output by the AGN is closely coupled to the cooling rate (Bîrzan et al., 2004; Dunn & Fabian, 2006; Rafferty et al., 2006), implying that AGN can regulate the growth of their host galaxy over long timescales. AGN feedback is fueled through black hole accretion, likely of the molecular gas that has condensed from the hot atmosphere (Pizzolato & Soker, 2005; Gaspari et al., 2013; Li & Bryan, 2014a). This establishes a feedback loop, wherein the ICM cools and condenses into the cold gas that accretes onto the nuclear black hole and fuels the energetic outbursts that reheat the surrounding hot phase.

While AGN feedback primarily affects the volume-filling hot atmosphere, recent ob-

servations indicate that it couples to the dense molecular phase as well. Fast, jet-driven outflows of ionized and molecular gas have been detected in radio galaxies (Morganti et al., 2005; Nesvadba et al., 2006; Alatalo et al., 2011; Dasyra & Combes, 2011; Tadhunter et al., 2014; Morganti et al., 2015). Direct interactions between radio jets and molecular gas have also been observed in BCGs. The molecular gas in M87 is located at the truncation of the radio lobe, appearing to be either excited or destroyed by AGN activity (Simionescu et al., 2018). Jet-induced star formation is also observed in Centaurus A (Salomé et al., 2017). In A1795 the radio jet is projected along the inner edge of a curved molecular filament, suggesting that the jet has either deflected off of the molecular gas or the gas is entrained in the expanding radio bubble (Russell et al., 2017b).

A broader consensus is emerging that the formation of cold gas in BCGs is also stimulated by AGN activity. The molecular filaments identified with either ALMA observations or through their nebular emission extend radially away from the galactic center and frequently trail X-ray cavities (e.g. Conselice et al., 2001; Hatch et al., 2006; Salomé et al., 2006, 2011; Lim et al., 2012; McDonald et al., 2012a; McNamara et al., 2014; Russell et al., 2014, 2016, 2017a; Vantyghem et al., 2016, 2018). Either molecular clouds are lifted directly by X-ray cavities or they have condensed from thermally unstable, low entropy gas originally in the cluster core that has been lifted by the cavity (Revaz et al., 2008; McNamara et al., 2016). The shallow velocity gradients along the filaments suggest that the molecular clouds are supported against freefall, and are potentially pinned to the hot atmosphere via magnetic fields (Fabian et al., 2008; Russell et al., 2016, 2017a; Vantyghem et al., 2016, 2018). Moreover, the velocities are well below the stellar velocity dispersion, so are too slow to escape the central galaxy in an outflow. Indeed, redshifted absorption lines imply that clouds are returning in a circulating flow and accreting onto the central supermassive black hole (David et al., 2014; Tremblay et al., 2016).

Here we present a multi-wavelength analysis of the RXJ0821+0752 (hereafter RXJ0821) galaxy cluster. We present ALMA observations of the CO(1-0) and CO(3-2) rotational emission lines tracing the molecular gas in the central galaxy alongside a new 63.5 ks *Chandra* X-ray observation. These ALMA observations were first presented in Vantyghem et al. (2017, hereafter V17), which used the intensities of the emission lines, including the ^{13}CO(3-2) line, to estimate the CO-to-H_2 conversion factor for the first time in a BCG. In this work we focus on the morphology and kinematics of the molecular gas, relating it to features in the X-ray image.

RXJ0821 contains one of the most gas-rich BCGs known. A strong CO detection from the IRAM 30-m telescope implied a molecular gas mass of $2 \times 10^{10}\,M_\odot$ (Edge, 2001, corrected for cosmology). Follow-up observations with the OVRO interferometer marginally resolved the cold gas, showing an extension west of the BCG (Edge & Frayer, 2003). Emis-

sion from the $1-0$ S series lines of H_2 was detected in the BCG but not in the western extension (Edge et al., 2002). The central galaxy also hosts a luminous emission-line nebula ($L_{H\alpha} = 2.55 \times 10^{42}$ erg s^{-1} – Bayer-Kim et al., 2002; Hatch et al., 2007) and an infrared luminosity, $L_{IR} = 8.47 \times 10^{44}$ erg s^{-1}, that implies a star formation rate of $37\,M_\odot$ yr^{-1} (Quillen et al., 2008; O'Dea et al., 2008). Unlike many other cool core clusters, the radio source in RXJ0821 is exceptionally weak. At 5 GHz the flux density is 0.85 ± 0.07 mJy, making it the third weakest radio source in the Brightest Cluster Survey (Bayer-Kim et al., 2002; Hogan et al., 2015a). The radio source is also offset from the BCG nucleus by 2.7 kpc. RXJ0821 may be undergoing an evolutionary phase dominated by the cooling flow.

Throughout this work we assume a standard Λ-CDM cosmology with $H_0 = 70$ km s^{-1} Mpc^{-1}, $\Omega_{m,0} = 0.3$, and $\Omega_{\Lambda,0} = 0.7$. At the redshift of RXJ0821 ($z = 0.11087$; see Section 5.2.2), the angular scale is $1'' = 2.0$ kpc and the luminosity distance is 510 Mpc.

5.2 Observations and Data Reduction

5.2.1 Chandra

RXJ0821.0+0752 was observed for 29 ks on 2014-12-15 (ObsID 17194) and 37 ks on 2014-12-28 (ObsID 17563) using the ACIS-S3 detector on the *Chandra X-ray Observatory*. The observations were reprocessed using CIAO version 4.5 and CALDB version 4.6.7. We applied charge transfer inefficiency and time-dependent gain corrections to the level 1 event files, which were then filtered to remove photons with bad grades. Periods affected by flares were identified and filtered using the LC_CLEAN script. The final exposure time of the cleaned data was 63.5 ks.

The final background-subtracted image, shown in Fig. 5.1 (left), was created by reprojecting the observations to match the position of the longest exposure (ObsID 17563) and summing all events in the $0.5-7$ keV energy range. Point sources were identified and removed using WAVDETECT and confirmed via visual inspection. Blank-sky backgrounds were extracted for each observation, processed the same way as the events files, and reprojected to the corresponding position on the sky. The blank-sky backgrounds were normalized to match the observed count rate in the $9.5-12$ keV energy range.

5.2.2 ALMA

The ALMA observations of RXJ0821+0752 are described in detail in V17. Briefly, the observations targeted the CO(1-0) and CO(3-2) lines, which, located at redshifted frequencies of 103.848 GHz and 311.528 GHz, fell in Bands 3 and 7, respectively. The observations (Cycle 4, ID 2016.1.01269.S, PI McNamara) were conducted on 2016 Oct 30 (Band 3; 86.7 minutes on source) and Nov 4 and 2016 Oct 1 (Band 7; 22.7 minutes on source). An additional baseband in the Band 7 observation also covered the ^{13}CO(3-2) line at 297.827 GHz. The remaining three Band 3 basebands and two Band 7 basebands were used to measure the sub-mm continuum emission. Both observations employed 40 antennas, with baselines ranging from $18 - 1124$ m for Band 3 and $15 - 3247$ m for Band 7.

The observations were calibrated in CASA version 4.7.0 (McMullin et al., 2007) using the pipeline reduction scripts. Continuum-subtracted data cubes were created using UVCONTSUB and CLEAN. Images of the line emission were reconstructed using Briggs weighting with a robust parameter of 2. An additional *uv* tapering was used to smooth the CO(3-2) image on scales below 0.1 arcsec. The final CO(1-0) and CO(3-2) data cubes had synthesized beams of $0.61'' \times 0.59''$ (P.A. $-70.4°$) and $0.21'' \times 0.165''$ (P.A. $37.2°$), respectively. The CO(1-0) and CO(3-2) images were binned to 3 and 5 km s^{-1} velocity channels, respectively. The RMS noise in the line-free channels were 0.5 and 1.1 mJy beam^{-1}, respectively.

Systemic Velocity

Throughout this work we adopt a systemic redshift of $z = 0.11087 \pm 0.00004$, measured using the spatially integrated ALMA CO spectra. This is consistent with longslit ($z = 0.110 \pm 0.001$; Crawford et al., 1995) and *VIMOS* integral field unit ($z = 0.11088$; Hamer et al., 2016) observations of the Hα + [N II] complex. As each of these measurements probes either the molecular or ionized gas within the BCG, they do not necessarily reflect the systemic stellar velocity. Crawford et al. (1995) also detected stellar absorption lines, reporting the same redshift as for the emission lines. However, the high uncertainties (300 km s^{-1}) prohibit us from using this value for the systemic velocity. An accurate measurement of the relative velocity between the gas and stars is crucial in understanding gas flows. Since an accurate stellar velocity is absent, we measure our velocities in the rest frame of the gas and interpret any gas flows cautiously.

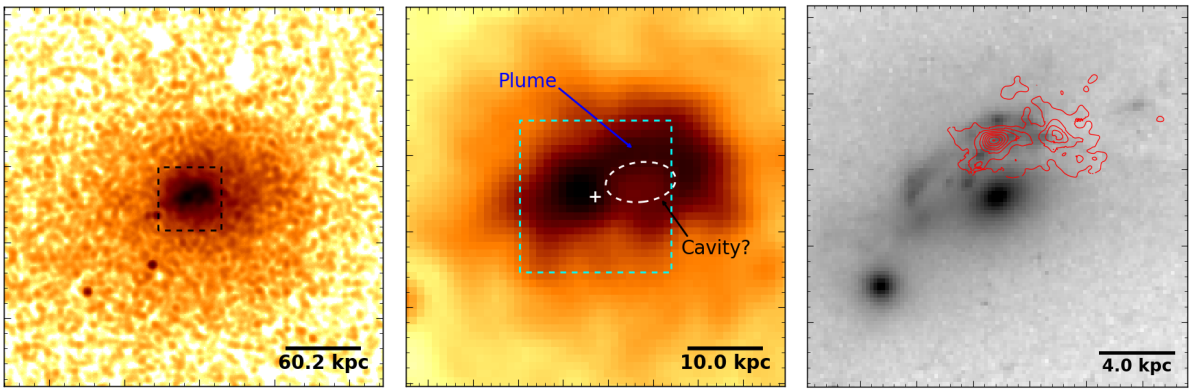

Figure 5.1: Background-subtracted *Chandra* X-ray surface brightness images (left and center) and an HST F606W optical image with contours of the CO(3-2) emission overlaid. The fields of view for the center and right panels are indicated by the dashed boxes in the left and center panels, respectively. The bright X-ray filament (plume) and putative X-ray cavity are indicated in the center panel.

5.3 Cluster X-ray Properties

In Fig. 1 we present the $0.5-7$ keV band *Chandra* X-ray image. On large scales the X-ray surface brightness is relatively smooth. No surface brightness edges indicative of shocks or cold fronts are evident in the image, although they may be present but not detected. Within the central 20 kpc the surface brightness distribution is more complex. An arc extends NW of the cluster center, curving southward after ~ 12 kpc. The elliptical surface brightness depression encompassed by this arc may correspond to an X-ray cavity. This is discussed further in Section 5.3.2.

5.3.1 Radial Profiles of Gas Properties

Spectra were extracted from eight annular regions extending out to 600 kpc. Each region had a minimum of 2500 net counts. The annuli were centered on the BCG nucleus as determined from the HST F606W image. The optical centroid is located 2 kpc SW of the peak X-ray flux. At radii of ~ 20 kpc the X-ray emission is better centered 3.3 kpc NW of the optical centroid. The radial profiles are only weakly affected by which of these three centroids is used. Since the cavity (see Section 5.3.2) is located close to the center, the cavity age depends strongly on the adopted centroid. The optical centroid was chosen

because it is the median of the centroids, best reflects the gravitating mass near the cluster center, and was used to measure the mass profile (Hogan et al., 2017b).

The spectroscopic analysis of the X-ray data was performed using XSPEC v12.7.1 (Arnaud, 1996). Spectral deprojection was performed using the geometric method DSDEPROJ (Sanders & Fabian, 2007; Russell et al., 2008). This removes the spectral contribution of gas along the line-of-sight projected into an annulus. The projected and deprojected spectra were both fit by a single temperature thermal model with photoelectric absorption, PHABS×APEC. The foreground hydrogen column density was fixed to the Galactic value of $N_H = 2.01 \times 10^{20}$ cm^{-2} (Kalberla et al., 2005). Temperature, normalization, and metallicity were all allowed to vary, with the metal abundance ratios taken from Anders & Grevesse (1989). The projected spectra were left unbinned and fit with C-statistics, while the deprojected spectra were grouped to a minimum of 25 counts per energy bin and fit with the χ^2 statistic.

The normalization of the APEC model is related to the gas density via

$$\text{norm} = \frac{10^{-14}}{4\pi[D_A\ (1+z)]^2} \int n_e n_H \mathrm{d}V, \tag{5.1}$$

where D_A is the angular diameter distance, V is the volume of the annulus, and $n_H = n_e/1.2$ is assumed to be constant within each annulus. The gas pressure is determined from density and temperature using the ideal gas law, $p = (n_e + n_H)\ kT = 1.8 n_e kT$. The entropy index of the gas is defined as $K = kT\ n_e^{-2/3}$. The cooling time, which is the time it would take for the gas to radiate away all of its thermal energy, is given by

$$t_{\text{cool}} = \frac{3}{2}\frac{p}{n_e n_H \Lambda(T,Z)}. \tag{5.2}$$

The cooling function, $\Lambda(T,Z)$, was determined from the bolometric X-ray luminosity, $L_x = \int n_e n_H \Lambda(T,Z)\mathrm{d}V$, which was obtained by integrating the unabsorbed thermal model between 0.1 and 100 keV. The projected and deprojected profiles for each of these quantities is shown in Fig. 5.2.

5.3.2 The X-ray "Cavity"

The X-ray image shown in Fig. 5.1 (center) shows a surface brightness depression located 6 kpc WNW of the BCG nucleus. The north side of the surface brightness depression is encompassed by an X-ray bright filament. Without an image of the radio source we cannot

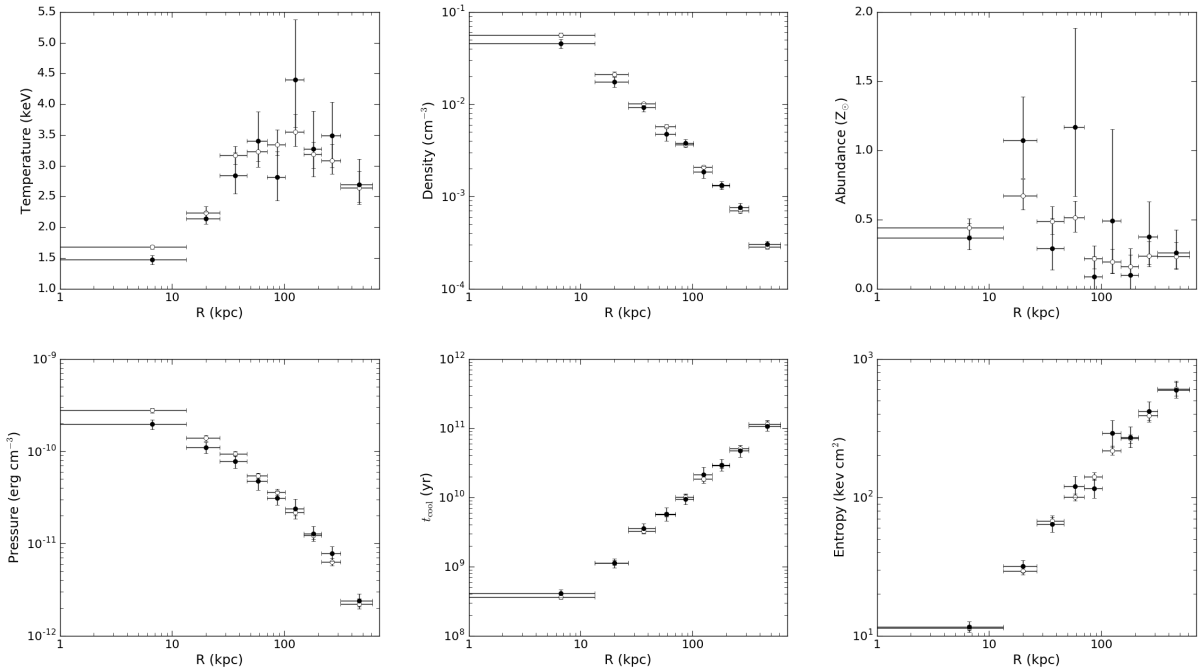

Figure 5.2: Projected (open circles) and deprojected (filled circles) profiles of X-ray derived quantities.

conclusively determine if this feature is an X-ray cavity. The existing radio data shows no extended structure on $2-5$ arcsec scales at 1.4 or 5 GHz, although the radio emission is offset along the direction of the X-ray filament (Bayer-Kim et al., 2002). Our ALMA imaging shows that the continuum emission at 117 and 343 GHz is similarly offset from the BCG nucleus and is coincident with the molecular gas. The lack of radio emission from the galactic center indicates that the AGN is currently quiescent, so the surface brightness depression may simply be a lack of bright emission when contrasted with the X-ray filament. Nevertheless, we measure the size of the surface brightness depression and compute its energetics should it be a real cavity. Throughout this work we refer to this feature as simply the X-ray cavity, though it should be taken with the caveat stated here.

The projected size of the X-ray cavity was determined by qualitatively fitting an ellipse to the surface brightness depression. The identified region is shown in Fig. 5.1. The enthalpy required to inflate the cavity is given by $E_{\rm cav} = 4pV$, where the prefactor is suitable for a relativistic gas filling the cavity volume. The pressure within the cavity, p, was determined by assuming that the cavity is in pressure balance with its surroundings, taking the deprojected pressure at a projected radius equal to the distance to the cavity center. The cavity volume was computed by assuming that its size along the line-of-sight is given by the geometric mean of the semi-major and semi-minor axes, $r = \sqrt{ab}$, so that $V = \frac{4}{3}\pi(ab)^{3/2}$.

We estimate the age of the cavity using both the buoyant rise time and sound crossing time (Bîrzan et al., 2004). The sound crossing time is simply a function of ICM temperature, and is given by

$$t_{c_s} = R/c_s = R\sqrt{\mu m_H/\gamma kT}, \tag{5.3}$$

where $\gamma = 5/3$ for an ideal gas. The buoyant rise time is the time taken for the cavity to rise to its current projected distance at its terminal velocity,

$$t_{\rm buoy} = R/v_t \sim R\sqrt{SC/2gV}. \tag{5.4}$$

Here $C = 0.75$ is the drag coefficient (Churazov et al., 2001) and S is the bubble cross-section, which is assumed to be its projected area. The acceleration under gravity is determined using the cluster mass profiles from Hogan et al. (2017b). We find that the two timescales are comparable, and adopt the buoyancy time when computing the mean cavity power, $P_{\rm cav} = E_{\rm cav}/t_{\rm buoy}$.

The size and energetics of the cavity and corresponding AGN outburst are summarized in Table 5.1. The power output by the AGN, 1.3×10^{43} erg s^{-1}, is low compared to other cool core clusters. It is ten times less powerful than the outburst in Perseus, which itself is only a moderately powerful system (Rafferty et al., 2006). Fueling the outburst through

Table 5.1: Cavity Measurements

a	4.7 kpc
b	2.6 kpc
R	6.4 kpc
$4pV$	4.2×10^{57} erg
$t_{\rm sc}$	10.1×10^{6} yr
$t_{\rm buoy}$	10.5×10^{6} yr
$P_{\rm cav}$	1.3×10^{43} erg s^{-1}
$M_{\rm acc}$	$2.4 \times 10^{4}\,{\rm M}_{\odot}$
$M_{\rm displaced}$	$2.3 \times 10^{8}\,{\rm M}_{\odot}$

accretion requires an accreted mass of $M_{\rm acc} = E_{\rm cav}/\epsilon c^2 = 2.4 \times 10^4\,{\rm M}_{\odot}$, assuming an efficiency of $\epsilon = 0.1$. Although no nuclear molecular gas has been detected, the accreted mass can easily be supplied by even a small fraction of the total molecular gas supply, which totals $10^{10}\,{\rm M}_{\odot}$.

5.3.3 Cooling of the Hot Atmosphere

To determine the amount of gas that may be cooling out of the hot atmosphere, we added an MKCFLOW component to the previous thermal model. This is a classical cooling flow model for gas at a constant pressure cooling through a specified temperature range. The maximum temperature was taken to be the mean temperature within that annulus, and the minimum temperature limit was set at 0.1 keV. The mass deposition rate yielded by this model is therefore an upper limit on the amount of gas that cools below 0.1 keV and condenses out of the ICM. Abundances in the cooling flow component were tied to the thermal model.

Following McDonald et al. (2010), we define the cooling radius, $r_{\rm cool}$, as the radius where the cooling time falls below 5 Gyr. From the profiles in Section 5.3.1 we obtain $r_{\rm cool} = 50$ kpc. A spectrum was extracted from this region and deprojected using the spectra from a series of overlying annuli using the same method as Section 5.3.1. The best-fitting mass deposition rate is $\dot{M}_{\rm cool} = 34 \pm 10\,{\rm M}_{\odot}\ {\rm yr}^{-1}$, and the luminosity of this cooling gas is 3.8×10^{42} erg s^{-1}. The total X-ray luminosity within this region is $L_X = 2.87 \pm 0.05 \times 10^{43}$ erg s^{-1}, so heating must offset $> 85\%$ of the radiative losses within the

central 50 kpc. This spectroscopic mass deposition rate is consistent with the measured star formation rate.

5.4 Molecular Gas Properties

Maps of integrated flux, velocity, and FWHM of the CO(1-0) and CO(3-2) lines were created by fitting the spectra extracted from individual pixels, averaged over a box the size of the synthesized beam, of the respective ALMA images. Up to two Gaussian components were used to model each pixel's spectrum. The significance of each component was tested using a Monte Carlo analysis with at least 2500 iterations. A detection required 3σ significance. The presence of one component was required before attempting to fit a second. Instrumental broadening has been incorporated into the model.

Fig. 5.3 presents the CO(1-0) and CO(3-2) integrated flux maps. These are updated versions of the flux maps presented in V17, using 2500 Monte Carlo iterations versus the 1000 iterations in V17. The fluxes of all velocity components have been summed together to create these maps. As discussed in V17, two bright clumps are situated along a 6 kpc long filament. The clumps account for more than half of the total line emission, and are surrounded by an envelope of diffuse emission. The diffuse emission extends to the NW in CO(1-0), while significant CO(3-2) emission is located north of the two clumps and does not extend as far to the NW.

All of this emission is spatially offset from the galactic center. The center of the brightest clump is 3 kpc north of the BCG's optical centroid. The other bright clump is 4.6 kpc NW of the optical centroid. The farthest extent of the filament is about 7 kpc from the galactic center.

In V17 we estimated that $< 1.2 \times 10^8\,M_\odot$ of molecular gas is present within a 2×2 kpc box placed at the optical center of the BCG. This region is not located in the field-of-view of Fig. 5.3. Contours of the total CO(3-2) flux are overlaid on the optical emission in Fig. 5.1 (right) for reference. Note that this mass limit was determined using the Galactic CO-to-H_2 conversion factor, which is double the value used in the rest of our mass estimates (see Section 5.4.1). We retained the Galactic conversion factor for this measurement in order to be conservative with the upper limit.

The maps of integrated flux, velocity centroid, and FWHM for each velocity component are shown in Fig. 4.4. These maps are presented for both CO(1-0) (left) and CO(3-2) (right). The main image is the velocity component with the largest flux. A second velocity component was significantly detected near the two bright peaks. This component is shown

in the inset plot in the upper left corner. The dashed box indicates the region shown in the second plot. These inset regions measure 8 kpc × 5 kpc in the CO(1-0) images and 6 kpc × 3 kpc in the CO(3-2) images.

The molecular filament is separated into two regions of distinct velocities. The main portion of the molecular filament, containing the two bright clumps and approximately indicated by the dashed boxes in Fig. 4.4, exhibits a narrow range of velocities. The velocities span 0 to 50 km s^{-1} throughout this region, with linewidths that are < 100 km s^{-1} FWHM. In the outer tail of the filament detected in CO(1-0) the velocity is blueshifted to -25 km s^{-1}. No velocity gradients are evident within either of these regions. The only velocity gradient is in between these regions, where the velocity transitions sharply from 25 km s^{-1} to -45 km s^{-1} over the span of 1.5 kpc.

5.4.1 Molecular Gas Mass

The integrated flux ($S_{\rm CO}\Delta v$) of the CO(1-0) line can be converted to molecular gas mass through (Solomon et al., 1987; Solomon & Vanden Bout, 2005; Bolatto et al., 2013)

$$M_{\rm mol} = 1.05 \times 10^4 \frac{X_{\rm CO}}{X_{\rm CO,gal}} \left(\frac{S_{\rm CO}\Delta v \; D_L^2}{1+z} \right) {\rm M}_\odot. \tag{5.5}$$

Here z is the redshift of the source, D_L is the luminosity distance in Mpc, and $S_{\rm CO}\Delta v$ is in Jy km s^{-1}.

The CO-to-H_2 conversion factor within the Milky Way and other nearby spiral galaxies is measured to be $X_{\rm CO,gal} = 2 \times 10^{20}$ cm^{-2} (K km s^{-1})$^{-1}$ (Bolatto et al., 2013). Between similar systems $X_{\rm CO}$ varies by about a factor of two. In V17 we used the ^{13}CO(3-2) emission line, in conjunction with the ^{12}CO 1-0 and 3-2 lines, to estimate the conversion factor in RXJ0821. We measured $X_{\rm CO} = 1.05 \times 10^{20}$ cm^{-2} (K km s^{-1})$^{-1}$, or equivalently $\alpha_{\rm CO} = 2.26\,{\rm M}_\odot$(K km s^{-1} pc^2)$^{-1}$. This is half the Galactic value. We have adopted this sub-Galactic value throughout this paper.

RXJ0821 is the only BCG for which a calibration of $X_{\rm CO}$ is available. This is an advantage over other systems, where the molecular gas mass may be overestimated. However, significant systematic uncertainties were unavoidable in the V17 analysis. In particular, the ^{13}CO(3-2) measurement provides a measure of the ^{13}CO column density, while N(H_2) is the desired quantity. This required the assumption of the ^{13}CO/H_2 abundance ratio, which is only known to a factor of a few. The subsolar metallicity of the central intracluster medium in RXJ0821 suggests that $X_{\rm CO}$ may have been underestimated by a factor of 2–3, which would bring its value in line with the Galactic measurement.

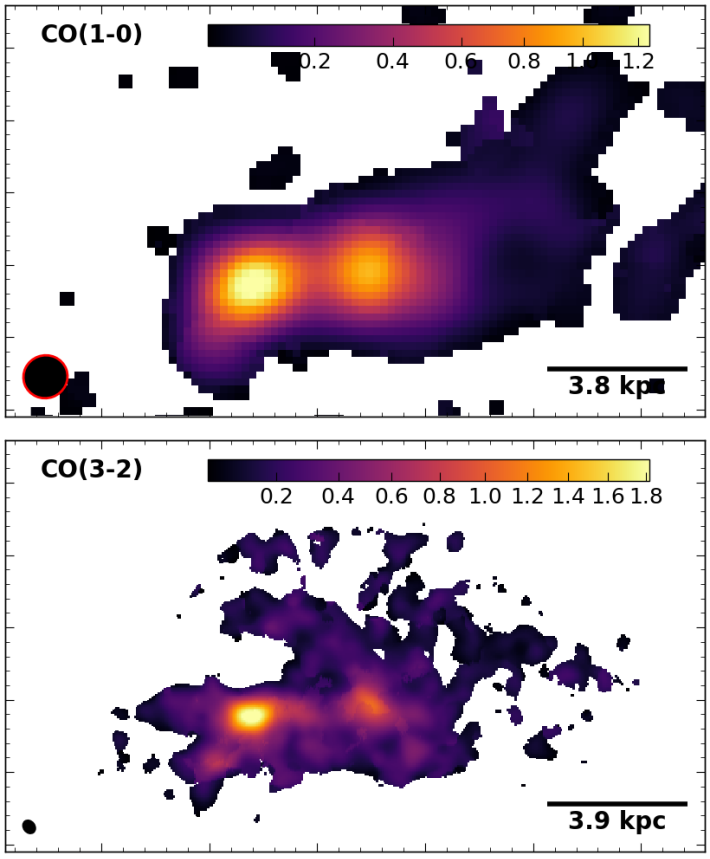

Figure 5.3: Maps of the CO(1-0) (top) and CO(3-2) (bottom) total fluxes, in Jy km s^{-1}. The 19.1 × 16.3 kpc field-of-view is the same in both images. The galactic center is not present in these images. The black ellipses in the lower left corners indicate the size of the synthesized beams.

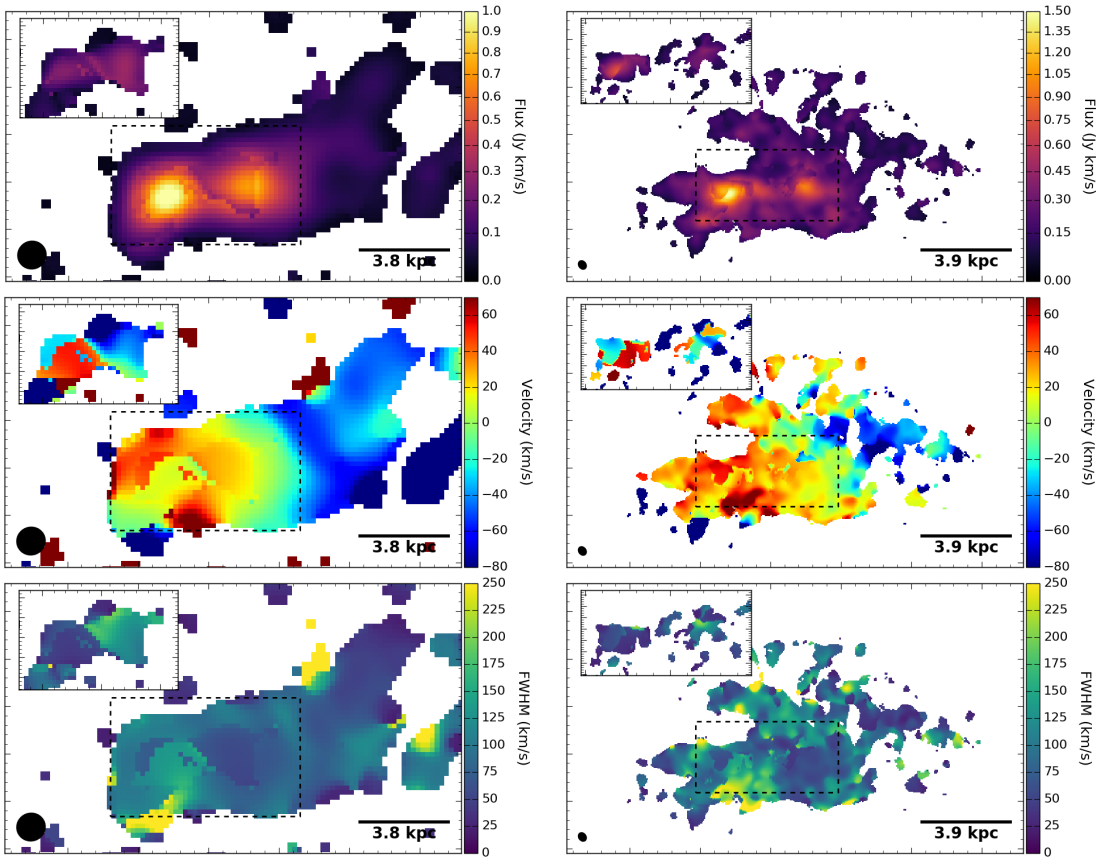

Figure 5.4: Maps of the CO(1-0) (left) and CO(3-2) (right) integrated flux (top), velocity centroid (middle), and full-width at half maximum (bottom) for multi-component fits to each pixel. The field-of-view is the same as Fig. 5.3. The additional axis in the upper left corner shows the second velocity component within the region indicated by the dashed box.

In spite of these systematic uncertainties, we still adopt the sub-Galactic value of $X_{\rm CO}$. As a result, our reported molecular gas masses are conservative. Even these conservative masses, as discussed later, place stringent demands on the energetics in this system. Reverting to a Galactic conversion factor simply amounts to multiplying the molecular gas masses by a factor of two.

Following V17, CO(3-2) line fluxes have been converted to molecular gas masses by assuming a CO (3-2)/(1-0) flux ratio of 8. This was measured from the ratio of integrated flux densities. Using the ratio of peak temperatures instead would give a lower line ratio of 6.4.

For total integrated CO(1-0) and CO(3-2) fluxes of 8.06 ± 0.08 and 65.6 ± 1.5 Jy km s^{-1}, respectively, the molecular gas mass is $(1.07 \pm 0.02) \times 10^{10}\,{\rm M}_{\odot}$.

5.5 Dust Continuum

Continuum maps from ALMA Bands 3 (98.8 GHz) and 7 (304.6 GHz) are presented in Fig. 5.5. No radio continuum is detected at the BCG nucleus. Instead, very faint, extended emission located near the two main clumps of molecular gas are present at both frequencies. The faint continuum emission in Fig. 5.5 is highlighted using black contours at uniform intervals of σ, where σ is 8.2 μJy beam^{-1} at 98.6 GHz and 28 μJy beam^{-1} at 304.6 GHz. White contours indicate the integrated CO(3-2) line emission from Fig. 5.3.

Measurements of the continuum flux density for both clumps (labelled as regions A and B in Fig. 5.5) are presented in Table 5.2. The box sizes used to extract the fluxes were chosen based on the size of each source, so, due to the different resolutions, are not the same for the two frequencies. Since the emission is extended, some flux is missing from the adopted regions and our measurements should be considered lower limits. Although each individual measurement is marginal, the combination of all four independent measurements corresponds to a 3.5σ detection of the continuum.

RXJ0821 is the third brightest *Spitzer* 70 μm source in a sample of 62 BCGs (Quillen et al., 2008). Its prominent red unresolved nucleus at 8 μm and high [O III](5007)/Hβ ratio suggests that it hosts a dusty AGN. The high IR flux and spatial coincidence with the molecular gas implies that the ALMA continuum also originates from dust emission. This is the best example of resolved dust continuum from ALMA.

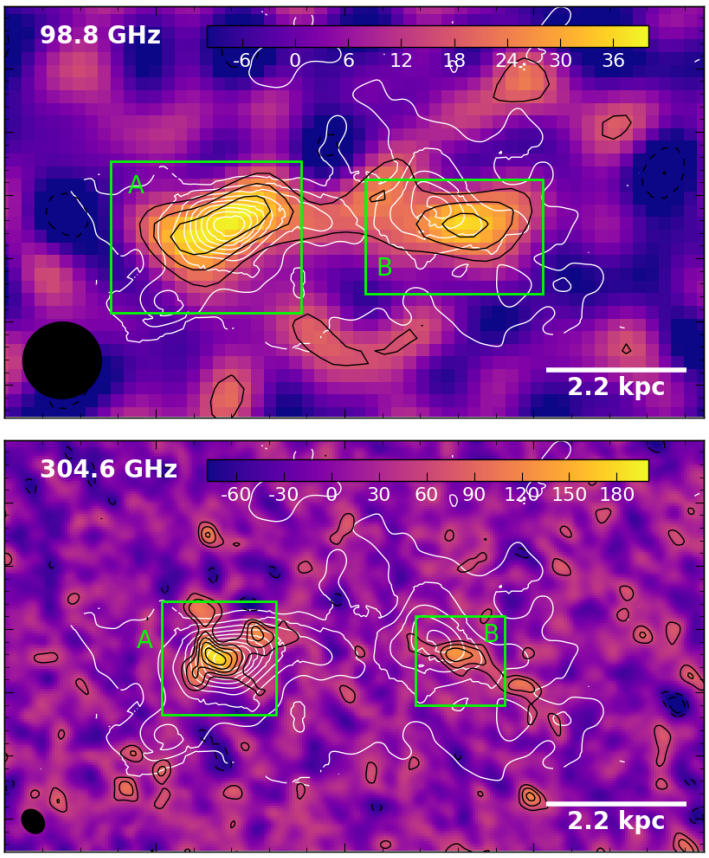

Figure 5.5: The 98.6 GHz (top) and 304.6 GHz (bottom) continuum sources. The continuum flux is traced by black contours at the [-3, -2, 2, 3, 4, 5, 6]$\times\sigma$ levels, where σ = 8.2 μJy beam^{-1} at 98.6 GHz and 28 μJy beam^{-1} at 304.6 GHz. The colorbar is in units of μJy beam^{-1}. The white contours correspond to the ALMA CO(3-2) flux (Fig. 5.3 bottom). The continuum measurements provided in Table 5.2 were extracted from the regions shown in green.

Table 5.2: Radio Continuum

Region	Frequency (GHz)	Flux Density (mJy)
A	98.8	0.066 ± 0.043
	304.6	0.90 ± 0.60
B	98.8	0.05 ± 0.03
	304.6	0.51 ± 0.37

5.6 Discussion

RXJ0821 presents an interesting challenge to our understanding of molecular gas formation and flows in BCGs. All of its 10^{10} $M_\odot$ of molecular gas is offset by ~ 4 kpc from the galactic center. This is among the most massive known molecular gas reservoirs in a BCG, and evidently none of it has settled into the underlying gravitational potential. Additionally, the narrow spread in both position and velocity indicates that the molecular gas has either formed rapidly, having had little time for infall, or it has been deposited abruptly.

Observations and simulations consistently support the hypothesis that ICM condensation is the primary source of cold gas in galaxy clusters (e.g. Rafferty et al., 2008; McDonald et al., 2010; Gaspari et al., 2013; Li & Bryan, 2014a; Russell et al., 2016; Vantyghem et al., 2016; Pulido et al., 2018). Most directly, the presence of cold gas and star formation is linked to short central cooling times (Cavagnolo et al., 2008; Rafferty et al., 2008; Pulido et al., 2018). Mergers are, in general, unable to account for the massive molecular reservoirs observed in BCGs. Even gas-rich spirals, such as the Milky Way, contain less gas than is present in typical BCGs. Merger rates are also unrelated to the presence of a cool core, so the cooling time threshold cannot be explained through mergers.

5.6.1 Gas Donated or Dispalced by an Infalling Galaxy

Despite the inability of mergers to form the molecular gas reservoirs of BCGs in general, the proximity of a nearby galaxy raises the possibility of a merger origin for the cold gas in RXJ0821. The galaxy SDSS J082102.46+075145.0 is located 7.7 kpc SE of the BCG nucleus. Optical spectroscopy indicates that its relative velocity is $+77 \pm 32$ km s^{-1} with respect to the BCG (Bayer-Kim et al., 2002). Blue emission from recent star formation connects the molecular gas reservoir to the nearby galaxy. These factors suggest that the two galaxies have either interacted in the past or are currently interacting.

A gas-rich elliptical can contribute at most a few $\times 10^8\,M_\odot$ of cold gas (Young et al., 2011). Tens to hundreds of merging ellipticals would be required to accumulate the $10^{10}\,M_\odot$ gas supply in RXJ0821.

Alternatively, the nearby galaxy could be the remnant bulge of an infalling spiral. However the Milky Way – a gas-rich spiral galaxy – contains only $10^9\,M_\odot$ of molecular gas (Heyer & Dame, 2015). The nearby galaxy is potentially a few times more massive than the Milky Way. Its SDSS magnitudes, corrected for evolution and the K-correction (Poggianti, 1997), yield an absolute i-band luminosity of $L_i = 1.35 \times 10^{10}\,L_\odot$. This includes a 25% correction for the underlying BCG flux, determined using a pair (source and background) of adjacent $1''$ radius apertures in the HST F606W image. For an i-band mass-to-light ratio of 2.0 (Bell et al., 2003), the total stellar mass is $2.7 \times 10^{10}\,M_\odot$. This is three times greater than the mass of the Milky Way's bulge ($0.91 \times 10^{10}\,M_\odot$; Licquia & Newman, 2015). The same increase in molecular gas mass would still be three times lower than the molecular gas mass of RXJ0821.

Atomic gas provides another avenue for producing the massive molecular gas reservoir. The pressure in cluster cores is high enough to convert virtually all atomic gas to molecular form (Blitz & Rosolowsky, 2006). The Milky Way contains $\sim 6 \times 10^9\,M_\odot$ of H I (Ferrière, 2001), and the nearby galaxy may have initially contained a few times more. The combination of the pre-existing molecular gas with the condensing H I could conceivably account for the $10^{10}\,M_\odot$ of cold gas in RXJ0821.

In order to strip molecular gas the galaxy must be infalling with a high velocity. Even large spirals containing $10^8\,M_\odot$ of molecular gas must be moving at 1000 km s^{-1} in order for their cold gas to be stripped 10 kpc from cluster cores (Kirkpatrick et al., 2009). Larger galaxies would require even faster velocities. The low relative velocity of 77 km s^{-1} indicates that, unless virtually all of its motion is along the plane of the sky, the nearby galaxy should have held onto all of its molecular gas.

H I is stripped much more easily than H_2, as its density is $2-3$ decades lower. It is unlikely that H I has survived long enough to condense into molecular gas. Indeed, spirals in cluster environments are deficient in H I (Haynes et al., 1984). Additionally, ram pressure tails differ morphologically from the gas in RXJ0821. When velocities are high enough to strip molecular gas, the resulting tail can extend tens of kpc outward from the infalling galaxy, occupying a wide range in both position and velocity (e.g. Jáchym et al., 2014, 2017).

Another possibility is that the $10^{10}\,M_\odot$ of molecular gas was initially central within the BCG but was dislodged by the infalling galaxy. Rings and partial rings of gas and young stars are observed following nearly head-on collisions with infalling galaxies (Appleton &

Struck-Marcell, 1996). The arcs of blue emission and molecular gas could be a partial ring driven outward by the interaction with the nearby galaxy. However, several lines of reasoning lead us to argue that this is not the case.

First, the molecular gas is coincident with an X-ray-bright plume (discussed further in Section 5.6.2). This correlation implicates ICM condensation as a formation mechanism and would not be caused by a minor merger. Next, these collisions do not remove the entire gas supply (Lynds & Toomre, 1976). Less than 1% of the molecular gas in RXJ0821 resides at the galactic center, so any mechanism that displaces the gas must be efficient. Moreover, the molecular gas occupies a narrow range in both space and velocity, which is inconsistent with a high speed collision. Finally, an infalling galaxy on its first passage through the cluster center would have a velocity in excess of 1000 km s^{-1} . The observed radial velocity of +77 km s^{-1} implies that the nearby galaxy would be travelling within 5° of the plane of the sky. This is possible, but statistically unlikely.

Overall the possibility that the cold gas has been either deposited or dislodged by a merger is not well-motivated by the observational data.

5.6.2 ICM Condensation

The spatial coincidence between molecular gas and the X-ray-bright plume (see Fig. 5.1) supports the possibility that the cold gas has condensed out of the hot atmosphere. ICM condensation is easiest in cluster cores, where the cooling time is shortest. When radiative cooling is approximately balanced by AGN heating condensation ensues via thermal instabilities (e.g. McCourt et al., 2012; Gaspari et al., 2013; Li & Bryan, 2014b; Voit, 2018). This requires the central gas with a short cooling time to be displaced from its equilibrium position long enough for the gas to cool. Two ways to accomplish this are uplift in the wakes of X-ray cavities and sloshing of the ICM.

Before discussing either of these possibilities, it is important to note that even condensation of the hot atmosphere has difficulty accounting for such a massive reservoir of molecular gas. The hot gas mass within the inner region (13.3 kpc radius) of the X-ray profiles (Fig. 5.2) contains $(1.27 \pm 0.14) \times 10^{10}\,M_{\odot}$, which is comparable to the molecular gas mass. The narrow spatial and velocity distributions indicate that the molecular gas formed rapidly and in a single cycle of cooling. Rapid condensation would deplete the central 10 kpc of its entire supply of hot gas, resulting in a rapid inflow to balance the pressure support lost as the gas condenses. This is not unprecedented. Eight of the 33 systems in Pulido et al. (2018) that contain significant CO emission have molecular gas masses that match or exceed the hot gas mass within 10 kpc.

Additionally, the mass deposition rate within the central 50 kpc is $< 34 \pm 10\,\mathrm{M}_\odot\ \mathrm{yr}^{-1}$ (see Section 5.3.3). Condensation persisting at this rate would form the $10^{10}\,\mathrm{M}_\odot$ of molecular gas in 3×10^8 yr. This is close to the central cooling time of 4×10^8 yr. However, star formation is also present in the BCG. Infrared measurements imply a star formation rate of $37\,\mathrm{M}_\odot\ \mathrm{yr}^{-1}$ (O'Dea et al., 2008). Condensation at this rate should therefore be largely offset by star formation, resulting in a slowly accumulating gas reservoir.

Non-radiative ICM cooling may help, but not completely, alleviate these demands. Heat transfer with the molecular gas (e.g. conduction, collisions, mixing) can hasten the overall rate of cooling. This would make it easier for a single cycle of cooling to produce the molecular flow, but still suffers from the lack of fuel in the central 10 kpc.

Stimulated Cooling

Stimulated cooling is emerging as a leading mechanism in triggering the formation of molecular gas in BCGs. In this mechanism, low entropy gas from the cluster core is lifted by rising X-ray cavities to an altitude where it becomes thermally unstable (Revaz et al., 2008; McNamara et al., 2016). Stimulated cooling was proposed in response to the growing number of ALMA observations with molecular filaments trailing X-ray cavities. The molecular gas in RXJ0821 also exhibits a connection with an X-ray cavity, as it is coincident with the bright X-ray plume that wraps around the northern side of the cavity.

ALMA observations of other BCGs have demonstrated that X-ray cavities are capable of lifting enough low entropy gas to form their trailing molecular filaments, although the coupling efficiencies must be high (e.g. McNamara et al., 2014; Russell et al., 2016, 2017a,b; Vantyghem et al., 2016). In RXJ0821, on the other hand, the cavity is far too feeble to have lifted $10^{10}\,\mathrm{M}_\odot$ of gas. Archimedes' principle provides a convenient metric to explore the feasibility of uplift behind a rising cavity. Cavities cannot lift more gas than they displace. The mass of the displaced ICM is given by $M_{\mathrm{displaced}} = n\mu m_H V$, where $n = n_e + n_H$ is the density of the surrounding gas. A total of $2.4 \times 10^8\,\mathrm{M}_\odot$ of hot gas has been displaced in inflating the X-ray cavity. This is 40 times smaller than the molecular gas mass. Only a few percent of the total molecular gas mass could have been uplifted by the cavity. While uplift behind X-ray cavities is a promising cold gas formation mechanism in other BCGs, it fails here.

The morphology of RXJ0821's molecular filament also differs somewhat from the filaments in other BCGs. Half of the gas in RXJ0821 is concentrated in two clumps surrounded by a diffuse, $2 - 5$ kpc wide envelope. Molecular filaments in other systems vary in length from $\sim 3 - 20$ kpc with unresolved widths that are $\lesssim 1$ kpc (e.g. Russell et al., 2016,

2017a,b; Vantyghem et al., 2016, 2018). Clumpy emission is also observed in BCGs (e.g. McNamara et al., 2014; Tremblay et al., 2016), but is often poorly resolved and coincident with the galactic center. The somewhat unique structure in RXJ0821 may be indicative of a different formation mechanism.

Sloshing

Condensation could also be triggered by sloshing motions in the ICM. Minor mergers can easily set the central peak of the ICM in motion with respect to the rest of the cluster (Ascasibar & Markevitch, 2006). These sloshing motions persist for several Gyr, potentially providing enough time for the central gas to cool. The low relative velocity and arcs of blue continua trailing the nearby galaxy suggest that a minor merger has occurred. Further indications of sloshing come from the mutual offsets between the X-ray peak, BCG nucleus, and the centroid of the X-ray emission on 20 kpc scales. The molecular gas is offset from each of these, but is coincident with the bright plume that extends from the X-ray peak.

Sloshing may also contribute to the formation of cold gas in other systems. A1795 hosts a 50 kpc long filament extending from the BCG (Fabian et al., 2001; McDonald & Veilleux, 2009; McDonald et al., 2012b). Fabian et al. (2001) argued that this filament was formed via gravitational focusing as the BCG passed through the ICM. Hamer et al. (2012) identified three clusters (A1991, A3444, and Ophiuchus) with X-ray peaks offset from the BCG by ~ 10 kpc. The nebular emission and molecular gas in these systems are coincident with the soft X-ray peak, implying a causal link between the lowest temperature ICM and the molecular gas. In each case the large offset between the BCG and X-ray peak is attributed to major or minor cluster mergers. The smaller offset in RXJ0821 requires a smaller perturbation.

Whether sloshing is able to account for all $10^{10}\,M_\odot$ of cold gas in RXJ0821 is unclear. It would still require the condensation of all of the ICM within the central 10 kpc, but this gas is already oscillating within the cluster potential. In stimulated cooling X-ray cavities would need to couple to and lift the same amount out of the cluster core, which is much more difficult. We therefore argue that sloshing is the mechanism responsible for triggering condensation in RXJ0821.

5.7 Conclusions

In this work we have performed a morphological analysis of ALMA CO(1-0) and CO(3-2) observations and presented a new 63.5 ks *Chandra* X-ray observation of the cool core cluster

RXJ0821.0+0752. This extends the previous analysis of the same ALMA data conducted in V17, where the analysis focused on using the line intensities, along with a ^{13}CO(3-2) detection, to constrain the CO-to-H_2 conversion factor.

The entire $10^{10}\,M_\odot$ supply of molecular gas is located in an 8 kpc long filament spatially offset from the galactic center by about 4 kpc. The emission is concentrated in two bright peaks surrounded by a diffuse, $2-5$ kpc wide envelope. It is coincident with a bright plume of X-ray emission situated alongside a putative X-ray cavity. The narrow spread in both position and velocity suggests that the molecular gas formed relatively quickly and in a single cycle of cooling.

The formation of cold gas in RXJ0821 differs from that of other BCGs, where stimulated cooling has lifted filaments of condensing gas out of the cluster core. Although the filament in RXJ0821 is also associated with an X-ray cavity, the cavity is too feeble to account for the observed gas distribution. Only a few percent of the total molecular gas mass could have been uplifted by the cavity.

Instead, ICM condensation in RXJ0821 has likely been triggered by sloshing motions induced by the interaction with a nearby galaxy. The BCG nucleus, X-ray peak, molecular gas, and arcs of recent star formation are all mutually offset, which is indicative of relative motions between the cooling ICM and BCG. Sloshing can trigger condensation by emulating uplift. The cooling time is shortest in the cluster core. Sloshing removes this gas from the center of the potential well, giving some of the gas time to cool by keeping it out of equilibrium.

Chapter 6

Summary & Future Work

In this thesis I presented ALMA observations of the molecular gas in the central galaxies of three cool core galaxy clusters. The CO(1-0) and CO(3-2) lines were used to map the distribution of molecular gas – a task that was not possible with previous generations of radio telescopes. Additionally, the detection of the ^{13}CO(3-2) line in one cluster enabled to calibration of the CO-to-H_2 conversion factor. By understanding the distribution of molecular gas, we learn more about cycles of heating and cooling undergone in galaxy clusters. This is integral in AGN feedback, which regulates the growth of galaxies by preventing them from overcooling.

In Chapter 2 I presented ALMA CO(1-0) and CO(3-2) observations of the BCG in the 2A 0335+096 galaxy cluster. The $1.1 \times 10^9\,M_\odot$ of molecular gas is distributed between two distinct structures: a series of clumps straddling the BCG nucleus and a 7 kpc long filament extending nearly radially outward. The velocity of the central component is reminiscent of rotation, with blueshifted and redshifted emission on opposite sides of the nucleus. However, the gas distribution does not resemble a structure in equilibrium, such as a ring or disk. South of the nucleus the gas is confined to two clumps of roughly equal mass, while the gas to the north extends in a plume oriented toward a nearby galaxy. This plume may indicate that a molecular disk did exist, but was disrupted by the passage of the companion galaxy through the BCG. The lack of any corresponding stellar disruption does not corroborate this hypothesis. The molecular filament exhibits a shallow velocity gradient, which is only consistent with free-fall if it lies within 25° of the plane of the sky. The filament is coincident with dust extinction, luminous Hα emission, and soft X-ray emission. The coincidence of gas over 5–6 decades in temperature strongly implicates condensation of the hot atmosphere as the dominant mechanism in producing the molecular gas. Indeed, the ICM mass deposition rate can form the molecular gas supply in only 10^8 yr,

which is rapid enough to sustain AGN feedback. Similar to the filaments in several other systems, the cooling filament is oriented directly toward an X-ray cavity. The molecular gas may therefore form via "stimulated cooling," where the central, low entropy gas is lifted by an X-ray cavity to an altitude where it becomes thermally unstable.

In Chapter 3 I used ALMA CO(1-0), CO(3-2), and ^{13}CO(3-2) observations of RXJ0821.0+0752 to estimate the CO-to-H_2 conversion factor for the first time in a BCG. We identified two distinct velocity components in the ^{12}CO emission, one of which matches closely to the velocity centroid and linewidth of the ^{13}CO(3-2) emission. Restricting the analysis to this component and making various simplifying assumptions, the CO-to-H_2 was estimated to be half of the Galactic value. These assumptions included local thermodynamic equilibrium and a molecular $^{13}CO/H_2$ abundance similar to that of the Milky Way. This work implies that the molecular gas masses in BCGs may have been overestimated by a factor of two. A lower X-factor would alleviate the high coupling efficiencies between molecular gas flows and the buoyant X-ray cavities that they trail. However, the systematic uncertainties in this analysis are large, and the object-to-object scatter from works using nearby galaxies are comparably high. Thus the adoption of a Galactic conversion factor is unlikely to introduce an overwhelming bias to the measurement of molecular gas mass in BCGs.

In Chapter 4 I presented ALMA CO(1-0) and CO(3-2) observations of the BCG in the RXCJ1504.1-0248 galaxy cluster. The morphology of its $1.9 \times 10^{10}\,M_\odot$ of molecular gas is complex and disturbed. About 80% of the gas is located near the galactic center, but does not exhibit the velocity structure of a rotationally-supported disk or ring. Instead, it simply appears to be clumpy with little coherent structure. The remaining 20% of the gas is distributed along a 20 kpc long filament that extends radially from the galactic center. It is coincident with bright X-ray emission along the edge of a putative X-ray cavity. Stimulated cooling is a plausible formation mechanism for the cold gas, although the case is not as clear as the systems with filaments directly trailing the cavity. Sloshing motions may contribute to uplifting the gas. The velocity gradient along the filament is smooth and shallow. It is consistent with free-fall if the filament lies within 20° of the plane of the sky. Even conservative estimates of the gas density along the filament imply that the molecular clouds should be falling ballistically through the ICM. However, their low velocities are comparable to those in similar systems. It is unlikely that the motion in each system is confined close to the plane of the sky, so the molecular gas is likely being supported against free-fall. Filamentary blue and UV emission is coincident with the molecular gas, indicating a star formation rate of $136\,M_\odot\ \mathrm{yr}^{-1}$. The time required for the molecular gas to be consumed by star formation, 1.4×10^8 yr, is comparable to both the central cooling time (2.3×10^8 yr) and the time for mass deposition from the ICM to form the molecular gas supply (2.4×10^8 yr). Star formation near the galactic center

is consistent with the Kennicutt-Schmidt law. The molecular filament exhibits elevated star formation surface densities, possibly because a finite supply of molecular gas is being consumed by star formation.

In Chapter 5 I returned to the ALMA observations of RXJ0821.0+0752, this time to study the morphology of the molecular gas alongside a new *Chandra* X-ray observation. RXJ0821.0+0752 is one of the most gas-rich BCGs known, but has one of the weakest radio sources. All $10^{10}\,M_{\odot}$ of its molecular gas is situated exclusively in an 8 kpc long clumpy filament that is entirely offset from the galactic center by 4 kpc. The cold gas is coincident with a bright X-ray filament and adjacent to a putative X-ray cavity. The cavity is too feeble to have lifted more than a few percent of the molecular gas. Instead, the molecular gas has likely formed as a result of sloshing motions in the ICM induced by the interaction with a nearby galaxy. This is the only system observed so far in which cavity uplift is clearly incapable of stimulated the production of its associated molecular filaments.

6.1 Synthesis: The Molecular Gas in BCGs

The ALMA observations presented in this thesis represent just three of the systems studied so far. To date eleven BCGs have been observed by ALMA, along with four group-centered elliptical galaxies. The emerging trend is that the molecular gas in BCGs is dynamically complex, defying straightforward classification. Nuclear gas, when present, is often clumpy and asymmetric, with little evidence for ordered motion. Filaments are common on larger scales and are often associated with X-ray cavities. The gas velocities are intrinsically low, lying well below that expected from freefall or virialization.

Perhaps the most prevalent characteristic of the molecular gas in BCGs is the lack of nuclear ordered motion. Some amount of nuclear gas is observed in every system except PKS0745-191 (Russell et al., 2016) and RXJ0821+0752 (Chapter 5). However, disks are absent in all but one system: Hydra A (Hamer et al. 2014, Rose et al. 2018, in preparation). Its nearly-symmetric molecular structure is 7 kpc in diameter and exhibits a smooth velocity gradient that is consistent with disk rotation. Rotation is a less stringent classification than a disk, being defined by opposing blue- and redshifted emission. Besides Hydra A, A1664 (Russell et al., 2014) and 2A0335+096 (Chapter 2) are the only two systems in which rotation is a possibility. However, they are both highly asymmetric, so the rotation does not correspond to a disk. Either a disk is forming, which is potentially the case in A1664, or one has recently been disrupted by the passage of a nearby galaxy, which is a possibility in 2A0335+096.

Another discovery enabled by ALMA is that molecular gas is often associated with AGN feedback. This comes in two forms: molecular filaments trailing X-ray cavities and a direct connection between the radio jet and a clump of molecular gas.

Molecular filaments have been observed in eight of the eleven BCGs. They extend radially several to several tens of kpc from the galactic centers. In all eight of these systems the filaments are associated with X-ray cavities. They either trail directly behind the cavities (A1835: McNamara et al. 2014, PKS0745: Russell et al. 2016, 2A0335: Chapter 2, Phoenix: Russell et al. 2017a, and A2597: Tremblay et al. 2018) or are projected along their perimeters (A1795: Russell et al. 2017b, RXCJ1504-0248: Chapter 4, and RXJ0821+0752: Chapter 5). The clearest example of this association is in the Phoenix cluster (Russell et al., 2017a), where several molecular filaments totaling a mass of $10^{10}\,M_\odot$ are located along the peripheries of a pair of X-ray cavities.

A direct connection between molecular gas and radio jets is less common, although this is partly due to the smaller physical resolution required to resolve it. Including the group-centered ellipticals, a jet–gas impact has been observed in four systems: A1795 (Russell et al., 2017b), Centaurus A (Salomé et al., 2017), M87 (Simionescu et al., 2018), and A2597 (Tremblay et al., 2018). In M87 the jet terminates at the position of a giant molecular association. Centaurus A and A2597 exhibit increased molecular linewidths at the jet's head. In A1795 the molecular filament is draped around the exterior of a radio bubble, and the jet is deflected by its impact with the dense clouds.

Low gas velocities are common in BCGs. In A1835, one of the first BCGs observed, the low velocities were initially attributed to a face-on disk (McNamara et al., 2014). However each subsequent observation revealed the same low velocities, making this interpretation untenable. In five systems (2A0335+096, RXCJ1504-0248, PKS0745-191, Phoenix, and A2597) the molecular filaments were used to test models of gravitational infall (see e.g. Chapters 2, 4). In all five cases the velocities are too low to have arisen from freefall. Sub-freefall velocities are therefore an intrinsic property of the molecular gas in BCGs. In RXCJ1504-0248 (Chapter 4) we further showed that ram pressure is ineffective at slowing dense molecular clouds. Either much of the molecular gas mass must be contained in a more diffuse envelope that is susceptible to ram pressure drag or another mechanism is responsible for slowing molecular clouds.

Several lines of evidence lead us to conclude that the molecular gas in BCGs is formed via condensation of the hot atmosphere. It has not been donated via gas-rich mergers. Most directly, samples of gas-rich BCGs demonstrate that molecular gas is preferentially observed in clusters with short central cooling times (e.g. Rafferty et al., 2008; Pulido et al., 2018). The molecular gas masses, morphologies, and velocities of individual systems

also continually support this conclusion. The molecular gas masses are higher than even most gas-rich spiral galaxies, and stripping an infalling spiral would require velocities well in excess of those observed. Careful consideration of a merger origin for the cold gas in 2A0335+095 and RXJ0821+0752 (Chapters 2 and 5), two of the only systems with central member galaxies, concluded that stripping could not be responsible for producing the observed molecular gas. Instead, molecular filaments are coincident with nebular and soft X-ray emission tracing temperatures of 10^4 and 10^7 K, respectively. The spatial correlation of filaments spanning 5–6 decades in temperature directly implicates condensation of the hot atmosphere as the formation mechanism for molecular gas.

Taken together, these observations imply that molecular clouds have condensed from low entropy ICM caught in the updraft of X-ray cavities (e.g. McNamara et al., 2016). This mechanism is referred to as "stimulated cooling." Low entropy gas in the cluster core is lifted to an altitude where its cooling time is shorter than the time it would take to return to its equilibrium position (e.g. Voit, 2018). The gas is too slow to escape the central galaxy, so will eventually return in an inflow. This mechanism is also emerging in simulations. Nonlinear overdensities generated following a cycle of AGN feedback are thermally unstable, forming molecular gas that fuels stochastic accretion onto central supermassive black holes (e.g. Gaspari et al., 2013; Li & Bryan, 2014b).

A1835 and the Phoenix cluster form an interesting pair when considered together. Both are among the most gas-rich BCGs known, with molecular gas masses of 5×10^{10} and $2 \times 10^{10}\,\mathrm{M}_\odot$, respectively. They also both contain $10^{10}\,\mathrm{M}_\odot$ molecular filaments associated with X-ray cavities. The interesting difference arises from their velocity profiles. The filaments in Phoenix are well-described by gravitational infall. The velocities are lowest at their maximal extent, and increase toward the galactic center. This contributes to central gas with the broadest linewidth ($\sim 600\,\mathrm{km\,s^{-1}}$ FWHM) of any BCG. A1835 shows the opposite velocity profile. Its gas velocities are lowest near the nucleus, reaching a maximum at their farthest extent. This dichotomy demonstrates that we are observing the molecular gas in BCGs at different stages of their evolution. Each observation is a snapshot of the bigger picture. Initially the gas condenses from outflowing gas uplifted by a cavity, but will eventually decouple and rain back onto the BCG.

The plausibility of stimulating cooling hinges on a cavity's ability to lift enough gas to form their trailing molecular filaments. By Archimedes' Principle, cavities cannot lift more gas than they displace. In all but one case the mass of hot gas displaced by the cavity exceeds the associated molecular gas mass by a factor of $2 - 10$. This implies an efficient but plausible coupling between the cavity and uplifted gas. These demands are further relaxed by factors of $3 - 5$ because the central gas, when it is in equilibrium, is neutrally buoyant and so is easier to lift (Su et al., 2017). The calibration of molecular gas

masses may be overestimated by a factor of two, which would also alleviate these demands on coupling (Chapter 4).

RXJ0821+0752 is an exception to the stimulated cooling paradigm (Chapter 5). The feeble cavity could have lifted only a few percent of its associated molecular flow. Instead, the molecular gas in this system has likely condensed from gas displaced from the cluster center by sloshing motions in the ICM. This emulates the effect of uplift that is critical in stimulated cooling. Overall stimulated cooling is a viable mechanism for forming the molecular filaments in seven of eight BCGs.

These observations offer profound insights into galaxy cluster evolution. AGN feedback, the mechanism responsible for heating the atmospheric gas and preventing cooling flows, is evidently stimulating the production of the coldest gas as well. Instead of settling into a long-lived structure to feed the central supermassive black hole over long timescales, the molecular gas is transient. Its stochastic accretion onto the central black hole on short (10^8 yr) timescales mediates the long-term stability of galaxy clusters.

6.2 Future Work

The observations presented in this thesis represent the discovery space enabled with the advent of ALMA. At the time of writing, the molecular gas in roughly 15 clusters and groups have been resolved. The next step is to combine these observations into a sample, comparing the objects in a homogeneous and statistically robust way. This work will exploit measurements of halo masses, star formation rates, AGN cavity powers, and other parameters to reveal the formation and ultimate fate of the molecular gas.

Future work will also aim to expand the sample of available targets considerably. The current assortment of BCGs with ALMA observations has focused primarily on the most gas-rich systems. Whether molecular filaments are as common in giant ellipticals as they are in BCGs is a critical problem in galaxy evolution. In BCGs the primary mechanism for molecular gas formation appears to be condensation of uplifted, warm gas. Observing the formation mechanism in low-mass systems would highlight this process as fundamental.

A thorough understanding of the molecular gas formation and flows in BCGs requires an accurate calibration of its mass. The approach used in this thesis to estimate the CO-to-H_2 conversion factor is both simple and crude, and should be regarded as somewhat preliminary as only one object was considered. In other BCGs the ^{13}CO(3-2) may be accessible simultaneously with the main CO(3-2) line, so our simple approach may be applied to other systems and the object-to-object variance can be determined. A more

significant advancement will be possible when several CO emission lines are observed in an individual system. With upwards of four ^{12}CO emission lines, possibly combined with about two ^{13}CO lines, a full excitation analysis can be performed. This will provide gas temperature, density, and column density without relying on the assumption of local thermodynamic equilibrium, removing a significant source of uncertainty. Moreover, if this analysis is spatially resolved, then variations in the physical conditions of the gas, as well as the CO-to-H_2 conversion factor, can be identified within the gas distribution.

References

Aalto, S., Booth, R. S., Black, J. H., & Johansson, L. E. B. 1995, A&A, 300, 369

Abazajian, K., Adelman-McCarthy, J. K., Agüeros, M. A., et al. 2004, AJ, 128, 502

Alatalo, K., Blitz, L., Young, L. M., et al. 2011, ApJ, 735, 88

Alatalo, K., Crocker, A. F., Aalto, S., et al. 2015, MNRAS, 450, 3874

Anders, E., & Grevesse, N. 1989, Geochim. Cosmochim. Acta, 53, 197

Antonucci, R., & Barvainis, R. 1994, AJ, 107, 448

Appleton, P. N., & Struck-Marcell, C. 1996, Fund. Cosmic Phys., 16, 111

Armus, L., Heckman, T., & Miley, G. 1987, AJ, 94, 831

Arnaud, K. A. 1996, in Astronomical Society of the Pacific Conference Series, Vol. 101, Astronomical Data Analysis Software and Systems V, ed. G. H. Jacoby & J. Barnes, 17

Ascasibar, Y., & Markevitch, M. 2006, ApJ, 650, 102

Babyk, I. V., McNamara, B. R., Nulsen, P. E. J., et al. 2018a, ApJ, 857, 32

—. 2018b, ArXiv e-prints, arXiv:1802.02589

Bally, J., & Langer, W. D. 1982, ApJ, 255, 143

Bauer, F. E., Condon, J. J., Thuan, T. X., & Broderick, J. J. 2000, ApJS, 129, 547

Bayer-Kim, C. M., Crawford, C. S., Allen, S. W., Edge, A. C., & Fabian, A. C. 2002, MNRAS, 337, 938

Bell, E. F., McIntosh, D. H., Katz, N., & Weinberg, M. D. 2003, ApJS, 149, 289

Best, P. N., von der Linden, A., Kauffmann, G., Heckman, T. M., & Kaiser, C. R. 2007, MNRAS, 379, 894

Bialy, S., & Sternberg, A. 2015, MNRAS, 450, 4424

Bigiel, F., Leroy, A., Walter, F., et al. 2008, AJ, 136, 2846

Binggeli, B. 1982, A&A, 107, 338

Bîrzan, L., Rafferty, D. A., McNamara, B. R., Wise, M. W., & Nulsen, P. E. J. 2004, ApJ, 607, 800

Bîrzan, L., Rafferty, D. A., Nulsen, P. E. J., et al. 2012, MNRAS, 427, 3468

Blanton, E. L., Sarazin, C. L., McNamara, B. R., & Wise, M. W. 2001, ApJ, 558, L15

Blitz, L., & Rosolowsky, E. 2006, ApJ, 650, 933

Boehringer, H., Voges, W., Fabian, A. C., Edge, A. C., & Neumann, D. M. 1993, MNRAS, 264, L25

Böhringer, H., Burwitz, V., Zhang, Y.-Y., Schuecker, P., & Nowak, N. 2005, ApJ, 633, 148

Bolatto, A. D., Jackson, J. M., & Ingalls, J. G. 1999, ApJ, 513, 275

Bolatto, A. D., Wolfire, M., & Leroy, A. K. 2013, ARA&A, 51, 207

Bourda, G., Charlot, P., Porcas, R. W., & Garrington, S. T. 2010, A&A, 520, A113

Bower, R. G., Benson, A. J., Malbon, R., et al. 2006, MNRAS, 370, 645

Braine, J., & Dupraz, C. 1994, A&A, 283, 407

Bridges, T. J., & Irwin, J. A. 1998, MNRAS, 300, 967

Burns, J. O. 1990, AJ, 99, 14

Burns, J. O., White, R. A., & Haynes, M. P. 1981, AJ, 86, 1120

Canizares, C. R., Clark, G. W., Jernigan, J. G., & Markert, T. H. 1982, ApJ, 262, 33

Canizares, C. R., Markert, T. H., & Donahue, M. E. 1988, in NATO Advanced Science Institutes (ASI) Series C, Vol. 229, NATO Advanced Science Institutes (ASI) Series C, ed. A. C. Fabian, 63–72

Canning, R. E. A., Sun, M., Sanders, J. S., et al. 2013, MNRAS, 435, 1108

Cardelli, J. A., Clayton, G. C., & Mathis, J. S. 1989, ApJ, 345, 245

Carilli, C. L., Perley, R. A., & Harris, D. E. 1994, MNRAS, 270, 173

Casoli, F., Dupraz, C., & Combes, F. 1992, A&A, 264, 55

Cavagnolo, K. W., Donahue, M., Voit, G. M., & Sun, M. 2008, ApJ, 683, L107

Cavagnolo, K. W., McNamara, B. R., Nulsen, P. E. J., et al. 2010, ApJ, 720, 1066

Cavaliere, A., & Fusco-Femiano, R. 1976, A&A, 49, 137

Churazov, E., Brüggen, M., Kaiser, C. R., Böhringer, H., & Forman, W. 2001, ApJ, 554, 261

Churazov, E., Forman, W., Jones, C., & Böhringer, H. 2000, A&A, 356, 788

Cicone, C., Maiolino, R., Sturm, E., et al. 2014, A&A, 562, A21

Conselice, C. J., Gallagher, III, J. S., & Wyse, R. F. G. 2001, AJ, 122, 2281

Cowie, L. L., & Binney, J. 1977, ApJ, 215, 723

Cowie, L. L., Hu, E. M., Jenkins, E. B., & York, D. G. 1983, ApJ, 272, 29

Crawford, C. S., Allen, S. W., Ebeling, H., Edge, A. C., & Fabian, A. C. 1999, MNRAS, 306, 857

Crawford, C. S., Edge, A. C., Fabian, A. C., et al. 1995, MNRAS, 274, 75

Crawford, C. S., Sanders, J. S., & Fabian, A. C. 2005, MNRAS, 361, 17

Croton, D. J., Springel, V., White, S. D. M., et al. 2006, MNRAS, 365, 11

Dame, T. M., Hartmann, D., & Thaddeus, P. 2001, ApJ, 547, 792

Danielson, A. L. R., Swinbank, A. M., Smail, I., et al. 2013, MNRAS, 436, 2793

Dasyra, K. M., & Combes, F. 2011, A&A, 533, L10

Dasyra, K. M., Combes, F., Oosterloo, T., et al. 2016, A&A, 595, L7

David, L. P., Lim, J., Forman, W., et al. 2014, ApJ, 792, 94

di Serego Alighieri, S., Gavazzi, G., Giovanardi, C., et al. 2007, A&A, 474, 851

Dickman, R. L. 1978, ApJS, 37, 407

Donahue, M., de Messières, G. E., O'Connell, R. W., et al. 2011, ApJ, 732, 40

Donahue, M., Sun, M., O'Dea, C. P., Voit, G. M., & Cavagnolo, K. W. 2007, AJ, 134, 14

Donahue, M., & Voit, G. M. 1993, ApJ, 414, L17

Donahue, M., Connor, T., Fogarty, K., et al. 2015, ApJ, 805, 177

Downes, D., & Solomon, P. M. 1998, ApJ, 507, 615

Draine, B. T., & Salpeter, E. E. 1979, ApJ, 231, 77

Dunn, R. J. H., & Fabian, A. C. 2006, MNRAS, 373, 959

Dunn, R. J. H., Fabian, A. C., & Taylor, G. B. 2005, MNRAS, 364, 1343

Dwarakanath, K. S., Owen, F. N., & van Gorkom, J. H. 1995, ApJ, 442, L1

Edge, A. C. 2001, MNRAS, 328, 762

Edge, A. C., & Frayer, D. T. 2003, ApJ, 594, L13

Edge, A. C., Stewart, G. C., Fabian, A. C., & Arnaud, K. A. 1990, MNRAS, 245, 559

Edge, A. C., Wilman, R. J., Johnstone, R. M., et al. 2002, MNRAS, 337, 49

Egami, E., Misselt, K. A., Rieke, G. H., et al. 2006, ApJ, 647, 922

Ehlert, S., McDonald, M., David, L. P., Miller, E. D., & Bautz, M. W. 2015, ApJ, 799, 174

Fabian, A. C. 1994, ARA&A, 32, 277

—. 2012, ARA&A, 50, 455

Fabian, A. C., Johnstone, R. M., Sanders, J. S., et al. 2008, Nature, 454, 968

Fabian, A. C., & Nulsen, P. E. J. 1977, MNRAS, 180, 479

Fabian, A. C., Sanders, J. S., Crawford, C. S., et al. 2003, MNRAS, 344, L48

Fabian, A. C., Sanders, J. S., Ettori, S., et al. 2001, MNRAS, 321, L33

Fabian, A. C., Sanders, J. S., Taylor, G. B., et al. 2006, MNRAS, 366, 417

Fabian, A. C., Sanders, J. S., Williams, R. J. R., et al. 2011, MNRAS, 417, 172

Farage, C. L., McGregor, P. J., & Dopita, M. A. 2012, ApJ, 747, 28

Ferland, G. J., Fabian, A. C., Hatch, N. A., et al. 2009, MNRAS, 392, 1475

Ferland, G. J., Fabian, A. C., & Johnstone, R. M. 1994, MNRAS, 266, 399

Ferrarese, L., & Merritt, D. 2000, ApJ, 539, L9

Ferrière, K. M. 2001, Reviews of Modern Physics, 73, 1031

Feruglio, C., Maiolino, R., Piconcelli, E., et al. 2010, A&A, 518, L155

Fogarty, K., Postman, M., Connor, T., Donahue, M., & Moustakas, J. 2015, ApJ, 813, 117

Forman, W., Kellogg, E., Gursky, H., Tananbaum, H., & Giacconi, R. 1972, ApJ, 178, 309

Forman, W., Nulsen, P., Heinz, S., et al. 2005, ApJ, 635, 894

Forman, W., Jones, C., Churazov, E., et al. 2007, ApJ, 665, 1057

Frerking, M. A., Langer, W. D., & Wilson, R. W. 1982, ApJ, 262, 590

Gaspari, M., Ruszkowski, M., & Oh, S. P. 2013, MNRAS, 432, 3401

Gaspari, M., Ruszkowski, M., & Sharma, P. 2012, ApJ, 746, 94

Gaspari, M., McDonald, M., Hamer, S. L., et al. 2018, ApJ, 854, 167

Gelderman, R. 1996, in Astronomical Society of the Pacific Conference Series, Vol. 88, Clusters, Lensing, and the Future of the Universe, ed. V. Trimble & A. Reisenegger, 168

Gendron-Marsolais, M., Hlavacek-Larrondo, J., Martin, T. B., et al. 2018, ArXiv e-prints, arXiv:1802.00031

Giacconi, R., Kellogg, E., Gorenstein, P., Gursky, H., & Tananbaum, H. 1971, ApJ, 165, L27

Giacintucci, S., Markevitch, M., Brunetti, G., Cassano, R., & Venturi, T. 2011, A&A, 525, L10

Gitti, M., Nulsen, P. E. J., David, L. P., McNamara, B. R., & Wise, M. W. 2011, ApJ, 732, 13

Grabelsky, D. A., & Ulmer, M. P. 1990, ApJ, 355, 401

Graham, A. W., Erwin, P., Trujillo, I., & Asensio Ramos, A. 2003, AJ, 125, 2951

Greve, T. R., Papadopoulos, P. P., Gao, Y., & Radford, S. J. E. 2009, ApJ, 692, 1432

Grossi, M., di Serego Alighieri, S., Giovanardi, C., et al. 2009, A&A, 498, 407

Gursky, H., Kellogg, E., Murray, S., et al. 1971, ApJ, 167, L81

Hamer, S. L., Edge, A. C., Swinbank, A. M., et al. 2012, MNRAS, 421, 3409

—. 2014, MNRAS, 437, 862

—. 2016, MNRAS, 460, 1758

Harrison, A., Henkel, C., & Russell, A. 1999, MNRAS, 303, 157

Hatch, N. A., Crawford, C. S., & Fabian, A. C. 2007, MNRAS, 380, 33

Hatch, N. A., Crawford, C. S., Fabian, A. C., & Johnstone, R. M. 2005, MNRAS, 358, 765

Hatch, N. A., Crawford, C. S., Johnstone, R. M., & Fabian, A. C. 2006, MNRAS, 367, 433

Häußler, B., Bamford, S. P., Vika, M., et al. 2013, MNRAS, 430, 330

Haynes, M. P., Giovanelli, R., & Chincarini, G. L. 1984, ARA&A, 22, 445

Heckman, T. M. 1981, ApJ, 250, L59

Heckman, T. M., Baum, S. A., van Breugel, W. J. M., & McCarthy, P. 1989, ApJ, 338, 48

Henkel, C., Asiri, H., Ao, Y., et al. 2014, A&A, 565, A3

Hernquist, L. 1990, ApJ, 356, 359

Heyer, M., & Dame, T. M. 2015, ARA&A, 53, 583

Hitomi Collaboration, Aharonian, F., Akamatsu, H., et al. 2016, Nature, 535, 117

Hlavacek-Larrondo, J., Fabian, A. C., Edge, A. C., et al. 2012, MNRAS, 421, 1360

Hogan, M. T., McNamara, B. R., Pulido, F., et al. 2017a, ApJ, 837, 51

Hogan, M. T., Edge, A. C., Hlavacek-Larrondo, J., et al. 2015a, MNRAS, 453, 1201

Hogan, M. T., Edge, A. C., Geach, J. E., et al. 2015b, MNRAS, 453, 1223

Hogan, M. T., McNamara, B. R., Pulido, F. A., et al. 2017b, ApJ, 851, 66

Hu, E. M., Cowie, L. L., & Wang, Z. 1985, ApJS, 59, 447

Huchra, J. P., Macri, L. M., Masters, K. L., et al. 2012, ApJS, 199, 26

Hudson, D. S., Mittal, R., Reiprich, T. H., et al. 2010, A&A, 513, A37

Humphrey, P. J., Buote, D. A., Gastaldello, F., et al. 2006, ApJ, 646, 899

Israel, F. P. 2009, A&A, 506, 689

Jáchym, P., Combes, F., Cortese, L., Sun, M., & Kenney, J. D. P. 2014, ApJ, 792, 11

Jáchym, P., Sun, M., Kenney, J. D. P., et al. 2017, ApJ, 839, 114

Jackson, J. M., Paglione, T. A. D., Carlstrom, J. E., & Rieu, N.-Q. 1995, ApJ, 438, 695

Jaffe, W., Bremer, M. N., & Baker, K. 2005, MNRAS, 360, 748

Johnstone, R. M., Fabian, A. C., & Nulsen, P. E. J. 1987, MNRAS, 224, 75

Johnstone, R. M., Hatch, N. A., Ferland, G. J., et al. 2007, MNRAS, 382, 1246

Kaastra, J. S., Ferrigno, C., Tamura, T., et al. 2001, A&A, 365, L99

Kalberla, P. M. W., Burton, W. B., Hartmann, D., et al. 2005, A&A, 440, 775

Kelly, B. C. 2007, ApJ, 665, 1489

Kenney, J. D. P., & Young, J. S. 1989, ApJ, 344, 171

Kennicutt, R. C., & Evans, N. J. 2012, ARA&A, 50, 531

Kennicutt, Jr., R. C. 1998, ARA&A, 36, 189

Kinney, A. L., Calzetti, D., Bohlin, R. C., et al. 1996, ApJ, 467, 38

Kirkpatrick, C. C., & McNamara, B. R. 2015, MNRAS, 452, 4361

Kirkpatrick, C. C., McNamara, B. R., & Cavagnolo, K. W. 2011, ApJ, 731, L23

Kirkpatrick, C. C., McNamara, B. R., Rafferty, D. A., et al. 2009, ApJ, 697, 867

Kormendy, J., Fisher, D. B., Cornell, M. E., & Bender, R. 2009, ApJS, 182, 216

Langer, W. D., & Penzias, A. A. 1990, ApJ, 357, 477

Lauer, T. R., Faber, S. M., Richstone, D., et al. 2007, ApJ, 662, 808

Lavaux, G., & Hudson, M. J. 2011, MNRAS, 416, 2840

Lebrun, F., Bennett, K., Bignami, G. F., et al. 1983, ApJ, 274, 231

Li, Y., & Bryan, G. L. 2014a, ApJ, 789, 54

—. 2014b, ApJ, 789, 153

Li, Y., Ruszkowski, M., & Bryan, G. L. 2017, ApJ, 847, 106

Li, Y., Ruszkowski, M., & Tremblay, G. 2018, ApJ, 854, 91

Licquia, T. C., & Newman, J. A. 2015, ApJ, 806, 96

Lim, J., Ao, Y., & Dinh-V-Trung. 2008, ApJ, 672, 252

Lim, J., Ohyama, Y., Chi-Hung, Y., Dinh-V-Trung, & Shiang-Yu, W. 2012, ApJ, 744, 112

Lin, Y.-T., Mohr, J. J., & Stanford, S. A. 2003, ApJ, 591, 749

Lynds, R. 1970, ApJ, 159, doi:10.1086/180500

Lynds, R., & Toomre, A. 1976, ApJ, 209, 382

Main, R., McNamara, B., Nulsen, P., Russell, H., & Vantyghem, A. 2015, ArXiv e-prints, arXiv:1510.07046

Mangum, J. G., & Shirley, Y. L. 2015, PASP, 127, 266

Mao, R.-Q., Schulz, A., Henkel, C., et al. 2010, ApJ, 724, 1336

Mazzotta, P., Edge, A. C., & Markevitch, M. 2003, ApJ, 596, 190

McCourt, M., Sharma, P., Quataert, E., & Parrish, I. J. 2012, MNRAS, 419, 3319

McDonald, M., Gaspari, M., McNamara, B. R., & Tremblay, G. R. 2018, ApJ, 858, 45

McDonald, M., & Veilleux, S. 2009, ApJ, 703, L172

McDonald, M., Veilleux, S., & Rupke, D. S. N. 2012a, ApJ, 746, 153

McDonald, M., Veilleux, S., Rupke, D. S. N., & Mushotzky, R. 2010, ApJ, 721, 1262

McDonald, M., Veilleux, S., Rupke, D. S. N., Mushotzky, R., & Reynolds, C. 2011, ApJ, 734, 95

McDonald, M., Wei, L. H., & Veilleux, S. 2012b, ApJ, 755, L24

McKee, C. F., & Ostriker, E. C. 2007, ARA&A, 45, 565

McMullin, J. P., Waters, B., Schiebel, D., Young, W., & Golap, K. 2007, in Astronomical Society of the Pacific Conference Series, Vol. 376, Astronomical Data Analysis Software and Systems XVI, ed. R. A. Shaw, F. Hill, & D. J. Bell, 127

McNamara, B. R. 2004, in The Riddle of Cooling Flows in Galaxies and Clusters of galaxies, ed. T. Reiprich, J. Kempner, & N. Soker

McNamara, B. R., & Jaffe, W. 1994, A&A, 281, 673

McNamara, B. R., Jannuzi, B. T., Elston, R., Sarazin, C. L., & Wise, M. 1996, ApJ, 469, 66

McNamara, B. R., Kazemzadeh, F., Rafferty, D. A., et al. 2009, ApJ, 698, 594

McNamara, B. R., & Nulsen, P. E. J. 2007, ARA&A, 45, 117

—. 2012, New Journal of Physics, 14, 055023

McNamara, B. R., Nulsen, P. E. J., Wise, M. W., et al. 2005, Nature, 433, 45

McNamara, B. R., & O'Connell, R. W. 1989, AJ, 98, 2018

McNamara, B. R., O'Connell, R. W., & Bregman, J. N. 1990, ApJ, 360, 20

McNamara, B. R., Rohanizadegan, M., & Nulsen, P. E. J. 2011, ApJ, 727, 39

McNamara, B. R., Russell, H. R., Nulsen, P. E. J., et al. 2016, ApJ, 830, 79

McNamara, B. R., Wise, M., Nulsen, P. E. J., et al. 2000, ApJ, 534, L135

McNamara, B. R., Russell, H. R., Nulsen, P. E. J., et al. 2014, ApJ, 785, 44

Milam, S. N., Savage, C., Brewster, M. A., Ziurys, L. M., & Wyckoff, S. 2005, ApJ, 634, 1126

Mitchell, R. J., Culhane, J. L., Davison, P. J. N., & Ives, J. C. 1976, MNRAS, 175, 29P

Morganti, R., Oosterloo, T., Oonk, J. B. R., Frieswijk, W., & Tadhunter, C. 2015, A&A, 580, A1

Morganti, R., Tadhunter, C. N., & Oosterloo, T. A. 2005, A&A, 444, L9

Morris, R. G., & Fabian, A. C. 2003, MNRAS, 338, 824

Nesvadba, N. P. H., Lehnert, M. D., Eisenhauer, F., et al. 2006, ApJ, 650, 693

Niederste-Ostholt, M., Strauss, M. A., Dong, F., Koester, B. P., & McKay, T. A. 2010, MNRAS, 405, 2023

Nishimura, A., Tokuda, K., Kimura, K., et al. 2015, ApJS, 216, 18

Nulsen, P. E. J. 1986, MNRAS, 221, 377

Nulsen, P. E. J., Hambrick, D. C., McNamara, B. R., et al. 2005, ApJ, 625, L9

Nulsen, P. E. J., Jones, C., Forman, W. R., et al. 2007, in Heating versus Cooling in Galaxies and Clusters of Galaxies, ed. H. Böhringer, G. W. Pratt, A. Finoguenov, & P. Schuecker, 210

O'Dea, C. P., Baum, S. A., & Gallimore, J. F. 1994, ApJ, 436, 669

O'Dea, C. P., Baum, S. A., Privon, G., et al. 2008, ApJ, 681, 1035

Oegerle, W. R., & Hill, J. M. 1994, AJ, 107, 857

Ogrean, G. A., Hatch, N. A., Simionescu, A., et al. 2010, MNRAS, 406, 354

Okabe, N., Umetsu, K., Tamura, T., et al. 2016, MNRAS, 456, 4475

Oonk, J. B. R., Jaffe, W., Bremer, M. N., & van Weeren, R. J. 2010, MNRAS, 405, 898

Panagoulia, E. K., Fabian, A. C., & Sanders, J. S. 2013, MNRAS, 433, 3290

Panagoulia, E. K., Fabian, A. C., Sanders, J. S., & Hlavacek-Larrondo, J. 2014, MNRAS, 444, 1236

Papadopoulos, P. P., van der Werf, P., Xilouris, E., Isaak, K. G., & Gao, Y. 2012, ApJ, 751, 10

Peng, C. Y., Ho, L. C., Impey, C. D., & Rix, H.-W. 2002, AJ, 124, 266

—. 2010, AJ, 139, 2097

Peterson, J. R., & Fabian, A. C. 2006, Phys. Rep., 427, 1

Peterson, J. R., Paerels, F. B. S., Kaastra, J. S., et al. 2001, A&A, 365, L104

Petitpas, G. R., & Wilson, C. D. 2000, ApJ, 538, L117

Petrov, L. 2013, AJ, 146, 5

Pineda, J. L., Goldsmith, P. F., Chapman, N., et al. 2010, ApJ, 721, 686

Pinkney, J., Holtzman, J., Garasi, C., et al. 1996, ApJ, 468, L13

Pizzolato, F., & Soker, N. 2005, ApJ, 632, 821

—. 2010, MNRAS, 408, 961

Planck Collaboration, Ade, P. A. R., Aghanim, N., et al. 2016, A&A, 594, A13

Poggianti, B. M. 1997, A&AS, 122, astro-ph/9608029

Prasad, D., Sharma, P., & Babul, A. 2015, ApJ, 811, 108

Protassov, R., van Dyk, D. A., Connors, A., Kashyap, V. L., & Siemiginowska, A. 2002, ApJ, 571, 545

Pulido, F. A., McNamara, B. R., Edge, A. C., et al. 2018, ApJ, 853, 177

Quillen, A. C., Zufelt, N., Park, J., et al. 2008, ApJS, 176, 39

Rafferty, D. A., McNamara, B. R., & Nulsen, P. E. J. 2008, ApJ, 687, 899

Rafferty, D. A., McNamara, B. R., Nulsen, P. E. J., & Wise, M. W. 2006, ApJ, 652, 216

Reiprich, T. H., & Böhringer, H. 2002, ApJ, 567, 716

Revaz, Y., Combes, F., & Salomé, P. 2008, A&A, 477, L33

Richings, A. J., & Faucher-Giguere, C.-A. 2017, ArXiv e-prints, arXiv:1706.03784

Rieke, G. H., Alonso-Herrero, A., Weiner, B. J., et al. 2009, ApJ, 692, 556

Robitaille, T. P., & Whitney, B. A. 2010, ApJ, 710, L11

Roediger, E., Brüggen, M., Simionescu, A., et al. 2011, MNRAS, 413, 2057

Romanishin, W., & Hintzen, P. 1988, ApJ, 324, L17

Rupke, D. S. N., & Veilleux, S. 2011, ApJ, 729, L27

Russell, H. R., Sanders, J. S., & Fabian, A. C. 2008, MNRAS, 390, 1207

Russell, H. R., McNamara, B. R., Edge, A. C., et al. 2014, ApJ, 784, 78

Russell, H. R., McNamara, B. R., Fabian, A. C., et al. 2016, MNRAS, 458, 3134

Russell, H. R., McDonald, M., McNamara, B. R., et al. 2017a, ApJ, 836, 130

Russell, H. R., McNamara, B. R., Fabian, A. C., et al. 2017b, MNRAS, 472, 4024

Sakelliou, I., Peterson, J. R., Tamura, T., et al. 2002, A&A, 391, 903

Salim, S., Rich, R. M., Charlot, S., et al. 2007, ApJS, 173, 267

Salomé, P., & Combes, F. 2003, A&A, 412, 657

Salomé, P., & Combes, F. 2004, in SF2A-2004: Semaine de l'Astrophysique Francaise, ed. F. Combes, D. Barret, T. Contini, F. Meynadier, & L. Pagani, 505

Salomé, P., Combes, F., Revaz, Y., et al. 2011, A&A, 531, A85

—. 2008, A&A, 484, 317

Salomé, P., Combes, F., Edge, A. C., et al. 2006, A&A, 454, 437

Salomé, Q., Salomé, P., Combes, F., & Hamer, S. 2016a, ArXiv e-prints, arXiv:1605.05986

Salomé, Q., Salomé, P., Combes, F., Hamer, S., & Heywood, I. 2016b, A&A, 586, A45

Salomé, Q., Salomé, P., Miville-Deschênes, M.-A., Combes, F., & Hamer, S. 2017, A&A, 608, A98

Sanders, D. B., Scoville, N. Z., Young, J. S., et al. 1986, ApJ, 305, L45

Sanders, J. S., & Fabian, A. C. 2007, MNRAS, 381, 1381

Sanders, J. S., Fabian, A. C., & Taylor, G. B. 2009, MNRAS, 396, 1449

Sarazin, C. L. 1988, X-ray emission from clusters of galaxies

Sarazin, C. L., Baum, S. A., & O'Dea, C. P. 1995, ApJ, 451, 125

Schlafly, E. F., & Finkbeiner, D. P. 2011, ApJ, 737, 103

Schwartz, D. A., Schwarz, J., & Tucker, W. 1980, ApJ, 238, L59

Scoville, N. Z., & Sanders, D. B. 1987, in Astrophysics and Space Science Library, Vol. 134, Interstellar Processes, ed. D. J. Hollenbach & H. A. Thronson, Jr., 21–50

Scoville, N. Z., Yun, M. S., Sanders, D. B., Clemens, D. P., & Waller, W. H. 1987, ApJS, 63, 821

SDSS Collaboration, Albareti, F. D., Allende Prieto, C., et al. 2016, ArXiv e-prints, arXiv:1608.02013

Serlemitsos, P. J., Smith, B. W., Boldt, E. A., Holt, S. S., & Swank, J. H. 1977, ApJ, 211, L63

Sharma, P., McCourt, M., Quataert, E., & Parrish, I. J. 2012, MNRAS, 420, 3174

Shostak, G. S., van Gorkom, J. H., Ekers, R. D., et al. 1983, A&A, 119, L3

Simionescu, A., Tremblay, G., Werner, N., et al. 2018, MNRAS, 475, 3004

Simionescu, A., Werner, N., Böhringer, H., et al. 2009, A&A, 493, 409

Simionescu, A., Werner, N., Finoguenov, A., Böhringer, H., & Brüggen, M. 2008, A&A, 482, 97

Singh, K. P., Westergaard, N. J., & Schnopper, H. W. 1986, ApJ, 308, L51

—. 1988, ApJ, 331, 672

Solomon, P. M., Rivolo, A. R., Barrett, J., & Yahil, A. 1987, ApJ, 319, 730

Solomon, P. M., Sanders, D. B., & Scoville, N. Z. 1979, ApJ, 232, L89

Solomon, P. M., & Vanden Bout, P. A. 2005, ARA&A, 43, 677

Sparks, W. B., Donahue, M., Jordán, A., Ferrarese, L., & Côté, P. 2004, ApJ, 607, 294

Sturm, E., González-Alfonso, E., Veilleux, S., et al. 2011, ApJ, 733, L16

Su, Y., Nulsen, P. E. J., Kraft, R. P., et al. 2017, ApJ, 847, 94

Sun, M., Jones, C., Forman, W., et al. 2006, ApJ, 637, L81

Tadhunter, C., Morganti, R., Rose, M., Oonk, J. B. R., & Oosterloo, T. 2014, Nature, 511, 440

Tamura, T., Bleeker, J. A. M., Kaastra, J. S., Ferrigno, C., & Molendi, S. 2001a, A&A, 379, 107

Tamura, T., Kaastra, J. S., Peterson, J. R., et al. 2001b, A&A, 365, L87

Tonnesen, S., Bryan, G. L., & Chen, R. 2011, ApJ, 731, 98

Tremblay, G. R., O'Dea, C. P., Baum, S. A., et al. 2015, MNRAS, 451, 3768

Tremblay, G. R., Oonk, J. B. R., Combes, F., et al. 2016, Nature, 534, 218

Tremblay, G. R., Combes, F., Oonk, J. B. R., et al. 2018, ArXiv e-prints, arXiv:1808.00473

Ueda, J., Iono, D., Yun, M. S., et al. 2014, ApJS, 214, 1

Valentijn, E. A., & Giovanelli, R. 1982, A&A, 114, 208

Vantyghem, A. N., McNamara, B. R., Russell, H. R., et al. 2014, MNRAS, 442, 3192

—. 2016, ApJ, 832, 148

Vantyghem, A. N., McNamara, B. R., Edge, A. C., et al. 2017, ApJ, 848, 101

Vantyghem, A. N., McNamara, B. R., Russell, H. R., et al. 2018, ArXiv e-prints, arXiv:1807.04331

Verdugo, C., Combes, F., Dasyra, K., Salomé, P., & Braine, J. 2015, A&A, 582, A6

Véron-Cetty, M.-P., & Véron, P. 2010, A&A, 518, A10

Villar-Martín, M., Sánchez, S. F., De Breuck, C., et al. 2006, MNRAS, 366, L1

Voit, G. M. 2018, ArXiv e-prints, arXiv:1803.06036

Voit, G. M., Cavagnolo, K. W., Donahue, M., et al. 2008, ApJ, 681, L5

Voit, G. M., & Donahue, M. 2015, ApJ, 799, L1

Voit, G. M., Meece, G., Li, Y., et al. 2017, ApJ, 845, 80

Vollmer, B., Braine, J., Pappalardo, C., & Hily-Blant, P. 2008, A&A, 491, 455

Walker, S. A., Kosec, P., Fabian, A. C., & Sanders, J. S. 2015, MNRAS, 453, 2480

Wall, W. F., Jaffe, D. T., Bash, F. N., et al. 1993, ApJ, 414, 98

Ward, J. S., Zmuidzinas, J., Harris, A. I., & Isaak, K. G. 2003, ApJ, 587, 171

Watson, W. D., Anicich, V. G., & Huntress, Jr., W. T. 1976, ApJ, 205, L165

Weinberger, R., Ehlert, K., Pfrommer, C., Pakmor, R., & Springel, V. 2017, MNRAS, 470, 4530

Weiß, A., Walter, F., & Scoville, N. Z. 2005, A&A, 438, 533

Werner, N., de Plaa, J., Kaastra, J. S., et al. 2006, A&A, 449, 475

Werner, N., Sun, M., Bagchi, J., et al. 2011, MNRAS, 415, 3369

Werner, N., Oonk, J. B. R., Canning, R. E. A., et al. 2013, ApJ, 767, 153

Werner, N., Oonk, J. B. R., Sun, M., et al. 2014, MNRAS, 439, 2291

Whiley, I. M., Aragón-Salamanca, A., De Lucia, G., et al. 2008, MNRAS, 387, 1253

White, D. A., Fabian, A. C., Johnstone, R. M., Mushotzky, R. F., & Arnaud, K. A. 1991, MNRAS, 252, 72

Wilman, R. J., Edge, A. C., McGregor, P. J., & McNamara, B. R. 2011, MNRAS, 416, 2060

Wilson, C. D., Howe, J. E., & Balogh, M. L. 1999, ApJ, 517, 174

Wise, M. W., McNamara, B. R., Nulsen, P. E. J., Houck, J. C., & David, L. P. 2007, ApJ, 659, 1153

Wolfire, M. G., Hollenbach, D., & McKee, C. F. 2010, ApJ, 716, 1191

Wu, J., Evans, II, N. J., Gao, Y., et al. 2005, ApJ, 635, L173

Young, A. J., Wilson, A. S., & Mundell, C. G. 2002, ApJ, 579, 560

Young, L. M., Bureau, M., Davis, T. A., et al. 2011, MNRAS, 414, 940

APPENDICES

Appendix A

Other Contributions

In addition to the research that I conducted in this thesis, I have also collaborated on several projects on similar topics. This Appendix summarizes the publications resulting from these projects. For each publication I participated in the scientific discussion and provided comments on drafts of the manuscripts.

A.1 Additional ALMA Observations of BCGs

The observations that I have presented in this thesis are part of a larger project aimed toward utilizing ALMA to further our understanding of molecular gas in galaxy clusters. In addition to the three targets that I have analyzed, I have collaborated on two more: PKS 0745-191 (Russell et al., 2016) and Abell 1795 (Russell et al., 2017b).

PKS0745-191 was observed in ALMA Cycle 1, which offered a significant improvement in sensitivity and resolution over Cycle 0 observations. The BCGs that had previously been observed with ALMA (A1664, A1835) were already indicative of massive molecular flows that were influenced by AGN feedback, but PKS 0745-191 strengthened this conclusion considerably. Very little of its molecular gas is coincident with the central AGN. All $4.6\times10^9\,M_\odot$ is situated in three $3-5$ kpc long filaments extending radially from the galactic center, two of which trail X-ray cavities. The velocities are low and linewidths are narrow, characteristics that have become increasingly common with subsequent BCG observations. The velocity structure is inconsistent with either a merger origin or gravitational free-fall of cooling gas. The projection of the filaments behind X-ray cavities strongly implicates AGN uplift as the trigger for their formation.

ALMA observations of A1795 painted a different picture of the interaction between AGN and molecular gas. Instead of molecular filaments trailing X-ray cavities, its filaments are projected around the outer edge of two radio bubbles. The smooth velocity gradients and close connection with the radio jets suggest that the filaments are gas flows that have been entrained by the expanding radio bubbles. However, the $3.2 \times 10^9\,\mathrm{M}_\odot$ of molecular gas contained in the two filaments is too large to have been lifted entirely by the radio bubbles. Stimulated cooling is still a plausible mechanism for forming the molecular gas, but multiple generations of AGN activity are required in order to account for the gas mass and distribution. The connection between molecular gas and radio jets then implies that the cold gas either deflects the expanding radio bubbles or is pushed aside and shaped as the bubbles inflate.

A.2 Thermal Instabilities in Clusters and Ellipticals

I have also collaborated on projects that study the formation of molecular gas by focusing on the hot atmosphere from which it condenses. These publications have used Chandra X-ray observations to investigate thermal instabilities within the ICM.

Thermal instabilities in cluster plasma rely critically on local dynamical timescales, such as the free-fall time. This requires an accurate representation of the cluster's gravitating mass on all scales, extending from its outskirts into the central galaxy. In Hogan et al. (2017a) we developed a technique for measuring cluster mass profiles over a wide radial range. We modeled the mass distribution using a singular isothermal sphere anchored to the mass of the BCG and an NFW profile fitted to the X-ray data. The method was tested on, and in good agreement with, a small sample of clusters with deep *Chandra* observations and good ancillary tracers of gravitating mass on both large and small scales.

This technique was subsequently applied to a much larger sample of galaxy clusters with the aim of identifying thresholds for thermal instabilities. This was performed in two companion papers, which used either luminous Hα emission (Hogan et al., 2017b) or single dish detections of molecular gas (Pulido et al., 2018) as a tracer of cold gas.

Motivated by prior observations and simulations, the cooling time (t_{cool}) and the ratio between the cooling and free-fall times ($t_{\mathrm{cool}}/t_{\mathrm{ff}}$) were both evaluated as potential indicators for gas condensation. Originally observational work argued that cold gas is present in systems with central cooling times below 0.5 Gyr, while more recent work argued that thermal instabilities ensued when $t_{\mathrm{cool}}/t_{\mathrm{ff}}$ falls below 10. With the more accurate mass profiles presented in Hogan et al. (2017b) and Pulido et al. (2018), we found that the

minimum $t_{\rm cool}/t_{\rm ff}$ lies between 10 and 30, rarely falling below 10. The narrow spread can plausibly result from selection effects. These works both find that $t_{\rm cool}/t_{\rm ff}$ provides no more predictive power for the onset of thermally unstable cooling than the cooling time alone.

AGN feedback must operate gently in cluster environments. The density profiles, when normalized to the median value at 100 kpc, show very little scatter in the centers of cool core clusters. However, these systems all experience feedback with differing powers. Systems with the most powerful jets evidently do not experience large swings in their central gas density.

The amount of molecular gas in a BCG is uncorrelated with either of the instability indicators. Molecular gas is only present below certain thresholds, but the mass is apparently unconnected to the severity of the thermal instability. Instead, molecular gas mass is strongly and positively correlated with both the central atmospheric gas density and mass. More massive clusters beget more molecular gas, provided their central cooling time is short. Additionally, the time required for molecular gas to be consumed in star formation is $\sim 5 \times 10^8$ yr on average, showing no trend with molecular gas mass.

We subsequently extended this X-ray analysis to lower mass early-type galaxies (Babyk et al., 2018a). We began by measuring the temperatures, X-ray luminosities, and total masses of these galaxies. The scaling relations between these quantities are steeper than expected from self-similarity. Additional heating, such as from supernovae or AGN feedback, are required to produce the observed relations.

In Babyk et al. (2018b) we presented entropy profiles of low mass galaxies and faint groups, combining them with our results from higher mass systems (Hogan et al., 2017b; Pulido et al., 2018). At large radii the entropy profiles of high mass systems scale slightly below the $K \propto R^{1.1}$ expected from purely gravitational halo assembly. Within $\sim 0.1 R_{2500}$ the entropy profiles of elliptical, lenticular, and spiral galaxies, in addition to BCGs, all scale as $K \propto R^{2/3}$. This consistency suggests that the entropy profile near the galaxy or cluster center is universal. This scaling is closely related to the central galaxy itself, and corresponds to a constant ratio of cooling time to free-fall time. It implies that AGN feedback is able to maintain a rough balance between heating and cooling throughout the entire $K \propto R^{2/3}$ region. As a result, the hot atmospheres of early-type galaxies are heated at a higher rate per gas particle than BCGs, which may explain why they are dormant.